Human Cytochrome P450 Enzymes in Drug Metabolism and Chemical Activation

by

Aaron G. Bart

A dissertation submitted in partial fulfillment
of the requirements for the degree of
Doctor of Philosophy
(Biophysics)
in the University of Michigan
2020

Doctoral Committee:

Professor Emily E. Scott, Chair
Professor Richard J. Auchus
Assistant Professor Aaron T. Frank
Assistant Professor Sarah C. Keane

Aaron G. Bart

agbart@umich.edu

ORCID iD: 0000-0002-8605-4151

Acknowledgements

I would like to thank everyone that has supported me throughout my graduate career. I am grateful to Dr. Fernando Estrada, Dr. Klaus Pors, Dr. Aggi Walsh, Dr. Ryan Takahashi, Dr. Xiaojing Wang, Dr. Elizabeth Gillam, Dr. Kurt Harris, Sarah Burris, Cara Loomis, and Nicholas Martinez for direct contributions in at least one of the projects described in this dissertation. Additionally, I would like to thank the many Scott Lab members for their various support through the years: Dr. Simone Brixius-Anderko, Dr. Elyse Petrunak, Dr. Natasha DeVore, Dr. Linda Blake, Dr. Malika Godamudunage, Dr. Rahul Yadav, Dr. Kathy Meneely, and many others.

I am also very grateful to Dr. Richard Auchus, Dr. Sarah Keane, and Dr. Aaron Frank for serving as committee members throughout my career as a graduate student at the University of Michigan. I would also specifically like to thank Dr. Victor Day, whom I first met as an undergraduate student. Victor taught me some of the fundamentals of crystallography and has continued to support me through the years as a graduate student. Additional thanks to Dr. Audrey Lamb, Dr. Mario Rivera, Dr. Roberto De Guzman, Dr. Yoshiaki Azuma, and Dr. Susan Egan for being on my committee when I started graduate school at the University of Kansas.

Most importantly, I am extremely grateful to my advisor Dr. Emily Scott who was willing to first take me into her lab as a biochemistry undergraduate student with little to no lab experience. I cannot thank her enough for her trust, mentorship, and support through the ups and downs. Dr. Scott has been on my side throughout the years and I feel so fortunate in being in her lab, she is quite possibly the best mentor any student could ask for.

TABLE OF CONTENTS

List of Tables

List of Figures

Abstract

The cytochrome P450 superfamily are heme-containing monooxygenases found ubiquitously in living organisms. In humans, P450 enzymes are essential in the metabolism of drugs, pollutants, and foods, as well as in endogenous biosynthetic pathways for steroids, fatty acids, and vitamins. Thus, these enzymes can be sources of deleterious effects in humans, with issues relating to drug safety and efficacy, metabolism of compounds into carcinogens or toxins, and disruptions of signaling pathways. Prediction of P450 metabolism and design of selective P450 inhibitors are of great importance for human health. Furthermore, leveraging the diversity in P450 catalysis holds promise as biocatalysts for production of synthetically difficult chemicals and green chemistry. In both health and as biocatalysts, limited understanding of P450 structure and conformational flexibility hinders the rational pursuit of these goals. Understanding P450 structure and flexibility is complicated by the diverse compounds P450 enzymes bind and metabolize, and by structural changes that may occur when P450 enzymes interact with modulatory protein partners. This dissertation explores structural features allowing human P450 enzymes to interact with a protein partner, bind and metabolize diverse substrates, and structural interactions which contribute to a thermostable P450 biocatalyst.

To understand how the catalytic modulator protein cytochrome b_5 exerts variable effects on P450 catalysis, b_5 complexes with different human drug-metabolizing P450 enzymes were characterized using NMR. These experiments revealed that P450 enzymes bind shared and distinct surfaces on b_5 and have varied complex affinity. Mutating key residues on b_5 confirmed the importance of individual b_5 amino acids and functional experiments helped link complex

formation to b_5 modulation of P450 function. The aspect of P450 flexibility in response to diverse ligands they interact with was probed through X-ray structures of the human P450 1A1, which has prominent roles in carcinogen and toxin activation. This work demonstrated that CYP1A1 undergoes conformational changes in the active site roof when bound to structurally diverse ligands, and also revealed channels allowing CYP1A1 to bind larger and nonplanar ligands. Increased understanding of CYP1A1 structural conformations provides a valuable resource for computational prediction of the binding, metabolism, and activation of drugs and chemicals. For utilization of mammalian P450 enzymes as efficient biocatalysts, obstacles such as poor thermostability and activity need to be resolved. The discovery that reconstructed ancestors of mammalian P450 enzymes have significantly improved thermostability provides a promising route for using these enzymes as biocatalysts, but structural contributors to this enhanced thermostability are unknown. Both structure and ligand binding of the mammalian ancestor of human CYP1B1 were characterized to examine sources for increased thermostability. The structures of the ancestor CYP1B1 display an open active site conformation deviating significantly in the roof elements in comparison to the closed structure of human CYP1B1. Substrate binding and activity reveal similar substrate profiles but altered regioselectivity for the metabolites. Comparison of the ancestral and human CYP1B1 structure suggest that gains in thermostability may occur through increased electrostatic and aromatic/cation stacking interactions between distinct secondary structure elements. The combined results of this dissertation provide valuable insight into P450 structure and conformational flexibility for improvements in drug design, predictions of metabolic outcomes, and development of thermostable P450 enzymes in biotechnology.

CHAPTER 1

Introduction

Cytochrome P450 enzymes are a superfamily of monooxygenases found in the majority of living organisms. P450 enzymes have evolved to accept a wide range of substrates. In humans 57 different cytochromes P450 provide many critical functions that range from generation of endogenous biomolecules such as hormones and fatty acids to roles in xenobiotic metabolism encompassing dietary, environmental, and pharmaceutical chemicals. A large repertoire of P450 transformations includes chemically difficult oxidation reactions. These reactions are enabled by activating molecular oxygen using a heme prosthetic group. There is considerable pharmaceutical interest in these enzymes because human P450 enzymes metabolize approximately 75% of the most commonly prescribed drugs (1). This large P450 contribution to drug metabolism can result in issues related to altered drug bioavailability and adverse drug-drug interactions. Moreover, from a toxicology perspective, P450 enzymes bioactivate toxins and chemical carcinogens that can be found in drugs, environmental pollutants, and dietary sources.

The wide variety of substrates catalyzed by cytochromes P450 occur through a number of different enzyme isoforms, with one example of a human isoform being CYP3A4. As a superfamily, P450 enzymes are arranged into families and subfamilies, classified by amino acid sequence identity. Families share approximately 40% or greater percent identity and are represented with an Arabic number, the "3" in the preceding example. P450 families are subdivided into subfamilies (55% amino acid identity), which are represented by capital letters,

1

such as "A" in CYP3A4. Finally, the terminal Arabic number specifies individual isoforms within

a subfamily. In humans the 57 P450 enzymes fall into 18 families and 41 subfamilies, which

typically share a major substrate type (Table 1.1). The majority of human P450 enzymes are in

the xenobiotic and steroid substrate classes and for the most part human P450 families 1-3 are

considered to be the major contributors towards drug metabolism. A significant number of P450

enzymes are also considered "orphans", in which their primary substrate class has not been

established (2). In this thesis, human P450 enzymes from the xenobiotic substrate class are the

focus.

Table 1.1 Major substrate classes for human cytochrome P450 enzymes.

Xenobiotics	Sterols	Fatty Acids	Eicosanoids	Vitamins	Unknown
1A1	1B1	2J2	4F2	2R1	2A7
1A2	7A1	2U1	4F3	24A1	2S1
2A6	7B1	4A11	4F8	26A1	2W1
2A13	8B1	4B1	5A1	26B1	4A22
2B6	11A1	4F11	8A1	26C1	4F22
2C8	11B1	4F12		27B1	4X1
2C9	11B2	4V2		27C1	4Z1
2C18	17A1				20A1
2C19	19A1				
2D6	21A2				
2E1	27A1				
2F1	39A1				
3A4	46A1				
3A5	51A1				
3A7					
3A43					

1.1 Cytochrome P450 Spectroscopic Features

Central to cytochrome P450 catalysis is the iron-containing heme prosthetic group, which

activates molecular oxygen. The heme group is buried within the protein environment, with the

iron proximally coordinated to an absolutely conserved cysteine. Unique spectral signals in the UV-visible range result from the P450 heme, and are sensitive to the chemical environment and redox state of the iron. The most intense of these absorbance signals is the Soret band. When the heme is in a resting state with distal water coordination, the Soret absorbance is ~418 nm (3). Both substrates and inhibitors of P450 enzymes can perturb the spin-state of the heme iron. Such an event typically results in at least three spectral modes, which are commonly viewed as optical difference spectra between the ligand-free and ligand-bound spectra (Figure 1.1). Difference spectrum resulting in migration of the Soret to shorter wavelengths (blue-shift) with a maximum at ~393 nm and minima at ~420 nm are termed "Type I" (shown as a blue trace in Figure 1.1). This "Type I" mode has been commonly characterized as a ligand displacing the distal water, but not itself coordinating to the heme iron, causing the iron to be in a penta-coordinate, high-spin state (4). Ligands that cause the Soret to shift to a longer wavelength (red shift) with a maximum at ~424 nm, and minimum at ~390 nm in the difference spectra are referred to as "Type II" (red trace in Figure 1.1). The "Type II" mode, observed often with nitrogen-containing heterocycles, is generally accepted to represent distal coordination to the iron by the ligand, resulting in a hexa-coordinate, low-spin state (4). A third mode, known as "Reverse Type I", is also observed, and is characterized by a difference spectrum with a maximum at 415-420 nm and minimum at ~393 nm (green trace Figure 1.1). This "Reverse Type I" mode is not well characterized but it is thought to be through coordination of the heme iron by a non-nitrogen heteroatom, or through a water-bridged ligand-to-iron interaction (5). These spectral characteristics are a useful way to determine how a ligand is oriented in the P450 active site. Additionally, observing these progressive spectral

changes as a function of ligand concentration is a convenient way to determine the dissociation constant (K_d).
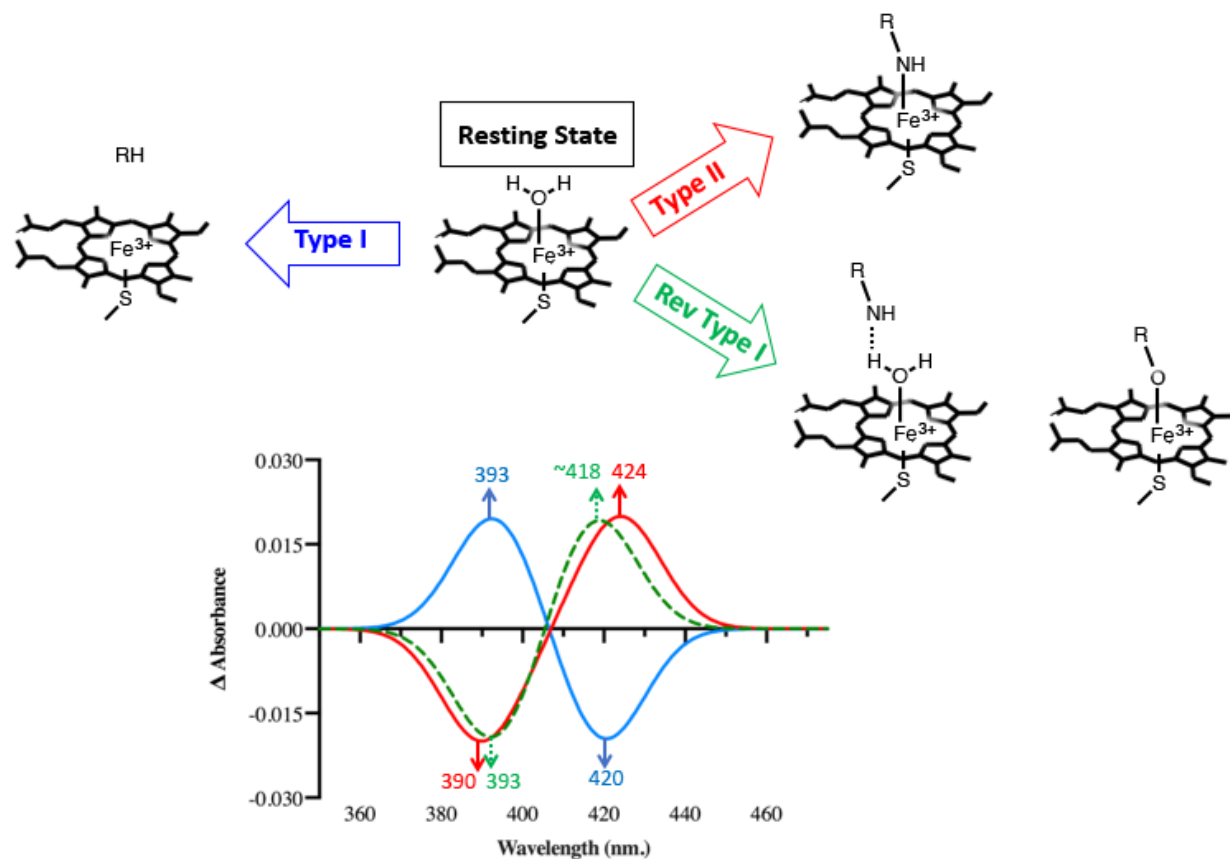
Figure 1.1 Ligand-induced spectral alterations in P450 enzymes. Ligands can perturb the heme iron coordination state resulting in unique changes to the UV-Vis spectral signal. Ligands (denoted as R) can displace a water typically coordinated to the heme in the resting state to cause one of three main difference spectra (type I: blue, type II: red, reverse type I: green).

In addition to the liganded state, the Soret band also provides a useful measurement of P450 concentration, purity, and stability. The concentration of the enzyme can be assessed using the Soret absorbance, extinction coefficient, and Beer's law. The relative purity can be measured by the ratio of Soret to ~280 nm absorbance. Additionally, both concentration and stability assessments can be performed using a reduced-carbon monoxide difference spectrum, in which the heme iron is chemically reduced from the ferric (Fe^{3+}) to ferrous (Fe^{2+}) state in the presence of carbon monoxide (6). Under these conditions the Soret absorbance red-shifts to ~450 nm due to carbon monoxide ligation (Figure 1.2). Generally, the presence of an absorbance peak at 450 nm

in this difference spectrum is consistent with active P450 enzyme and can be quantitated using an extinction coefficient. Alternatively, the reduced CO-difference spectrum can also produce an absorbance peak with a wavelength of 420 nm, which indicates a disruption of the heme-thiolate interaction and has been considered to be an inactive form of these enzymes (7).
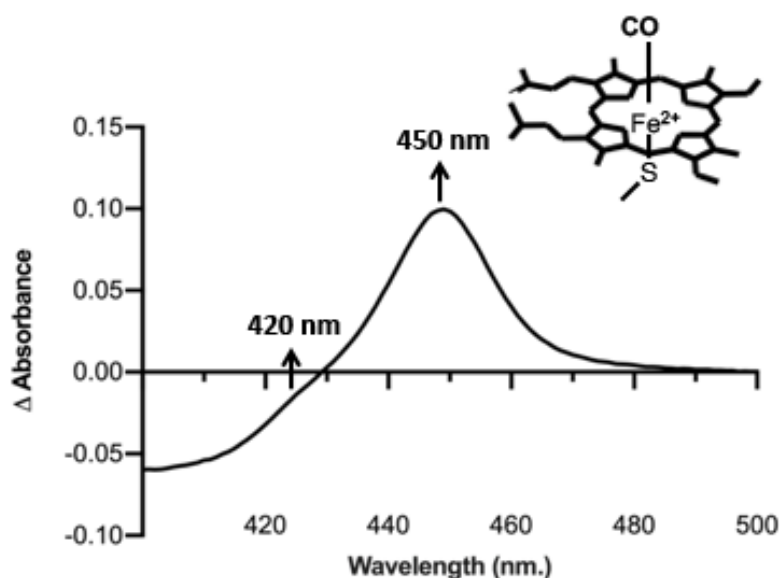
Figure 1.2 P450 CO-difference spectrum. Spectral changes of a P450 enzyme when reduced and bound to carbon monoxide gives characteristic Soret absorbance at ~450 nm for which the enzyme superfamily is named.

1.2 Cytochrome P450 Catalytic Cycle

P450 catalysis is represented in a cyclical reaction mechanism, involving multiple steps (Figure 1.3). In general, the initial or resting state of the cycle is water coordination to the heme iron, serving as a distal ligand (*a*). The next step is typically substrate (R-H) binding in close proximity to the heme iron, displacing the distally coordinated water (*b*). Substrate binding induces an increase in redox potential, which makes the heme iron a more favorable electron acceptor. For the endoplasmic reticulum (ER)-bound P450 enzymes discussed in this dissertation thesis the flavin-containing protein cytochrome P450 reductase (CPR) transfers one electron from NADPH to the P450, transitioning the heme iron from a ferric to ferrous state (*b* to *c*). Molecular oxygen then rapidly binds to the ferrous iron (*c* to *d*). In continuation of the cycle, a second electron

5

can be delivered by CPR or in some cases a heme-containing protein termed cytochrome b_5 (d to

e), to generate a peroxo-ferric species (e). Subsequently two protonation events occur, first

forming a hydroperoxo intermediate (f), and then an oxyferryl complex (g) after oxygen cleavage.

This oxyferryl iron state, termed "compound I", is thought to be the main oxidizing species for

P450 enzymes, first abstracting a hydrogen from the substrate and then rebounding to form the

product metabolite (represented as R-OH, step h). The resulting metabolite is released by the P450

and water again coordinates to the heme iron (h to a) to regenerate the initial state (a).
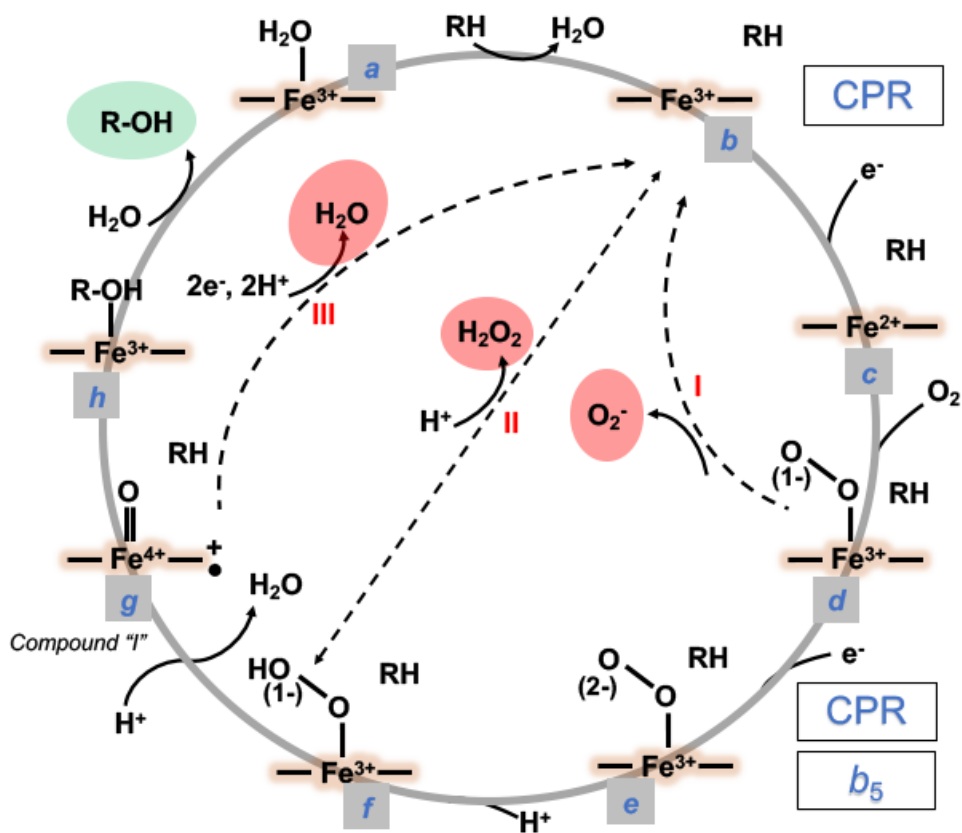
Figure 1.3 General cytochrome P450 catalytic cycle. Main productive pathway steps are shown on the grey circle (labeled steps a-h). Nonproductive shunt pathways are indicated with dashed lines (pathways I-III). P450 substrate is denoted as RH, and metabolized product as R-OH. Figure adapted from Denisov *et al*. (8).

In addition to productive completion of the catalytic cycle as illustrated above, P450

enzymes also have three nonproductive pathways or shunts. These shunts ultimately regenerate

the ferric P450, but depending on which part of the catalytic cycle they occur produce either

superoxide (I), hydrogen peroxide (II), or extra water (III) (Figure 1.3). The efficiency with which a P450 enzyme uses NADPH reducing equivalents for product formation versus shunting pathways is the coupling efficiency. Funneling of reducing equivalents into the nonproductive shunt pathways is observed in most xenobiotic metabolizing human P450 enzymes, which typically have very low coupling efficiency compared to the more efficient bacterial P450 enzymes.

1.3 Structure of Cytochrome P450

The overall fold of the cytochrome P450 superfamily is highly conserved. It consists of a single globular domain composed of 12 major alpha-helices (designated A-L), a beta-sheet region of 3-4 sheets, and a varied number of shorter helices (denoted with a prime) (Figure 1.4). Despite conservation of the global fold, substantial diversity in the amino acid sequence, differential positioning of secondary structure components, and potentially varied conformational dynamics, permit the wide range of accommodated substrates and reactions that P450 enzymes perform. The P450 fold forms around the heme prosthetic group, which is roughly located in the center of the enzyme and forms a "floor" in the active site cavity (Figure 1.4, black sticks). Residing underneath, or proximal to the heme is the coordinated cysteine thiolate which is located in a loop region (Figure 1.4, shown in orange) just prior to the L helix. The top or distal face of the heme is flanked by the I helix (Figure 1.4, yellow) which spans the breadth of the P450, and contains a generally conserved alcohol/acid residue pair implicated in P450 protonation steps. Other structural elements such as the B-C loop (sometimes forming a short helix termed B′) (Figure 1.4, blue), and variable loop regions (Figure 1.4, red and magenta) form the remaining sides of the active site cavity. The most distal portions of the active site cavity or roof are formed by helices F through G (Figure 1.4, green), which are perpendicular to the I helix, and have been implicated

in ligand entry and egress routes, particularly for many hydrophobic substrates which are thought

to access the buried active site from the membrane-bound face of the catalytic domain.
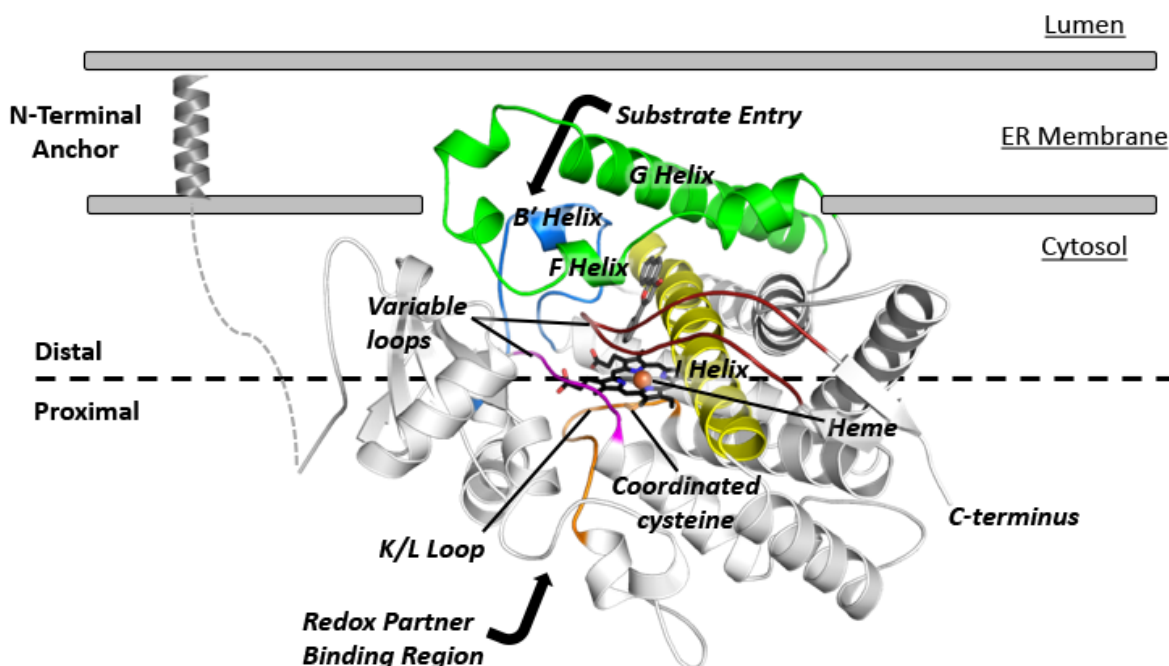
Figure 1.4 Global structure of a human cytochrome P450 enzyme located in the ER. In addition to membrane anchoring through a N-terminal helix, ER-bound mammalian P450 enzymes have partial membrane insertion of the globular domain. Major structural elements typically forming the enclosed active site cavity are colored and labeled. The two halves of the globular heme containing domain are commonly referred to as distal and proximal sides, this separation is by the plane of the heme (shown as a bold dashed line). Structure shown is human CYP1A1 bound to ANF (PDB code: 4I8V).

While prokaryotic cytochromes P450 are soluble enzymes, the mammalian P450 enzymes

are membrane-bound and those involved in xenobiotic metabolism are largely localized in the

endoplasmic reticulum. These ER-bound P450 enzymes possess an N-terminal transmembrane

helix, which in part secures them to the cytosolic face of the ER membrane. Additionally, the

membrane-bound mammalian P450 enzymes have regions forming the distal protein surface,

namely the F/G loop (sometimes forming short helices designated F′ and G′), the exterior of which

are largely hydrophobic and partially embedded into the membrane. Even with deletion of the N-

terminal anchoring helix, recombinantly-expressed mammalian P450 enzymes are retained in

membrane fractions, and require high ionic strength and/or detergent to extract the protein from

the membrane. Deletion of the N-terminal anchoring helix is a common modification used to generate higher recombinant P450 expression levels and greater solubility in mammalian P450 enzymes (9). Almost all of the crystal structures of mammalian cytochromes P450 have been solved without the anchoring membrane helix. These truncated enzymes still retain catalytic function consistent with the idea that the membrane helix likely serves as a tether and does not influence the structure of the heme-containing catalytic domain.

P450 structures have generally been solved in what is colloquially termed a closed state, where the cavity above the heme is isolated from the protein exterior (as shown in Figure 1.4). In order for ligands to access the active site, P450 enzymes must make conformational adjustments to allow for ligand entrance, as well as for product egress. Some isoforms have been solved in both open and closed states (8), and comparisons between these states have largely pointed towards conformational changes occurring primarily in the F/G region associated with the membrane (10). These conformational motions can lead to access channels for substrate entry. Additionally, entrance of typically hydrophobic substrates through the F/G region logically makes sense since this region of the P450 would typically be embedded or in contact with the membrane, allowing for energetically more favorable partitioning of hydrophobic substrates into the P450.

1.4 Interactions of P450 with P450 Reductase and Cytochrome b_5

To perform catalysis, P450 enzymes require electrons. For the human ER-bound enzymes, these are primarily delivered by NADPH-cytochrome P450 oxidoreductase (CPR). CPR is a diflavin protein containing the cofactors flavin adenine dinucleotide (FAD) and flavin mononucleotide (FMN). These flavins are located on separate domains, named for the cofactor they respectively bind, joined by a short flexible hinge (Figure 1.5). CPR, like P450 enzymes, are anchored onto the ER membrane. For CPR this is through a N-terminal membrane binding domain

preceding the FMN domain. A current proposal on how electron transfer occurs between CPR and P450 enzymes is as follows: 1) NADPH binds to the CPR FAD domain. 2) The FAD flavin is reduced. 3) An interflavin electron transfer from FAD to FMN cofactors occurs. 4) The FAD and FMN domains move apart. 5) The exposed FMN domain forms protein-protein contacts with the proximal surface of a P450 enzyme. 6) The reduced FMN cofactor transfers one electron to the P450 heme (11). The interaction between CPR and P450 enzymes has been partially defined through site-directed mutagenesis and crosslinking studies (12-15) for some mammalian P450 isoforms, and is thought to be governed through a combination of electrostatic and van der Waals interactions (11). In general, the primary interaction surfaces are the negatively charged surface around the CPR FMN and the positively charged proximal surface of the P450.

In addition to P450 reductase, some cytochrome P450 enzymes can also receive electrons from the heme-containing protein cytochrome b_5 (16,17). Cytochrome b_5 is a relatively small protein with an approximate molecular weight of 15 kDa. In terms of structural topology, b_5 is partitioned into a globular heme-containing domain, a C-terminal membrane anchored helix, and a flexible linker connecting the two (Figure 1.5) (11). The heme of b_5 is in a partially solvent-exposed cleft, with coordination by two histidine residues on the proximal and distal positions, and functions as a one-electron acceptor and donor. This heme-exposed face of b_5 is composed of four helical elements ($\alpha 2$-$\alpha 5$), which contain multiple negatively charged aspartates and glutamates, and possesses a convex shape. No structures of the cytochrome b_5/P450 complex are currently available, however much information has been gained for multiple P450 isoforms through a combination of mutagenesis, cross-linking, and some NMR studies (16,18-22). Similar to CPR, b_5 also binds the P450 proximal surface. This interaction has been postulated to be driven through electrostatic pairing between the two proteins, however there appear to be some

differences in which b_5 residues are important for interactions with individual P450 enzymes (18,22-24). It is thought that b_5 and CPR largely compete for the same binding surface on P450 enzymes, because b_5 can inhibit reduction of ferric P450 by CPR under certain conditions (25), and NMR shows direct displacement (26,27). Although cytochrome b_5 and CPR have been shown to have mutually exclusive binding behavior, the interaction area is thought to not be completely shared because certain proximal P450 mutations have differential effects on binding either b_5 or CPR (12,26).
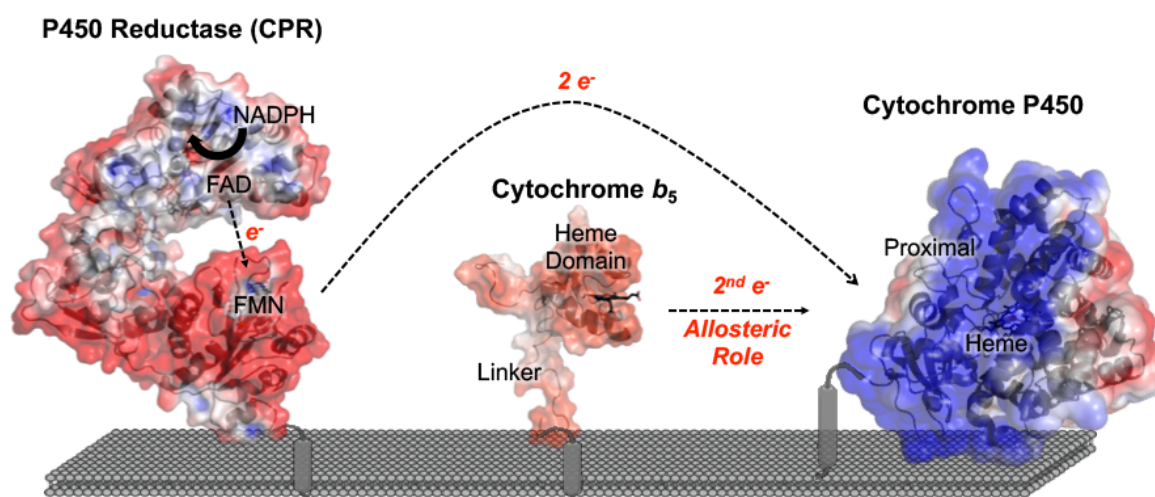
Figure 1.5 The eukaryotic, ER-bound cytochrome P450 protein system. Proteins P450 reductase (CPR) and cytochrome b_5 can act as electron donating partners and/or allosteric modulators of P450 enzymes. Proteins are shown in electrostatic surface representation. Both CPR and b_5 have large anionic surfaces areas, while cytochrome P450 enzymes typically have a cationic-charged proximal surface.

A high-resolution complex between any mammalian P450 enzyme and partner protein (CPR or b_5) remains to be solved. Although important residues have been identified for some P450 isoforms, residue information for many of the human P450 isoforms have not been reported. In addition to specific residues on the P450 forming complexes with b_5 or CPR, little is known if conformational changes in the proteins are induced by complex formation.

1.5 P450 Modulation by Cytochrome b_5 : Proposed Mechanisms

The exact roles that b_5 plays in catalysis has long been quite enigmatic (25,28-30). In general, b_5 is not required for P450 catalysis. Rather it functions as a modulator of P450 reactions. As a modulator, b_5 has been reported to have diverse responses on P450 reactions ranging from increasing P450 productive turnover of substrates, to having no measurable effect on product formation, and even inhibiting P450 catalysis (17,25). These varied effects appear to be dependent on both the P450 isoform and substrate under study, and in some cases the assay conditions. Even with these different responses, cytochrome b_5 has frequently displayed the ability to increase coupling of the P450 catalytic cycle, by reducing unproductive reducing equivalent consumption via shunt pathways (31,32).

Numerous mechanisms for how cytochrome b_5 alters P450 activity have been proposed. A major mechanism has been through b_5 functioning as a redox partner in P450 catalysis. Cytochrome b_5 is capable of donating the second electron to P450 enzymes, but typically is not capable of supplying the first electron due to the high redox potential relative to ferric P450 (32). Delivery of the second electron is thought to be one of the rate-limiting steps in the catalytic cycle, and it has been hypothesized that b_5 can donate this electron at a faster rate than CPR (33). Faster delivery of the second electron would presumably prevent decomposition of the oxy-ferrous P450 species through the superoxide shunting pathway, and allow for a greater percentage of NADPH to be utilized to support product formation.

Experiments showing increases of P450 turnover with redox-silent b_5, either through heme removal or substitution with Zn-protoporphyrin IX, have also prompted an alternative mechanism (17,19,34). This has been proposed as an allosteric role, where the physical interaction between a P450 and cytochrome b_5 causes conformational changes in the P450 (19,32) This allosteric

mechanism is supported by the ability of b_5 binding to influence the spectral spin state of some P450 enzymes (35). This suggests that binding of b_5 on the proximal P450 surface can transmit conformational changes into the heme active site. Cytochrome b_5 has also been proposed to modulate proton delivery to a P450 heme intermediate (36), which would likely occur through conformational alterations affecting the proton delivery network. Recently NMR experiments on the steroidogenic P450 17A1, which is modulated by b_5, displayed perturbations of resonances in distal areas of the P450 (I helix and F/G region) (37), approximately 25-35 Å away from the b_5 binding site. These observations suggest b_5 could modulate substrate positioning since residues in the F/G region can form direct and indirect interactions with substrates. Alterations in substrate positioning may lead to more precise binding geometry during catalysis, and could be an avenue for increased coupling and product formation. Lastly it is possible that b_5 modulation occurs through multiple steps within the catalytic cycle, that the mechanisms employed are isoform/substrate dependent, or a combination of mechanisms are operative. Regardless of the mechanisms employed, cytochrome b_5 binding has significant implications for P450 catalysis. Chapter 2 of this dissertation explores the b_5/P450 interaction by probing the complexes through solution NMR.

1.6 Cytochrome P450 Enzymes Involved in Pro-carcinogenic and Toxin Activation

P450 enzymes can generate a variety of products from substrates they metabolize. These products or metabolites often possess differing chemical properties from the original substrate, thus having the potential for altered interactions with the body. For xenobiotic human P450 enzymes a common metabolic route is generating metabolites with increased water solubility, thereby leading to excretion or enabling further metabolism with eventual elimination from the body. In some cases, P450-mediated drug metabolites can increase the pharmacological activity

towards the drug target. One example is the breast cancer drug tamoxifen which has significantly

increased anticancer activity once it is metabolically converted to the active metabolite endoxifen,

which is predominately mediated by CYP2D6 (38). Accordingly, poor response to this anticancer

drug has been observed in patients possessing low CYP2D6 activity (39). Besides forming

metabolites destined for elimination or playing roles in prodrug activation, P450 enzymes can also

bioactivate compounds, resulting in metabolites with carcinogenic and/or toxic properties (40-42).

This has important implications since many chemical carcinogens require enzymatic bioactivation

to be genotoxic and P450 enzymes are considered major contributors to this process (43). Human

P450 isoforms that generate carcinogenic metabolites, include those in Figure 1.6. Almost half of

this activation is by the family 1 (CYP1) human cytochrome P450 enzymes, which include three

isoforms, CYP1A1, CYP1A2, and CYP1B1 (44).
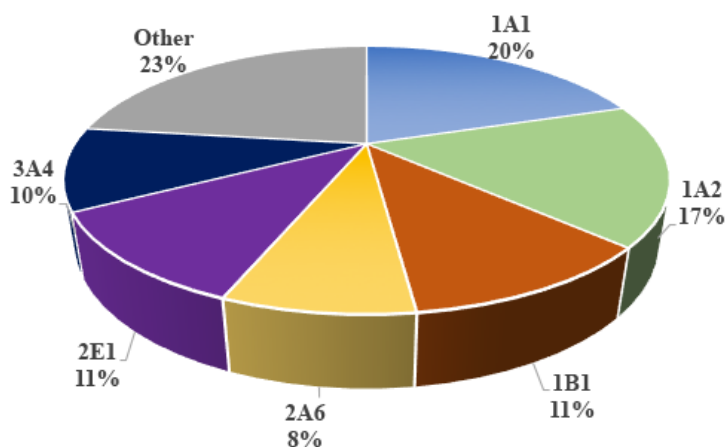
Figure 1.6 Contribution of human P450 isoforms in the activation of known carcinogens. Figure adapted and data from Rendic and Guengerich (44).

Within the human CYP1 family, the CYP1A2 isoform is considered one of the major

xenobiotic metabolizing P450 enzymes, representing about 15% of the total P450 pool in the liver

and contributing to the metabolism of many common drug substrates, including acetaminophen

and caffeine (45). In contrast, isoforms CYP1A1 and CYP1B1 are largely found in extrahepatic

tissues with relatively low constitutive expression levels (45). Expression of CYP1A1 has been predominately found in the lungs (46,47), whereas CYP1B1 expression in normal tissues on a mRNA level is distributed into areas such as the kidney, prostate, uterus, and mammary gland to name a few (48). High expression of CYP1B1 has been shown in a large variety of different tumor tissues on a protein level (49).

Common substrates for the CYP1 enzymes include small molecule scaffolds such as polycyclic aromatic hydrocarbons (PAHs), and heterocyclic and aryl amines (48). These substrate classes possess physical chemical features such as high planarity and aromaticity, and low molecular weight. Crystal structures of the human enzymes CYP1A1, CYP1A2, and CYP1B1 have been solved, all in complex with a small, aromatic hydrocarbon compound known as alpha-naphthoflavone (ANF) (50-52). The active site cavity for all three of the P450 enzymes are narrow, planar pockets, consistent with the common substrate classes observed for these enzymes.

As discussed previously both CYP1A1 and CYP1B1 enzymes are not constitutively expressed at high levels, however these CYP1 family members are significantly induced by some xenobiotics, including combustion smoke constituents. This occurs via the aryl hydrocarbon receptor (AhR), which is activated by binding agonist molecules, many of which are known CYP1 substrates, resulting in AhR translocation into the nucleus (Figure 1.7). Once in the nucleus, AhR binds specific xenobiotic response elements leading to transcriptional activation of family 1 P450 genes (53). This is reflected by both CYP1A1 and CYP1B1 upregulation in smokers and ex-smokers versus non-smokers, with chemicals found in cigarette smoke known to be AhR agonists (54).
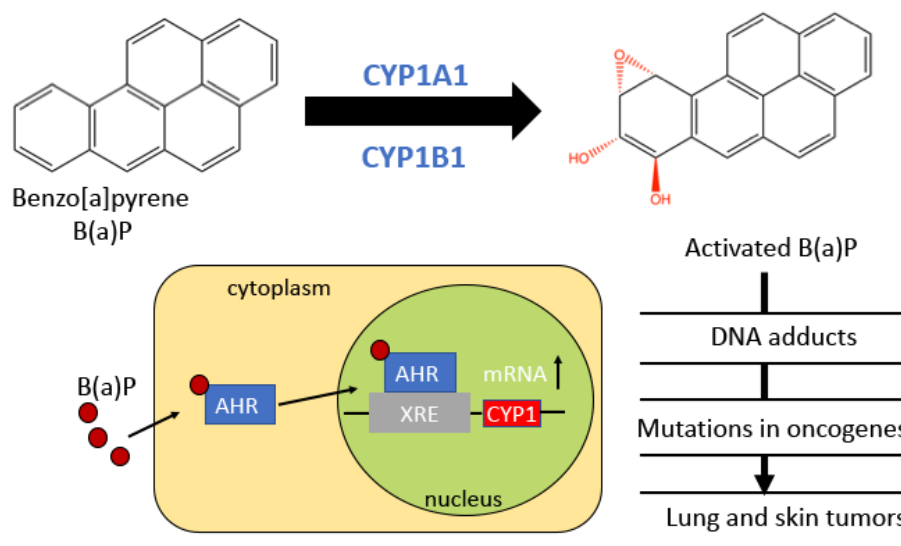
Figure 1.7 Bioactivation of a primary environmental pollutant, benzo[a]pyrene (B[a]P). This bioactivation process of B[a]P into a potent carcinogen is mediated by CYP1A1 and CYP1B1. The family 1 P450 enzymes are highly inducible. Many CYP1 substrates (including B[a]P) activate the aryl-hydrocarbon receptor (AhR) resulting in transcriptional upregulation of these P450 enzymes, and thus increased production of carcinogenic compounds.

1.7 CYP1A1 Role in Metabolic Activation of Tyrosine Kinase Inhibitors

An area of rapid drug development has been targeted kinase inhibitors for the treatment of various cancer types, with more recent expansion into other disease areas (55). In the span of just 15 years, ~30 small molecule kinase inhibitors have been approved for clinical use, with many more currently in clinical trials (56). One of the proposed advantages of these targeted therapies in oncology has been the potential of reduced toxicities in comparison to conventional chemotherapy. However, a number of kinase inhibitors have received "black box warnings" from the FDA for life-threating issues due to various toxicities (56). Although occurring only in a subset of patients, the toxicities associated with these drugs can limit the use of these potentially lifesaving therapeutics. The underlaying mechanism of how hepatotoxicity is induced by some of these kinase inhibitors still is largely unknown. However, insight into possible initiation mechanisms can be garnered from other drug classes that cause hepatotoxicity or drug-induced liver injury (DILI). DILI generally stems from reactive metabolite generation, resulting in direct toxicity and/or immune responses (57). Due to their abundance in the liver, cytochrome P450 enzymes

16

have been major sources of DILI for a number of different drugs. Additionally, a number of studies have linked specific human P450 isoforms to the generation of reactive metabolites. Currently these have included the clinically available tyrosine kinase inhibitors: dasitinib, gefitinib, erlotinib, lapatinib, imatinib, axitinib, ponatinib, and sunitinib, as well some investigational tyrosine kinase inhibitors (56).

The human cytochrome P450 enzyme CYP1A1 has been associated with producing reactive metabolites for a number of these kinase inhibitors (58-60). The role of CYP1A1 in this process is interesting since it is not expressed significantly in the liver. However relatively few studies have measured CYP1A1 expression on a protein or activity level in the human liver, and of these studies CYP1A1 expression has varied widely between liver preparations and individuals (61-63). Furthermore, a number of clinical drugs, including some of the tyrosine kinase inhibitors, such as erlotinib and axitinib, have considerable interindividual variability in drug pharmacokinetics, and have shown associations with a history of smoking (64,65). This could indicate CYP1A1 liver expression has wide interindividual variability and/or is induced through AhR ligands such as those found in cigarette or combustion smoke. Other toxicities, such as interstitial lung disease, have also been reported for some of the tyrosine kinase inhibitors such as imatinib, gefitinib, and erlotinib, and generally correlated with smoking as a risk factor (59,66,67).

The ability of CYP1A1 to accommodate and ultimately metabolize these larger and structurally diverse kinase inhibitors is difficult to rationalize from a structural perspective given the previously known CYP1A1 restrictive active site dimensions. The inability of the initial CYP1A1 structure with ANF to predict how these larger classes of compounds are accommodated is not only a question specific to CYP1A1. The scope of conformational malleability is an open question for many human P450 enzymes. To date 24 of the 57 human P450 structures by X-ray crystallography

have been solved. Of these roughly 20% only have a single crystal structure. Are the current range of P450 structures sufficient to explain known substrate and inhibitor scopes? Chapters 3 and 4 of this dissertation focus on addressing this question of P450 structural malleability, specifically for the human CYP1A1 enzyme, by solving new structures complexed with ligands with increased structural diversity. Ultimately the goal of these investigations is to generate the structural resources to predict the carcinogenic or toxic metabolite generation of new compounds.

1.8 P450 Prodrug Strategy for Engineered Duocarmycins in Cancer Therapy

P450 metabolism is known to activate numerous prodrug compounds. In many cases this feature was not initially designed into the drug, but rather found to occur during characterization (68). Due to the reaction diversity of cytochrome P450 enzymes and tissue selective sites of expression for some P450s, prodrugs designed for specific activation hold promise for targeting drug action to selective cells and tissues. This is in contrast to enzymes common in prodrug activation that are expressed systemically such as esterases (69). One attractive prodrug strategy has been to develop extremely potent chemotherapeutics that are activated only in specific tumor tissues. Recently a scaffold based on the highly cytotoxic duocarmycins has been engineered for P450-mediated prodrug activation (Figure 1.8) (70). The duocarmycins represent a family of natural product compounds, first isolated from *Streptomyces* (71). These compounds are exceptionally potent cytotoxic agents which bind and alkylate DNA in a sequence-selective manner. Clinically the duocarmycins, and derivatives of these compounds, were found to have extreme systemic toxicity profiles, due to nonspecific effects, which halted their development (71). Due to their potency and mechanisms of action, interest has still been maintained in using engineered duocarmycins clinically, with various approaches to target the drugs in tumors. These

include antibody-drug conjugates or masking of a DNA-alkylating chloromethylindoline moiety with subsequent reduction or cleavage in tumor cells (72,73).

P450-mediated activation of pro-duocarmycins has been developed utilizing a *seco*-duocarmycin scaffold (Figure 1.8). This eliminates the DNA-alkylating cyclopropane and a key hydroxyl moiety (70). These *seco*-duocarmycins are designed for P450 enzymes to selectively install a hydroxyl group at a key site, resulting in spontaneous regeneration of the alkylating cyclopropane (Figure 1.8, bioactivation pathway). Previously this site-specific oxidation was found to be exclusively performed by two human P450 enzymes, CYP1A1 and CYP2W1, and not by the major hepatic P450 enzymes (74). CYP1A1, as described previously, has variable expression levels in different tissues, with the most common site of expression in the lungs. There are some indications of overexpression of CYP1A1 in tumor tissues, however numerous studies have found expression in normal tissues as well (75). In contrast CYP2W1, considered an orphan P450, has been only found in select tumor tissues. Significant mRNA and protein levels of CYP2W1 have been found in approximately a third of adult colon cancers (76). Thus, selective bioactivation of *seco*-duocarmycins by CYP2W1 needs to be achieved over CYP1A1. The crystal structure of CYP2W1 has not been solved yet, hindering precise structure-based drug design. However, the CYP2W1 active site structure has been predicted to be most similar to CYP1A1, based on both overlapping substrate profiles and high identity in specific substrate recognition site (SRS) regions (77). Initial functionalization of the DNA binding subunit has so far only resulted in gaining selectivity of CYP1A1 over CYP2W1, the opposite of the desired selectivity (74).

Recently, further engineering of the *seco*-duocarmycins has investigated the bioactivation and selectivity effects of chirality of the chloromethyl moiety (Figure 1.8). The binding and structural orientations of the separated enantiomers of *seco*-duocarmycin derivatives in the

19

CYP1A1 active site are the basis of research presented in Chapter 5 of this dissertation. Results

of this research are aimed at furthering the selectivity of these potent cancer therapeutics for

specific activation in tumor cells.
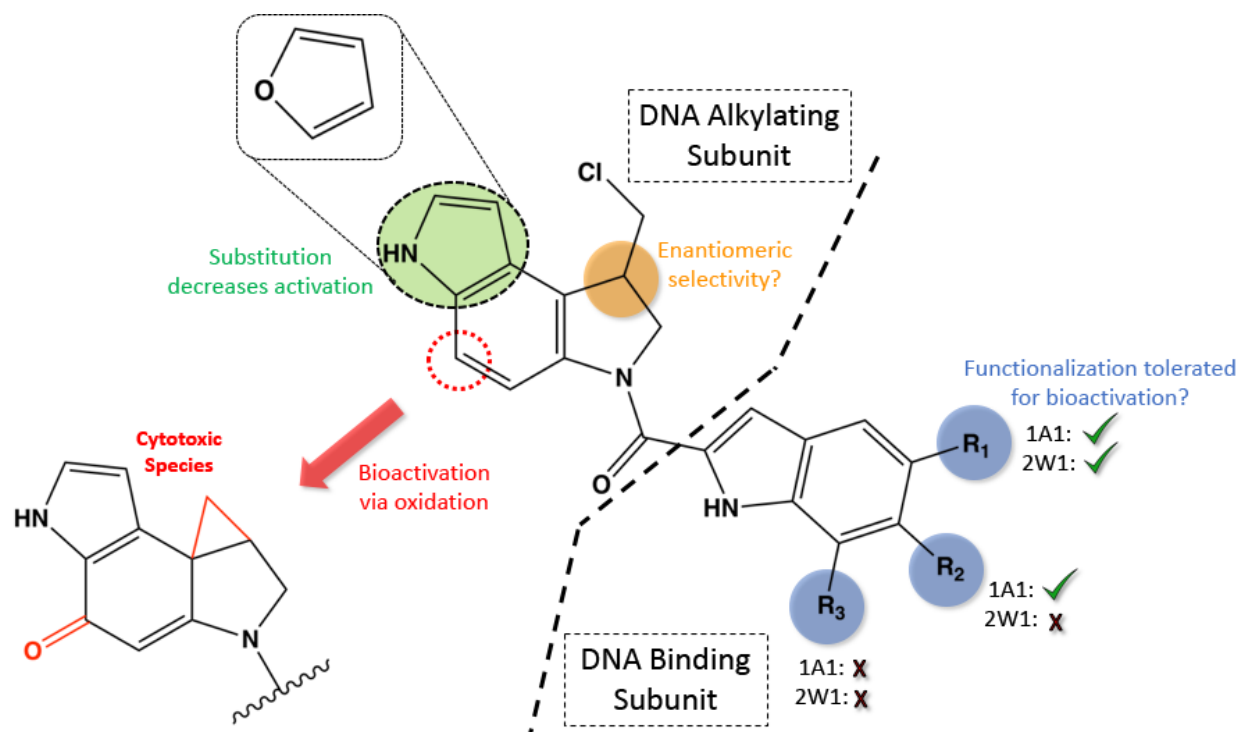
Figure 1.8 **General scaffold and previous modifications on designed *seco*-duocarmycin prodrugs.** Substitution/functionalization to the scaffold and changes to bioactivation into cytotoxic species were reported by Sheldrake *et al*. (74).

1.9 Ancestral Reconstructed P450 Enzymes with Higher Thermostabilities for Industrial Applications

The use of enzymes as biocatalysts has been an attractive route towards generating

synthetically difficult, expensive, or unsustainable chemicals compounds. For enzymes to be

useful biocatalysts, they often require high turnover rates and extended stability in reaction

conditions. Due to the diverse and often regio-specific functionalization P450 enzymes can

perform, especially on inert C-H bonds, use of cytochromes P450 as has had immense interest (78-

81). Largely, the soluble bacterial P450 enzymes have been used for this purpose due to their

already high turnover, stability, and high expression yields. However, the bacterial enzymes often

have restrictive substrate profiles, limiting the array of useful compounds that could be produced. In contrast, many mammalian P450 enzymes have broad substrate scopes, but are disadvantaged due to poor stability in terms of thermal and solvent tolerances and often low activity (82). Methods which have been used to improve the stability and activity of these enzymes have broadly been either through rational or semi-rational mutagenesis (if a structure is available or if structure-function relationships are well established) or directed evolution approaches (83,84). While these methods have been applied successfully, these approaches often require multiple rounds of time-consuming screening and yield only incremental improvements (82). An alternative approach has been through the reconstruction of ancestral P450 linages, which have shown a fairly robust correlation between evolutionary age and gains in the thermal stability (82,85). Recent work utilizing this approach has shown that very large enhancements in thermostability can be gained with ancestors of the major drug metabolizing human enzyme 3A4 (82). Reconstructed mammalian P450 ancestors as starting templates hold promise for the development of highly stable and efficient biocatalysts for producing medicines, industrial chemicals, and as mediators for green chemistry. Chapter 6 reports on the first structure of an ancestral reconstructed P450 enzyme. This enzyme known as N98-1B1-mammal, is the ancestral CYP1B1 mammalian ancestor. In this chapter, examination of structural and catalytic differences between the ancestral CYP1B1 and the extant human CYP1B1 are performed, with the goal of deciphering structural elements that may contribute to enhanced thermostability.

1.10 Conclusions

The catalysis performed by human cytochrome P450 enzymes has a wide range of importance in drug metabolism, prodrug activation, carcinogen/toxin formation, and as biocatalysts. To understand, predict, as well as take advantage of P450 catalysis, we need a high-

resolution understanding of P450 enzymes and their interactions with ligands and redox partners. The malleability of the P450 active sites upon binding different ligands and potentially partner proteins can make the development of selective inhibitors or sites of metabolism prediction for substrates challenging or impossible even if structures of the P450 are known. These uncertainties impede the development of safer and more effective pharmaceutical agents, prevention of carcinogenic and toxin bioactivation, and engineering of P450 enzymes as biocatalytic tools.

1.11 References

1. Wienkers, L. C., and Heath, T. G. (2005) Predicting in vivo drug interactions from in vitro drug discovery data. *Nat Rev Drug Discov* **4**, 825-833

2. Guengerich, F. P., and Cheng, Q. (2011) Orphans in the Human Cytochrome P450 Superfamily: Approaches to Discovering Functions and Relevance in Pharmacology. *Pharmacological reviews* **63**, 684-699

3. Schenkman, J. B., and Jansson, I. (2006) Spectral analyses of cytochromes P450. *Methods Mol Biol* **320**, 11-18

4. Isin, E. M., and Guengerich, F. P. (2008) Substrate binding to cytochromes P450. *Analytical and Bioanalytical Chemistry* **392**, 1019-1030

5. Lockart, M. M., Rodriguez, C. A., Atkins, W. M., and Bowman, M. K. (2018) CW EPR parameters reveal cytochrome P450 ligand binding modes. *J Inorg Biochem* **183**, 157-164

6. Omura, T., and Sato, R. (1964) The Carbon Monoxide-Binding Pigment of Liver Microsomes. Ii. Solubilization, Purification, and Properties. *The Journal of biological chemistry* **239**, 2379-2385

7. Perera, R., Sono, M., Sigman, J. A., Pfister, T. D., Lu, Y., and Dawson, J. H. (2003) Neutral thiol as a proximal ligand to ferrous heme iron: implications for heme proteins that lose cysteine thiolate ligation on reduction. *Proceedings of the National Academy of Sciences of the United States of America* **100**, 3641-3646

8. Denisov, I. G., Makris, T. M., Sligar, S. G., and Schlichting, I. (2005) Structure and chemistry of cytochrome P450. *Chemical Reviews* **105**, 2253-2277

9. Wester, M. R., Stout, C. D., and Johnson, E. F. (2002) Purification and crystallization of N-terminally truncated forms of microsomal cytochrome P450 2C5. *Methods Enzymol* **357**, 73-79

10. Johnson, E. F., and Stout, C. D. (2013) Structural diversity of eukaryotic membrane cytochrome P450s. *The Journal of biological chemistry* **288**, 17082-17090

11. Waskell, L. K., JJ. (2015) *Cytochrome P450: Structure, Mechanism and Biochemistry*, 4th ed., Springer, New York

12. Bridges, A., Gruenke, L., Chang, Y. T., Vakser, I. A., Loew, G., and Waskell, L. (1998) Identification of the binding site on cytochrome P450 2B4 for cytochrome b_5 and cytochrome P450 reductase. *The Journal of biological chemistry* **273**, 17036-17049

13. Shimizu, T., Tateishi, T., Hatano, M., and Fujiikuriyama, Y. (1991) Probing the Role of Lysines and Arginines in the Catalytic Function of Cytochrome-P450d by Site-Directed Mutagenesis - Interaction with Nadph-Cytochrome-P450 Reductase. *Journal of Biological Chemistry* **266**, 3372-3375

14. Cvrk, T., and Strobel, H. W. (2001) Role of LYS271 and LYS279 residues in the interaction of cytochrome P4501A1 with NADPH-cytochrome P450 reductase. *Archives of biochemistry and biophysics* **385**, 290-300

15. Bumpus, N. N., and Hollenberg, P. F. (2010) Cross-linking of human cytochrome P450 2B6 to NADPH-cytochrome P450 reductase: Identification of a potential site of interaction. *Journal of Inorganic Biochemistry* **104**, 485-488

16. Im, S. C., and Waskell, L. (2011) The interaction of microsomal cytochrome P450 2B4 with its redox partners, cytochrome P450 reductase and cytochrome b(5). *Archives of biochemistry and biophysics* **507**, 144-153

17.   Yamazaki, H., Nakamura, M., Komatsu, T., Ohyama, K., Hatanaka, N., Asahi, S., Shimada, N., Guengerich, F. P., Shimada, T., Nakajima, M., and Yokoi, T. (2002) Roles of NADPH-P450 reductase and apo- and holo-cytochrome b_5 on xenobiotic oxidations catalyzed by 12 recombinant human cytochrome P450s expressed in membranes of *Escherichia coli. Protein expression and purification* **24**, 329-337

18.   Estrada, D. F., Laurence, J. S., and Scott, E. E. (2013) Substrate-modulated cytochrome P450 17A1 and cytochrome b_5 interactions revealed by NMR. *The Journal of biological chemistry* **288**, 17008-17018

19.   Auchus, R. J., Lee, T. C., and Miller, W. L. (1998) Cytochrome b_5 augments the 17,20-lyase activity of human P450c17 without direct electron transfer. *The Journal of biological chemistry* **273**, 3158-3165

20.   Gao, Q., Doneanu, C. E., Shaffer, S. A., Adman, E. T., Goodlett, D. R., and Nelson, S. D. (2006) Identification of the interactions between cytochrome P450 2E1 and cytochrome b_5 by mass spectrometry and site-directed mutagenesis. *The Journal of biological chemistry* **281**, 20404-20417

21.   Zhao, C., Gao, Q., Roberts, A. G., Shaffer, S. A., Doneanu, C. E., Xue, S., Goodlett, D. R., Nelson, S. D., and Atkins, W. M. (2012) Cross-linking mass spectrometry and mutagenesis confirm the functional importance of surface interactions between CYP3A4 and holo/apo cytochrome b(5). *Biochemistry* **51**, 9488-9500

22.   Ahuja, S., Jahr, N., Im, S. C., Vivekanandan, S., Popovych, N., Le Clair, S. V., Huang, R., Soong, R., Xu, J., Yamamoto, K., Nanga, R. P., Bridges, A., Waskell, L., and Ramamoorthy, A. (2013) A model of the membrane-bound cytochrome b_5-cytochrome P450 complex from NMR and mutagenesis data. *The Journal of biological chemistry* **288**, 22080-22095

23.   Peng, H. M., and Auchus, R. J. (2014) Two surfaces of cytochrome b_5 with major and minor contributions to CYP3A4-catalyzed steroid and nifedipine oxygenation chemistries. *Archives of biochemistry and biophysics* **541**, 53-60

24.   Peng, H. M., and Auchus, R. J. (2013) The action of cytochrome b(5) on CYP2E1 and CYP2C19 activities requires anionic residues D58 and D65. *Biochemistry* **52**, 210-220

25.   Zhang, H. M., Hamdane, D., Im, S. C., and Waskell, L. (2008) Cytochrome b(5) inhibits electron transfer from NADPH-cytochrome P450 reductase to ferric cytochrome P4502B4. *Journal of Biological Chemistry* **283**, 5217-5225

26.   Estrada, D. F., Laurence, J. S., and Scott, E. E. (2016) Cytochrome P450 17A1 Interactions with the FMN Domain of Its Reductase as Characterized by NMR. *Journal of Biological Chemistry* **291**, 3990-4003

27.   Gentry, K. A., Zhang, M., Im, S. C., Waskell, L., and Ramamoorthy, A. (2018) Substrate mediated redox partner selectivity of cytochrome P450. *Chemical communications* **54**, 5780-5783

28.   Porter, T. D. (2002) The roles of cytochrome b5 in cytochrome P450 reactions. *Journal of biochemical and molecular toxicology* **16**, 311-316

29.   Guryev, O. L., Gilep, A. A., Usanov, S. A., and Estabrook, R. W. (2001) Interaction of apo-cytochrome b(5) with cytochromes P4503A4 and P45017A: Relevance of heme transfer reactions. *Biochemistry* **40**, 5018-5031

30.   Yamazaki, H., Shimada, T., Martin, M. V., and Guengerich, F. P. (2001) Stimulation of cytochrome P450 reactions by apo-cytochrome b(5) - Evidence against transfer of heme

from cytochrome P450 3A4 to apo-cytochrome b_5, or heme oxygenase. *Journal of Biological Chemistry* **276**, 30885-30891

31. Peng, H. M., Im, S. C., Pearl, N. M., Turcu, A. F., Rege, J., Waskell, L., and Auchus, R. J. (2016) Cytochrome b(5) activates the 17,20-lyase activity of human cytochrome P450 17A1 by increasing the coupling of NADPH consumption to androgen production. *Biochemistry* **55**, 4356-4365

32. Zhang, H., Im, S. C., and Waskell, L. (2007) Cytochrome b_5 increases the rate of product formation by cytochrome P450 2B4 and competes with cytochrome P450 reductase for a binding site on cytochrome P450 2B4. *The Journal of biological chemistry* **282**, 29766-29776

33. Schenkman, J. B., and Jansson, I. (2003) The many roles of cytochrome b_5. *Pharmacology & therapeutics* **97**, 139-152

34. Yamazaki, H., Johnson, W. W., Ueng, Y. F., Shimada, T., and Guengerich, F. P. (1996) Lack of electron transfer from cytochrome b(5) in stimulation of catalytic activities of cytochrome P450 3A4 - Characterization of a reconstituted cytochrome P450 3A4 NADPH-cytochrome P450 reductase system and studies with apo-cytochrome b(5). *Journal of Biological Chemistry* **271**, 27438-27444

35. Zhang, M., Huang, R., Im, S. C., Waskell, L., and Ramamoorthy, A. (2015) Effects of Membrane Mimetics on Cytochrome P450-Cytochrome b(5) Interactions Characterized by NMR Spectroscopy. *Journal of Biological Chemistry* **290**, 12705-12718

36. Pearl, N. M., Wilcoxen, J., Im, S., Kunz, R., Darty, J., Britt, R. D., Ragsdale, S. W., and Waskell, L. (2016) Protonation of the Hydroperoxo Intermediate of Cytochrome P450 2B4 Is Slower in the Presence of Cytochrome P450 Reductase Than in the Presence of Cytochrome b5. *Biochemistry* **55**, 6558-6567

37. Estrada, D. F., Skinner, A. L., Laurence, J. S., and Scott, E. E. (2014) Human cytochrome P450 17A1 conformational selection: modulation by ligand and cytochrome b_5. *The Journal of biological chemistry* **289**, 14310-14320

38. Desta, Z., Ward, B. A., Soukhova, N. V., and Flockhart, D. A. (2004) Comprehensive evaluation of tamoxifen sequential biotransformation by the human cytochrome P450 system in vitro: Prominent roles for CYP3A and CYP2D6. *Journal of Pharmacology and Experimental Therapeutics* **310**, 1062-1075

39. Beverage, J. N., Sissung, T. M., Sion, A. M., Danesi, R., and Figg, W. D. (2007) CYP2D6 Polymorphisms and the impact on tamoxifen therapy. *J Pharm Sci-Us* **96**, 2224-2231

40. Shimada, T., and Guengerich, F. P. (2006) Inhibition of human cytochrome P450 1A1-, 1A2-, and 1B1-mediated activation of procarcinogens to genotoxic metabolites by polycyclic aromatic hydrocarbons. *Chemical research in toxicology* **19**, 288-294

41. Su, T., Bao, Z., Zhang, Q. Y., Smith, T. J., Hong, J. Y., and Ding, X. (2000) Human cytochrome P450 CYP2A13: predominant expression in the respiratory tract and its high efficiency metabolic activation of a tobacco-specific carcinogen, 4-(methylnitrosamino)-1-(3-pyridyl)-1-butanone. *Cancer research* **60**, 5074-5079

42. Baird, W. M., Hooven, L. A., and Mahadevan, B. (2005) Carcinogenic polycyclic aromatic hydrocarbon-DNA adducts and mechanism of action. *Environmental and Molecular Mutagenesis* **45**, 106-114

43. Guengerich, F. P., and Shimada, T. (1998) Activation of procarcinogens by human cytochrome P450 enzymes. *Mutat Res-Fund Mol M* **400**, 201-213

44.   Rendic, S., and Guengerich, F. P. (2012) Contributions of human enzymes in carcinogen metabolism. *Chem. Res. Tox.* **25**, 1316-1383

45.   Guengerich, F. P. (2015) Human cytochrome P450 enzymes. in *Cytochrome P450: Structure, Mechanism, and Biochemistry* (Ortiz de Montellano, P. R. ed.), 4th Ed., Springer International Publishing, Cham, Switzerland. pp 523-785

46.   Shimada, T., Yun, C. H., Yamazaki, H., Gautier, J. C., Beaune, P. H., and Guengerich, F. P. (1992) Characterization of human lung microsomal cytochrome P-450 1A1 and its role in the oxidation of chemical carcinogens. *Molecular pharmacology* **41**, 856-864

47.   Kim, J. H., Sherman, M. E., Curriero, F. C., Guengerich, F. P., Strickland, P. T., and Sutter, T. R. (2004) Expression of cytochromes P450 1A1 and 1B1 in human lung from smokers, non-smokers, and ex-smokers. *Toxicology and applied pharmacology* **199**, 210-219

48.   Shimada, T., Hayes, C. L., Yamazaki, H., Amin, S., Hecht, S. S., Guengerich, F. P., and Sutter, T. R. (1996) Activation of chemically diverse procarcinogens by human cytochrome P-450 1B1. *Cancer Res.* **56**, 2979-2784

49.   Murray, G. I., Taylor, M. C., McFadyen, M. C. E., McKay, J. A., Greenlee, W. F., Burke, M. D., and Melvin, W. T. (1997) Tumor-specific expression of cytochrome P450 CYP1B1. *Cancer research* **57**, 3026-3031

50.   Walsh, A. A., Szklarz, G. D., and Scott, E. E. (2013) Human cytochrome P450 1A1 structure and utility in understanding drug and xenobiotic metabolism. *The Journal of biological chemistry* **288**, 12932-12943

51.   Sansen, S., Yano, J. K., Reynald, R. L., Schoch, G. A., Griffin, K. J., Stout, C. D., and Johnson, E. F. (2007) Adaptations for the oxidation of polycyclic aromatic hydrocarbons exhibited by the structure of human P450 1A2. *The Journal of biological chemistry* **282**, 14348-14355

52.   Wang, A., Savas, U., Stout, C. D., and Johnson, E. F. (2011) Structural characterization of the complex between alpha-naphthoflavone and human cytochrome P450 1B1. *The Journal of biological chemistry* **286**, 5736-5743

53.   Denison, M. S., and Nagy, S. R. (2003) Activation of the aryl hydrocarbon receptor by structurally diverse exogenous and endogenous chemicals. *Annual review of pharmacology and toxicology* **43**, 309-334

54.   Nebert, D. W., Dalton, T. P., Okey, A. B., and Gonzalez, F. J. (2004) Role of aryl hydrocarbon receptor-mediated induction of the CYP1 enzymes in environmental toxicity and cancer. *Journal of Biological Chemistry* **279**, 23847-23850

55.   Wu, P., Nielsen, T. E., and Clausen, M. H. (2016) Small-molecule kinase inhibitors: an analysis of FDA-approved drugs. *Drug discovery today* **21**, 5-10

56.   Jackson, K. D., Durandis, R., and Vergne, M. J. (2018) Role of Cytochrome P450 Enzymes in the Metabolic Activation of Tyrosine Kinase Inhibitors. *Int J Mol Sci* **19**

57.   David, S., and Hamilton, J. P. (2010) Drug-induced Liver Injury. *US Gastroenterol Hepatol Rev* **6**, 73-80

58.   Lin, D., Kostov, R., Huang, J. T. J., Henderson, C. J., and Wolf, C. R. (2017) Novel Pathways of Ponatinib Disposition Catalyzed By CYP1A1 Involving Generation of Potentially Toxic Metabolites. *Journal of Pharmacology and Experimental Therapeutics* **363**, 12-19

59.   Li, X., Kamenecka, T. M., and Cameron, M. D. (2010) Cytochrome P450-mediated bioactivation of the epidermal growth factor receptor inhibitor erlotinib to a reactive electrophile. *Drug Metab Dispos* **38**, 1238-1245

60. Li, J., Zhao, M., He, P., Hidalgo, M., and Baker, S. D. (2007) Differential metabolism of gefitinib and erlotinib by human cytochrome P450 enzymes. *Clinical cancer research : an official journal of the American Association for Cancer Research* **13**, 3731-3737

61. Drahushuk, A. T., McGarrigle, B. P., Larsen, K. E., Stegeman, J. J., and Olson, J. R. (1998) Detection of CYP1A1 protein in human liver and induction by TCDD in precision-cut liver slices incubated in dynamic organ culture. *Carcinogenesis* **19**, 1361-1368

62. Nakamura, H., Ariyoshi, N., Okada, K., Nakasa, H., Nakazawa, K., and Kitada, M. (2005) CYP1A1 is a major enzyme responsible for the metabolism of granisetron in human liver microsomes. *Current Drug Metabolism* **6**, 469-480

63. Lang, D., Radtke, M., and Bairlein, M. (2019) Highly Variable Expression of CYP1A1 in Human Liver and Impact on Pharmacokinetics of Riociguat and Granisetron in Humans. *Chemical research in toxicology* **32**, 1115-1122

64. Lu, J. F., Eppler, S. M., Wolf, J., Hamilton, M., Rakhit, A., Bruno, R., and Lum, B. L. (2006) Clinical pharmacokinetics of erlotinib in patients with solid tumors and exposure-safety relationship in patients with non-small cell lung cancer. *Clin Pharmacol Ther* **80**, 136-145

65. Chen, Y., Suzuki, A., Tortorici, M. A., Garrett, M., LaBadie, R. R., Umeyama, Y., and Pithavala, Y. K. (2015) Axitinib plasma pharmacokinetics and ethnic differences. *Invest New Drug* **33**, 521-532

66. Takano, T., Ohe, Y., Kusumoto, M., Tateishi, U., Yamamoto, S., Nokihara, H., Yamamoto, N., Sekine, I., Kunitoh, H., Tamura, T., Kodama, T., and Saijo, N. (2004) Risk factors for interstitial lung disease and predictive factors for tumor response in patients with advanced non-small cell lung cancer treated with gefitinib. *Lung Cancer* **45**, 93-104

67. Hamilton, M., Wolf, J. L., Rusk, J., Beard, S. E., Clark, G. M., Witt, K., and Cagnoni, P. J. (2006) Effects of smoking on the pharmacokinetics of erlotinib. *Clinical cancer research : an official journal of the American Association for Cancer Research* **12**, 2166-2171

68. Ortiz de Montellano, P. R. (2013) Cytochrome P450-activated prodrugs. *Future Med Chem* **5**, 213-228

69. Rautio, J., Kumpulainen, H., Heimbach, T., Oliyai, R., Oh, D., Jarvinen, T., and Savolainen, J. (2008) Prodrugs: design and clinical applications. *Nature Reviews Drug Discovery* **7**, 255-270

70. Pors, K., Loadman, P. M., Shnyder, S. D., Sutherland, M., Sheldrake, H. M., Guino, M., Kiakos, K., Hartley, J. A., Searcey, M., and Patterson, L. H. (2011) Modification of the duocarmycin pharmacophore enables CYP1A1 targeting for biological activity. *Chemical communications* **47**, 12062-12064

71. Ghosh, N., Sheldrake, H. M., Searcey, M., and Pors, K. (2009) Chemical and Biological Explorations of the Family of CC-1065 and the Duocarmycin Natural Products. *Current Topics in Medicinal Chemistry* **9**, 1494-1524

72. Lambert, J. M. (2005) Drug-conjugated monoclonal antibodies for the treatment of cancer. *Current Opinion in Pharmacology* **5**, 543-549

73. Jin, W., Trzupek, J. D., Rayl, T. J., Broward, M. A., Vielhauer, G. A., Weir, S. J., Hwang, I., and Boger, D. L. (2007) A unique class of duocarmycin and CC-1065 analogues subject to reductive activation. *Journal of the American Chemical Society* **129**, 15391-15397

74. Sheldrake, H. M., Travica, S., Johansson, I., Loadman, P. M., Sutherland, M., Elsalem, L., Illingworth, N., Cresswell, A. J., Reuillon, T., Shnyder, S. D., Mkrtchian, S., Searcey, M., Ingelman-Sundberg, M., Patterson, L. H., and Pors, K. (2013) Re-engineering of the

duocarmycin structural architecture enables bioprecursor development targeting CYP1A1 and CYP2W1 for biological activity. *Journal of medicinal chemistry* **56**, 6273-6277

75. Androutsopoulos, V. P., Spyrou, I., Ploumidis, A., Papalampros, A. E., Kyriakakis, M., Delakas, D., Spandidos, D. A., and Tsatsakis, A. M. (2013) Expression Profile of CYP1A1 and CYP1B1 Enzymes in Colon and Bladder Tumors. *PLoS One* **8**, e82487

76. Karlgren, M., Gomez, A., Stark, K., Svard, J., Rodriguez-Antona, C., Oliw, E., Bernal, M. L., Ramon y Cajal, S., Johansson, I., and Ingelman-Sundberg, M. (2006) Tumor-specific expression of the novel cytochrome P450 enzyme, CYP2W1. *Biochemical and biophysical research communications* **341**, 451-458

77. Karlgren, M., and Ingelman-Sundberg, M. (2007) Tumour-specific expression of CYP2W1: Its potential as a drug target in cancer therapy. *Expert Opin Ther Tar* **11**, 61-67

78. Bernhardt, R. (2006) Cytochromes P450 as versatile biocatalysts. *Journal of biotechnology* **124**, 128-145

79. Gillam, E. M. (2005) Exploring the potential of xenobiotic-metabolising enzymes as biocatalysts: Evolving designer catalysts from polyfunctional cytochrome P450 enzymes. *Clin Exp Pharmacol P* **32**, 147-152

80. Arnold, F. H. (2018) Directed Evolution: Bringing New Chemistry to Life. *Angew Chem Int Edit* **57**, 4143-4148

81. Labinger, J. A., and Bercaw, J. E. (2002) Understanding and exploiting C-H bond activation. *Nature* **417**, 507-514

82. Gumulya, Y., Baek, J. M., Wun, S. J., Thomson, R. E. S., Harris, K. L., Hunter, D. J. B., Behrendorff, J. B. Y. H., Kulig, J., Zheng, S., Wu, X. M., Wu, B., Stok, J. E., De Voss, J. J., Schenk, G., Jurva, U., Andersson, S., Isin, E. M., Boden, M., Guddat, L., and Gillam, E. M. J. (2018) Engineering highly functional thermostable proteins using ancestral sequence reconstruction. *Nat Catal* **1**, 878-888

83. Cirino, P. C., and Arnold, F. H. (2003) A self-sufficient peroxide-driven hydroxylation biocatalyst. *Angew Chem Int Edit* **42**, 3299-3301

84. Kumar, S., and Halpert, J. R. (2005) Use of directed evolution of mammalian cytochromes P450 for investigating the molecular basis of enzyme function and generating novel biocatalysts. *Biochemical and biophysical research communications* **338**, 456-464

85. Gumulya, Y., Huang, W. L., D'Cunha, S. A., Richards, K. E., Thomson, R. E. S., Hunter, D. J. B., Baek, J. M., Harris, K. L., Boden, M., De Voss, J. J., Hayes, M. A., Isin, E. M., Andersson, S., Jurva, U., and Gillam, E. M. J. (2019) Engineering Thermostable CYP2D Enzymes for Biocatalysis Using Combinatorial Libraries of Ancestors for Directed Evolution (CLADE). *Chemcatchem* **11**, 841-850

CHAPTER 2

Structural and Functional Effects of Cytochrome b_5 Interactions with Human Cytochrome P450 Enzymes[*]

2.1 Summary

The small heme-containing protein cytochrome b_5 can facilitate, inhibit, or have no effect on cytochrome P450 catalysis, often in a P450-dependent and substrate-dependent manner that is not well understood. Herein solution NMR was used to identify b_5 residues interacting with different human drug-metabolizing P450 enzymes. NMR results revealed that P450 enzymes bound to either b_5 α4-5 (CYP2A6 and CYP2E1) or this region and α2-3 (CYP2D6 and CYP3A4) and suggested variation in the affinity for b_5. Mutations of key b_5 residues suggest that not only are different b_5 surfaces responsible for binding different P450 enzymes, but that these different complexes are relevant to the observed effects on P450 catalysis.

2.2 Introduction

Cytochrome P450 (P450) monooxygenases have vital roles in both the metabolism of xenobiotics including drugs and in the biosynthesis of endogenous compounds such as steroids, vitamins, fatty acids, and eicosanoids. While the ability of P450 enzymes to oxidize such substrates requires interaction with a redox partner protein, catalysis can additionally be modulated by interactions with the membrane-bound heme protein cytochrome b_5 (b_5). Cytochrome b_5 has a

---

complex influence, such that P450 catalysis can be stimulated, not affected, or even inhibited, prompting numerous investigations into the mechanism(s) by which these varied responses are elicited (1,2). Proposals have largely focused on 1) b_5 functioning in a purely redox role of electron delivery or 2) as an allosteric modulator of P450 conformation. Metal-substituted, redox-silent forms of b_5 still stimulate certain P450 reactions (4,5), supporting a purely allosteric role for b_5, at least in some cases. Allosteric modulation of P450 conformation could result in alterations in substrate binding, electron or proton delivery, or coupling of NADPH consumption to metabolite formation (1,2,3).

Regardless of the mechanism, the capability of b_5 to modulate P450 catalysis relies on direct binding between b_5 and a P450. Insights into individual P450/b_5 complexes gained from mutagenesis (3,4), chemical modification (5), and cross-linking studies (6,7) are consistent with the convex, negatively charged, heme-exposed face of b_5 (Figure 2.1A) transiently interacting with the concave, largely positively charged, proximal face of P450 enzymes (Figure 2.1B). This proximal P450 face is the same surface to which the required redox partners bind (NADPH-cytochrome P450 reductase (CPR) for microsomal P450 enzymes), underscoring the necessity of transient interactions between P450 and its protein partners (3,8).
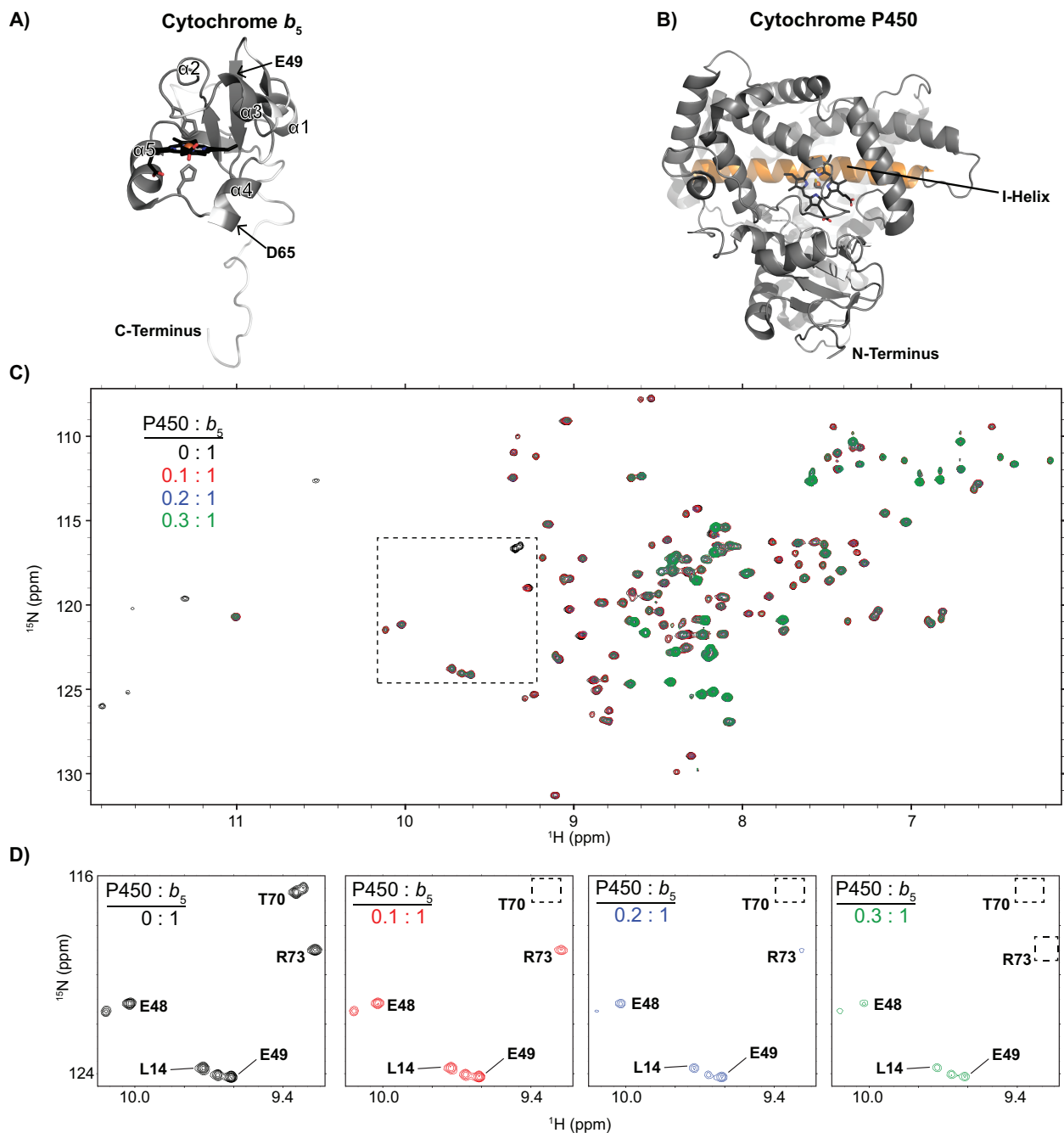
Figure 2.1 General structures of proteins in this study and overview of their interaction as monitored by NMR. A, structure of the human cytochrome b_5 soluble domain (residues 1-107), as determined by NMR (PDB 2I96). The heme and coordinating histidine residues are shown as sticks. Alpha helices labeled 1-5. The locations of E49 and D65 in helices 3 and 4 are indicated. B, P450 structure (CYP2A6, PDB 1Z10) viewed from the proximal face proposed to interact with b_5. The heme is again shown as sticks. As a reference, the I helix is highlighted (orange) on the distal side of the heme where the active site is located. C, the ^{1}H-^{15}N HSQC NMR spectra of the soluble domain of human cytochrome b_5 titrated with increasing amounts of unlabeled CYP2A6 saturated with coumarin is representative of the type of changes seen for all P450 enzymes examined herein. Progressive signal loss or line-broadening of most b_5 resonances occurs with increasing concentrations of P450, indicating progressive complex formation between the two proteins. D, a selected region of the NMR spectra (the region indicated as dashed box in panel C) is shown with increasing P450 to demonstrate differential line broadening effects. In this example with CYP2A6, some resonances are broadened to a greater extent (T70, R73) than others (L14, E48, and E49).

31

Fundamental questions persist with regard to P450/b_5 interactions: How variable is the binding interface between b_5 and different P450 enzymes? Do the affinities vary? Could differences in the b_5/P450 interaction underlie the different effects b_5 has on P450 catalysis? To complicate matters, the effects that b_5 has on catalysis can depend not only on the P450 enzyme, but also the P450 substrate being metabolized (9-11) and experimental parameters, including the ratio of P450 to b_5 (10). Differences in b_5 effects with different substrates has fueled interest in whether conformational linking exists between the P450 active site cavity and the P450 proximal face interacting with b_5 and CPR (8,12,13).

Since there are no X-ray structures available of b_5 interacting with any P450, solution NMR is an attractive high-resolution approach to decoding these transient binding interactions. Previous studies of ^{15}N-labeled b_5 binding to increasing concentrations of unlabeled human steroidogenic CYP17A1 enzyme or rabbit CYP2B4 revealed only small chemical shift perturbations, but more pronounced decreases in the intensity of b_5 resonances (4,15). These line-broadening effects may result from a number of potential sources. Binding of the smaller ~16 kDa b_5 to a larger P450 enzyme (~50-55 kDa) would enhance the transverse relaxation rate, but could also result in paramagnetic effects from the P450 heme, and/or alter the protein-protein interaction to fall within the intermediate exchange time-scale (8,14). Thus, while progressive line broadening occurs upon formation of increasing amounts of the reversible P450/b_5 complex, there is not necessarily a 1:1 correspondence between signal loss and amount of complex formed, which prevents the determination of meaningful K_d values. Regardless, the degree of broadening has varied between these two different P450 enzymes, the P450 ligands present, and experimental conditions such as the presence of lipid mimic systems (8,14,15), providing various insights into these P450/b_5 interactions. Both CYP17A1 and CYP2B4 studies reported that certain b_5 resonances are

broadened substantially more than the average. Since most of the b_5 amino acids have been assigned to specific resonances (16), such differential line broadening has been used to successfully map out specific b_5 residues that transiently interact with CYP17A1 and CYP2B4 (8,14).

The current study employed such solution NMR experiments to identify and compare b_5 residues interacting with the human xenobiotic cytochrome P450 enzymes 2A6, 2D6, 2E1, and 3A4. Results indicate that both shared and distinct interaction surfaces on b_5 are present in these respective complexes. Additionally, substantial differences between CYP2D6 and the other P450 enzymes examined are consistent with different relative affinities of the complex with b_5. Key b_5 residues identified using this approach were subsequently validated by performing mutagenesis and evaluating both complex formation and effects on catalysis. This comparison of P450/b_5 complexes provides a physical basis to begin understanding the ability of b_5 to differentially modulate P450 catalytic activities.

2.3 Experimental Procedures

2.3.1   Generation of the soluble domain of human cytochrome b_5 with ^{15}N-labeling for NMR experiments

A synthetic, codon-optimized gene encoding the soluble domain (residues 1-107) of human microsomal cytochrome b_5 with a C-terminal His$_6$ tag (Genewiz) was cloned into the *NcoI* and *BamHI* restriction sites of pET15b and transformed into *E. coli* C41 (DE3) cells already containing the pGro7 plasmid (Takara Bio) for expression of GroEL/GroES chaperones. Transformed cells were selected by growing cells for ~18 hours at 37 °C on a non-inducing minimal media plate (MDAG-11) (17) supplemented with carbenicillin (100 µg/mL) and chloramphenicol (20 µg/mL) to select for the b_5 and chaperone plasmids, respectively. All subsequent cultures contained these

antibiotics. A single colony was picked and grown for ~16 hours at 37 °C with shaking (250 rpm) in a 50 mL liquid culture of non-inducing minimal media MDAG-135 (17). Expression cultures consisted of 1 liter of a defined minimal media (48 mM Na_2HPO_4, 22 mM KH_2PO_4, 9 mM NaCl, 19 mM ^{15}N NH_4Cl, 53 mM glucose, 4 mM $MgSO_4$, and trace metals) inoculated with 5 mL of the liquid starter culture. Cells were grown with shaking (250 rpm) at 37 °C, to an optical density at 600 nm ($O.D._{600}$) of 0.3, at which point the heme precursor δ-aminolevulinic acid (ALA, to 1 mM) and the chaperone inducer L-arabinose (to 13 mM) were added. After $O.D._{600}$ reached 0.7-0.8, b_5 expression was induced by adding 0.4 mM IPTG and the temperature and shaking were reduced to 30 °C and 225 rpm, respectively. Cultures were subsequently grown for 20 hours prior to harvesting and freezing the cell pellet at -80 °C. Purification was initiated by resuspending cells in lysis buffer (500 mM KPi, 100 mM NaCl, 15% glycerol, 1 mM EDTA, pH 7.4) with the addition of 1 mM PMSF. Resuspended cells were lysed by a French press and heme reconstitution performed as described (18). Lysed cells were clarified by ultracentrifugation at 140,000 x g and loaded onto a pre-equilibrated 25 mL Ni-NTA column (Qiagen) with loading buffer (100 mM KPi, 20% glycerol, 200 mM NaCl, 20 mM imidazole, pH 7.4), washed with an additional 8 CV of loading buffer, and eluted using a 6 CV of elution buffer (loading buffer with 200 mM imidazole). Eluted fractions with $A_{413}/A_{280} > 4.0$ were pooled and concentrated prior to loading on a Superdex 200 Increase 10/300 GL column (GE Healthcare) and run with gel filtration buffer (50 mM KPi, 20% glycerol, 100 mM NaCl, pH 7.4). The protein sample was then exchanged into a storage buffer (50 mM KPi, 10% glycerol, pH 7.4) using a HiTrap desalting column (GE Healthcare). Final protein preparation was evaluated by SDS-PAGE and UV-visible spectroscopy ($A_{413}/A_{280} > 6.0$) and quantified using an extinction coefficient of 117 mM^{-1} cm^{-1} at 413 nm (19). Aliquots

were stored at -80 °C until use. Samples for NMR were created by exchanging labeled b_5 into

NMR buffer (50 mM KPi, 50 mM NaCl, 10% D_2O, pH 6.5) through dilution and centrifugation.

2.3.2 Generation of full length human cytochrome b_5 for catalytic assays

A synthetic, codon-optimized DNA sequence encoding full-length human cytochrome b_5

plus a C-terminal His_6 tag was generated (GenScript) and cloned into pET-15b vector using

restriction enzymes *Nco*I and *Bam*HI. Expression of full length b_5 was similar to the soluble

domain of b_5 except 1) expression cultures were grown in Terrific broth, 2) induction was

performed with 0.1 mM IPTG at an O.D.$_{600}$ of 1.1, and 3) induced cultures were grown at 20 °C

with 250 rpm shaking for 44 hours. Purification of full length b_5 was initiated by resuspending

cells in resuspension buffer (100 mM KPi, 20% glycerol, 1 mM EDTA, pH 7.4) supplemented

with 1X HALT protease inhibitor cocktail (Thermo Fisher) and 1 mM PMSF. Cells were lysed

and reconstituted with heme as described above for the soluble domain. Membrane fractions were

isolated by ultracentrifugation at 140,000 x g for 30 min. and b_5 extracted using resuspension

buffer with the addition of 0.2 M NaCl and 1% (w/v) CHAPS. Extracted membranes were pelleted

by a second ultracentrifuge step at 140,000 x g for 30 min. and the b_5-containing supernatant loaded

onto a Ni-NTA column (Qiagen) and washed as described for the soluble domain of b_5 but with

the addition of 0.5% (w/v) CHAPS. Eluted fractions with A_{413}/A_{280} > 2.0 were pooled,

concentrated and loaded on a Sepharcryl S-200 HR column (GE Healthcare) equilibrated and run

with gel filtration buffer (50 mM KPi, 20% glycerol, 100 mM NaCl, 0.05% (w/v) CHAPS, pH

7.4), and exchanged into storage buffer as described above. Protein purity was assessed on SDS-

PAGE, and UV-visible spectroscopy was used to confirm degree of heme incorporation (A_{413}/A_{280}

= 3.0) and quantify dithionite-reduced b_5 (18).

2.3.3 Generation of full length human NADPH-cytochrome P450 reductase for catalytic assays

A construct encoding full length human NADPH-cytochrome P450 reductase preceded by the ompA signal peptide and followed by a His$_6$ tag was cloned into pET-29a(+) using *Nde*I and *Hind*III. Expression of reductase was performed as previously described for a truncated CPR construct (20) with modifications. Modifications to the expression included 1) transformation and generation of the starter culture as described for soluble b_5, 2) supplementation of expression cultures with 2 mg/L riboflavin, and 3) shaking at 200 rpm after induction. Full length CPR was also purified in a similar manner to a previously described method (20), with modifications: 1) membrane fractions after cell lysis were isolated by ultracentrifugation at 140,000 x g for 25 min. prior to detergent extraction, 2) omission of the ammonium sulfate precipitation step, and 3) addition of a second nickel affinity column after elution from Octyl-Sepharose 4 Fast Flow (GE Healthcare) resin in order to deplete detergent. Final reductase samples were evaluated on SDS-PAGE and by UV-visible spectroscopy. CPR was quantitated by flavin absorbance of the fully oxidized protein at 454 nm with an extinction coefficient of 21.4 mM^{-1}cm^{-1} (21).

2.3.4 Generation of P450 enzymes for NMR and catalytic assays

All cytochrome P450 enzymes were the forms previously used to generate crystallographic structures and result in catalytically active protein omitting the N-terminal transmembrane helix and adding a C-terminal His tag. Constructs and expression and purification of human CYP2A6 (22) and CYP2E1 (23) were reported previously. Synthetic, codon-optimized genes encoding CYP2D6 and CYP3A4 were generated (Genscript) to match the reported constructs (24,25), cloned into the pCWori vector, and expressed and purified as described in these same publications with some modifications. Briefly *E. coli* DH5α containing the pGro7 plasmid (Takara Bio) was

36

used to express the P450 enzymes. Transformation and starter cultures were performed as described for soluble b_5. Proteins were purified by isolating spheroplasts (26), lysis by French press, detergent extraction using 4.8 mM CYMAL-5 (CYP2A6 and CYP2E1) or 14 mM CHAPS (CYP2D6 and CYP3A4). After extraction, lysate was clarified by ultracentrifugation at 104,000 x g and purified through Ni-NTA, carboxymethyl cellulose ion-exchange, and size-exclusion chromatography. All proteins were depleted of detergent during ion exchange chromatography, exchanged into storage buffer (50 mM KPi, 10% glycerol, pH 7.4), and frozen as aliquots at -80 °C. P450 samples were evaluated by SDS-PAGE and UV-visible spectroscopy. The reduced-carbon monoxide difference spectra revealed, at most, only trace amounts of P420.

2.3.5   Mutagenesis

Single amino acid mutants of cytochrome b_5 E49Q and D65N were produced by the QuikChange Lightning site-directed mutagenesis kit (Stratagene) for the full-length construct and commercially (GENEWIZ) for the soluble-domain construct. The complete genes were verified by sequencing and protein expressed and purified as described for the respective wild-type constructs.

2.3.6   NMR Spectroscopy

NMR experiments were acquired at 298 K using a Bruker Avance III HD 800 MHz with a QCI cryogenic probe. Data were processed using NMRPipe (27) and visualized and analyzed using Sparky (T.D. Goddard and D. G. Kneller, Sparky 3, University of California, San Francisco). Assignments for the backbone amide signals for human soluble domain of b_5 were transferred from the deposited chemical shifts in the Biological Magnetic Resonance Data Bank (accession number: 6921) (16). All of the 2D ^{15}N-HSQC experiments were obtained on ^{15}N-labeled, soluble domain b_5 (0.1 mM) in NMR buffer (50 mM KPi, 50 mM NaCl, 10% D_2O, pH 6.5) acquired with 64 scans

and 128 increments, which took about 2.5 hours. The signal for each individual resonance was measured as peak height, with the value at 0:1 P450:b_5 defined as 100% signal. For each titration point within a series, a new sample of labeled b_5 was prepared and a defined molar amount of an unlabeled P450 enzyme added to the sample. For samples including P450 enzyme, the peak height for each resonance was expressed as a percentage of the resonance peak height in the absence of the P450. Concentration of the P450 substrate was saturating and constant between samples (500 µM coumarin for 2A6, 500 µM chlorzoxazone (CZN) for 2E1, 2 mM dextromethorphan (DXM) for 2D6, 5 mM *p*-nitrophenol (*p*NP) for 2A6, or 200 µM nifedipine (NFP) for 3A4). NMR experiments were performed with both b_5 and P450 in their oxidized states. At the conclusion of each NMR experiment, samples were collected from the NMR tube, centrifuged to determine if any precipitation had occurred, and evaluated in terms of the reduced-carbon monoxide difference spectrum.

2.3.7   Cytochrome P450 catalytic assays

All catalytic assays were performed by incubating a P450 with full-length human P450 reductase and full-length human b_5 (when applicable) at a 1:2:0 ratio for minus b_5 reactions or a 1:2:2 ratio for b_5 containing reactions for 20 minutes at room temperature. The amounts of P450 enzyme were 10 (coumarin assay) or 50 pmol (*p*NP assay) CYP2A6; 50 pmol CYP2D6 (DXM); 50 pmol CYP2E1 (CZN assay); and 50 pmol CYP3A4 (NFP assay). This protein mixture was added to the same buffer used for NMR experiments, except for the nifedipine assay which used an assay buffer consisting of 40 mM HEPES, 30 mM MgCl$_2$, pH 7.4. The reactions also contained the respective P450 substrate (0-128 µM coumarin, 0-600 µM CZN, 0-1600 µM *p*NP, 0-1000 µM DXM, 0-250 µM nifedipine). For the nifedipine assay all reactions were performed in amber vials. The reactions were pre-incubated at 37 °C for 3 min, then initiated with 1 mM NADPH and

allowed to proceed at 37 °C for 10 min (coumarin, CZN, and *p*NP assays) or 15 min (DXM assay) or 20 min (nifedipine assay). Reactions were terminated by addition of diluted perchloric acid (acetonitrile for the nifedipine assay), placed on ice, and centrifuged at 5,000 x g for 5 min prior to injection onto a Luna C18 (5 μm, 150 x 4.60 mm, Phenomenex) column at a flow rate of 1 mL/min (0.75 mL/min for the nifedipine assay). Separation on HPLC was obtained using the following mobile phase solutions for each of the respective assays. For separation of coumarin and its 7-OH metabolite the mobile phase consisted of 50%/50% 20 mM KPi, pH 2.8/methanol. For CZN and its 6-OH metabolite the mobile phase consisted of 75%/25% 20 mM KPi, pH 2.8/acetonitrile to elute product, then a sharp gradient to 40%/60% to elute substrate, followed by reequilibration to 75%/25%. For *p*NP and its 4-nitrocatechol metabolite the mobile phase consisted of 73%/27% 10 mM KPi, pH 3.5/acetonitrile. For DXM and its O-demethylated metabolite dextrorphan the mobile phase consisted of 50%/50% 10 mM KPi, pH 3.5/50% acetonitrile and 100% methanol (250/200 v/v). For nifedipine and its metabolite dehydronifedipine the mobile phase consisted of 45%/55% water/methanol. Metabolite detection occurred by fluorescence for coumarin (355 nm excitation, 460 nm emission) and DXM (280 nm excitation, 310 nm emission) assays, and by ultraviolet absorbance for CZN (287 nm), *p*NP (345 nm), and NFP (270 nm) assays. The amounts of the different metabolites produced were calculated using authentic standards prepared in the same method as samples. Each reaction at each substrate concentration was performed at least in duplicate. Data were fit to the Michaelis-Menten equation using Graphpad Prism.

2.3.8 Measurement of NADPH Consumption

NADPH consumption during the various P450 reactions was measured by creating reaction samples similar to the catalytic assays except for the following: 1) 100 pmol P450 was used to

increase signal/noise, 2) reactions were scaled up to 1 mL in the respective assay buffer containing the maximum substrate concentration used in turnover reactions, 3) NADPH concentration was reduced to 0.5 mM to reduce background, and 4) reactions were allowed to proceed for 10 min. CYP2A6(pNP) samples required the use of 2 mm path length cuvettes due to high substrate absorbance, so these reactions used 50 pmol P450 and a final volume of 500 μL. Rates of NADPH consumption were measured by monitoring linear decreases in absorbance at 340 nm. The amount of NADPH consumed was calculated using an extinction coefficient of 6.22 mM^{-1} cm^{-1}. Control reactions omitting P450 provided the background NADPH consumption, which was subtracted. The amount of product at the end of each reaction was measured using the same methods described for each catalytic assay. Coupling efficiencies were calculated by dividing metabolite product formation in these experiments by their respective NADPH consumption. All measurements were performed in duplicate.

2.4 Results/Discussion

2.4.1 Rationale for experimental scope

The specific human P450 enzymes included in this study were selected for their importance in clinical drug metabolism, diversity across the xenobiotic P450 subfamily, and the range of b_5 effects on metabolite production as reported in the literature. Cytochrome b_5 reportedly stimulates CYP2E1-mediated oxidation of a number of different substrates, including acetaminophen, aniline, N-nitrosodimethylamine, and chlorzoxazone (28,29), but may play a redox role, as apo-b_5 does not increase product formation (30,31). The influence of b_5 on the major drug-metabolizing P450 enzyme CYP3A4 has been widely documented, with numerous CYP3A4-mediated reactions showing stimulation in the presence of both holo and apo-b_5 (32). CYP2A6 coumarin 7-hydroxylation has also been reported to be stimulated 1.5 to 2.5-fold by b_5 (30,33-35). CYP2D6

is a clinically significant P450 enzyme because of its ability to metabolize a wide array of pharmaceuticals and its high degree of polymorphism (36), but whose metabolite production is reportedly less influenced by b_5, at least with *in vitro* experiments (30,31,37,38). All of these human P450 enzymes in this study were the N-terminally truncated, C-terminally His-tagged forms used to determine X-ray crystallographic structures. They are expressed recombinantly in the significant quantities required to make multiple NMR samples, are highly purified, and functionally active without lipid addition. The latter aspect provides a common environment across NMR and catalytic assays and avoids variation due to variability in P450 incorporation into lipid.

Each P450 enzyme was saturated with a substrate to additionally stabilize the P450 proteins under NMR-compatible conditions. From significant previous experience with P450 enzymes produced for crystallographic studies, it is clear that high-affinity ligands often greatly improve the stability of these flexible, promiscuous enzymes. They also did so under conditions where the NMR experiments could be collected: 10-100 µM P450 in glycerol-free, low ionic-strength buffer at 25 °C for several hours. Additionally, previous reports on P450/b_5 interactions have indicated a greater affinity of the complex between the two proteins when P450 substrate is present (5). In this study, classical substrates with a single or at least one major metabolite were preferred, as this might be expected to simplify interaction modes by promoting a more homogenous P450 conformation, as well as permitting quantification of a single product in catalytic assays. Thus, CYP2E1 was saturated with the muscle relaxant chlorzoxazone (CZN), CYP3A4 with the hypotensive drug nifedipine (NFP), CYP2D6 with the cough suppressant dextromethorphan (DXM), and CYP2A6 with coumarin and *p*-nitrophenol (*p*NP). Of these substrates, addition of coumarin, chlorzoxazone, and dextromethorphan to CYP2A6, CYP2E1, and CYP2D6,

respectively, yielded shifts in the difference spectra indicating a transition from low spin to high spin, facilitating the ability to monitor protein saturation. The intrinsic absorbance of nifedipine and *p*-nitrophenol impaired such observations for CYP3A4 and CYP2A6, respectively. Under these conditions none of the samples resulted in visible precipitation and the reduced-carbon monoxide difference spectra were unchanged from the freshly purified P450 protein.

While NMR-observed titrations necessarily involved various concentrations of P450, other experiments were designed to reflect ratios of P450:CPR:b_5 often used in P450 functional assays in the literature. This is important as thoroughly demonstrated in studies on the rabbit CYP2B4 by Waskell and coworkers (10). Herein all catalytic assays used 1:2:2 ratios of P450 to CPR to b_5, rather than optimizing these ratios for maximal turnover with individual P450/substrate combinations as is frequently done. In NMR experiments this same ratio of P450 to b_5 was used to evaluate the b_5 mutants (0.5:1 P450:b_5, which is the same as 1:2 in the assays). To ensure that these ratios are accurate, special precautions were taken to avoid frequent problems with the quality and quantification of reductase and b_5. Cytochrome b_5 was reconstituted with heme during purification to avoid large amounts of apo-b_5 that can otherwise occur when polypeptide production exceeds heme production and which could also possibly bind P450. Reductase was purified to remove as much as possible of the proteolyzed form that can reduce cytochrome c, might be able to bind P450, but is not able to reduce P450 and promote catalysis. Thus, reductase was quantitated by flavin content instead of cytochrome *c* reduction. Reductase was also quantitated by total protein from the bicinchoninic acid assay using bovine serum albumin as a standard and was no more than 30% higher than quantitation by flavin absorbance. Both b_5 and reductase were the human forms to match the human P450 enzymes, rather than the rat versions often employed. Finally, because electrostatics are likely involved in both steering and binding

between b_5 and P450 enzymes, to provide additional consistency the same buffer was used in NMR experiments and all catalytic assays, with the exception of the CYP3A4 nifedipine metabolism assay, which required slightly different conditions (*vide infra*).

Finally, although the effects of b_5 on P450 catalysis are often simply evaluated by monitoring differences in metabolite formation in the presence and absence of b_5, b_5 may also have other effects not readily detected by this approach. It has been reported that b_5 can change the amount of NADPH consumed per amount of product formation (% coupling) (1), which wouldn't necessarily alter the amount of product formed. For this reason, NADPH consumption and its coupling to product formation was also evaluated in the absence and presence of wild type and mutant b_5 proteins.

2.4.2   Interactions and catalytic effects of b_5 on CYP2A6

When the 2D HSQC spectrum of ^{15}N-labeled b_5 alone is collected (*e.g.* Figure 2.1C, black), the intensity of each resonance is by definition 100%. As reported previously for CYP17A1 and CYP2B4, titrations of ^{15}N-b_5 with increasing concentrations of 2A6(coumarin) result in few chemical shifts, but line broadening occurs and the intensity of most resonances decreases (Figure 2.1C), with more marked reductions for specific residues (Figure 2.1D). Because the dominant features are changes in intensity and because such overlaid spectra are difficult to comprehend visually, each resonance in each series of spectra was analyzed and the percentage of intensity remaining plotted graphically (*e.g.* Figure 2.2A).
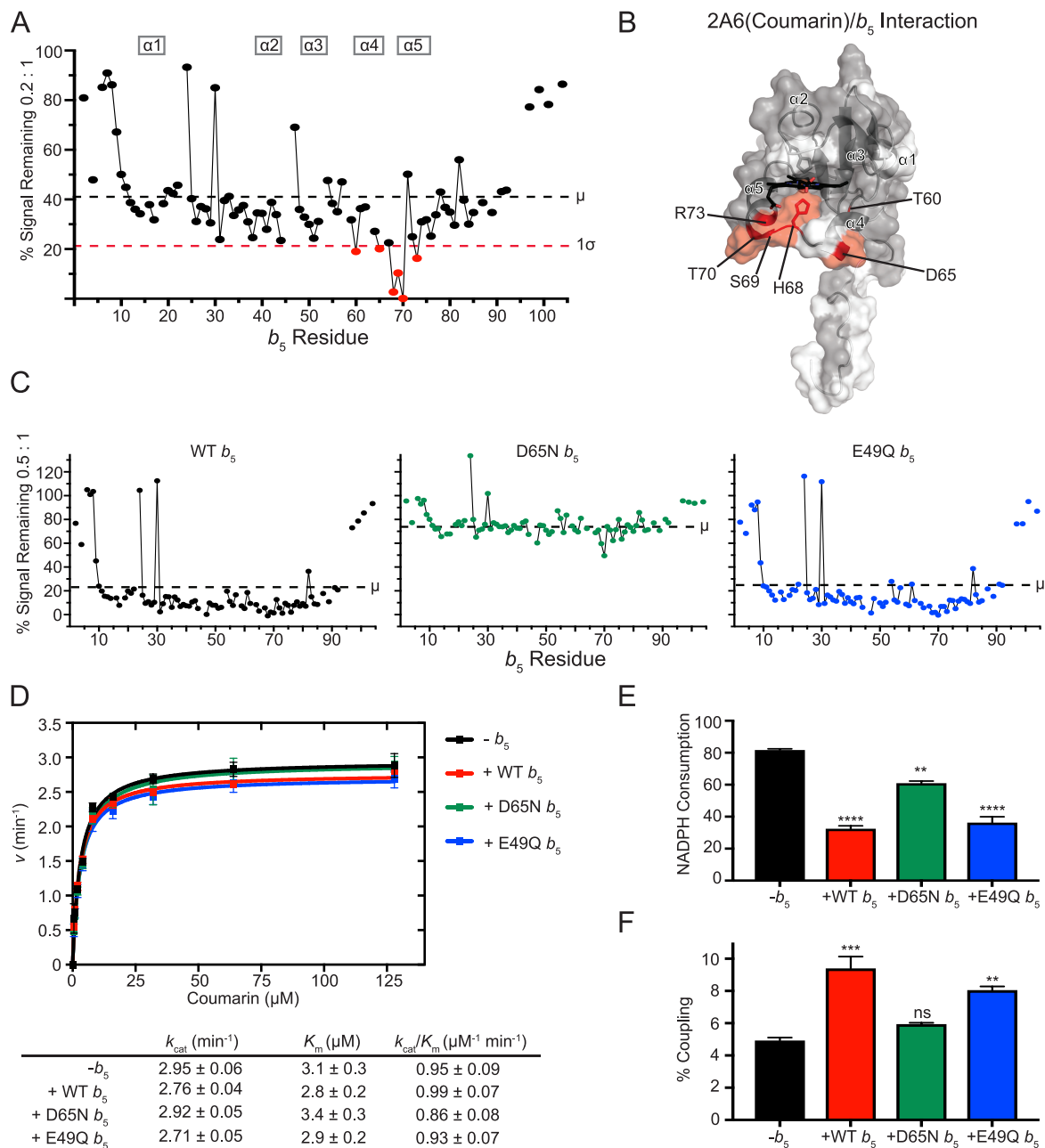
Figure 2.2 Interaction of CYP2A6(coumarin) with ^{15}N-b_5 by NMR and b_5 modulation of CYP2A6 catalysis. A, a single NMR spectrum of 0.2:1 CYP2A6(coumarin):^{15}N-b_5 is shown graphically. The intensity of each b_5 resonance (circle) corresponding to an individual b_5 residues (x axis) is plotted as a percentage of that resonance's intensity in the absence of P450 (y axis). Fine lines between circles indicate continuous assignments for sequential b_5 amino acids. Gaps in the line between circles indicate that one or more intervening b_5 amino acids have not been assigned to an individual resonance in the spectrum (also shown in white in Figure 2B). The average (μ) and average minus one standard deviation (1σ) are indicated on the plot by black and red dashed lines, respectively, and constitute the selection criteria of b_5 residues involved in P450 binding (red circles). B, on the surface of the human soluble domain b_5 structure (PDB: 2I96) residues displaying differential broadening effects colored red, while residues that have assigned NMR resonances that are not differentially affected by P450 addition are colored grey, and unassigned residues are colored white. C, resonance intensity plots as in 2A, but comparing the effects of line broadening between WT b_5 and b_5 mutants D65N and E49Q at a fixed 0.5:1 CYP2A6(coumarin):^{15}N-b_5 ratio. D, the effects of wild type and mutant b_5 proteins on Michaelis-Menten kinetic parameters of CYP2A6-mediated coumarin 7-hydroxylation. Each sample was generated in duplicate with standard deviation illustrated by error bars. Steady-state kinetic constants below are shown with standard deviation. E, measurement of NADPH consumed (nmol NADPH/min/nmol CYP2A6) for the CYP2A6 coumarin reaction at a fixed coumarin concentration of

44

For CYP2A6(coumarin) reductions in the average b_5 signal intensity occur even at very low P450:b_5 ratios. At a CYP2A6(coumarin):b_5 ratio of 0.1:1 an average of ~68% of the original signal remained. As expected with increasing formation of the complex, the average intensities continued to decrease as more and more CYP2A6(coumarin) was added. At 0.2:1 on average ~41% of the original signal intensity remained (Figure 2.2A, black dashed line). At 0.3:1, 0.4:1, and 0.5:1 approximately 35%, 26%, and 22% of the original signal remained.

At titration points with ~40-60% reduction in intensity there is enough P450/b_5 complex formed to clearly identify specific b_5 amino acids whose resonances are differentially broadened compared to the average. For CYP2A6(coumarin) this corresponds to the 0.2:1 ratio, which reveals a number of b_5 resonances were broadened more than one standard deviation (Figure 2.2A, red dashed line) from the average (Figure 2.2A, black dashed line), consistent with the involvement of these b_5 residues in binding CYP2A6(coumarin). These b_5 resonances correspond to residues T60, D65, H68, S69, T70, and R73, which cluster on b_5 helices 4 and 5 and the loop connecting them (Figure 2.2B, red).

In order to further examine the role of specific b_5 residues interacting with CYP2A6(coumarin), a series of mutations were examined. Residues D65 and E49 were selected based on 1) their location on the b_5 surface, 2) previous evidence that electrostatic pairing is important in b_5/P450 complex formation (4,8), 3) locations on distinct b_5 faces (Figure 2.1A), and 4) their location in or near binding interfaces identified herein (*vide infra*). D65 is located in b_5 α4, while E49 is in b_5 α3. The effects of the charge-neutralizing E49Q and D65N mutations on P450 interactions with b_5 were evaluated at a P450:b_5 ratio of 0.5:1 for all P450 enzymes. As indicated above, under these conditions with wild type b_5, the intensity for the average b_5 resonance

decreases to ~22% of the original signal (Figure 2.2C, left panel). However, when the b_5 mutant D65N was mixed with CYP2A6(coumarin) at the same ratio, the overall line broadening was much less—to only 76% of the original (Figure 2.2C, middle panel)—consistent with decreased complex formation between b_5 D65N and CYP2A6(coumarin) compared to wild type b_5. Conversely, mixing the b_5 mutant E49Q with CYP2A6(coumarin) yielded average line broadening (to ~25%, Figure 2.2C, right panel) similar to wild type b_5 (22%, Figure 2.2C, left panel), suggesting that this mutation did not adversely affect formation of the b_5/CYP2A6(courmarin) complex. These results suggest that while the anionic charge on D65 in b_5 helix 4 has a significant role in b_5 binding to CYP2A6(coumarin), that E49 in b_5 helix 3 has little to no effect on complex formation.

In order to relate these structural observations to enzymatic function, coumarin metabolism assays were subsequently employed. Under our conditions there was no significant effect of b_5 on CYP2A6 7-hydroxycoumarin formation. Neither k_{cat} or K_m were substantially altered in the presence of b_5 (Figure 2.2D). Thus, it was not surprising that neither the D65N or E49Q b_5 mutants altered coumarin metabolism (Figure 2.2D).

Although the presence of wild type b_5 did not alter formation of the 7-hydroxycoumarin product, coupling studies revealed that NADPH consumption was reduced by ~60% (Figure 2.2E, red). Thus, wild type b_5 increased productive coupling of the reaction by ~1.9-fold (Figure 2.2F, red). The b_5 D65N mutant which appeared to decrease b_5 binding to CYP2A6(coumarin) in the NMR experiments yielded a much smaller decrease in NADPH consumption (Figure 2.2E, green) and had similar coupling to when b_5 was not present (Figure 2.2F, green vs. black). The E49Q b_5 which did not appear to alter b_5 binding to CYP2A6(coumarin) in the NMR experiments functioned more like wild type b_5, with a similar NADPH consumption (Figure 2.2E blue vs. red) and productive coupling (Figure 2.2 blue vs. red). Overall wild type and E49Q b_5 acted similarly,

with 1.9 and 1.6-fold increases in coupling, respectively, while D65N has little effect on coupling (a 1.2-fold increase in coupling over reactions without b_5).

While the effects of b_5 on NADPH consumption observed herein are consistent with the ~50% reduction previously reported for CYP2A6 coumarin 7-hydroxylation (33,35), there have also been reports that b_5 can increase product formation in the range of 1.5 to 2.5-fold (30,33-35). However, no such increase in 7-hydroxycoumarin was observed herein. This apparent discrepancy could be due to other differences in experimental conditions. Of particular importance are the protein ratios used for P450:CPR:b_5 in catalytic assays. Experimental evidence to date strongly supports mutually-exclusive, overlapping binding sites for CPR and b_5 on the proximal face of P450 enzymes. As a result, the ratio and relative affinities of reductase and b_5 for a particular P450 would dictate the observed effects (1). At high relative ratios and/or affinities, b_5 could inhibit required reduction of ferric P450 by reductase, while at lower relative ratios and/or affinities b_5 may exert stimulatory effects on other steps of the P450 catalytic cycle to increase coupling (13). That b_5 significantly inhibits NADPH consumption without changes in product formation suggests that for this enzyme(substrate) combination the 1:2:2 ratio may balance the inhibitory and stimulatory effects of b_5. However, other significant differences, for example in the species and quantitation of b_5 and reductase, the presence of lipid, etc., may also contribute to different observations across the literature with respect to b_5 effects on product formation.

Regardless, NMR and functional assays herein consistently suggest that D65N in b_5 helix 4 is important in both binding to CYP2A6(coumarin) and in improving coupling of NADPH consumption to product formation. More broadly the NMR data suggest that b_5 surface residues in both helix 4 and helix 5 are involved in binding to CYP2A6(coumarin).

2.4.3 Interaction and catalytic effects of b_5 on CYP2E1

CYP2E1-mediated oxidation of many different substrates is reportedly stimulated by b_5. These include chlorzoxazone, acetaminophen, aniline, and *N*-nitrosodimethylamine (28,29). Studies suggest that b_5 may play a redox role with CYP2E1, as apo-b_5 does not increase product formation (30,31).

NMR experiments performed in this study revealed that titration of b_5 with CYP2E1(chlorzoxazone), like CYP2A6(coumarin), also caused fairly substantial overall broadening at moderate P450:b_5 ratios. At 1:0.25, for example, an average of ~55% signal remained (Figure 2.3A) and by 1:0.5 only ~28% of the original signal was present (Figure 2.3C). The resonances for b_5 residues V34, H68, S69, T70, and S76 had signal losses more than one standard deviation below this average (Figure 2.3A). Each of these residues except for V34 reside on α5 or the preceding loop (Figure 2.3B). This result is consistent with a monofacial interaction between b_5 and CYP2E1(CZN) involving α5 and nearby residues.
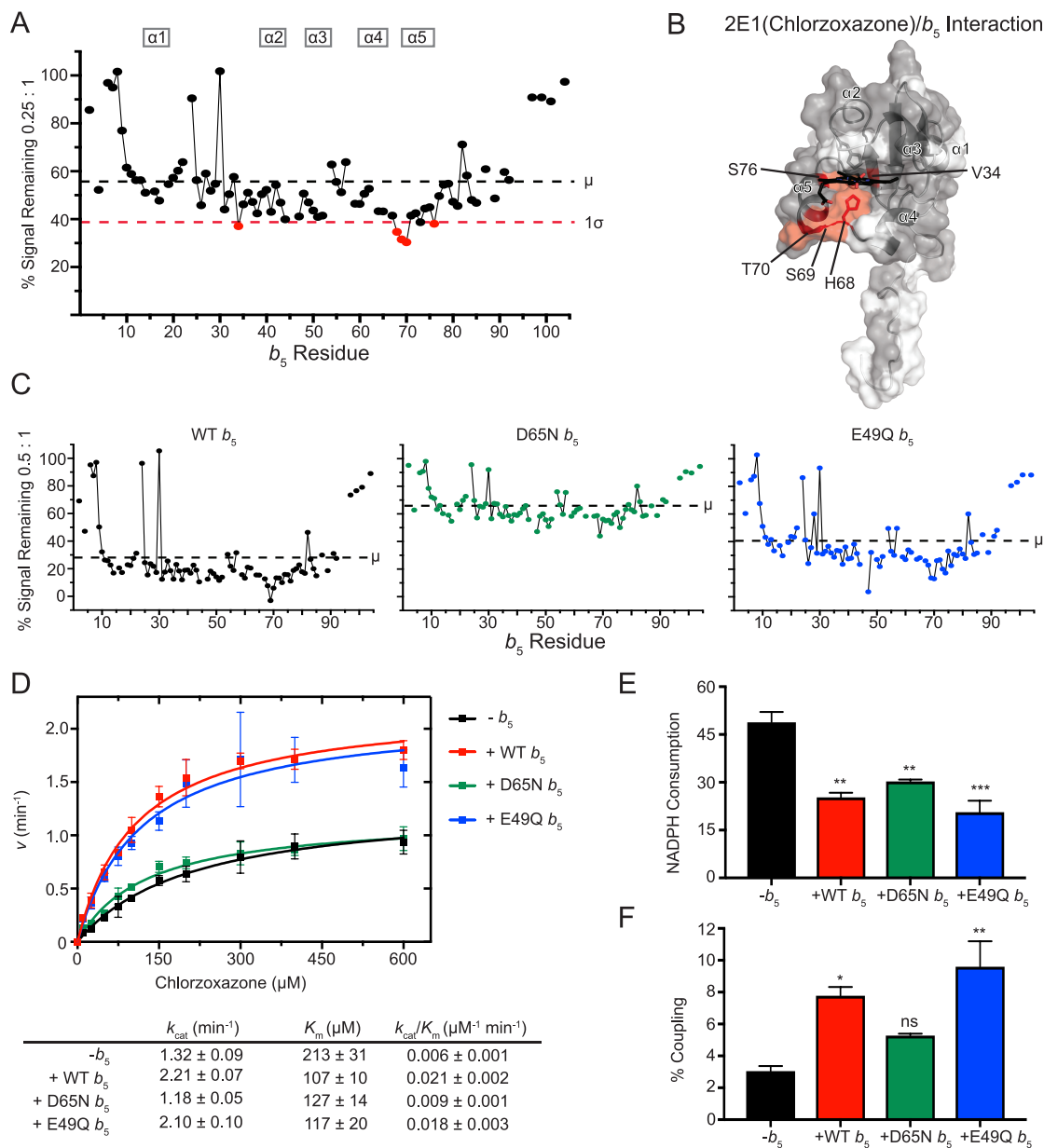
Figure 2.3 Interaction of CYP2E1(chlorzoxazone) with ^{15}N-b_5 by NMR and b_5 modulation of CYP2E1 catalysis. A, a single NMR spectrum of 0.25:1 CYP2E1(CZN):^{15}N-b_5 is shown graphically as described in Figure 2A. B, mapping of differentially affected residues (red) on human b_5. Legend as described in Figure 2B. C, resonance intensity plots comparing line broadening for wild type b_5 and b_5 mutants at a 0.5:1 CYP2E1(CZN):^{15}N-b_5 ratio. D, effect of wild type and mutated b_5 on Michaelis-Menten kinetic parameters of CYP2E1-mediated chlorzoxazone 6-hydroxylation. Each sample was generated in triplicate with standard deviation illustrated by error bars. Steady-state kinetic constants below are shown with standard deviation. E, NADPH consumed (nmol NADPH/min/nmol CYP2E1) for CYP2E1-mediated chlorzoxazone metabolism at a fixed chlorzoxazone concentration of 600 μM. Samples were generated in duplicate with the standard deviation illustrated by error bars. F, percent coupling of CYP2E1-mediated chlorzoxazone 6-hydroxylation. Samples were generated in duplicate with the standard deviation illustrated by error bars. ns, >0.05; **, P≤0.01; ***, P≤0.001; ****, P ≤ 0.0001.

Consistent with the above idea, when evaluated at a consistent P450:b_5 ratio of 0.5:1, the

b_5 D65N mutant had less loss of average signal intensity (to 66%; Figure 2.3C, middle panel) than

wild type b_5 (Figure 2.3C, left panel).   This suggests the D65N b_5 mutant reduces binding to CYP2E1(CZN). Notably, the E49Q mutant on the opposite b_5 surface had an intermediate effect on average signal intensity to ~41% of the original signal.

Comparison of the mutational effects are clearer when evaluating chlorzoxazone 6-hydroxylation. Consistent with previous literature reports (39,40), the effect of wild type b_5 on 2E1 chlorzoxazone 6-hydroxylation was pronounced, with both an increased k_{cat} and decreased K_m (Figure 2.3D). Specifically, experiments herein revealed an ~1.7-fold increase in k_{cat} and a 2-fold decrease in K_m, yielding an ~3.5-fold increase in k_{cat}/K_m.   The E49Q b_5 mutant performed very similar to wild type b_5 (Figure 2.3D), suggesting that this residue is not critical. However, using the b_5 mutant D65N in these reactions yielded substrate metabolism and steady-state kinetic parameters more similar to when b_5 was not present at all (Figure 2.3D). Thus, the surface near D65 is important in both b_5 binding to CYP2E1(CZN) and stimulation of product formation.

Coupling between NADPH consumption and product formation are typically very poor for CYP2E1 in general. Under the current conditions in the absence of b_5, CYP2E1 coupling was only ~3%. Addition of wild type b_5 significantly decreased the NADPH consumption by 48% (Figure 2.3E) while increasing product formation, resulting in increased coupling of the reaction by ~2.5-fold (Figure 2.3F). The b_5 mutant E49Q behaved similarly to wild type b_5 in that NADPH consumption was decreased to a similar extent (Figure 2.3E) and combined with increased product formation the coupling increased ~3.1-fold (Figure 2.3F)—slightly more than in the presence of wild type b_5. The b_5 mutant D65N also reduced NADPH consumption (~38%, Figure 2.3E), but had little effect on product formation, thus increasing coupling by ~1.7-fold when compared to reactions in the absence of b_5 (Figure 2.3F).

Interactions between b_5 and CYP2E1 have previously been studied using cross-linking of the complex coupled with mass spectrometry. Those studies also identified residues on the same surface of b_5: D58 and E61 in one study (6) and D58 and D65 in another study (41). In the latter study these interactions were further tested for their functional role and both residues appeared to be important in b_5 stimulation of the 6-hydroxylation of CZN (41). Unfortunately, the resonance for D58 in b_5 has not been assigned, but it would be predicted to experience differential line broadening. Overall the current experiments and previous studies support the concept that the region surrounding D65 is involved in both physical interaction between b_5 and CYP2E1 and increases observed in product formation.

2.4.4 Interaction and catalytic effects of b_5 on CYP3A4

Influence of b_5 on CYP3A4 has been reported broadly. A number of CYP3A4-mediated reactions are stimulated by both holo and apo-b_5 (32), which may support a more allosteric role for b_5. The current studies evaluated interactions and the effects of b_5 on the hypotensive drug nifedipine (NFP).

Using solution NMR to visualize the interaction between CYP3A4(NFP) and b_5 it was clear that considerable broadening occurred for the average b_5 resonance with low concentrations of CYP3A4(NFP), suggesting substantial formation of the P450/b_5 complex. With a CYP3A4(NFP):b_5 ratio of 1:0.1, 85% of the average b_5 signal remained. Additional CYP3A4(NFP) resulted in further decreases in the average resonance signal (1:0.2 = ~59%, 1:0.3 = ~59%, 1:0.4 = ~41%, 1:0.5 = ~29%).

Although the trends were similar throughout the titration range, differential line broadening was most distinct at the 0.2:1 ratio of CYP3A4(NFP):b_5 (Figure 2.4A). Residues of b_5 differentially broadened more than one standard deviation below the average are L41, E42, H44,

51

G47, E48, E49, L51, R52, H68, S69, A72, and R73 (Figure 2.4A). These residues cluster on helices 2, 3, and 5, as well as the loop between helices 2 and 3, and the loop preceding helix 5 (Figure 2.4B). This suggests that these two faces of b_5 are likely to interact with CYP3A4(NFP).
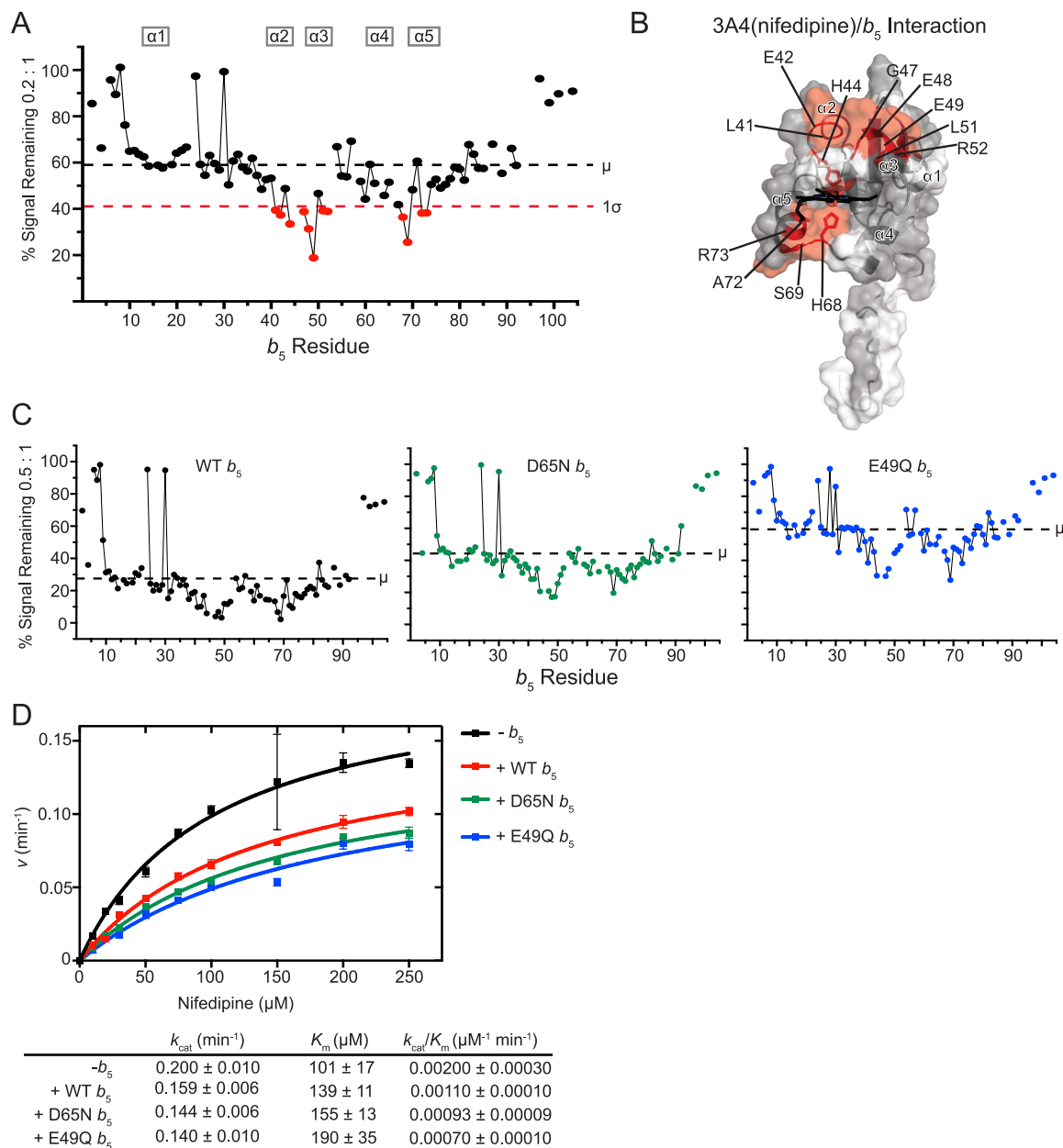
Figure 2.4 Figure 4. Interaction of CYP3A4(nifedipine) with ^{15}N-b_5 as determined by NMR and catalytic modulation of b_5 on CYP3A4 mediated metabolism of nifedipine. A, b_5 resonance intensity plot at a 0.2:1 (CYP3A4(nifedipine):^{15}N-b_5) ratio normalized to the free b_5 resonance intensity. The average (μ) and 1 SD minus average (1σ) lines are indicated on the plot and base the selection criteria of b_5 binding hot-spots. B, human soluble domain b_5 structure (PDB: 2I96) with residues displaying differential broadening effects colored in red, residues which are assigned in the NMR spectrum are colored in grey, and unassigned residues are colored white. C, b_5 resonance intensity plots comparing the effects of line broadening between WT b_5 and b_5 mutants D65N and E49Q at a fixed 0.5:1 (CYP3A4(nifedipine):^{15}N-b_5) ratio. D, effect of WT b_5 and mutants on Michaelis-Menten kinetic parameters of CYP3A4 mediated oxidation of nifedipine. Each sample was generated in duplicate with standard deviation illustrated by error bars. Steady-state kinetic constants below are shown with standard deviation.

To evaluate the significance of these two surfaces, the b_5 mutants D65N and E49Q were used to further evaluate the physical interaction between b_5 and CYP3A4(NFP). As with the other

enzymes, this was conducted at the P450:b_5 ratio of 0.5:1. While CYP3A4(NFP) resulted in a signal reduction to an average of 29% for wild type b_5 (Figure 2.4C, left panel), this effect was dampened for both b_5 mutants. At this same ratio, ~45% of the average signal remained for D65N (Figure 2.4C, middle panel) and ~60% for E49Q (Figure 2.4C, right panel). Thus, both mutations appeared to reduce CYP3A4(NFP)/b_5 complex formation. Notably, even though the overall average intensities were higher for each b_5 mutant compared to wild type, distinctive differential broadening still occurred (Figure 2.4C, middle and right panels), suggesting that specific interactions between b_5 and 3A4(nifedipine) were not completely disrupted by either single point mutation.

CYP3A4 converts nifedipine to dehydronifedipine. The addition of wild type b_5 to such reactions resulted in inhibition of this reaction (Figure 2.4D). The addition of b_5 both decreased the k_{cat} and increased the K_m such that the k_{cat}/K_m was almost half that when b_5 was not present. Literature has reported varied stimulation of nifedipine by b_5, typically ~1.3 to 3-fold increased product formation (30,42). The differences in these observations may lie in the protein ratios used to perform the experiments. Peng & Auchus (42) used a 1:2:4 ratio in their assays, while Yamazaki *et al.* (30) used a 1:4:1 ratio. The overlapping b_5 and reductase binding sites and the variability in these results under different conditions may suggest that at higher concentrations of b_5 relative to reductase that b_5 may begin to outcompete reductase binding, resulting in an overall reduction in product formation while lower relative concentrations of b_5 could be stimulatory. However there were also other potentially significant differences between how the assays were accomplished in different reports, including the presence of lipid, the constructs or buffer used. CYP3A4-mediated metabolism seems to be more sensitive to these environmental parameters than many other P450 enzymes. Notably, the single b_5 mutants D65N and E49Q had effects on nifedipine oxidation most

similar to wild type b_5. Thus, the two-point interactions between CYP3A4(NFP) and b_5 are not disrupted enough by the single point mutations to ameliorate the effect of b_5 on product formation. Unfortunately, NADPH consumption and coupling of the 3A4(nifedipine) reaction were not successful due to low turnover rates of the reaction under the conditions employed for all the assays herein.

Overall, the differential line broadening of NMR signal suggests that CYP3A4(NFP) interacts with b_5 over the widest surface area for any of the b_5/P450 complexes in this study. Interactions between CYP3A4 and b_5 have been reported previously in cross-linking and mutational studies. Zhao *et al.* used mass spectrometry to identify crosslinks between the two proteins, residues on human b_5 identified were E42 or E48, and E61, which are located on $\alpha2$, $\alpha3$, and the start of $\alpha4$ (7). Another study reported similar residues, where mutations in human b_5 residues E48, E49, D58, and D65 had significant decreases in the ability of b_5 to enhance CYP3A4-mediated testosterone and nifedipine oxidation (42). Moreover, the b_5 double mutant D58G/D65G significantly impaired the ability to form cross-links with CYP3A4, while the double mutant E48G/E49G had reduced stimulation but was highly dependent on the type of phospholipid in the assay (42). Overall, the current NMR data of the CYP3A4/b_5 complex is consistent with reported interactions in these previous studies, but highlights additional residues.

2.4.5   Interaction and catalytic effects of b_5 on CYP2D6

CYP2D6 metabolizes numerous pharmaceuticals including many antidepressants and antipsychotics. It exhibits substantial polymorphism in humans (36). To assess whether 2D6 forms a complex with b_5 NMR-monitored titrations of ^{15}N-b_5 with CYP2D6 were carried out using a saturating amount of its common antitussive substrate dextromethorphan (DXM). The titrations resulted in line broadening, consistent with complex formation between the two proteins, but

required much higher concentrations of CYP2D6 than any of the other drug-metabolizing enzymes in this study. For example, it takes a 1:1 CYP2D6(DXM):b_5 ratio before the average signal intensity drops to about half (48%, Figure 2.5A). In comparison, CYP2A6(coumarin) had more signal reduction by a 0.2:1 ratio.
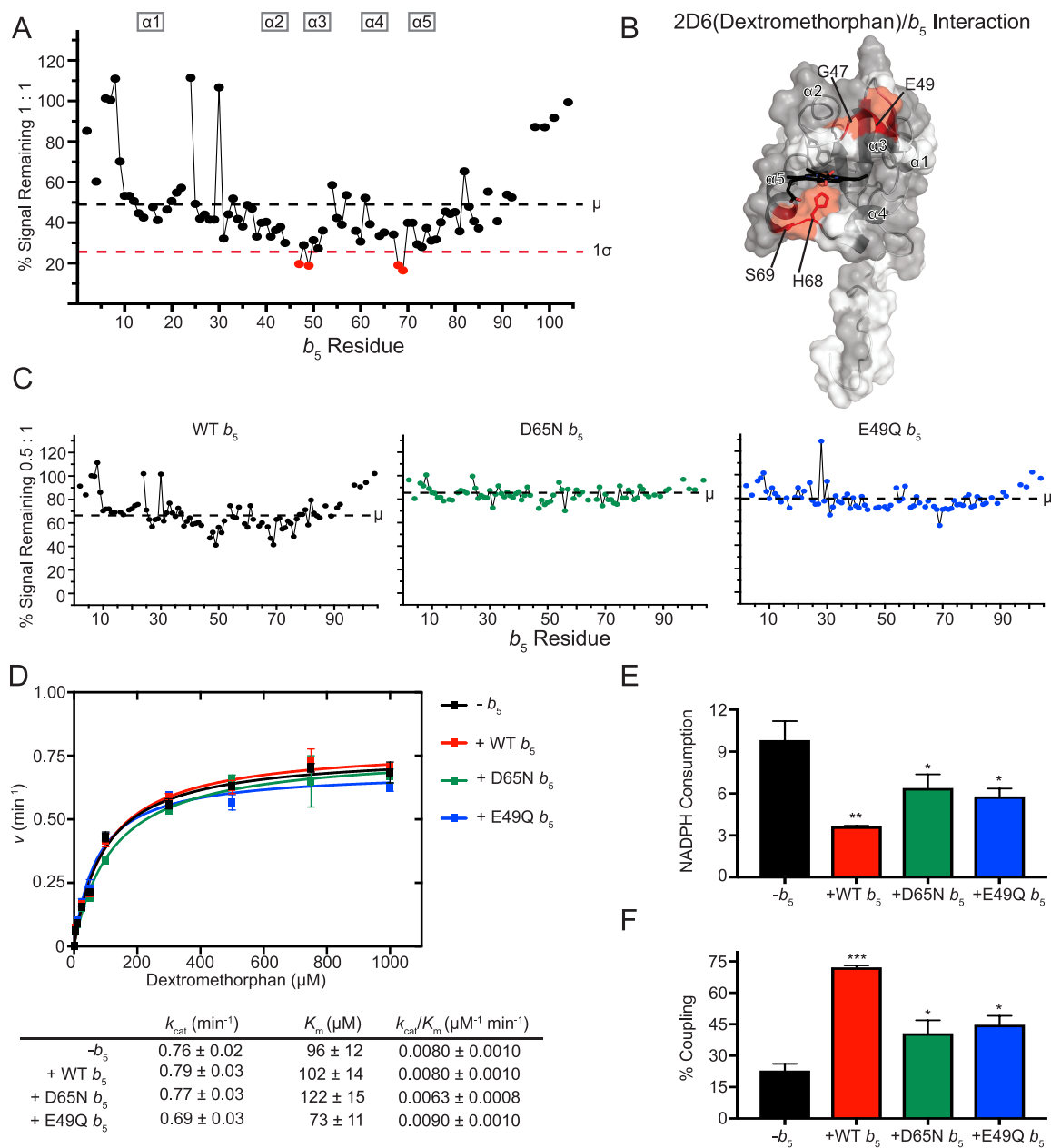
Figure 2.5 Figure 5. Interaction of CYP2D6(dextromethorphan) with ^{15}N-b_5 as determined by NMR and catalytic modulation of b_5 on CYP2D6 mediated metabolism of dextromethorphan. A, b_5 resonance intensity plot at a 1 : 1 (CYP2D6(DXM):^{15}N-b_5) ratio normalized to the free b_5 resonance intensity. The average (μ) and 1 SD minus average (1σ) lines are indicated on the plot and base the selection criteria of b_5 binding hot-spots. B, human soluble domain b_5 structure (PDB: 2I96) with residues displaying differential broadening effects colored in red, residues which are assigned in the NMR spectrum are colored in grey, and unassigned residues are colored white. C, b_5 resonance intensity plots comparing the effects of line broadening between WT b_5 and b_5 mutants D65N and E49Q at a fixed 0.5:1 (CYP2D6(DXM):^{15}N-b_5) ratio. D, effect of WT b_5 and mutants on Michaelis-Menten kinetic parameters of CYP2D6 mediated O-demethylation of dextromethorphan. Each sample was generated in triplicate with standard deviation illustrated by error bars. Steady-state kinetic constants below are shown with standard deviation. E, measurement of NADPH consumed (nmol NADPH / min / nmol CYP2D6) for CYP2D6 dextromethorphan reaction at a fixed dextromethorphan concentration of 1 mM. Samples were generated in duplicate with the standard deviation illustrated by error bars. F, percent coupling of CYP2D6 mediated O-demethylation of dextromethorphan. Samples were generated in duplicate with the standard deviation illustrated by error bars. *: $P \leq 0.05$, **: $P \leq 0.01$, ***: $P \leq 0.001$.

Within these data, the resonances for four residues are broadened more than one standard deviation from the average. G47, E49, H68, and S69 are all differentially broadened (Figure 2.5A). On the b_5 surface these residues fall into two disconnected regions of b_5: the start of $\alpha3$ (G47 and E49) and the loop between $\alpha4$ and $\alpha5$ (H68 and S69) (Figure 2.5B). This data suggests that when a complex is formed at higher concentrations of CYP2D6(DXM), that both faces of b_5 are involved.

To probe the importance of these distinct faces, the E49Q and D65N b_5 mutants were also evaluated for their ability to bind CYP2D6(DXM). At the uniform ratio of 0.5:1, wild type b_5 retained an average signal intensity of 69% (Figure 2.5C, left panel), but both mutants retained even more signal intensity. E49Q and D65N retained ~80%, and ~84% of the signal intensity, respectively (Figure 2.5C, right and middle panels). This is consistent with both charges contributing to the b_5/CYP2D6(DXM) complex when it does occur.

To link these structural observations with the effects of b_5 on CYP2D6 dextromethorphan metabolism, both wild type and mutant b_5 proteins were employed in steady-state turnover assays. Similar to other *in vitro* reports on CYP2D6 reactions (30,43), the presence of wild type b_5 had no significant effects on kinetics of metabolite formation from dextromethorphan (Figure 2.5D). Thus, not surprisingly, neither b_5 mutant altered product formation.

When NADPH consumption was measured, however, the presence of b_5 did result in a two-thirds reduction (Figure 2.5E) and therefore an increase in coupling (from ~23% to ~72%; Figure 2.5F). Each of the single E49Q and D65N b_5 mutants also reduced NADPH consumption (to ~59% and ~65%, respectively; Figure 2.5E), but not as effectively as wild type b_5. Thus the ~2.0-fold increases in coupling with E49Q and D65N b_5, were less than the ~3-fold increase in coupling observed for wild type b_5 (Figure 2.5F).

CYP2D6(DXM) interaction with b_5 appeared to be similar to CYP3A4(NFP) in that opposite surfaces of b_5 were implicated, but extensive broadening of b_5 resonances did not occur until an equal molar (1:1) ratio of 2D6(DXM):b_5, a feature that would be consistent with a weaker interaction with CYP2D6(DXM) compared to the other P450/b_5 pairs studied. Most previous studies have reported no b_5 stimulation of CYP2D6-mediated *in vitro* bufuralol 1'-hydroxylation, tamoxifen 4-hydroxylation, or acetaminophen conversion to its toxic metabolite NAPQI (30,31,37,38). There is one conflicting report indicating that b_5 could modulate CYP2D6 metabolite formation *in vivo*, as mice humanized for CYP2D6 have decreased bufuralol and debrisoqine turnover upon hepatic deletion of the b_5 gene. This could be ameliorated by the addition of membranes containing b_5 (44).

2.4.6   Interactions and catalytic effects of b_5 on CYP2A6 saturated with *p*-nitrophenol

To begin to probe the effects that the identity of a given P450 substrate might have on interactions with b_5, the interactions of CYP2A6 saturated with *p*-nitrophenol (*p*NP) were also investigated using NMR and functional assays and compared with earlier results for CYP2A6(coumarin).

When ^{15}N-b_5 was titrated with CYP2A6(*p*NP) differential line broadening was observed for very similar residues observed with 2A6(coumarin). Specifically, b_5 residues significantly affected were E64, H68, S69, T70, and R73 (Figure 2.6A), which comprise b_5 α4, α5, and the intervening loop (Figure 2.6B). However, the average reduction in signal was not as pronounced when CYP2A6 was saturated with *p*NP as it was when CYP2A6 was saturated with coumarin. For example, at a P450:b_5 ratio of 1:0.5, ~49% of the average b_5 signal remained for the CYP2A6(*p*NP)/b_5 mixture (Figure 2.6C, left panel), compared to ~22% remaining signal for the CYP2A6(coumarin)/b_5 mixture (Figure 2.2C, left panel).
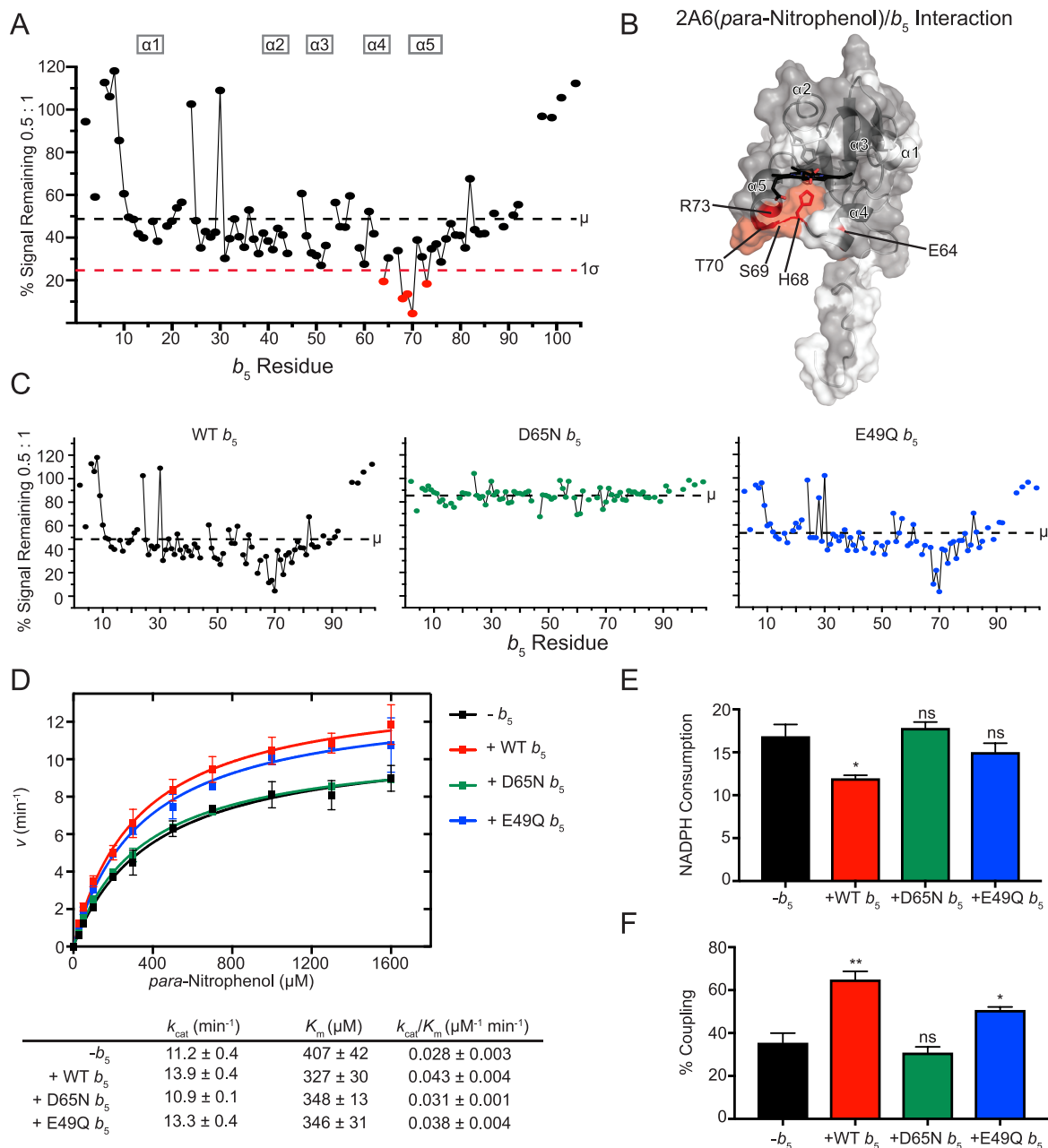
Figure 2.6 Interaction of CYP2A6(*p*NP) with ^{15}N-*b*$_5$ as determined by NMR and catalytic modulation of *b*$_5$ on CYP2A6 mediated metabolism of *para*-nitrophenol. A, *b*$_5$ resonance intensity plot at a 0.5:1 (CYP2A6(*p*NP):^{15}N-*b*$_5$) ratio normalized to the free *b*$_5$ resonance intensity. The average (μ) and 1 SD minus average (1σ) lines are indicated on the plot and base the selection criteria of *b*$_5$ binding hot-spots. B, human soluble domain *b*$_5$ structure (PDB: 2I96) with residues displaying differential broadening effects colored in red, residues which are assigned in the NMR spectrum are colored in grey, and unassigned residues are colored white. C, *b*$_5$ resonance intensity plots comparing the effects of line broadening between WT *b*$_5$ and *b*$_5$ mutants D65N and E49Q at a fixed 0.5:1 (CYP2A6(*p*NP):^{15}N-*b*$_5$) ratio. D, effect of WT *b*$_5$ and mutants on Michaelis-Menten kinetic parameters of CYP2A6 mediated 2-hydroxylation of *p*NP. Each sample was generated in duplicate with standard deviation illustrated by error bars. Steady-state kinetic constants below are shown with standard deviation. E, measurement of NADPH consumed (nmol NADPH / min / nmol CYP2A6) for CYP2A6 *p*NP reaction at a fixed *p*NP concentration of 1.6 mM. Samples were generated in duplicate with the standard deviation illustrated by error bars. F, percent coupling of CYP2A6 mediated 2-hydroxylation of *p*NP. Samples were generated in duplicate with the standard deviation illustrated by error bars. ns: $P > 0.05$, *: $P \leq 0.05$, **: $P \leq 0.01$.

60

The importance of D65 in forming the complex between b_5 and CYP2A6(pNP) was similar to that observed with the substrate coumarin. At the uniform 0.5:1 P450:b_5 ratio, the b_5 D65N mutation retained more signal average intensity (~86%, Figure 2.6C, middle panel) than wild type b_5, (49% signal remaining, Figure 2.6C, left panel), consistent with reduced complex formation for the mutant. By comparison, under the same conditions the b_5 E49Q mutant had an average intensity (54%, Figure 2.6C, right panel) much more similar to wild type b_5, suggesting that this b_5 residue does not play a significant role in binding CYP2A6(pNP).

The effects of these b_5 mutants on formation of a CYP2A6(pNP)/b_5 complex correlated with observations of the kinetics of CYP2A6 $para$-nitrophenol metabolism to 4-nitrocatechol. While wild type b_5 modestly stimulated the reaction with both an increase in k_{cat} and decrease in K_m, resulting in an overall ~1.5-fold increase in catalytic efficiency (Figure 2.6D), the b_5 mutant E49Q performed very similarly (Figure 2.6D), suggesting this residue is not critical for b_5 simulation of CYP2A6-mediated pNP metabolism. In contrast, reactions substituting the b_5 mutant D65N resulted in steady-state kinetic parameters more similar to reactions containing no b_5 at all (Figure 2.6D), suggesting that D65 is critical for the b_5 stimulation of CYP2A6-mediated pNP oxidation. It has previously been reported that CYP2A6-mediated pNP oxidation is not significantly altered by the presence of b_5 (45). However these results were obtained at a single pNP concentration that was relatively low (5 μM) and at a CYP2A6:CPR ratio of 1:5.8 (45). The CYP2A6 pNP assays performed in the current study used a range of pNP concentrations (25 μM to 1600 μM), and a CYP2A6:CPR ratio of 1:2. Thus, differences in experimental parameters could contribute to observed differences in b_5 stimulation and again suggest that the ratio of b_5 to CPR is likely to determine the outcome since these two proteins both bind, and likely compete for, the P450 proximal surface.

Evaluation of NADPH coupling herein revealed that wild type b_5 decreased NADPH consumption by ~30% (Figure 2.6E) and increased coupling of NADPH consumption to formation of the 4-nitrocatechol product formation 1.8-fold (Figure 2.6F). By comparison, neither the E49Q or D65N mutation significantly altered NADPH consumption (Figure 2.6E). However, the increased product formation observed for the b_5 E49Q results in a ~1.4-fold increase in coupling, while the absence of effect of D65N b_5 on product formation and NADPH consumption meant coupling was the same as in the absence of b_5 (Figure 2.6F). Thus, these studies also support a significant role for D65, but less so for E49.

Overall, the NMR and mutation data herein suggests that the b_5 surface involved in binding to CYP2A6(*p*NP) (Figure 2.6B) is very similar to the b_5 surface binding CYP2A6(coumarin) (Figure 2.2B). Mutation studies confirmed that D65 on one face of b_5 plays a significant role in both CYP2A6/b_5 interactions, while E49 on the opposing b_5 face had relatively little contribution. The greater degree of line broadening occurring with the substrate coumarin compared to *p*NP is potentially consistent with a stronger b_5 interaction with CYP2A6(coumarin) compared to CYP2A6(*p*NP). However, we cannot exclude effects due to possible differences in CYP2A6 paramagnetism when bound to different ligands. CYP2A6(coumarin) results in almost complete conversion to high-spin, while the CYP2A6(*p*NP) spin state cannot be readily assessed because of significant *p*NP absorbance in the region of interest. Using immobilized CYP2A6 and biotinylated b_5, Guengerich and coworkers found no difference in binding for unliganded CYP2A6 vs. CYP2A6 bound to coumarin (38). Like the structural data, the effects of b_5 mutants in turnover assays support an important role for D65N in coupling and metabolite formation. In contrast, E49Q performed more similarly to wild type enzyme, suggesting this residue isn't critical for changes in CYP2A6-mediated *p*NP metabolism. In both CYP2A6-mediated coumarin and *p*NP

metabolism, b_5 increased coupling ~2-fold. However, this mostly stemmed from a decrease in NADPH utilization for coumarin hydroxylation, while for pNP oxidation both decreased NADPH consumption and increased metabolite formation contributed. Thus, though the b_5 residues binding CYP2A6 are conserved across these two substrates, the effects on CYP2A6 catalysis vary.

2.4.7 Comparison of P450/b_5 interactions across P450 enzymes and substrates

Of the four human P450 enzymes surveyed all of them were found to interact with cytochrome b_5 and to do so predominately on at least one of the surfaces surrounding the heme-exposed face of b_5. This is in general agreement with studies assessing b_5 interactions with CYP17A1 (4,8), CYP2B4 (14), CYP3A4 (7,42), and CYP2E1 (6,41). However, the use of NMR allows one to simultaneously probe all possible b_5 residues involved in the interaction without modifying either interacting partner aside from isotopic labeling. As a result, this study identified two b_5 surfaces differentially interacting with different xenobiotic P450 enzymes. All four P450 enzymes in this study interacted with H68 and S69 on the loop between α4 and α5. Three of them (CYP2A6, CYP2E1, and CYP3A4) additionally interacted with adjacent residues in b_5 α5. In addition to this patch on one side of the heme, CYP2D6 and CYP3A4 can also bind to the opposite surface of b_5, α3, with CYP3A4 having the broadest interaction surface for both regions. Notably, CYP2A6 saturated with either coumarin or pNP interacted with the same face of b_5, but it remains to be seen if this is true for other P450/substrate pairs. It is clear that across these P450/substrate pairs and across the different binding interfaces observed that b_5 consistently increases coupling but may or may not alter product formation, as was also seen for rabbit CYP2B4 (10).

While the current NMR studies provide detailed structural information about the P450/b_5 interaction, they are not well suited to the determination of dissociation constants. However, it is notable that CYP2D6(DXM) was a very distinct outlier in terms of the amount of line broadening

observed for b_5 resonances compared to CYP3A4(NFP), CYP2A6(coumarin or pNP), CYP2E1(CZN), and even CYP17A1 in a previous parallel study (8). Although other explanations are possible, the simplest explanation is that this observation is consistent with less complex formation. A study evaluating the physical interaction between P450 enzymes immobilized on a plastic plate and biotinylated b_5 ranked the affinities as unliganded CYP3A4>CYP2A6~CYP2D6>CYP2E1, but noted that much less CYP2D6/b_5 complex was formed in these experimental conditions as well (38).

2.5 Conclusions

In conclusion, it appears that cytochrome b_5 interacts with different drug-metabolizing P450 enzymes with both shared and distinct surfaces. Disruption of these surfaces correlates with functional effects on metabolite production and/or NADPH consumption. Thus in the absence of X-ray structures, solution NMR is a high-resolution technique to examine these transient P450 interactions with other proteins. Further work remains to map the P450 residues involved in binding b_5, compare b_5 and reductase competition for binding different P450 enzymes, and the mechanism(s) by which b_5 modulates P450 catalysis.

2.6 References

1. Waskell, L., and Kim, J.-J. P. (2015) Electron transfer partners of cytochrome P450. in *Cytochrome P450*, Springer. pp 33-68
2. Schenkman, J. B., and Jansson, I. (2003) The many roles of cytochrome b_5. *Pharmacol. Ther.* **97**, 139-152
3. Bridges, A., Gruenke, L., Chang, Y. T., Vakser, I. A., Loew, G., and Waskell, L. (1998) Identification of the binding site on cytochrome P450 2B4 for cytochrome b_5 and cytochrome P450 reductase. *J. Biol. Chem.* **273**, 17036-17049
4. Naffin-Olivos, J. L., and Auchus, R. J. (2006) Human cytochrome b_5 requires residues E48 and E49 to stimulate the 17,20-lyase activity of cytochrome P450c17. *Biochemistry* **45**, 755-762
5. Tamburini, P. P., White, R. E., and Schenkman, J. B. (1985) Chemical characterization of protein-protein interactions between cytochrome P-450 and cytochrome b_5. *J. Biol. Chem.* **260**, 4007-4015
6. Gao, Q., Doneanu, C. E., Shaffer, S. A., Adman, E. T., Goodlett, D. R., and Nelson, S. D. (2006) Identification of the interactions between cytochrome P450 2E1 and cytochrome b_5 by mass spectrometry and site-directed mutagenesis. *J. Biol. Chem.* **281**, 20404-20417
7. Zhao, C., Gao, Q., Roberts, A. G., Shaffer, S. A., Doneanu, C. E., Xue, S., Goodlett, D. R., Nelson, S. D., and Atkins, W. M. (2012) Cross-linking mass spectrometry and mutagenesis confirm the functional importance of surface interactions between CYP3A4 and holo/apo cytochrome b(5). *Biochemistry* **51**, 9488-9500
8. Estrada, D. F., Laurence, J. S., and Scott, E. E. (2013) Substrate-modulated cytochrome P450 17A1 and cytochrome b_5 interactions revealed by NMR. *J. Biol. Chem.* **288**, 17008-17018
9. Gorsky, L. D., and Coon, M. J. (1986) Effects of conditions for reconstitution with cytochrome b_5 on the formation of products in cytochrome P-450-catalyzed reactions. *Drug Metab. Dispos.* **14**, 89-96
10. Gruenke, L. D., Konopka, K., Cadieu, M., and Waskell, L. (1995) The stoichiometry of the cytochrome P-450-catalyzed metabolism of methoxyflurane and benzphetamine in the presence and absence of cytochrome b(5). *J. Biol. Chem.* **270**, 24707-24718
11. Katagiri, M., Kagawa, N., and Waterman, M. R. (1995) The role of cytochrome b_5 in the biosynthesis of androgens by human P450c17. *Arch. Biochem. Biophys.* **317**, 343-347
12. Estrada, D. F., Skinner, A. L., Laurence, J. S., and Scott, E. E. (2014) Human cytochrome P450 17A1 conformational selection: modulation by ligand and cytochrome b_5. *J. Biol. Chem.* **289**, 14310-14320
13. Zhang, H., Im, S. C., and Waskell, L. (2007) Cytochrome b_5 increases the rate of product formation by cytochrome P450 2B4 and competes with cytochrome P450 reductase for a binding site on cytochrome P450 2B4. *J. Biol. Chem.* **282**, 29766-29776
14. Ahuja, S., Jahr, N., Im, S. C., Vivekanandan, S., Popovych, N., Le Clair, S. V., Huang, R., Soong, R., Xu, J., Yamamoto, K., Nanga, R. P., Bridges, A., Waskell, L., and Ramamoorthy, A. (2013) A model of the membrane-bound cytochrome b_5-cytochrome P450 complex from NMR and mutagenesis data. *J. Biol. Chem.* **288**, 22080-22095
15. Zhang, M., Le Clair, S. V., Huang, R., Ahuja, S., Im, S. C., Waskell, L., and Ramamoorthy, A. (2015) Insights into the role of substrates on the interaction between cytochrome b(5) and cytochrome P450 2B4 by NMR. *Sci. Rep.* **5**

16. Nunez, M., Guittet, E., Pompon, D., van Heijenoort, C., and Truan, G. (2010) NMR structure note: oxidized microsomal human cytochrome b_5. *J. Biomol. NMR* **47**, 289-295

17. Studier, F. W. (2005) Protein production by auto-induction in high-density shaking cultures. *Protein Expression Purif.* **41**, 207-234

18. Mulrooney, S. B., and Waskell, L. (2000) High-level expression in *Escherichia coli* and purification of the membrane-bound form of cytochrome b(5). *Protein Expression Purif.* **19**, 173-178

19. Strittmatter, P., and Velick, S. F. (1956) The isolation and properties of microsomal cytochrome. *J. Biol. Chem.* **221**, 253-264

20. Peng, H. M., Im, S. C., Pearl, N. M., Turcu, A. F., Rege, J., Waskell, L., and Auchus, R. J. (2016) Cytochrome b(5) activates the 17,20-lyase activity of human cytochrome P450 17A1 by increasing the coupling of NADPH consumption to androgen production. *Biochemistry* **55**, 4356-4365

21. Oprian, D. D., and Coon, M. J. (1982) Oxidation-reduction states of FMN and FAD in NADPH-cytochrome-P-450 reductase during reduction by NADPH. *J. Biol. Chem.* **257**, 8935-8944

22. DeVore, N. M., Smith, B. D., Urban, M. J., and Scott, E. E. (2008) Key residues controlling phenacetin metabolism by human cytochrome P450 2A enzymes. *Drug Metab. Dispos.* **36**, 2582-2590

23. Porubsky, P. R., Meneely, K. M., and Scott, E. E. (2008) Structures of human cytochrome P-450 2E1. Insights into the binding of inhibitors and both small molecular weight and fatty acid substrates. *J. Biol. Chem.* **283**, 33698-33707

24. Wang, A., Savas, U., Hsu, M. H., Stout, C. D., and Johnson, E. F. (2012) Crystal structure of human cytochrome P450 2D6 with prinomastat bound. *J. Biol. Chem.* **287**, 10834-10843

25. Yano, J. K., Wester, M. R., Schoch, G. A., Griffin, K. J., Stout, C. D., and Johnson, E. F. (2004) The structure of human microsomal cytochrome P450 3A4 determined by X-ray crystallography to 2.05-A resolution. *J. Biol. Chem.* **279**, 38091-38094

26. Wester, M. R., Stout, C. D., and Johnson, E. F. (2002) Purification and crystallization of N-terminally truncated forms of microsomal cytochrome P450 2C5. *Methods Enzymol* **357**, 73-79

27. Delaglio, F., Grzesiek, S., Vuister, G. W., Zhu, G., Pfeifer, J., and Bax, A. (1995) NMRPipe: A multidimensional spectral processing system based on UNIX pipes. *J. Biomol. NMR* **6**, 277-293

28. Chen, W. Q., Koenigs, L. L., Thompson, S. J., Peter, R. M., Pettie, A. E., Trager, W. F., and Nelson, S. D. (1998) Oxidation of acetaminophen to its toxic quinone imine and nontoxic catechol metabolites by baculovirus-expressed and purified human cytochromes P450 2E1 and 2A6. *Chem. Res. Toxicol.* **11**, 295-301

29. Yamazaki, H., Nakano, M., Gillam, E. M., Bell, L. C., Guengerich, F. P., and Shimada, T. (1996) Requirements for cytochrome b_5 in the oxidation of 7-ethoxycoumarin, chlorzoxazone, aniline, and N-nitrosodimethylamine by recombinant cytochrome P450 2E1 and by human liver microsomes. *Biochem. Pharmacol.* **52**, 301-309

30. Yamazaki, H., Nakamura, M., Komatsu, T., Ohyama, K., Hatanaka, N., Asahi, S., Shimada, N., Guengerich, F. P., Shimada, T., Nakajima, M., and Yokoi, T. (2002) Roles of NADPH-P450 reductase and apo- and holo-cytochrome b_5 on xenobiotic oxidations catalyzed by 12 recombinant human cytochrome P450s expressed in membranes of *Escherichia coli. Protein Expr. Purif.* **24**, 329-337

31. Yamazaki, H., Gillam, E. M., Dong, M. S., Johnson, W. W., Guengerich, F. P., and Shimada, T. (1997) Reconstitution of recombinant cytochrome P450 2C10(2C9) and comparison with cytochrome P450 3A4 and other forms: effects of cytochrome P450-P450 and cytochrome P450-b_5 interactions. *Arch. Biochem. Biophys.* **342**, 329-337

32. Yamazaki, H., Shimada, T., Martin, M. V., and Guengerich, F. P. (2001) Stimulation of cytochrome P450 reactions by apo-cytochrome b(5) - Evidence against transfer of heme from cytochrome P450 3A4 to apo-cytochrome b_5, or heme oxygenase. *J. Biol. Chem.* **276**, 30885-30891

33. Yun, C. H., Kim, K. H., Calcutt, M. W., and Guengerich, F. P. (2005) Kinetic analysis of oxidation of coumarins by human cytochrome P450 2A6. *J. Biol. Chem.* **280**, 12279-12291

34. Soucek, P. (1999) Expression of cytochrome P450 2A6 in *Escherichia coli*: purification, spectral and catalytic characterization, and preparation of polyclonal antibodies. *Arch. Biochem. Biophys.* **370**, 190-200

35. Tan, Y. Z., Patten, C. J., Smith, P., and Yang, C. S. (1997) Competitive interactions between cytochromes P450 2A6 and 2E1 for NADPH-cytochrome P450 oxidoreductase in the microsomal membranes produced by a baculovirus expression system. *Arch. Biochem. Biophys.* **342**, 82-91

36. Guengerich, F. P. (2015) Human cytochrome P450 enzymes. in *Cytochrome P450: Structure, Mechanism, and Biochemistry* (Ortiz de Montellano, P. R. ed.), 4th Ed., Springer International Publishing, Cham, Switzerland. pp 523-785

37. Dehal, S. S., and Kupfer, D. (1997) CYP2D6 catalyzes tamoxifen 4-hydroxylation in human liver. *Cancer Res.* **57**, 3402-3406

38. Shimada, T., Mernaugh, R. L., and Guengerich, F. P. (2005) Interactions of mammalian cytochrome P450, NADPH-cytochrome P450 reductase, and cytochrome b(5) enzymes. *Arch. Biochem. Biophys.* **435**, 207-216

39. Gillam, E. M., Guo, Z., and Guengerich, F. P. (1994) Expression of modified human cytochrome P450 2E1 in *Escherichia coli*, purification, and spectral and catalytic properties. *Arch. Biochem. Biophys.* **312**, 59-66

40. Chen, W., Peter, R. M., McArdle, S., Thummel, K. E., Sigle, R. O., and Nelson, S. D. (1996) Baculovirus expression and purification of human and rat cytochrome P450 2E1. *Arch. Biochem. Biophys.* **335**, 123-130

41. Peng, H. M., and Auchus, R. J. (2013) The action of cytochrome b(5) on CYP2E1 and CYP2C19 activities requires anionic residues D58 and D65. *Biochemistry* **52**, 210-220

42. Peng, H. M., and Auchus, R. J. (2014) Two surfaces of cytochrome b_5 with major and minor contributions to CYP3A4-catalyzed steroid and nifedipine oxygenation chemistries. *Arch. Biochem. Biophys.* **541**, 53-60

43. Yu, A., Dong, H., Lang, D., and Haining, R. L. (2001) Characterization of dextromethorphan O- and N-demethylation catalyzed by highly purified recombinant human CYP2D6. *Drug Metab. Dispos.* **29**, 1362-1365

44. Henderson, C. J., McLaughlin, L. A., Scheer, N., Stanley, L. A., and Wolf, C. R. (2015) Cytochrome b_5 is a major determinant of human cytochrome P450 CYP2D6 and CYP3A4 activity in vivo. *Mol. Pharmacol.* **87**, 733-739

45. Fukami, T., Katoh, M., Yamazaki, H., Yokoi, T., and Nakajima, M. (2008) Human cytochrome P450 2A13 efficiently metabolizes chemicals in air pollutants: naphthalene, styrene, and toluene. *Chem. Res. Toxicol.* **21**, 720-725

CHAPTER 3

Structures of Human Cytochrome P450 1A1 with Bergamottin and Erlotinib Reveal Active-Site Modifications for Binding of Diverse Ligands[*]

3.1 Summary

Human cytochrome P450 1A1 (CYP1A1) is an extrahepatic enzyme involved in the monooxygenation of structurally-diverse compounds ranging from natural products to drugs and protoxins. Because CYP1A1 has a role in human carcinogenesis, inhibiting its activity may potentially aid in cancer chemoprevention, whereas utilizing CYP1A1's oxidative activity could help selectively activate anticancer prodrugs. Such potential therapeutic purposes require detailed knowledge of CYP1A1's interactions with potential ligands. Known CYP1A1 ligands also vary substantially in size and it has not been apparent from a single existing CYP1A1 structure how larger, structurally diverse ligands are accommodated within the enclosed active site. Here, two new X-ray structures with the natural product furanocoumarin bergamottin (2.85 Å) and the lung cancer drug erlotinib (3.0 Å resolution) revealed binding orientations consistent with the formation of innocuous metabolites and of toxic metabolites, respectively. They also disclosed local changes in the roof of the active site that enlarge the active site and ultimately form a channel to the protein exterior. Although further structural modifications would be required to accommodate the largest CYP1A1 ligands, knowing which components of the active site are malleable provides powerful

---

information for those attempting to use computational approaches to predict compound binding and substrate metabolism by this clinically relevant monooxygenase.

3.2 Introduction

The superfamily of enzymes known as cytochrome P450 monooxygenases has vital functions in the metabolism and detoxification of a large variety of drugs and environmental toxins. However, in other instances P450 enzymes have been known to initiate deleterious effects, such as the production of reactive intermediates leading to toxic and carcinogenic effects (1). One human CYP enzyme with a particular propensity toward activation of protoxins and procarcinogens is CYP1A1, a highly inducible, extrahepatic P450. CYP1A1 has a preference for substrates that are polycyclic aromatic hydrocarbons, such as the environmental pollutant benzo[*a*]pyrene (2). Due to the roles of CYP1A1 in human carcinogenesis, inhibition of CYP1A1 activity has been considered as a potential target for cancer chemoprevention (3,4). In contrast, other efforts have been explored for utilizing CYP1A1 oxidative metabolism to activate anticancer prodrugs in a tissue selective manner (5,6).

To employ either CYP1A1 inhibition or leverage its oxidative power for therapeutic purposes requires detailed knowledge of the active site interactions with potential ligands. A single crystal structure of CYP1A1 was previously determined, in complex with the small molecule inhibitor α-naphthoflavone (ANF) (7). This structure revealed a narrow and closed active site not much larger than the ANF ligand itself. Structures of the other family 1 human P450 enzymes, CYP1A2 (8) and CYP1B1 (9), also have a single structure each, also containing ANF as the bound ligand, and similarly reveal relatively small, planar active sites. However, xenobiotic-metabolizing P450 enzymes often have rather flexible structures to accommodate the variety of substrates an individual enzyme interacts with, so it can be difficult to extrapolate a range of

potential P450/ligand interactions from a single structure. In particular, a number of known 1A1 substrates and inhibitors reported in the literature reveal substrate and inhibitor sizes and geometries that are not compatible with the dimensions of the currently defined CYP1A1/ANF active site.

The purpose of the current study was to probe CYP1A1 active site flexibility and potentially capture CYP1A1 in conformationally distinct states that would be useful in trying to employ CYP1A1 as a potential therapeutic target. To accomplish this, ligands with high CYP1A1 affinity and larger sizes were co-crystallized with the CYP1A1 enzyme. This study describes two novel CYP1A1 structures, one with the epidermal growth factor receptor (EGFR) inhibitor erlotinib used in anticancer therapy, and another with the furanocoumarin P450 inhibitor bergamottin. These new structures of CYP1A1 provide insight into some of the structural rearrangements that allow for the accommodation of diverse CYP1A1 ligand structures.

3.3 Experimental Procedures

3.3.1 Protein Expression and Purification

Expression of human CYP1A1 was performed using a construct encoding a N-terminal truncation spanning residues 2-34 that was replaced with the sequence AKKTSS and a C-terminal 6 histidine tag (7). Expression was based on the previously described method (7) with a number of modifications, for clarity a detailed protocol is listed. The pKK1A1(MAK)H_6 plasmid was transformed into *E. coli* DH5α cells that also included the pGro7 plasmid encoding the chaperone GroEl/ES (Takara Bio Inc.). Transformed cells were grown for 18 hours at 37 °C on minimal media plates (MDAG-11) using the formulation described in (10) plus 2 μM thiamine, 100 μg/ml carbenicillin, and 20 μg/ml chloramphenicol. A single colony was picked and inoculated into a

50 ml starter culture composed of a defined minimal media (MDAG-135) described in (10) with the supplemental thiamine and antibiotics described above. This starter culture was grown for 16 hours at 37 °C, 300 rpm shaking. Expression cultures were grown using 250 ml Terrific Broth supplemented with 100 µg/ml carbenicillin, and 20 µg/ml chloramphenicol in 1 liter Erlenmeyer flasks. Typical expression volumes were 3.5 liters. Expression cultures were inoculated with 3 ml of the grown starter culture and incubated at 37 °C with shaking (250 rpm) until an optical density at 600 nm ($O.D._{600}$) of 0.4 was reached. Arabinose was then added at 2 mg/ml and δ-aminolevulinic acid at 1 mM to the cultures, the temperature and shaking were reduced to 25 °C and 225 rpm. Once $O.D._{600}$ reached 0.6, CYP1A1 expression was induced by 1 mM IPTG, cultures were grown for an additional 48 hours.

A number of modifications were also made to the purification method for CYP1A1 described in Walsh *et al.* (7) so a detailed protocol is included herein. CYP1A1 purification was initiated by resuspending cells in resuspension buffer consisting of 20 mM potassium phosphate, 20% (v/v) glycerol, pH 7.4, 1 mM phenylmethanesulfonyl fluoride, and 0.3 mg/ml lysozyme. After stirring for 20 minutes at room temperature, an equal volume of 4 °C water was added and stirring continued for an additional 10 minutes at 4 °C. All subsequent purification steps were carried out at 4 °C. The mixture was centrifuged at 7,500 x g for 15 minutes to isolate spheroplasts, which were gently washed with resuspension buffer twice, then resuspended with the aid of a Dounce homogenizer in lysis buffer consisting of 500 mM potassium phosphate, 300 mM NaCl, 20% (v/v) glycerol, pH 7.4, and 1 mM PMSF. The resulting resuspension was lysed by French press using one pass at 16,000 psi internal cell pressure. Detergent extraction of CYP1A1 was performed on this lysate by adding 1% (w/v) CHAPS and stirring for 1 hour. Cell lysate was clarified by ultracentrifugation at 142,000 x g and the supernatant loaded onto a 25 ml pre-

equilibrated Ni-NTA column (Qiagen) with loading buffer consisting of 100 mM potassium phosphate, 200 mM NaCl, 20% (v/v) glycerol, 0.5% (w/v) CHAPS, pH 7.4. Nonspecifically bound proteins were washed off the column using 6 column volumes (CV) of loading buffer and 10 CV of loading buffer containing 3 mM histidine. CYP1A1 was then eluted with a linear gradient from 3 mM histidine-containing loading buffer to elution buffer (10 mM potassium phosphate, 100 mM NaCl, 20% (v/v) glycerol, 0.5% (w/v) CHAPS, 80 mM histidine, 2 mM EDTA) over 6 CV. Eluted fractions possessing a UV absorbance of $A_{419}/A_{280} > 0.8$ were pooled, diluted 2-fold with CM wash buffer (10 mM potassium phosphate, 100 mM NaCl, 20% (v/v) glycerol, 0.5% (w/v) CHAPS, 1 mM EDTA, pH 7.4) and loaded onto three 5-ml pre-equilibrated Hi-Trap carboxymethyl-Sepharose fast-flow columns (GE Healthcare) connected in series (total 15 ml column volume). The column was washed with 10 CV of CM wash buffer, then CYP1A1 eluted using a 6 CV linear gradient from CM wash buffer to SEC buffer (50 mM potassium phosphate, 500 mM NaCl, 20% (v/v) glycerol, 0.5% (w/v) CHAPS, 1 mM EDTA, pH 7.4) followed by 100% SEC buffer for an additional 4 CV. Fractions with $A_{419}/A_{280} > 1$ were pooled and concentrated to 4 ml, centrifuged at 10,000 x g to remove any precipitated protein, then loaded onto a pre-equilibrated Superdex 200 gel filtration column (GE Healthcare) run with the same SEC buffer. Major peaks exhibiting a $A_{419}/A_{280} > 1.1$ were pooled and evaluated by SDS-PAGE, UV-Vis spectroscopy, and the reduced-carbon monoxide difference assay (11). Protein was quantitated using the Soret in the absolute spectrum in the presence of saturating imidazole and an extinction coefficient of 100 mM^{-1}cm^{-1}. Purified CYP1A1 was flash frozen in aliquots in a dry-ice/ethanol slurry, and stored at -80 °C until use for experiments.

Full-length human NADPH-cytochrome P450 reductase was expressed and purified as described (12). Purity was assessed by SDS-PAGE. UV-visible spectroscopy was used to quantify reductase using the extinction coefficient of 21.4 $mM^{-1}cm^{-1}$ at 454 nm for oxidized protein (13).

3.3.2 CYP1A1 Inhibition Assays

Ligands were evaluated according to their ability to inhibition of CYP1A1-mediated metabolism of the P450 Glo™ substrate luciferin-ME EGE (Promega). Inhibition assays for CYP1A1 were performed starting with pre-incubation of CYP1A1 and full-length human reductase at a 1:2 ratio (to give a final concentration of 10 nM CYP1A1 and 20 nM reductase in reaction) in 400 mM potassium phosphate pH 7.4 buffer at room temperature for 20 minutes. The substrate luciferin-ME EGE was added to the pre-incubated protein to give a final concentration during the assay of 4 μM, which is equal to the previously-determined K_m. Protein with substrate was then dispensed into a white 96-well microplate (Corning), respective inhibitor added (serially diluted stocks in DMSO to maintain constant 0.5% solvent concentration) and incubated at room temperature for 3 minutes prior to starting reactions with NADPH at a final concentration of 100 μM in 50 μl total reaction volume. Reactions were allowed to proceed at room temperature for 45 minutes. Reactions were stopped and development of luminescence was initiated by the addition of 50 μl of the Luciferin Detection Reagent with esterase (Promega). To convert luminescence into activity, a standard curve using D-luciferin was performed alongside the reaction samples. Control samples without inhibitor and controls to determine background luminescence were also used. Prior to reading the luminescence the microplate was incubated at 25 °C for 20 minutes. The luminescence signal was measured by a GloMax® Discover plate reader (Promega) at 25 °C using a 1 second integration time per well. The data were fit to the dose response-inhibitor (four

parameter) equation to determination of the IC_{50} (Graph-Pad Prism). Each inhibitor concentration was evaluated in duplicate.

3.3.3 Ligand Binding Assays

Binding of ligands to CYP1A1 was monitored using a double-beam UV-visible spectrophotometer (Shimadzu Scientific Instruments) at 20 °C. CYP1A1 was diluted into SEC buffer to a concentration of 1 μM, and equally divided into the two chambers of two 1-cm path length tandem cuvettes (sample and reference). The other chamber contained only SEC buffer. Stock solutions of ligands were created in DMSO (0.2-10 mM). Ligands were titrated into the CYP1A1-containing chamber of the sample cuvette and the buffer only chamber of the reference cuvette. An equal volume of DMSO was titrated into the buffer chamber of the sample cuvette and the CYP1A1-containing chamber of the reference cuvette to correct for solvent and dilution effects to the spectra. Absorbance was monitored from 300 to 500 nm. Dissociation constants were determined by non-linear regression fitting (GraphPad Prism) of the change in absorbance versus ligand concentration using a tight binding equation described previously (14).

3.3.4 Co-Crystallization, Data Collection, Structure Determination

Purified CYP1A1 was concentrated to 17 mg/ml (bergamottin) or 20 mg/ml (erlotinib) by three iterative centrifugal ultrafiltration steps that involved dilution with SEC buffer containing 0.4 M ammonium nitrate and either 20 μM bergamottin or 20 μM erlotinib. Crystals of CYP1A1 with the respective ligands were grown using the sitting drop vapor diffusion method in either 24-well plates (bergamottin) or 96-well plates (erlotinib). Plates were set up at 20 °C by mixing 1 μl CYP1A1/bergamottin with 1 μl of a crystallization solution (0.2 M potassium phosphate dibasic, 20% (w/v) PEG 3350, 15% (v/v) glycerol) or 0.75 μl CYP1A1/erlotinib with 0.75 μl crystallization

74

solution (0.2 M potassium phosphate dibasic, 20% (w/v) PEG 3350, 10% (v/v) glycerol, 0.5% (w/v) n-dodecyl-N,N-dimethylamine-N-oxide). Plates were sealed and equilibrated against 300 μl (bergamottin) or 50 μl (erlotinib) of the respective crystallization solution at 4 °C. Triangular prism crystals grew over 2-3 days and were harvested at 5-6 days. CYP1A1/bergamottin crystals were cryoprotected using the bergamottin crystallization solution containing 30% (w/v) PEG 3350, while CYP1A1/erlotinib crystals were cryoprotected with erlotinib crystallization solution containing 20% (v/v) glycerol. Crystals were flash cooled in liquid nitrogen and diffraction data were collected on beamline 9-2 at the Stanford Synchrotron Radiation Lightsource. Integration of the data and scaling were performed using XDS (15) and AIMLESS (16). Structures were solved using molecular replacement via Phaser (17) with the CYP1A1/ANF structure (7) as a search model, (PDB 4I8V, molecule A) resulting in log likelihoods of 20,276 (1A1/Bergamottin) and 12,779 (1A1/Erlotinib). Building and refinement of the models were iteratively performed using the programs Coot (18) and PHENIX (19) respectively. Torsion-angle NCS restraints were used during refinement with Chain A as the reference selection for the other NCS-related chains. Ligand restraints were generated using PHENIX eLBOW (20) with AM1 geometry optimization. Active site void volumes were calculated using VOIDOO (21), with probe radius = 1.4 Å and grid spacing = 1.0. All figures were prepared using PyMOL (22).

Table 3.1 Data collection and refinement statistics.

	CYP1A1/bergamottin (6DWM)	CYP1A1/erlotinib (6DWN)
Data Collection		
Space Group	$P2_12_12_1$	$P2_12_12_1$
Cell Dimensions (Å)	65.33, 194.76, 236.14	64.86, 195.08, 238.01
Molecules/a.u.	4	4
Resolution (Å)[a]	39.36-2.85 (2.91-2.85)	39.02-2.99 (3.07-2.99)
Total reflections[a]	472,057 (27,104)	404,855 (24,710)
Unique reflections[a]	71,615 (4,361)	61,715 (4,346)
Redundancy[a]	6.6 (6.2)	6.6 (5.7)
R_{pim}[a]	0.060 (0.671)	0.053 (0.755)
$<I/\sigma(I)>$ [a]	8.6 (1.7)	9.6 (1.3)
CC1/2[a]	0.994 (0.499)	0.997 (0.698)
Completeness (%)[a]	99.7 (97.1)	99.6 (96.1)
Refinement		
Resolution (Å)	39.36-2.85	38.98-3.00
No. reflections	71,343	61,261
R/R_{free} (%)	0.204 / 0.240	0.241 / 0.261
Ramachandran (%) Favored/Allowed/Outliers	97.42 / 2.53/ 0.05	97.61 / 2.39 / 0
No. non-H atoms/B factors ($Å^2$)		
Protein	15,006 / 75.31	14,852 / 89.10
Ligand	100 / 65.57	103 / 80.85
Heme	172 / 54.68	172 / 77.59
CHAPS	61 / 98.12	56 / 95.69
Glycerol	12 / 83.38	- / -
Water	46 / 46.14	4 / 66.56
RMSD bond (Å)	0.004	0.004
RMSD angle (°)	0.655	0.589
Coordinate error (max. likelihood based) (Å)	0.37	0.40

[a] Statistics for highest resolution shell shown in parentheses.

3.4 Results and Discussion

3.4.1   Inhibition of CYP1A1 by Structurally Diverse Ligands

The previous crystal structure of CYP1A1 was with the planar, fused multicyclic ligand α-naphthoflavone enclosed within a narrow, planar active site (7). Many CYP1A1 substrates and inhibitors do include features of various fused aromatic ring systems, often elongated in one dimension. The active site cavity for the CYP1A1/ANF structure conforms to these aspects, but it is not particularly helpful in discerning how other CYP1A1 ligands with larger sizes and/or varying dimensions are accommodated by the active site. While some human cytochrome P450 enzymes have multiple structures demonstrating significant flexibility in active site conformation to accommodate different ligand classes, the CYP1 family enzymes have often been assumed to be comparatively static, in part because of the absence of structural evidence otherwise. To probe the malleability of the CYP1A1 active site, reported CYP1A1 ligands (substrates and/or inhibitors) that possessed a range of different chemical features and shapes were identified as potential candidates for crystallography. The ligands were broadly segmented into the following classes: azole inhibitors, tyrosine kinase inhibitors, anticancer prodrugs, and natural products from the furanocoumarin and stilbenoid classes.

To provide a ranking according to the potency of their interactions with CYP1A1, IC_{50} values were determined (*e.g.* Table 3.2) for each ligand. About half of the compounds tested had reasonably potent inhibition of CYP1A1-mediated activity (Table 3.2), defined herein as $IC_{50} < 1$ µM. This series included a number of azoles, which are often potent, broad spectrum P450 inhibitors. Not surprisingly then, the azoles clotrimazole, miconazole, and tioconazole were three of the four most potent inhibitors. These are all smaller azoles (MW 344-417 g/mol) with a compact overall structure. Larger azoles with extended structures like ketoconazole and

posaconazole (MW 531 and 700 g/mol) were 4- to 7-fold less potent but still had IC_{50} values in the nanomolar range.   However, fluconazole which is smaller and has an overall structure more similar to miconazole and tioconazole did not significantly inhibit CYP1A1, so size is certainly not the only consideration.
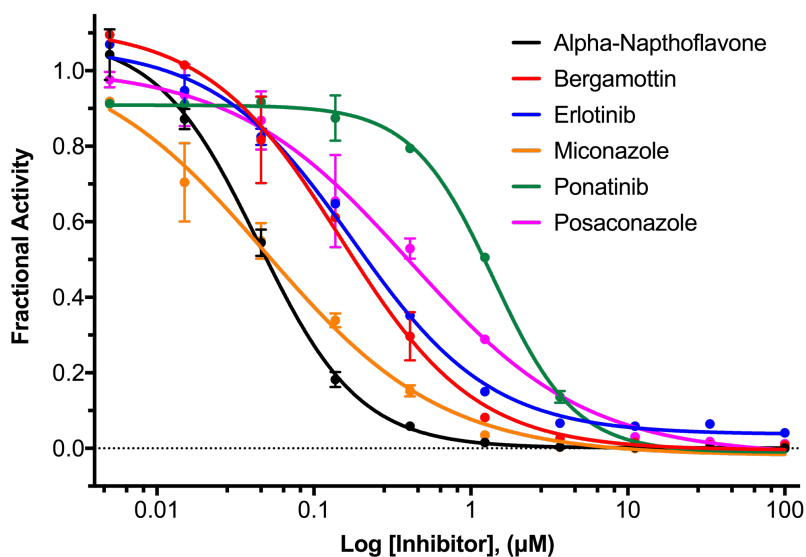
Figure 3.1 Representative IC_{50} Curves. Determination of IC_{50} values was performed using duplicate samples at each inhibitor concentration. Non-linear curve fitting to the data was accomplished using a four-parameter logistic curve in GraphPad Prism.

One of the interests of CYP1A1 in human health is its role in cancer, both as a potential generator of carcinogenic species and in the metabolism of certain anti-cancer drugs, such as tyrosine kinase inhibitors. Some of the tyrosine kinase inhibitor drugs CYP1A1 has been demonstrated to interact with include erlotinib (23), imatinib (24), and ponatinib (25), which were also tested for their inhibitory potency. These drugs displayed nanomolar to low micromolar IC_{50} values, with erlotinib being the most potent ($IC_{50} = 180 \pm 10$ nM). Again, it was the more extended imatinib and ponatinib that were less potent inhibitors ($IC_{50} > 1$ μM), perhaps indicating that they might not fit the CYP1A1 active site as well. Metabolism of erlotinib and ponatinib by CYP1A1 have been reported to generate reactive electrophilic metabolites that may contribute to some of the observed life-threatening toxicities associated with these drugs (25,26).

CYP1A1 has yet another connection to cancer therapeutics in that the tissue location and metabolic capability of CYP1A1 have suggested its utility in the activation of several different prodrugs to reactive electrophilic species leading to DNA damage and cell death (6,27,28). This included the benzothiazole GW610 (29), which current results suggested had a fairly potent IC_{50} of 300 ± 80 nM. In contrast, the compound AQ4N is activated by CYP1A1 to the active topoisomerase inhibitor AQ4 under hypoxic conditions (30), but under normoxic conditions evaluated herein showed essentially no inhibition of CYP1A1.
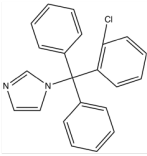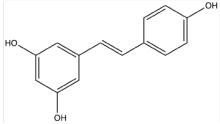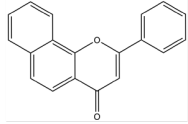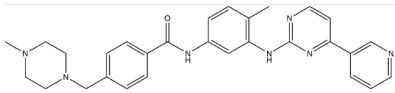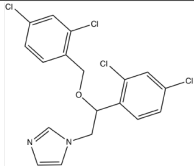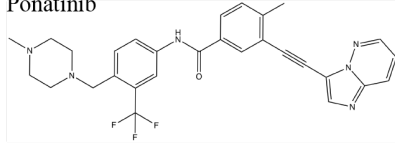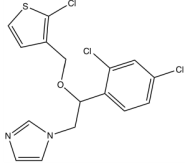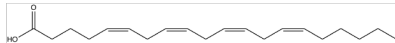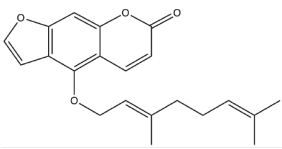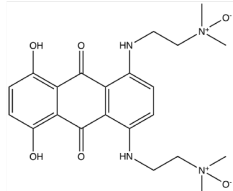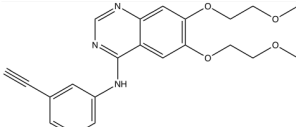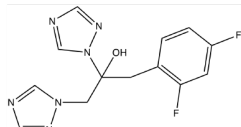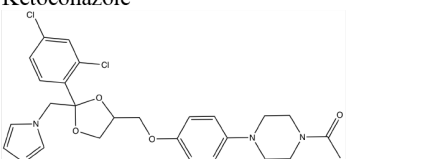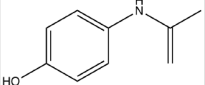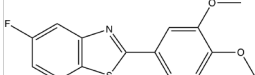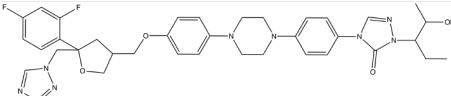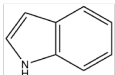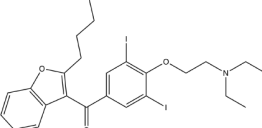
Two natural products were suggested as CYP1A1 ligands in the literature and were tested. The first was the furanocoumarin bergamottin found in grapefruit and other citrus and well known to inhibit CYP3A4 and cause variations on CYP3A4-mediated metabolism of common drugs (31). Bergamottin also displayed potent inhibition of CYP1A1, with an IC_{50} of 140 ± 20 nM. Bergamottin also inhibits CYP1A2, but with attenuated potency (32,33). This could potentially be due to size and shape complementarity of the respective active sites. At least in the ANF-bound structures, CYP1A1 possesses a slightly larger active site volume compared to CYP1A2 (7), which may allow for greater accommodation of the larger furanocoumarin compounds. Additionally, comparison of selective ligand features between CYP1A1 and CYP1A2, suggested a preference of CYP1A1 for ligands with longer strip-like geometry, while CYP1A2 selective compounds were more triangular in shape (34). The other natural product suggested in the literature to interact with CYP1A1 was the *trans*-stilbene resveratrol found in red wine. Herein resveratrol was an order of magnitude less potent than bergamottin at inhibiting CYP1A1 activity. The resveratrol IC_{50} value of ~ 1.4 μM was more similar to the tyrosine kinase drugs imatinib and ponatinib.

A number of other diverse compounds ranging from moieties such as imidazole and indole to the analgesic acetaminophen were also tested for inhibitory potency towards CYP1A1.

Additionally endogenous fatty acids, such as arachidonic acid (35) have been reported to be efficiently metabolized by CYP1A1. The small chemical moieties indole, imidazole, and drug acetaminophen resulted in exceedingly weak inhibition of CYP1A1 activity, with IC_{50} values greater than 100 µM. The binding affinity of these small compounds are likely weak, and may not make extensive interactions with the active site. The endogenous arachidonic acid substrate was only weakly inhibitory with an IC_{50} value of 3.8 µM.

Overall, this screen of many CYP1A1 ligands suggested that several of the imidazole azoles, bergamottin, and erlotinib had significantly different structures from α-naphthoflavone but IC_{50} values less than 200 nM and might be good candidates for structural studies probing the flexibility of the CYP1A1 active site.

Table 3.2 Inhibition of CYP1A1 given as IC$_{50}$ ± standard error.

Ligand	IC$_{50}$ (nM)	Ligand	IC$_{50}$ (nM)
Clotrimazole	17 ± 4	Resveratrol	1,370 ± 70
α-Napthoflavone	44 ± 2	Imatinib	1,380 ± 90
Miconazole	50 ± 10	Ponatinib	1,390 ± 50
Tioconazole	70 ± 10	Arachidonic Acid	3,800 ± 200
Bergamottin	140 ± 20	AQ4N	20,000 ± 6,000
Erlotinib	180 ± 10	Fluconazole	>50,000
Ketoconazole	280 ± 90	Acetaminophen	>100,000
GW 610	300 ± 80	Imidazole	>100,000
Posaconazole	410 ± 70	Indole	>100,000
Amiodarone	640 ± 40		

3.4.2 Characterization of Bergamottin and Erlotinib Binding to CYP1A1

As examples of structurally diverse CYP1A1 ligands with relatively low IC_{50} values, the binding of bergamottin and erlotinib were further characterized by determining their affinities and binding modes via UV spectroscopy. Tandem cuvettes were employed to blank out the intrinsic absorbance of both bergamottin and erlotinib, which overlap the wavelength range of the P450 heme Soret peak monitored to detect ligand binding. Titration of CYP1A1 with either bergamottin or erlotinib resulted in a blue shift of the Soret peak, with a peak forming at ~391 nm and a trough at 427-429 nm when observed in difference mode (Figure 3.2A & B). Such a Type I binding profile is indictive of displacement of the water from the heme iron. The K_d for bergamottin was 370 ± 40 nM (Figure 3.2A), which is in a similar range to its IC_{50} value determined herein and the dissociation constant for ANF (~300 nM) reported previously (7). The K_d measured for erlotinib was 1.07 ± 0.04 μM (Figure 3.2B), indicating that erlotinib binds to the CYP1A1 resting state with lower affinity compared to bergamottin and ANF. However both ligands have affinities and solubilities that can support saturation of CYP1A1 for structure determination.
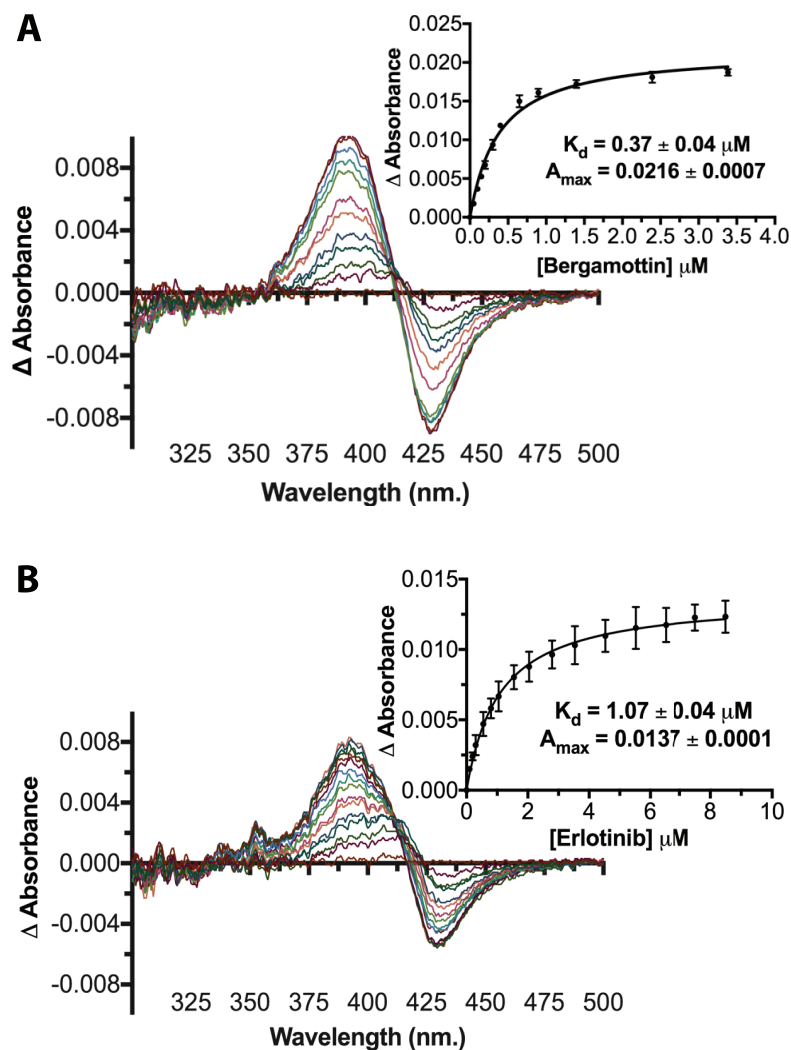
Figure 3.2 Bergamottin and erlotinib binding to CYP1A1. Absorbance difference spectra of CYP1A1 (1 μM) titrated with increasing concentration of A) bergamottin and B) erlotinib reveal type I shifts, with peaks forming at ~391 nm and troughs at 427-429 nm. Insets are the change of absorbance (peak-trough) vs. compound concentration fit by nonlinear regression to the tight-binding equation. K_d and absorbance maximum (A_{max}) are given ± standard error.

3.4.3 Overall CYP1A1 X-Ray Structures

Structures were subsequently determined with both bergamottin and erlotinib at resolutions of 2.85 Å and 3.0 Å, respectively. Both structures solved in the $P2_12_12_1$ space group with very similar unit cell dimensions, and contained four copies of the protein within the asymmetric unit. For both structures, all four copies within the asymmetric unit were very similar, though two of them tended to be more disordered with regions of weaker electron density for some protein side-chains and the active site ligand. The 1A1/erlotinib structure disorder prevented reliable modeling

of the loop between E and F helices in one molecule (D). Like the previous CYP1A1/ANF crystal structure, the loop connecting the H and I helices had significant disorder in both the CYP1A1/bergamottin and CYP1A1/erlotinib structures of most molecules and could only be reliably modeled in one chain for each respective co-crystal structure. This most complete and best defined molecule (molecule A) will be specifically referenced in the following discussion.

The overall tertiary structure of the two new CYP1A1 ligand complexes with bergamottin and with erlotinib are highly similar to the previously determined structure of CYP1A1 with the ligand ANF (Figure 3.3). Compared to the previous CYP1A1/ANF structure, the new structures with bergamottin and erlotinib both had root mean square deviations of 0.37 Å for Cα atoms. A distinctive feature of the previous CYP1A1/ANF structure—one conserved in the homologous CYP1A2 and CYP1B1 structures but not other human P450 enzymes—is a disruption in the helical character of the F helix as it passes over the active site. This five-residue break in the F helix is also present in the two new CYP1A1 structures. It has been postulated that this disruption of the F-helix could be significant in terms of allowing flexibility in substrate binding and dynamics (7).
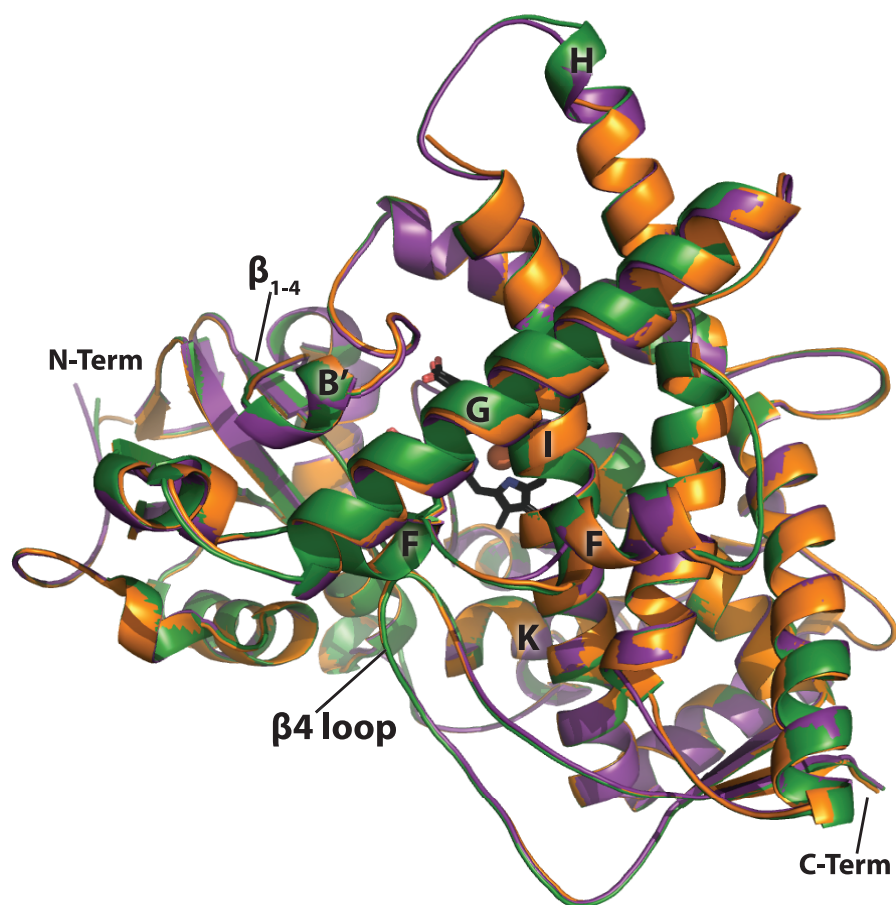
Figure 3.3 CYP1A1 structures bound to bergamottin (orange), erlotinib (green), and previously determined *α*-napthoflavone (purple), all superimposed by Cα atoms.

The density does support the localization of some additional small molecules from the crystallization solutions. In both structures a molecule of the detergent CHAPS is found on the protein surface oriented lengthwise along the G helix of some molecules, distant from the active site.

3.4.4 Bergamottin Binding to CYP1A1

In all four of the molecules in the asymmetric unit bergamottin is positioned similarly in the CYP1A1 active site. Its fused psoralen ring system is oriented distal from the heme, with π-π interactions to the parallel side chain of the F-helix residue Phe-224. The geranyloxy chain of bergamottin extends towards the heme, bending at the 3' position so that the rest of the chain lies

over the hez, slightly off center of the iron. The terminal dimethyl portion of this ligand chain is directed toward a cluster of hydrophobic residues that are part of the β_4 and K/β_{1-4} loops, including Val382 (Figure 3.4A). These residues close off the bottom portion of the CYP1A1 active site cavity opposite from the I-helix. There is a hydrogen bond formed between the ketone oxygen of the bergamottin psoralen moiety and the side chain nitrogen of Asn222. This combination of interactions between bergamottin and the CYP1A1 active site result in the 6' and 7' carbons of the geranyloxy chain closest to the heme iron, at distances of 4.8 Å and 5.1 Å, respectively, suggesting that oxidation might occur at one or more of these positions.
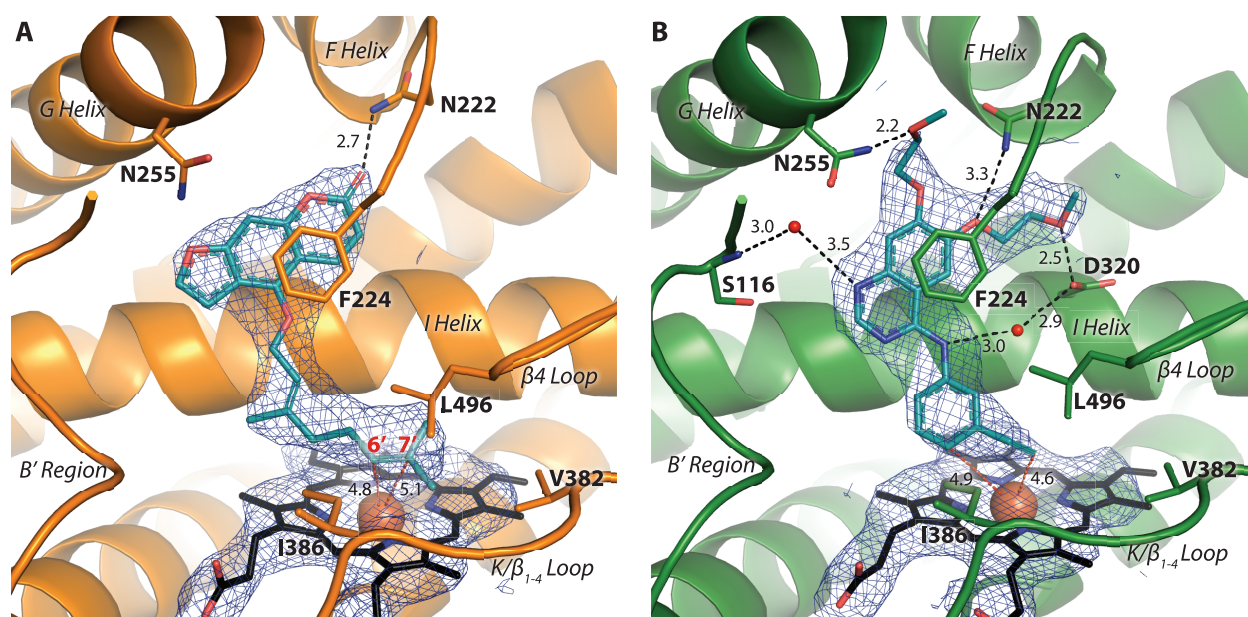
Figure 3.4 CYP1A1 active site interactions with A) bergamottin and B) erlotinib. Shown are polar CYP1A1 active site residues (sticks) that make hydrogen-bonds (black dashed lines) with the ligands. Electron density is shown as $2F_o - F_c$ simulated annealing composite omit maps (blue mesh) contoured at 1.0 σ. Heme is shown as black sticks. Key sites of metabolism are indicated by red dashed lines to the heme iron. Distances for hydrogen-bonds and ligand-heme iron distances (red dashed lines) are shown in Å.

Reports of bergamottin metabolism by P450 enzymes in the literature are few but important in terms of the "grapefruit juice effect" wherein metabolism of the furan ring of the psoralen moiety results in reactive intermediates causing mechanism-based inhibition of the P450 enzyme, while metabolism on the geranyloxy chain produces stable metabolites (36). Metabolism by CYP1A1

has not been previously reported, but the Hollenberg group investigated bergamottin metabolism by CYP3A4 (31), CYP3A5, and CYP2B6 (36). Bergamottin is a potent mechanism-based inhibitor of CYP3A4, consistent with metabolism on the psoralen ring. For CYP3A5 the primary metabolite involved oxidization at the 1'-carbon of the geranyl-oxy chain leading to cleavage of the geranyl chain to form bergaptol. In contrast, CYP2B6 produced major metabolites from oxidations on the terminal end of the geranyl-oxy chain. Both CYP3A5 and CYP2B6 were also capable of generating bergamottin metabolites that formed glutathione conjugates following furan ring oxidation, but the dominant metabolite was different for each enzyme, suggesting different preferences for bergamottin orientation in the respective active sites.

The current crystal structure of CYP1A1 with bergamottin suggests that this enzyme prefers to bind bergamottin more like CYP2B6 than CYP3A5 and would be more likely to oxidize the terminal portion of the geranyl chain. The current CYP1A1 structure does not indicate the potential for complete reorientation of bergamottin within the active site cavity, which would be necessary for reactive metabolites. Though this cannot be ruled out, the observed orientation would suggest CYP1A1 would have less tendency towards bergamottin bioactivation compared to other P450 enzymes, due to the specific interactions with the CYP1A1 active site cavity that dictate ligand orientation.

3.4.5 CYP1A1 Bergamottin Metabolism

In order to determine whether the binding pose for bergamottin in the CYP1A1 active site is consistent with metabolite generation, turnover assays were performed with human CYP1A1 and human NADPH-cytochrome P450 reductase. CYP1A1 produced at least four major metabolites at different substrate concentrations. At low concentrations of bergamottin only one major metabolite was observed. At higher concentrations a second metabolite was observed, then

a third metabolite (Figure 3.5). The third metabolite coelutes with authentic 6',7'-dihydroxybergamottin, while the other two metabolites are slightly less polar, suggesting they are likely to be the individual 6'-hydroxy and 7'-hydroxy products. The identity of the much more polar fourth metabolite is unknown. Overall, however, the metabolite profile is generally consistent with the binding orientation observed in the X-ray structure.
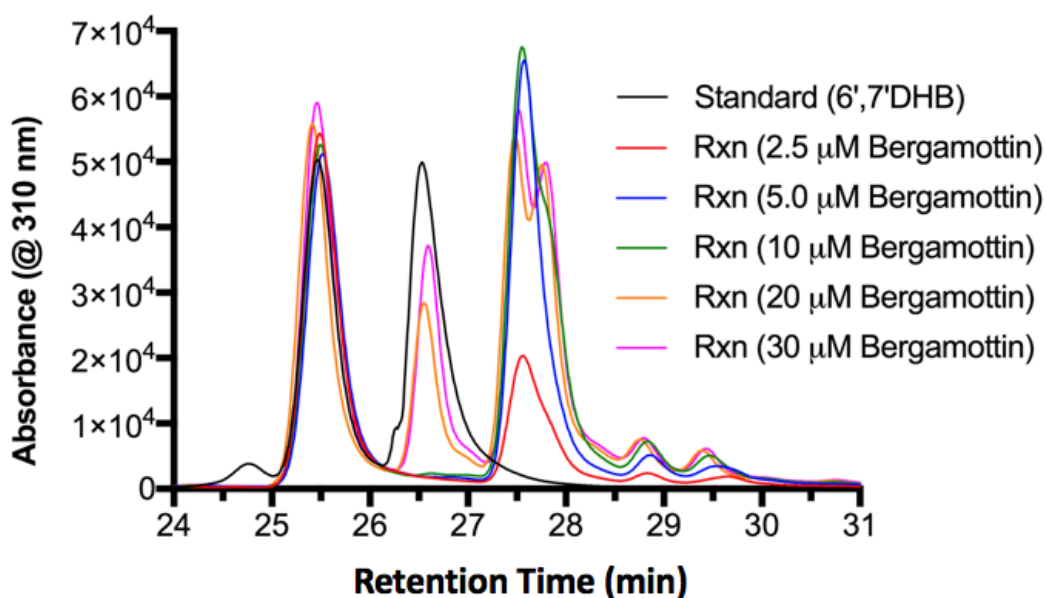
Figure 3.5 Bergamottin metabolism by CYP1A1 yields one major metabolite that coelutes with authentic 6',7'-dihydroxybergamottin (26.6 min) and two slightly less polar metabolites (27.6 and 27.7 min) that occur at lower substrate concentrations and are likely the individual 6'-monohydroxy and 7'-monohydroxy metabolites. Thus at least three major metabolites are consistent with the bergamottin orientation observed in the X-ray structure.

3.4.6 Erlotinib Binding to CYP1A1

Erlotinib, marketed as Tarceva, is a tyrosine kinase inhibitor that inhibits the epidermal growth factor receptor (EGFR) and was approved for treatment of non-small cell lung cancer (NSCLC). The use of erlotinib has been related to a number of adverse drug effects including rash (37), skin toxicities (38), and diarrhea (39) that vary in severity, with more life-threating effects such as pulmonary toxicity (40) and toxic epidermal necrolysis (Tarceva package insert). Metabolism of erlotinib and other kinase inhibitors by P450 enzymes can generate reactive

metabolites and could explain some of the associated toxicities of these drugs (25,26). In humans, erlotinib is metabolized primarily by P450 enzymes CYP3A4, CYP3A5, and CYP1A1, with the latter extrahepatic enzyme playing an important role in the lung, and in pharmacokinetic variability (23). Of particular clinical significance is the inducibility of CYP1A1. Tobacco smoke can increase CYP1A1 expression levels in the lung (41,42), which in turn can have large effects on erlotinib clearance (43,44). As a result, higher concentrations of erlotinib may be required to treat NSCLC in smokers (45).

Cocrystallization of CYP1A1 with the EGFR inhibitor erlotinib revealed this ligand binding in a slot-like, planar active site, with its planar quinazoline core distal to the heme making π-π interactions with the aromatic side chain of Phe224 (Figure 3.4B). The terminal alkyne moiety is clearly positioned above the heme and extends into a pocket formed by hydrophobic residues of the β4 and K/β$_{1-4}$ loops, similar to positioning of the geranyloxy chain of bergamottin. The two 2-methoxyethoxy sidechains of erlotinib extend away from the heme towards the roof of the CYP1A1 active site, one positioned between the F and G helices and the other sidechain protruding between the F and I helices underneath the F helix break. Erlotinib appears to potentially form a number of hydrogen bonding contacts with the CYP1A1 active site (Figure 3.4B). Two of these involve Asp320. If protonated, Asp320 is positioned to be a hydrogen bond donor to one of the side chain oxygens. Asp320 also appears to make a water-mediated interaction with the nitrogen connecting the quinazoline and phenyl-acetylene moieties but this active site water could only be reliably modeled into molecule A and B, which had the best electron density. Additionally, Asp222 makes a potential hydrogen bonding interaction with an oxygen on the methoxyethoxy sidechain (Figure 3.4B). The subterminal oxygen of the other side chain hydrogen bonds with the

side chain Asn255. Finally, a nitrogen of the quinazoline core forms a water-mediated hydrogen bond the backbone of Ser116.

The primary metabolic reactions in humans are *O*-demethylation of the methoxyethoxy side chain, oxidation of the terminal alkyne, and hydroxylation of the *para* position on the phenyl-acetylene moiety (46). The position of erlotinib observed in the CYP1A1 crystal structure is consistent with metabolism of either the terminal alkyne carbon or the *para* carbon of the aromatic aniline ring. The distances to the iron are 4.6 Å and 4.9 Å for the terminal alkyne and *para* carbons, respectively. Oxidation at these two positions of erlotinib are significant in terms of their potential to produce reactive species that might underlie erlotinib-associated toxicities. The 4-hydroxylation of the phenyl-acetylene carbon results in formation of a para-hydroxyanaline, which can be oxidized by P450 to form the reactive quinoneimine. Conversely, oxidation of the terminal alkyne can result in reactive oxirene or ketene intermediates (26).

Li *et al.* detected glutathione conjugates of erlotinib metabolism by CYP1A1. These conjugates were formed on the aniline ring, consistent with CYP1A1 hydroxylation at the *para* position and consistent with the orientation observed herein. Mechanism-based inactivation of CYP1A1 was not observed, suggesting the initial hydroxylated product may be released prior to formation of the reactive quinoneimine (26). Indeed, *p*-hydroxyerlotinib is the major metabolite circulating in human plasma (26). In contrast, CYP3A4 and CYP3A5 oxidize the terminal alkyne (47), resulting in reactive intermediates that do result in adduction of these P450 enzymes and mechanism-based inactivation. The fact that CYP1A1 is not inactivated suggests that CYP1A1 does not modify the terminal alkyne. Reports indicate that both CYP3A4/5 and CYP1A1 (23) can also generate active, non-toxic des-methyl metabolites of the side chains, suggesting that both enzymes can bind erlotinib in multiple orientations.

3.4.7 Comparison of all Three CYP1A1 Structures Yields Insights into Residues Involved in Accommodating Diverse Ligand Structures

The new co-crystal structures of CYP1A1 in this study have many overall structural elements consistent with the previous CYP1A1/ANF structure. Thus, the CYP1A1 structure accommodates bergamottin and erlotinib with minimal perturbations of the tertiary and secondary structure. Both bergamottin and erlotinib are positioned in the active site with their respective planar components in the same plane that ANF adopted and other known CYP1A1 ligands that were previously docked into the experimental CYP1A1/ANF structure (7). This common binding plane is likely driven by the conserved orientation of Phe224 which has favorable π-π interactions and sandwiches the planar ligand core against the I helix.
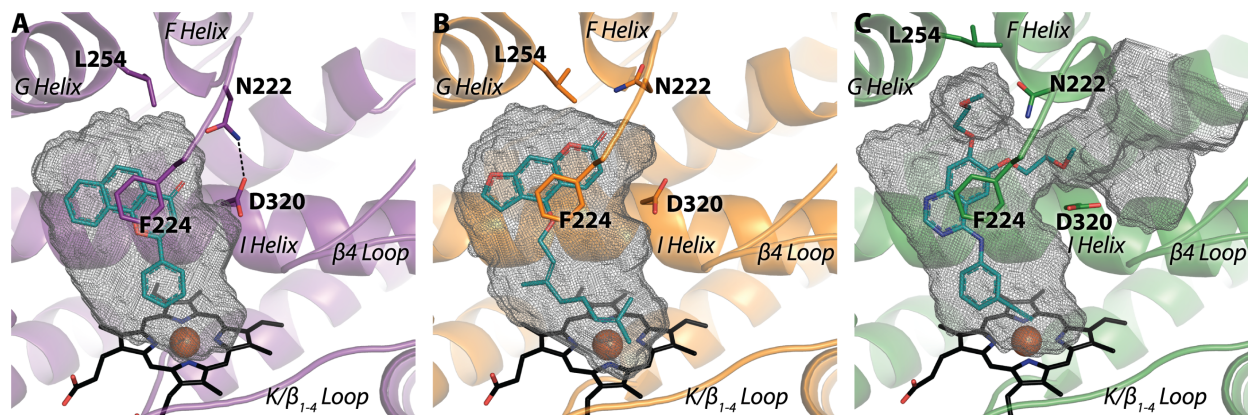
Figure 3.6 Active site cavities for CYP1A1 structures with A) α-naphthoflavone, B) bergamottin, and C) erlotinib. The side chains of Asn222 and Leu254 (sticks) display altered positioning between the structures, contributing to expansion of the CYP1A1 active site cavity.

Within this overall context, however, important differences arise in a key localized portion of the structure. The unusual break in the F helix for the CYP1A1 structure appears to assist in accommodation of different CYP1A1 ligands. While the active sites with ANF and bergamottin are enclosed (Figure 3.6A&B), in the erlotinib structure Asn222 in the F helix break adjusts its positioning, resulting in an opening that extends the active site cavity to the surface (Figure 3.6C). One of the methoxyethoxy chains of erlotinib extends into this channel between the F-helix break

and portions of the β4-loop. Since the open channel in the CYP1A1/erlotinib structure extends to bulk solvent, the end of the channel was artificially closed to permit comparison of active site volumes. It appears that concerted torsioning of the Asn222 and Leu254 side chains approximately doubles the volume of the CYP1A1/erlotinib active site (806 $Å^3$) compared to those for the CYP1A1/ANF (408 $Å^3$) and CYP1A1/bergamottin (456 $Å^3$) structures (Figure 3.6). In the CYP1A1/ANF structure, this channel is closed by hydrogen bonding between Asn222 and I helix residue Asp320 (Figure 3.6A). In the CYP1A1/bergamottin structure, Asn222 is torsioned in yet a different way, breaking the interaction with Asp320 but not opening the channel (Figure 3.6B). In each case the various rotamers of Asn222 (Figure 3.7) are accommodated by differential positioning of the spatially adjacent G helix residue Leu254. Larger CYP1A1 substrates and inhibitors might utilize an expanded version of this channel to access the active site. Certainly the channel as currently observed would have to widen further to accommodate entry/exit of just the current substrates or their metabolites.
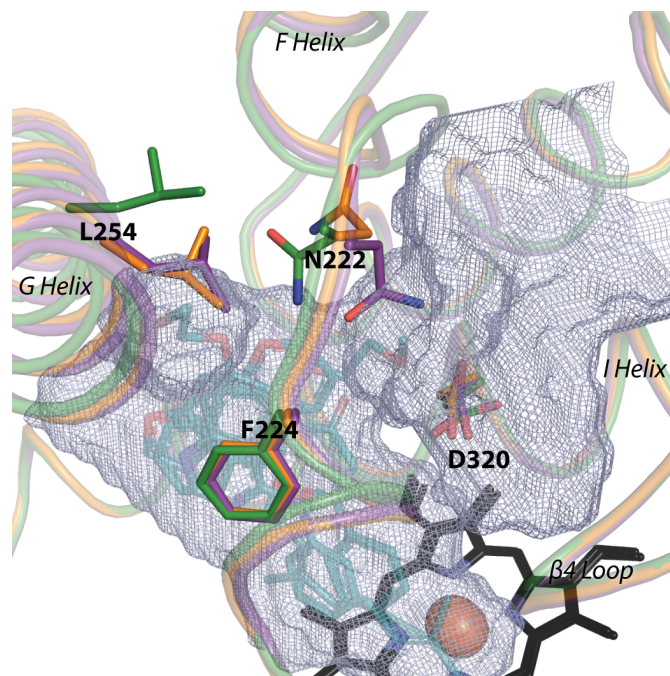
Figure 3.7 CYP1A1 structures with erlotinib (green), bergamottin (orange), and ANF (purple) are overlaid with the active site cavity for erlotinib (grey mesh). F helix residue Asn222 and adjacent G helix Leu254 (sticks) display altered positioning between the structures, and are in part responsible for expansion of the 1A1 active site cavity. The orientation is from the protein distal surface looking down through the active site roof to the heme (black sticks).

3.5 Conclusions

In summary, two new experimental structures with erlotinib and bergamottin are consistent with known metabolism. The erlotinib structure suggests that CYP1A1 participates in the first step in formation of chemically reactive metabolites that may contribute to lung and other toxicities. On the other hand, bergamottin interacts with CYP1A1 in an orientation suggestive of innocuous metabolite generation. In combination, the known structures suggest that while many of the structural elements of the CYP1A1 active site are rigid, that structurally diverse, somewhat larger ligands can be accommodated by local modifications. The structures of CYP1A1 with bergamottin and erlotinib in this study establish one approach by which CYP1A1 accommodates somewhat larger ligands. This consists of side-chain repositioning in the roof of the CYP1A1 active site, even generating a channel to the surface in the erlotinib structure. It is possible that even larger CYP1A1 ligands like ketoconazole and posaconazole might be accommodated by

further expanding the channel observed in the erlotinib structure. Knowing which components of the active site are malleable and which are not provides powerful information for those attempting to use computational approaches to predict compound binding and substrate metabolism for such enzymes.

3.6 References

1. Rendic, S., and Guengerich, F. P. (2012) Contributions of human enzymes in carcinogen metabolism. *Chem. Res. Tox.* **25**, 1316-1383

2. Shimada, T., and Fujii-Kuriyama, Y. (2004) Metabolic activation of polycyclic aromatic hydrocarbons to carcinogens by cytochromes P450 1A1 and 1B1. *Cancer Sci.* **95**, 1-6

3. Chun, Y. J., Ryu, S. Y., Jeong, T. C., and Kim, M. Y. (2001) Mechanism-based inhibition of human cytochrome P450 1A1 by rhapontigenin. *Drug Metab. Dispos.* **29**, 389-393

4. Androutsopoulos, V. P., Spyrou, I., Ploumidis, A., Papalampros, A. E., Kyriakakis, M., Delakas, D., Spandidos, D. A., and Tsatsakis, A. M. (2013) Expression profile of CYP1A1 and CYP1B1 enzymes in colon and bladder tumors. *PLoS One* **8**, e82487

5. Sutherland, M., Gill, J. H., Loadman, P. M., Laye, J. P., Sheldrake, H. M., Illingworth, N. A., Alandas, M. N., Cooper, P. A., Searcey, M., Pors, K., Shnyder, S. D., and Patterson, L. H. (2013) Antitumor activity of a duocarmycin analogue rationalized to be metabolically activated by cytochrome P450 1A1 in human transitional cell carcinoma of the bladder. *Mol. Cancer Ther.* **12**, 27-37

6. Bruno, R. D., and Njar, V. C. (2007) Targeting cytochrome P450 enzymes: a new approach in anti-cancer drug development. *Bioorg. Med. Chem.* **15**, 5047-5060

7. Walsh, A. A., Szklarz, G. D., and Scott, E. E. (2013) Human cytochrome P450 1A1 structure and utility in understanding drug and xenobiotic metabolism. *J. Biol. Chem.* **288**, 12932-12943

8. Sansen, S., Yano, J. K., Reynald, R. L., Schoch, G. A., Griffin, K. J., Stout, C. D., and Johnson, E. F. (2007) Adaptations for the oxidation of polycyclic aromatic hydrocarbons exhibited by the structure of human P450 1A2. *J. Biol. Chem.* **282**, 14348-14355

9. Wang, A., Savas, U., Stout, C. D., and Johnson, E. F. (2011) Structural characterization of the complex between alpha-naphthoflavone and human cytochrome P450 1B1. *J. Biol. Chem.* **286**, 5736-5743

10. Studier, F. W. (2014) Stable expression clones and auto-induction for protein production in E. coli. *Methods Mol. Biol.* **1091**, 17-32

11. Omura, T., and Sato, R. (1964) The carbon monoxide-binding pigment of liver microsomes. I. Evidence for its hemoprotein nature. *J. Biol. Chem.* **239**, 2370-2378

12. Bart, A. G., and Scott, E. E. (2017) Structural and functional effects of cytochrome b_5 interactions with human cytochrome P450 enzymes. *J. Biol. Chem.* **292**, 20818-20833

13. Oprian, D. D., and Coon, M. J. (1982) Oxidation-reduction states of FMN and FAD in NADPH-cytochrome-P-450 reductase during reduction by NADPH. *J. Biol. Chem.* **257**, 8935-8944

14. DeVore, N. M., Smith, B. D., Wang, J. L., Lushington, G. H., and Scott, E. E. (2009) Key residues controlling binding of diverse ligands to human cytochrome P450 2A enzymes. *Drug Metab. Dispos.* **37**, 1319-1327

15. Kabsch, W. (2010) XDS. *Acta Crystallogr., Sect. D: Biol. Crystallogr.* **66**, 125-132

16. Evans, P. R., and Murshudov, G. N. (2013) How good are my data and what is the resolution? *Acta Crystallogr., Sect. D: Biol. Crystallogr.* **69**, 1204-1214

17. McCoy, A. J., Grosse-Kunstleve, R. W., Adams, P. D., Winn, M. D., Storoni, L. C., and Read, R. J. (2007) Phaser crystallographic software. *J. Appl. Crystallogr.* **40**, 658-674

18. Emsley, P., Lohkamp, B., Scott, W. G., and Cowtan, K. (2010) Features and development of Coot. *Acta Crystallogr., Sect. D: Biol. Crystallogr.* **66**, 486-501

19. Adams, P. D., Afonine, P. V., Bunkoczi, G., Chen, V. B., Davis, I. W., Echols, N., Headd, J. J., Hung, L. W., Kapral, G. J., Grosse-Kunstleve, R. W., McCoy, A. J., Moriarty, N. W., Oeffner, R., Read, R. J., Richardson, D. C., Richardson, J. S., Terwilliger, T. C., and Zwart, P. H. (2010) PHENIX: a comprehensive Python-based system for macromolecular structure solution. *Acta Crystallogr., Sect. D: Biol. Crystallogr.* **66**, 213-221

20. Moriarty, N. W., Grosse-Kunstleve, R. W., and Adams, P. D. (2009) electronic Ligand Builder and Optimization Workbench (eLBOW): a tool for ligand coordinate and restraint generation. *Acta Crystallogr. D Biol. Crystallogr.* **65**, 1074-1080

21. Kleywegt, G. J., and Jones, T. A. (1994) Detection, delineation, measurement and display of cavities in macromolecular structures. *Acta Crystallogr., Sect. D: Biol. Crystallogr.* **50**, 178-185

22. Schrodinger, L. (2010) The PyMOL Molecular Graphics System, Version 1.8.6.2.

23. Li, J., Zhao, M., He, P., Hidalgo, M., and Baker, S. D. (2007) Differential metabolism of gefitinib and erlotinib by human cytochrome P450 enzymes. *Clin. Cancer. Res.* **13**, 3731-3737

24. Rochat, B., Zoete, V., Grosdidier, A., von Grunigen, S., Marull, M., and Michielin, O. (2008) In vitro biotransformation of imatinib by the tumor expressed CYP1A1 and CYP1B1. *Biopharm. Drug Dispos.* **29**, 103-118

25. Lin, D., Kostov, R., Huang, J. T. J., Henderson, C. J., and Wolf, C. R. (2017) Novel pathways of ponatinib disposition catalyzed by CYP1A1 involving generation of potentially toxic metabolites. *J. Pharmacol. Exp. Ther.* **363**, 12-19

26. Li, X. H., Kamenecka, T. M., and Cameron, M. D. (2010) Cytochrome P450-mediated bioactivation of the epidermal growth factor receptor inhibitor erlotinib to a reactive electrophile. *Drug Metab. Dispos.* **38**, 1238-1245

27. Fortin, S., Charest-Morin, X., Turcotte, V., Lauvaux, C., Lacroix, J., Cote, M. F., Gobeil, S., and R, C. G. (2017) Activation of phenyl 4-(2-oxo-3-alkylimidazolidin-1-yl)benzenesulfonates prodrugs by CYP1A1 as new antimitotics targeting breast cancer cells. *J. Med. Chem.* **60**, 4963-4982

28. Androutsopoulos, V. P., Tsatsakis, A. M., and Spandidos, D. A. (2009) Cytochrome P450 CYP1A1: wider roles in cancer progression and prevention. *BMC Cancer* **9**, 187

29. Stone, E. L., Citossi, F., Singh, R., Kaur, B., Gaskell, M., Farmer, P. B., Monks, A., Hose, C., Stevens, M. F., Leong, C. O., Stocks, M., Kellam, B., Marlow, M., and Bradshaw, T. D. (2015) Antitumour benzothiazoles. Part 32: DNA adducts and double strand breaks correlate with activity; synthesis of 5F203 hydrogels for local delivery. *Bioorg. Med. Chem.* **23**, 6891-6899

30. Yakkundi, A., McErlane, V., Murray, M., McCarthy, H. O., Ward, C., Hughes, C. M., Patterson, L. H., Hirst, D. G., McKeown, S. R., and Robson, T. (2006) Tumor-selective drug activation: a GDEPT approach utilizing cytochrome P450 1A1 and AQ4N. *Cancer Gene Ther.* **13**, 598-605

31. He, K., Iyer, K. R., Hayes, R. N., Sinz, M. W., Woolf, T. F., and Hollenberg, P. F. (1998) Inactivation of cytochrome P450 3A4 by bergamottin, a component of grapefruit juice. *Chem. Res. Toxicol.* **11**, 252-259

32. Olguin-Reyes, S., Camacho-Carranza, R., Hernandez-Ojeda, S., Elinos-Baez, M., and Espinosa-Aguirre, J. J. (2012) Bergamottin is a competitive inhibitor of CYP1A1 and is antimutagenic in the Ames test. *Food Chem. Toxicol.* **50**, 3094-3099

33. Cai, Y., Baer-Dubowska, W., Ashwood-Smith, M. J., Ceska, O., Tachibana, S., and DiGiovanni, J. (1996) Mechanism-based inactivation of hepatic ethoxyresorufin O-dealkylation activity by naturally occurring coumarins. *Chem. Res. Toxicol.* **9**, 729-736

34. Liu, J., Sridhar, J., and Foroozesh, M. (2013) Cytochrome P450 family 1 inhibitors and structure-activity relationships. *Molecules* **18**, 14470-14495

35. Schwarz, D., Kisselev, P., Ericksen, S. S., Szklarz, G. D., Chernogolov, A., Honeck, H., Schunck, W. H., and Roots, I. (2004) Arachidonic and eicosapentaenoic acid metabolism by human CYP1A1: highly stereoselective formation of 17(R),18(S)-epoxyeicosatetraenoic acid. *Biochem. Pharmacol.* **67**, 1445-1457

36. Kent, U. M., Lin, H. L., Noon, K. R., Harris, D. L., and Hollenberg, P. F. (2006) Metabolism of bergamottin by cytochromes P4502B6 and 3A5. *J. Pharmacol. Exp. Ther.* **318**, 992-1005

37. Wacker, B., Nagrani, T., Weinberg, J., Witt, K., Clark, G., and Cagnoni, P. J. (2007) Correlation between development of rash and efficacy in patients treated with the epidermal growth factor receptor tyrosine kinase inhibitor erlotinib in two large phase III studies. *Clin. Cancer. Res.* **13**, 3913-3921

38. Kiyohara, Y., Yamazaki, N., and Kishi, A. (2013) Erlotinib-related skin toxicities: treatment strategies in patients with metastatic non-small cell lung cancer. *J. Am. Acad. Dermatol.* **69**, 463-472

39. Cappuzzo, F., Ciuleanu, T., Stelmakh, L., Cicenas, S., Szczesna, A., Juhasz, E., Esteban, E., Molinier, O., Brugger, W., Melezinek, I., Klingelschmitt, G., Klughammer, B., Giaccone, G., and investigators, S. (2010) Erlotinib as maintenance treatment in advanced non-small-cell lung cancer: a multicentre, randomised, placebo-controlled phase 3 study. *Lancet Oncol.* **11**, 521-529

40. Liu, V., White, D. A., Zakowski, M. F., Travis, W., Kris, M. G., Ginsberg, M. S., Miller, V. A., and Azzoli, C. G. (2007) Pulmonary toxicity associated with erlotinib. *Chest* **132**, 1042-1044

41. McLemore, T. L., Adelberg, S., Liu, M. C., McMahon, N. A., Yu, S. J., Hubbard, W. C., Czerwinski, M., Wood, T. G., Storeng, R., Lubet, R. A., and et al. (1990) Expression of CYP1A1 gene in patients with lung cancer: evidence for cigarette smoke-induced gene expression in normal lung tissue and for altered gene regulation in primary pulmonary carcinomas. *J. Natl. Cancer Inst.* **82**, 1333-1339

42. Kim, J. H., Sherman, M. E., Curriero, F. C., Guengerich, F. P., Strickland, P. T., and Sutter, T. R. (2004) Expression of cytochromes P450 1A1 and 1B1 in human lung from smokers, non-smokers, and ex-smokers. *Toxicol. Appl. Pharmacol.* **199**, 210-219

43. Lu, J. F., Eppler, S. M., Wolf, J., Hamilton, M., Rakhit, A., Bruno, R., and Lum, B. L. (2006) Clinical pharmacokinetics of erlotinib in patients with solid tumors and exposure-safety relationship in patients with non-small cell lung cancer. *Clin. Pharmacol. Ther.* **80**, 136-145

44. Hamilton, M., Wolf, J. L., Rusk, J., Beard, S. E., Clark, G. M., Witt, K., and Cagnoni, P. J. (2006) Effects of smoking on the pharmacokinetics of erlotinib. *Clin. Cancer. Res.* **12**, 2166-2171

45. Hughes, A. N., O'Brien, M. E., Petty, W. J., Chick, J. B., Rankin, E., Woll, P. J., Dunlop, D., Nicolson, M., Boinpally, R., Wolf, J., and Price, A. (2009) Overcoming CYP1A1/1A2 mediated induction of metabolism by escalating erlotinib dose in current smokers. *J. Clin. Oncol.* **27**, 1220-1226

46.   Ling, J., Johnson, K. A., Miao, Z., Rakhit, A., Pantze, M. P., Hamilton, M., Lum, B. L., and Prakash, C. (2006) Metabolism and excretion of erlotinib, a small molecule inhibitor of epidermal growth factor receptor tyrosine kinase, in healthy male volunteers. *Drug Metab. Dispos.* **34**, 420-426

47.   Zhao, H., Li, S., Yang, Z., Peng, Y., Chen, X., and Zheng, J. (2018) Identification of ketene-reactive intermediate of erlotinib possibly responsible for inactivation of P450 enzymes. *Drug Metab. Dispos.* **46**, 442-450

CHAPTER 4

Human Cytochrome P450 1A1 Adapts Active Site for Atypical Nonplanar Substrate[*]

4.1 Summary

The human cytochrome P450 1A1 (CYP1A1) is well-known for chemical activation of procarcinogens and often has a substrate scope towards small and highly planar compounds. Substrates deviating from these characteristics are certainly known, but how these larger and nonplanar substrates are accommodated and oriented within the CYP1A1 active site is not understood. Herein a new X-ray structure of CYP1A1 bound to the pan-Pim kinase inhibitor GDC-0339 reveals how the CYP1A1 active site cavity is reconfigured to bind larger and nonplanar compounds. The shape and size of the cavity are controlled by structural elements in the active site roof, with major changes in the conformation of the F helix break and relocation of Phe224 from the active site to the protein surface. This altered CYP1A1 active site architecture is consistent with the proposed mechanism for CYP1A1 generation of an unusual aminoazepane-rearranged metabolite for this substrate.

4.2 Introduction

Many human cytochrome P450 enzymes are promiscuous monooxygenases capable of metabolizing chemically and morphologically diverse sets of drugs, environmental contaminants,

---

and endogenous compounds. While some generalizations can be made about the substrate scope of an individual P450 enzyme based on known active site characteristics such as size and features of the residues lining the cavity (1,2), there are also many examples of validated substrates and inhibitors that do not conform to known active site bounds. This indicates that we do not yet understand the full range of active site malleability for different human P450 enzymes. These limitations in our knowledge of the conformational flexibility of a P450 enzyme significantly retards the utility of structure to predict drug metabolism, carcinogen/toxin activation, and to design selective P450 inhibitors.

Cytochrome P450 1A1 is a human enzyme most well-known for its role in chemical carcinogenesis (3). Until recently there was only a single structure of human cytochrome P450 1A1 (CYP1A1) available (4). This structure, solved with the compact, highly planar ligand α-naphthoflavone (ANF; molecular weight 272 g/mol) revealed a spatially complementary enclosed, highly planar active site. This void is compatible with a subset of known CYP1A1 ligands (4) with low molecular weights (200-500 g/mol) and compact structures like benzo[a]pyrene (252 g/mol), but not its larger and nonplanar CYP1A1 substrates. While CYP1A1 has not historically not been recognized for playing an extensive role in drug metabolism, Jungmann and Lang recently reported that screening a library of 650 drugs revealed ~35% had appreciable metabolism by CYP1A1 (5). This diverse library probably represents the most unbiased evaluation of CYP1A1 substrates. Those with appreciable metabolism typically have molecular weights from 200-500 g/mol, but surprising exceptions of larger compounds include the macrolide antibiotic troleandomycin (813 g/mol), the muscle relaxant atracurium (929 g/mol), the macrolide antibiotic tylosin (916 g/mol) and even the immunosuppressant cyclosporin A (1202 g/mol) and the decapeptide gonadotropin releasing hormone agonist gosrelin (1269 g/mol). Clearly

conformational changes must occur to accommodate such ligands. Recently two additional structures of CYP1A1 were solved with two ligands larger than alpha-naphthoflavone that had both planar and nonplanar constituents, the natural product bergamottin (338 g/mol) and the tyrosine kinase inhibitor erlotinib (393 g/mol) (6). These structures revealed conformational alterations allowing for a more extended substrate profile for CYP1A1. The structure with erlotinib was particularly important because CYP1A1 is known to bioactivate tyrosine kinase inhibitor drugs into reactive metabolites that have been implicated in patient toxicities (7-9). However, all three structures of CYP1A1 demonstrated a planar active site and thus did not answer the question of how nonplanar ligands are accommodated.

Genentech researchers recently demonstrated that CYP1A1 could efficiently metabolize the pan-Pim kinase inhibitor GDC-0339 (5-amino-*N*-(5-((4*R*,5*R*)-4-amino-5-fluoroazepan-1-yl)-1-methyl-1*H*-pyrazol-4-yl)-2-(2,6-difluorophenyl)thiazole-4-carboxamide) (10). CYP1A1 converted the flexible, nonplanar GDC-0339 into an unusual aminoazepane-rearranged metabolite (G-1025, Figure 4.1A), with the proposed mechanism requiring a highly nonplanar intermediate (10). This intramolecular rearrangement was difficult to rationalize based on any of the currently known CYP1A1 structures with highly planar active sites. To help understand how CYP1A1 is able to accommodate this larger and potentially non-planar substrate, CYP1A1 was cocrystallized with GDC-0339. The observed orientation of GDC-0339 in CYP1A1 is consistent with initiation of the proposed rearrangement reaction mechanism (10) and also reveals the ability of CYP1A1 to deviate from the previously observed planar active site through conformational flexibility involving the F helix portion of the active site roof. This new structure furthers our understanding of the plasticity of this human enzyme, revealing how CYP1A1 accommodates and metabolizes a more diverse substrate profile than could be previously rationalized.
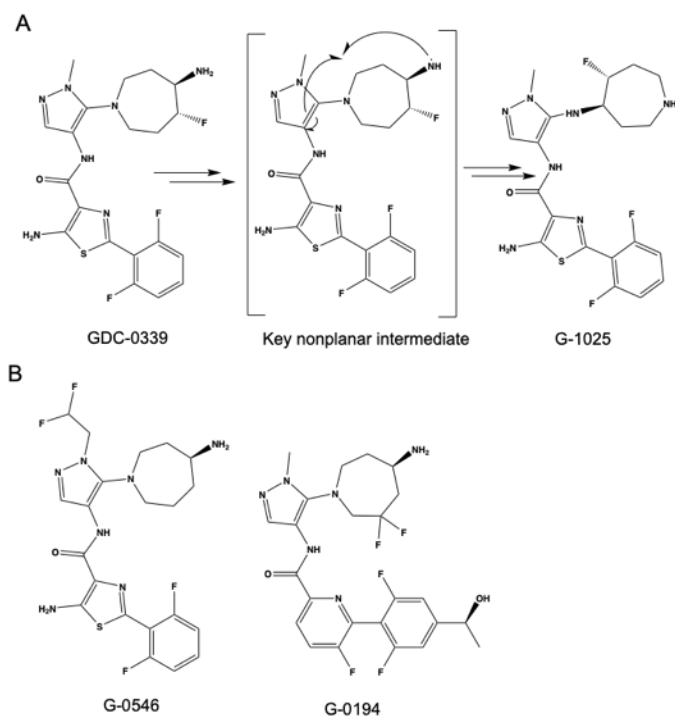
Figure 4.1 Pim kinase inhibitor GDC-0339, its metabolite G-1025, and analogs. A) GDC-0339 is reported to undergo a CYP1A1-mediated rearrangement to G-1025 via a key nonplanar intermediate. B) Structures of close-in analogs G-0546 and G-0194 used for spectral binding experiments.

4.3 Experimental Procedures

4.3.1   Materials

GDC-0339 and two structurally related compounds, G-0546 and G-0194, (Figure 4.1B) were synthesized at Genentech Inc (South San Francisco, CA) and provided for research purposes.

4.3.2   Protein Expression and Purification

Human CYP1A1 was generated using a construct containing a synthetic, codon-optimized gene with an N-terminal truncation and C-terminal 6x histidine tag, as described previously (4). Expression and purification of the CYP1A1 construct was performed without modification as described (6). Protein purity was assessed by SDS-PAGE. The reduced carbon monoxide-difference spectrum was used to evaluate protein quality (11). Protein concentration was

102

quantified by UV-Vis spectroscopy, from the absorbance of the Soret peak with an extinction coefficient of 100 mM^{-1}cm^{-1} in a buffer containing 50 mM potassium phosphate, 500 mM NaCl, 20% (v/v) glycerol, 250 mM imidazole, 0.5% (w/v) CHAPS, 1 mM EDTA, pH 7.4.

4.3.3 Ligand Binding Assays

Assays to measure ligand binding to CYP1A1 were performed in tandem cuvettes as described previously (6). Ligand binding data was determined in duplicate. Each of the ligands examined herein bound tightly enough (K_d values <400 nM) that significant ligand is depleted from solution and the assumption that ligand concentration doesn't substantially change is not valid. Thus the quadratic equation for tight binding ligands was used to fit the data (12).

4.3.4 Crystallization, Data Collection, and Structure Determination

Cocrystallization of purified CYP1A1 with the pan-Pim kinase inhibitor GDC-0339 was performed as previously described (6), with a few modifications as listed below. Purified CYP1A1 was saturated with ligand by addition of 100 μM GDC-0339 (stock in 100% DMSO) to dilute protein and subsequently concentrated by centrifugal ultrafiltration to 20 mg/mL, measured by the Soret peak in the buffer described above. Crystals of CYP1A1 with GDC-0339 were grown using the sitting-drop vapor diffusion method in 96-well plates by mixing 0.75 μL CYP1A1 saturated with GDC-0339 with 0.75 μL crystallization solution (0.2 M potassium phosphate dibasic, 20% PEG 3350, 10% glycerol, 1 mM hexadecyltrimethylammonium bromide). Triangular-prism shaped crystals grew over three to five days, and were cryoprotected using the crystallization solution plus 20% glycerol before being flash cooled in liquid nitrogen. A dataset was collected on a single crystal at Advanced Photon Source LS-CAT beamline 21-ID-G. Data processing was performed using HKL2000 (13), and an initial structure solution was obtained by molecular replacement via Phaser (14) with the CYP1A1/bergamottin structure (6) (PDB 6DWM, molecule

A), with a log likelihood score of 1,244. This solution placed two copies of CYP1A1 in the asymmetric unit, chains A and B. This partial structure, along with the PDB 6DWM, molecule A, were used in Phaser to find a third copy, chain C, with a log likelihood score of 6,549. Additional electron density and packing indicated the presence of a fourth copy of CYP1A1 in the asymmetic unit, chain D, which was modeled by partially building helices and then using the secondary structure matching alogrithm in COOT to superpose the competely built chain A onto the partial model for chain D. This was followed by a round of simulated annealing using torsion angles in PHENIX. Manual model building and refinement were performed using COOT (15) and PHENIX (16), respectively. Coordinates and restraints for GDC-0339 were generated using PHENIX eLBOW (17) with AM1 geometry optimization. Calculation of the active site void volume was performed using VOIDOO (18), with probe radius set to 1.4 Å and grid spacing of 1.0. Crystal structure figures were prepared using PyMOL (19).

Table 4.1 Data collection and refinement statistics.

	CYP1A1/GDC-0339
Data Collection	
Space Group	$P2_12_12_1$
Cell Dimensions (Å)	65.15, 195.90, 236.98
Molecules/a.u.	4
Resolution (Å)[a]	50.00-3.16 (3.21-3.16)
Total reflections[a]	343,766 (13,457)
Unique reflections[a]	52,336 (2,539)
Redundancy[a]	6.6 (5.3)
R_{pim}[a]	0.102 (0.786)
$<I/\sigma(I)>$ [a]	16.5 (1.8)
CC1/2[a]	0.991 (0.490)
Completeness (%)[a]	99.6 (97.6)
Refinement	
Resolution (Å)	49.32-3.17
No. reflections	52,207
R/R_{free} (%)	24.0 / 26.7
Ramachandran (%)	92.39 / 6.90 / 0.71
No. non-H atoms/B factors (Å^2)	
Protein	14,918 / 81.27
Ligand	32 / 87.42
Heme	172 / 68.31
NO_3	4 / 64.02
Water	10 / 61.61
RMSD bond (Å)	0.005
RMSD angle (°)	0.706
Coordinate error (max. likelihood based) (Å)	0.43

[a] Statistics for highest resolution shell shown in parentheses.

4.4 Results

4.4.1   Binding of GDC-0339 and analogs to CYP1A1

Spectral binding experiments were employed in order to further examine the binding mode and affinity of GDC-0339 towards human CYP1A1. Titrations of GDC-0339 to CYP1A1 resulted in unusual spectral shifts, with the difference spectra revealing an absorbance peak emerging at approximately 414-415 nm and a shallow trough at 437 nm (Figure 4.2A). These changes do not correspond to classical P450 ligand binding modes of Type I, Type II, or reverse Type I. However, fitting these spectral changes required the tight-binding equation and revealed that CYP1A1 has very high affinity for GDC-0339 at 51 ± 5 nM (Figure 4.2A inset). By comparison, bergamottin and erlotinib, two other good CYP1A1 substrates, bind with affinities of 370 nM and 1 µM, respectively.
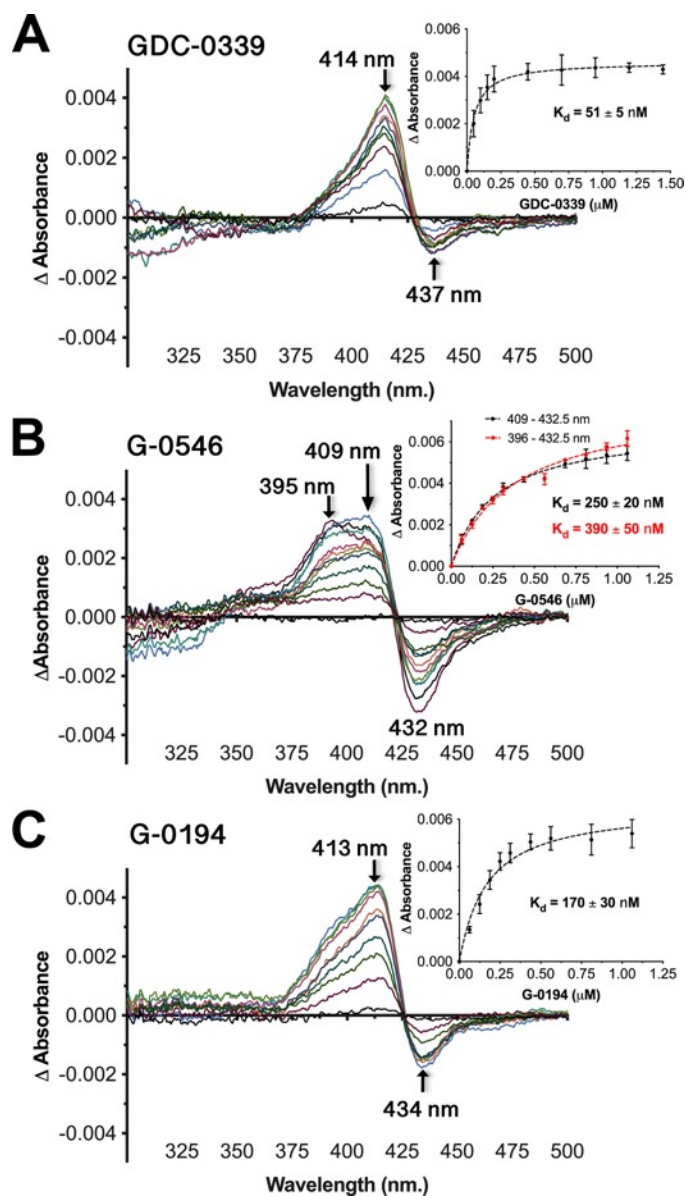
Figure 4.2 CYP1A1 (1 μM) spectral binding assays with GDC-0339 (*A*), G-0546 (*B*), and G-0194 (*C*) result in atypical binding response. *Inserts*, the peak-trough absorbance change versus compound concentration fit by nonlinear regression to a tight-binding equation. K_d is given ± S.E. (*error bars*).

Binding assays were also performed with two analogs of GDC-0339 (Figure 4.1B), to determine if various extensions on this ligand framework could also be accommodated by CYP1A1. G-0546 was selected to probe the impact of an increased bulk such as a difluoromethyl group on the pyrazole moiety relatively close to the center of rearrangement. The CYP1A1 catalyzed rearrangement was observed for the methyl (in place of difluoromethyl) analog of G-

0546 (10). Titrations of G-0546 resulted in a broad peak, which has approximate λ_{max} values of 409 nm and 395-396 nm, and a pronounced trough at 432-433 nm (Figure 4.2B). This spectral response is consistent with G-0546 binding in the active site and furthermore suggests multiple binding modes, with the λ_{max} of 409 nm most similar to the observations with GDC-0339 and the λ_{max} at 395-396 more representative of a typical Type I binding profile where the ligand displaces a water from the heme iron. If the amino-azepane moiety of G-0546 is directed towards the heme, as the metabolite G-1025 suggests, addition of the bulky difluoromethane group on the pyrazole could logically alter the ligand's spatial relationship to the heme iron, giving rise to the classical Type I character. The binding affinity of G-0546 was 250 ± 20 nM (using the absorbance at 409 nm) or 390 ± 50 nM (using the absorbance at 396 nm) (Figure 4.2B insert). Both K_d values indicate that the substitutions in G-0546 (Figure 4.1B) weaken the binding in comparison to the 1A1/GDC-0339 complex (K_d 50 nM).

The second analog tested was G-0194 (Figure 4.1B), which differs from GDC-0339 in three areas. 1) G-0194 replaces the central aminothiazole with a slightly larger fluoropyridine and removes the aniline NH_2 group. 2) G-0194 adds a second fluorine and both fluorine groups are at the γ-position of the amine group on the amino-azepane ring in contrast to the β-position in GDC-0339. 3) G-0194 adds a hydroxyethyl group extending from the difluorophenyl moiety. Knowing that the γ-difluoro-amino-azepane moiety could still rearrange, we were interested to know how the increased diversity away from the center of rearrangement could impact CYP1A1's binding and catalysis. Spectral changes from G-0194 titrations to CYP1A1 resulted in responses similar to GDC-0339, where difference spectra evolved an absorbance peak at 413-414 nm and a smaller trough at ~434 nm (Figure 4.2C). The broader, bifurcated peak observed for G-0546 was not present. This is consistent with the major changes in structure of G-0194 are further distant from

the amino-azepane epicenter. The K_d for G-0194 binding to CYP1A1 was 170 ± 30 nM (Figure 4.2C insert), which is intermediate between the other two compounds examined herein. Due to multiple changes to the analogs it is unknown which specific alterations are attributed to effects on binding mode and/or affinity.

4.4.2 CYP1A1 Structure with GDC-0339

Since CYP1A1 produced a unique rearranged GDC-0339 metabolite and unusual spectral behavior upon binding, an X-ray structure was determined using co-crystallization (3.17 Å). The space group and unit cell dimensions were similar to previously determined CYP1A1 structures (4,6). There were four copies of the protein within the asymmetric unit, with weaker electron density for chains C and D.

Among these four copies of the CYP1A1 protein, there are three types of structures. Molecule B has some density for only the ligand azepane ring, located low in the active site just above the heme, consistent with partial occupancy of GDC-0339, and the conformation of the F helix forming part of the active site roof is similar to that observed in previous structures, most similar to the CYP1A1 structure with α-naphthoflavone bound. Molecules C and D have essentially no active side density consistent with the ligand in the active site and the poor density for side chains in the F helix preclude definition of their orientation either into or out of the active site. However, the active site of molecule A contains electron density clearly defining an elongated conformation of the GDC-0339 ligand in concert with significant corresponding differences in the F helix and upper active site (Figure 4.3).
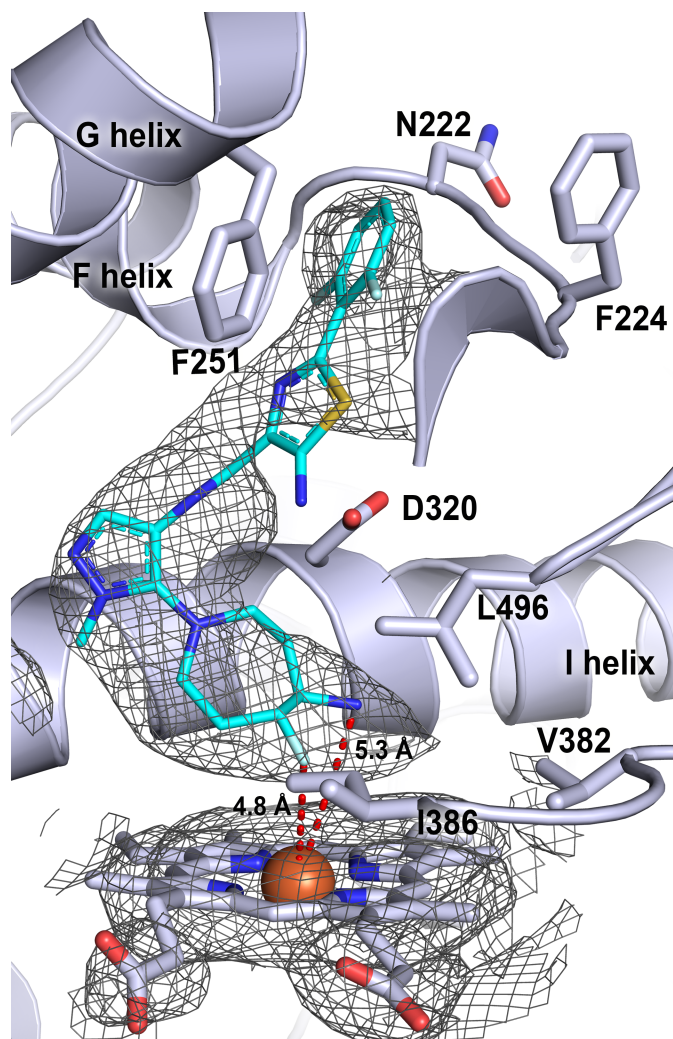
Figure 4.3 CYP1A1 (light blue ribbons and sticks) active site with GDC-0339 (cyan sticks) bound. Heteroatoms are as indicated: nitrogen, royal blue; oxygen, red; sulfur yellow; fluorine, light blue; iron, rust. Electron density is shown as $2F_o - F_c$ composite omit map contoured at 1.0 σ (grey mesh) for ligand and heme. Distances from the heme iron to the closest GDC-0339 atoms are shown by red dashed lines and labeled with the respective distances.

Correct orientation of GDC-0339 within the active site density was aided by the large, seven-membered fluoro-amino-azepane ring. This ring system is located closest to the heme with the fluorine and primary amine approximately 4.8 and 5.3 Å from the iron, respectively (Figure 4.3). This binding orientation is consistent with the mechanism proposed by Takahashi *et al.* where production of the rearranged metabolite was initiated by hydrogen abstraction at the primary amine on the fluoro-amino-azepane (10). Moving away from the heme-oriented fluoro-amino-azepane ring, the ligand methyl-pyrazole is directed toward the central I helix (Figure 4.3). The subsequent

amide linkage directs both the aminothiazole and difluorophenyl moieties of ligand towards the roof of the active site and the F helix. The aminothiazole has less electron density, suggesting that it may adopt multiple conformations. Regardless, the ligand aminothiazole and difluorophenyl rings occupy the space where Phe224 and the protein backbone between the two halves of the F helix normally reside in structures with other ligands.

Despite the high affinity, as measured in spectral assays here and reflected in efficient GDC-0339 turnover by and potent competitive inhibition for CYP1A1 (10), there are relatively few specific interactions between GDC-0339 and CYP1A1. The fluorine group on the fluoro-amino-azepane is confined by hydrophobic residues such as V382 and L496 from the K/β_{1-4} and β4 loops near the bottom of the active site (Figure 4.3). The aromatic thiazole ring has favorable pi-pi edge-to-face interaction with Phe251 on the G helix (Figure 4.3). Overall, slightly weaker density is observed for the aminothiazole and fluoropyridine moieties of GDC-0339 as it begins to extend towards the roof and edge of the active site bounds. This suggests less complete immobilization of the ligand in this area, while the methyl-pyrazole and fluoro-amino-azepane moieties lie in a more confined environment near the heme.

4.5 Discussion

Many CYP1A1 substrates share physicochemical features of high planarity, aromaticity, small size, and compact shape. The structural basis for this profile was evident when the first CYP1A1 structure, bound to ANF, was solved (4). This structural architecture was also observed in the other family 1 human P450 enzymes, 1A2 (20) and 1B1 (21). Synthetic derivatives based on the flavonoid core like 4'-propargyloxy-β-naphthoflavone (22), and tyrosine kinase inhibitors (6-8) suggested the capacity of CYP1A1 to accommodate more elongated ligands which still maintain a predominately planar shape. A recent report revealed CYP1A1-mediated metabolism

of the flexible, nonplanar Pim-kinase inhibitor GDC-0339. This compound inhibited CYP1A1 competitively and with greater potency than α-naphthoflavone when phenacetin was used as a substrate (10), indicating GDC-0339 binds in close proximity to the heme and with high affinity. Based on the rearranged metabolite and structural analogs of GDC-0339, Takahashi *et al.* proposed that CYP1A1 initiated the reaction through hydrogen abstraction from the primary amine on the fluoro-amino-azepane moiety (10), indicating this group on GDC-0339 would be close to the heme iron. This rearrangement mechanism involves the compound folding on itself in the active site with interactions between this primary amine radical and the adjacent methylpyrazole (10), also strongly suggesting the CYP1A1 active site would have to be substantially reconfigured to allow such a reaction.

4.5.1   Binding of GDC-0339 and analogs to CYP1A1

In general, the bulkier analogs had decreased affinity to CYP1A1 compared to GDC-0339, although binding was still in the nanomolar range. The main spectral binding changes induced by all three of these compounds do not correspond to common P450 binding modes. They are most similar to observations reported for CYP46A1 binding bicalutamide (23). In this case there is crystallographic evidence of the bicalutamide cyano group hydrogen bonding to a water molecule, which is in turn coordinated to the heme iron. While it was possible that the primary amine of the fluoro-amino-azepane also hydrogen bonds to a water coordinated to the heme iron, this is not consistent with the X-ray structure herein. Addition of difluoromethane on the pyrazole adjacent to the fluoro-amino-azepane ring in G-0546 might reposition the ligand, consistent with the addition of a classical Type I response for displacement of the heme-coordinated water. For all three ligands, the net absorbance change in the spectral binding experiments is low. This suggests

a low proportion of CYP1A1 is binding GDC-0339 despite high affinity and is consistent with ligand occupancy in only one of the four CYP1A1 molecules in the asymmetric unit.

4.5.2 CYP1A1 Structure with GDC-0339

Since the top of the GDC-0339 ligand occupies the space where the F helix normally resides in structures with other ligands, this region is substantially reconfigured (Figure 4.4). As in most human P450 enzymes, this F helix forms the roof of the active site. In CYP1 enzymes there is typically a break in this helix as it passes over the active site. The positioning of this break is key in determining whether the CYP1A1 active site is enclosed or open to the surface and its preference for planar ligands. In the α-naphthoflavone complex, F helix residue Asn222 hydrogen bonds to I helix Asp320 to close off access to the protein exterior between these two structural elements (Figure 4.4A). In the bergamottin complex, these two side chains torsion so that there is no longer a hydrogen bond between them and a little additional space is made available to accommodate the furanocoumarin ring (6). In the erlotinib complex, both Asn222 and Asp320 torsion farther apart, opening up a channel between them all the way to the protein surface (Figure 4.4B). In each of these latter two structures, Asn222 instead interacts with various oxygens in the ligands and the torsions of the side chains occur without changing the backbone conformation of the F helix break (Figure 4.4B). However, in this new GDC-0339 structure, the protein backbone between the two halves of the F helix adopts an entirely new conformation, with the Asn222 side chain disordered on the protein surface and not interacting with the ligand at all (Figure 4.4C). The second important impact of F helix break reconfiguration is positioning of Phe224. In all other known CYP1A1 structures, the F helix backbone conformation positions Phe224 to project into the active site, pi-pi stacking with the planar portions of ligands (Figure 4.4A and 4.4B). This is a key feature reinforcing planarity in the middle and top portions of the CYP1A1 active site.

113

With nonplanar GDC-0339, however, the new conformation of the F helix break instead projects Phe224 in the opposite direction, projecting from the protein surface toward solvent (Figure 4.4C). Distances between the nearest side chain atoms of Asp320 and Asn222 vary from 3.5 Å in the hydrogen bond in the α-naphthoflavone structure to 6.2 Å in the erlotinib structure, to 10 Å in the GDC-0339 structure.
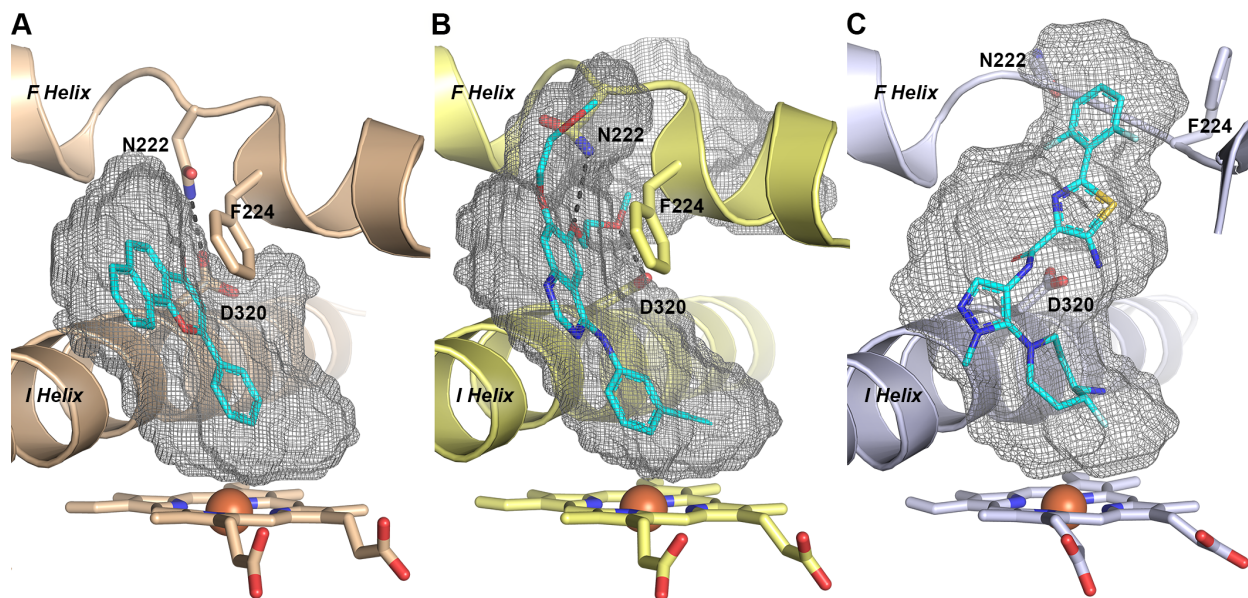
Figure 4.4 Comparison of active-site cavities for CYP1A1 structures with α-naphthoflavone (*A*), erlotinib (*B*), and GDC-0339 (*C*). Heteroatoms are as indicated: nitrogen, blue; oxygen, red; sulfur yellow; fluorine, light blue; iron, rust. The F helix break conformation in the CYP1A1/GDC-0339 structure results in both Phe-224 and Asn-222 positioned outside of the active-site, with increased width of the cavity volume compared to the much more planar nature of the CYP1A1 structures and active sites shown in (*A*) and (*B*). Black dashed lines indicate hydrogen-bonds.

Restructuring of the F helix break as observed in the CYP1A1/GDC-0339 structure and repositioning Phe224 outside the active site significantly expand the active site cavity. Comparisons to other CYP1A1 co-crystal structures (Figure 4.4, grey mesh) reveal that the volume of the CYP1A1/GDC-0339 active site at 820 Å^3 is much larger than structures with α-naphthoflavone (408 Å^3, Figure 4.4A) or bergamottin (456 Å^3) and similar to erlotinib (806 Å^3). Although the CYP1A1 structures with GDC-0339 and erlotinib structures have similar cavity volumes, the identity of the repositioned residues and structural elements differed and the shape

of the upper active site/channel is different. Expansions in the CYP1A1/erlotinib active site cavity were largely a result of torsioning of Asn222 (F helix break), Asp320 (I helix), and Leu254 (G helix), with an additional offset of the G helix away for the active site (Figure 4.4B). In contrast, the CYP1A1/GDC-0339 active site increased substantially more in width at about the level of the aminothiazole ring (Figure 4.4C).

This increased width of the middle of the active-site cavity is interesting in the context of the proposed GDC-0339 rearrangement mechanism (10). The mechanism that was proposed to form the rearranged metabolite would proceed through an intramolecular tetrahedral intermediate occurring between the pyrazole and primary amine radical (Figure 4.1A), which likely would have to be accommodated within the active site. The reconfiguration of the F helix break, to swing Phe224 outside the active site cavity may not only accommodate the nonplanar substrate, but also permit the formation of this 3-dimensional intermediate. Therefore, the F helix break conformation observed in this crystal structure might help prime CYP1A1 for accommodating large deviations to the normally highly planar active site, such as the GDC-0339 rearrangement intermediate. Notably none of the five residues in the middle of this F helix break are conserved in human CYP1A2, which could correlate with the selectivity for GDC-0339 metabolism by CYP1A1 over CYP1A2 (10). The F helix break in CYP1A2 may not be able to adopt a conformation consistent with the binding of GDC-0339 in this orientation.

The therapeutic target for GDC-0339 are the Pim kinases, where the ligand is a potent pan-inhibitor designed to interact with the ATP binding pocket. Recently a structure of GDC-0339 bound to Pim-1 was reported (24). When bound to Pim-1, GDC-0339 adopts a compact U-shaped conformation (Figure 4.5, grey sticks). In contrast when GDC-0339 is bound to CYP1A1, the conformation is much more extended (Figure 4.5, green sticks). GDC-0339 is metabolized

efficiently by CYP1A1 to form the rearranged metabolite G-1025, which displays 10- to 20-fold reduction in potency towards Pim isoforms (10). This likely results from loss of key salt-bridges formed between the primary amine on the fluoro-amino-azepane with an acidic region in the Pim kinase (24). Engineering conformational constraints into GDC-0339 to favor the U-shaped Pim-compatible conformation may be desirable to reduce its binding to and metabolic deactivation by CYP1A1, as a strategy to sustain its efficacy and avoid multiple myeloma drug resistance. CYP1A1 expression levels and activity have previously been shown to have a resistance role in for the multiple myeloma drug bortezomib (25).
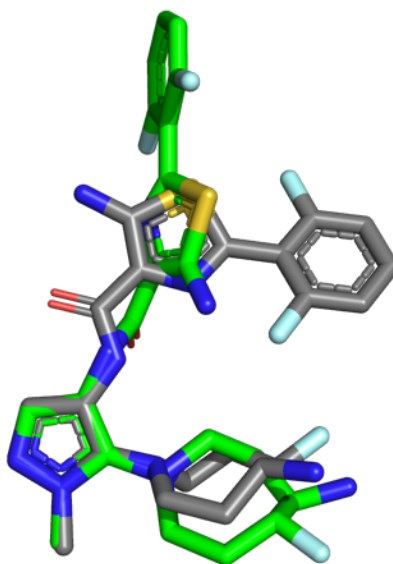
Figure 4.5 Comparison of the GDC-0339 conformation when bound to CYP1A1 (green sticks) versus the conformation bound to Pim-1 (grey sticks, PDB Code: 6NO9) reveals significant conformational differences that could be used to decrease CYP1A1 metabolism.

4.6 Conclusions

In conclusion, our structural investigations into CYP1A1 revealed that this enzyme has greater degrees of conformational malleability than previously observed, permitting the binding and metabolism of nonplanar compounds and their likely intermediates. Specifically, this structure

demonstrates the CYP1A1 active site can increase approximately twice in volume and rearrange both polar and aromatic residues. Even larger nonplanar CYP1A1 substrates such as the macrolide antibiotics troleandomycin and tylosin, the immunosuppressant cyclosporin A, and the decapeptide gosrelin may take advantage of this nonplanarity and/or protrude outside of the active site through the channel observed. The roles observed for CYP1A1 in chemical carcinogenesis and the generation of reactive metabolites underscore the importance in predicting chemical liabilities of various dietary compounds, pollutants, and drugs. This more complete understanding of the structural elements contributing to flexibility within the CYP1A1 active site should help in predicting a broader range of substrates potentially susceptible to CYP1A1 bioactivation, and in some cases aid in engineering drugs to remove CYP1A1-mediated metabolic liabilities.

4.7 References

1. Johnson, E. F., and Stout, C. D. (2013) Structural diversity of eukaryotic membrane cytochrome P450s. *The Journal of biological chemistry* **288**, 17082-17090
2. Scott, E. E., and Godamudunage, M. P. (2018) Structures of human cytochrome P450 enzymes: Variations on a theme. in *O2-dependent Heme Enzymes* (Ikeda-Saito, M., and Raven, E. eds.), Royal Society of Chemistry. pp
3. Rendic, S., and Guengerich, F. P. (2012) Contributions of human enzymes in carcinogen metabolism. *Chem. Res. Tox.* **25**, 1316-1383
4. Walsh, A. A., Szklarz, G. D., and Scott, E. E. (2013) Human cytochrome P450 1A1 structure and utility in understanding drug and xenobiotic metabolism. *The Journal of biological chemistry* **288**, 12932-12943
5. Jungmann, N., and Lang, D. (2019) Drug Library Screening for Human CYP1A1 Substrates. in *International Society for the Study of Xenobiotics*, International Society for the Study of Xenobiotics, Portland, OR
6. Bart, A. G., and Scott, E. E. (2018) Structures of human cytochrome P450 1A1 with bergamottin and erlotinib reveal active-site modifications for binding of diverse ligands. *The Journal of biological chemistry* **293**, 19201-19210
7. Li, X. H., Kamenecka, T. M., and Cameron, M. D. (2010) Cytochrome P450-mediated bioactivation of the epidermal growth factor receptor inhibitor erlotinib to a reactive electrophile. *Drug Metab. Dispos.* **38**, 1238-1245
8. Lin, D., Kostov, R., Huang, J. T. J., Henderson, C. J., and Wolf, C. R. (2017) Novel Pathways of Ponatinib Disposition Catalyzed By CYP1A1 Involving Generation of Potentially Toxic Metabolites. *Journal of Pharmacology and Experimental Therapeutics* **363**, 12-19
9. Li, X., Kamenecka, T. M., and Cameron, M. D. (2009) Bioactivation of the epidermal growth factor receptor inhibitor gefitinib: implications for pulmonary and hepatic toxicities. *Chemical research in toxicology* **22**, 1736-1742
10. Takahashi, R. H., Wang, X., Segraves, N. L., Wang, J., Chang, J. H., Khojasteh, S. C., and Ma, S. (2017) CYP1A1-Mediated Intramolecular Rearrangement of Aminoazepane in GDC-0339. *Drug Metab Dispos* **45**, 1084-1092
11. Omura, T., and Sato, R. (1964) The carbon monoxide-binding pigment of liver microsomes. I. Evidence for its hemoprotein nature. *The Journal of biological chemistry* **239**, 2370-2378
12. DeVore, N. M., Smith, B. D., Wang, J. L., Lushington, G. H., and Scott, E. E. (2009) Key residues controlling binding of diverse ligands to human cytochrome P450 2A enzymes. *Drug Metab Dispos* **37**, 1319-1327
13. Otwinowski, Z., and Minor, W. (1997) Processing of X-ray diffraction data collected in oscillation mode. *Methods Enzymol* **276**, 307-326
14. McCoy, A. J., Grosse-Kunstleve, R. W., Adams, P. D., Winn, M. D., Storoni, L. C., and Read, R. J. (2007) Phaser crystallographic software. *Journal of applied crystallography* **40**, 658-674
15. Emsley, P., Lohkamp, B., Scott, W. G., and Cowtan, K. (2010) Features and development of Coot. *Acta Crystallogr. D* **66**, 486-501
16. Adams, P. D., Afonine, P. V., Bunkoczi, G., Chen, V. B., Davis, I. W., Echols, N., Headd, J. J., Hung, L. W., Kapral, G. J., Grosse-Kunstleve, R. W., McCoy, A. J., Moriarty, N. W.,

Oeffner, R., Read, R. J., Richardson, D. C., Richardson, J. S., Terwilliger, T. C., and Zwart, P. H. (2010) PHENIX: a comprehensive Python-based system for macromolecular structure solution. *Acta Crystallogr. D* **66**, 213-221

17.   Moriarty, N. W., Grosse-Kunstleve, R. W., and Adams, P. D. (2009) electronic Ligand Builder and Optimization Workbench (eLBOW): a tool for ligand coordinate and restraint generation. *Acta Crystallogr. D* **65**, 1074-1080

18.   Kleywegt, G. J., and Jones, T. A. (1994) Detection, delineation, measurement and display of cavities in macromolecular structures. *Acta Crystallogr. D* **50**, 178-185

19.   DeLano, W. L. (2017) The PyMOL Molecular Graphics System. version 1.8.6.2 Ed., Schrodeinger, LLC, New York

20.   Sansen, S., Yano, J. K., Reynald, R. L., Schoch, G. A., Griffin, K. J., Stout, C. D., and Johnson, E. F. (2007) Adaptations for the oxidation of polycyclic aromatic hydrocarbons exhibited by the structure of human P450 1A2. *The Journal of biological chemistry* **282**, 14348-14355

21.   Wang, A., Savas, U., Stout, C. D., and Johnson, E. F. (2011) Structural characterization of the complex between alpha-naphthoflavone and human cytochrome P450 1B1. *The Journal of biological chemistry* **286**, 5736-5743

22.   Liu, J. W., Taylor, S. F., Dupart, P. S., Arnold, C. L., Sridhar, J., Jiang, Q., Wang, Y. J., Skripnikova, E. V., Zhao, M., and Foroozesh, M. (2013) Pyranoflavones: A Group of Small-Molecule Probes for Exploring the Active Site Cavities of Cytochrome P450 Enzymes 1A1, 1A2, and 1B1. *Journal of medicinal chemistry* **56**, 4082-4092

23.   Mast, N., Zheng, W., Stout, C. D., and Pikuleva, I. A. (2013) Binding of a cyano- and fluoro-containing drug bicalutamide to cytochrome P450 46A1: unusual features and spectral response. *The Journal of biological chemistry* **288**, 4613-4624

24.   Wang, X. J., Blackaby, W., Allen, V., Chang, G. K. Y., Chang, J. H., Chiang, P. C., Diene, C., Drummond, J., Do, S., Fan, E., Harstad, E. B., Hodges, A., Hu, H. Y., Jia, W., Kofie, W., Kolesnikov, A., Lyssikatos, J. P., Ly, J., Matteucci, M., Moffat, J. G., Munugalavadla, V., Murray, J., Nash, D., Noland, C. L., Del Rosario, G., Ross, L., Rouse, C., Sharpe, A., Slaga, D., Sun, M. H., Tsui, V., Wallweber, H., Yu, S. F., and Ebens, A. J. (2019) Optimization of Pan-Pim Kinase Activity and Oral Bioavailability Leading to Diaminopyrazole (GDC-0339) for the Treatment of Multiple Myeloma. *Journal of medicinal chemistry* **62**, 2140-2153

25.   Xu, D. H., Hu, J. S., De Bruyne, E., Menu, E., Schots, R., Vanderkerken, K., and Van Valckenborgh, E. (2012) Dll1/Notch activation contributes to bortezomib resistance by upregulating CYP1A1 in multiple myeloma. *Biochemical and biophysical research communications* **428**, 518-524

CHAPTER 5

Metabolism and Structural Interactions of Pro-Duocarmycins with Cytochrome P450 Enzymes 1A1 and 2W1[*]

5.1 Introduction

Human cytochrome P450 enzymes are perhaps most broadly recognized for their capacity to convert xenobiotics, including drugs, into metabolites that are more readily cleared from the body. However, in the process some foreign chemicals are activated to reactive intermediates or toxins that have significant adverse effects and/or initiate disease. One such example is the metabolism of a ring-opened form of nicotine by lung cytochrome P450 2A13 to a metabolite that forms DNA adducts and can thus initiate lung cancer in smokers (1). However, this attribute of cytochrome P450 enzymes to bioactivate foreign molecules can also be used advantageously to activate prodrugs *in vivo*. Cytochrome P450 enzymes activate a range of anticancer prodrugs including FDA-approved DNA-alkylating cyclophosphamide/ifosfamide and dacarbazine/procarbazine compounds, the thymidylate synthase inhibitor tegafur, the nonsteroidal antiandrogen flutamide, the selective estrogen receptor modulator tamoxifen, and the bioreductive topoisomerase II inhibitor AQ4N (reviewed in (2)).

The ultrapotent cytotoxic duocarmycin natural products also have significant anticancer potential, but the absence of selectivity for cancer cells absolutely prevents systemic use. A number of novel duocarmycin prodrugs, *seco*-duocarmycins, have been developed (3-5) that are

---

[*] The contents of this chapter are currently in preparation with collaborator Dr. Klaus Pors for journal submission.

bioactivated by two cytochrome P450 enzymes expressed in selected tissues: CYP1A1 and CYP2W1. CYP1A1 is an inducible, primarily extrahepatic enzyme present in lung, placenta, and endothelial cells of the skin, intestine, and bladder. Literature reports of CYP1A1 expression levels vary significantly between tissues and individuals (6,7). If endogenous CYP1A1 is present and tissue-specific, then it's ability to activate *seco*-duocarmycins might be useful. But if CYP1A1 normal vs. cancerous tissue levels are similar or endogenous levels are high in an individual or tissue, then selective duocarmycin bioactivation would be much reduced. On the other hand, CYP2W1 is selectively expressed in colon cancer tissues (8-13) where its ability to activate *seco*-duocarmycins could be a promising therapy for colorectal tumors. Additionally, mice harboring human colon cancer xenografts expressing CYP2W1 have shown significant tumor growth inhibition upon administration of a *seco*-duocarmycin, with no signs of host toxicity (4). This suggests that this approach holds promise for selective colon tumor targeting, without systemic toxicity if selectivity can be engineered for CYP2W1 over CYP1A1.

Both CYP1A1 and CYP2W1 bioactivate the *seco*-duocarmycin prodrug, ICT2700 by hydroxylation at a specific position on a chloromethyl indoline substructure at one end of the molecule (Figure 5.1, red circle) (3). The hydroxylated chloromethyl indoline then undergoes a spontaneous spirocyclization reaction such that the chlorine atom is released and a cyclopropyl ring forms on the indoline ring system (5). The indole at the opposite end of the molecule serves as a DNA-recognition motif and binds DNA in a sequence-selective manner, so that the unstable cyclopropane ring is appropriately located to form DNA adducts that are lethal to the cell. Thus, site-specific hydroxylation by CYP1A1 or CYP2W1 is essential for bioactivation of *seco*-duocarmycin compounds.
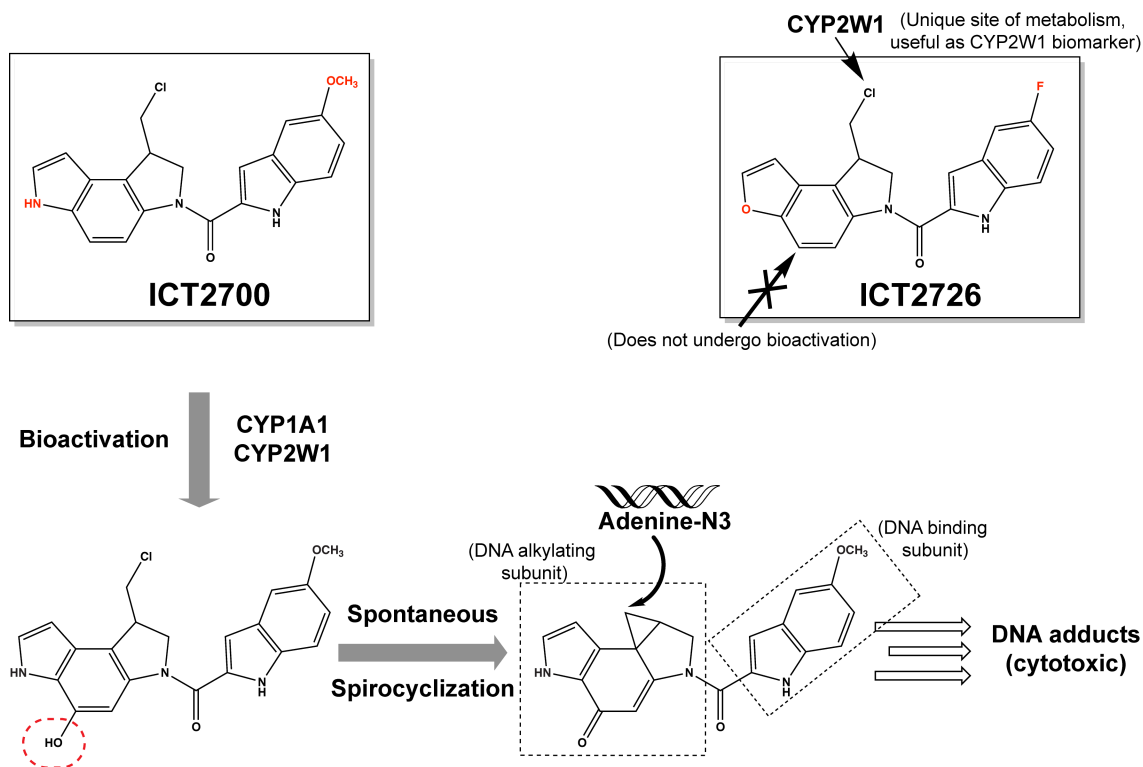
Figure 5.1 Duocarmycin analogs ICT2700 and ICT2726 (shown in boxes, differences colored in red). The ICT2700 analog has been reported to undergo bioactivation by CYP1A1 and CYP2W1 via a specific hydroxylation (red dotted oval) on the chloromethyl indoline substructure (4). Spontaneous spirocyclization occurs producing a reactive cyclopropane moiety. DNA adenine bases can be alkylated with this reactive group leading to cytotoxic DNA adducts. The ICT2726 analog does not undergo bioactivation. Instead this analog can serve as a biomarker for CYP2W1 activity because it forms a unique non-toxic metabolite specific to CYP2W1 (3).

The specificity of cytochrome P450 hydroxylation is highly dependent on ligand orientation in the active site with the desired site of metabolism adjacent to the heme iron. While no experimental structures are available for CYP2W1, there are several structures available for CYP1A1 with other ligands bound in the active site. The initial CYP1A1 structure was with α-naphthoflavone housed within a highly planar, slot-like enclosed active site (14). Recently several other structures of CYP1A1 have been solved with the furanocoumarin bergamottin from grapefruit juice and the tyrosine kinase inhibitor erlotinib (15) and significant portions of these molecules and their active sites are also planar. One half of ICT2700 and ICT2726 (Figure 5.1) consists of an indole core while the other half consists of another indole with a fused furan or pyrrole ring. These fused ring systems confer a high degree of planarity which would correspond

122

well to a highly planar and narrow CYP1A1 active site, but they are connected by a linker that does not constrain the two ring systems to the same plane. The chloromethyl arm of these duocarmycins deviates significantly from planarity. Depending on the overall orientation of these ligands in the CYP1A1 active site, this functional group could sterically clash with narrow portions of the active site. While flexibility has been observed in certain structural elements in CYP1A1, it is not clear how these ICT ligands would be accommodated or known if the *seco*-duocarmycin molecules would cause structural perturbations.

To optimize clinical utility, the *seco*-duocarmycin scaffold should be further modified for selective activation, preferably by CYP2W1, due to its exclusive expression in tumor tissue. Binding and activation by CYP1A1 should be reduced. Previous studies (3) suggested that functionalization of the *seco*-duocarmycin DNA-binding motif improved the selectivity for activation by CYP1A1 over CYP2W1, but structural changes favoring selective CYP2W1 activation are unknown. Additional engineering is needed to engender absolute selectivity for CYP2W1, but this has been impaired by the absence of information about how these CYP1A1 and CYP2W1 interact with current *seco*-duocarmycins. Thus, the goal of the current study was to characterize the interactions of synthetic *seco*-duocarmycins with CYP1A1 and CYP2W1. Of specific interest is determining how CYP1A1 and CYP2W1 bind the prodrug duocarmycin (ICT2700) and a biomarker version (ICT2726). This latter analog is selectively metabolized by CYP2W1 to produce a unique nontoxic metabolite that can be used to identify CYP2W1-expressing cells prior to treatment. The current work examined the binding of enantiomers of both ICT2700 and ICT2726 to CYP1A1 and CYP2W1, as well as determining structures of CYP1A1 with the *S*-enantiomers of each compound. This revealed key interactions that could be used to

design second generation *seco*-duocarmycins with improved selectivity for CYP2W1 activation *in vivo*.

5.2 Experimental Procedures

5.2.1 Isolation of Pro-duocarmycin Stereoisomers

The stereoisomers of the *seco*-duocarmycin analogs ICT-2700 and ICT-2726 were a gift from Klaus Pors.

5.2.2 Protein Expression and Purification

Human CYP1A1 and CYP2W1 enzymes were generated that had truncation of the N-terminal membrane-anchoring helix to increase solubility and addition of a C-terminal histidine tag to facilitate purification. The construct for CYP1A1 has been described (14). For CYP2W1, a synthetic codon-optimized gene was generated in which the resulting amino acid sequence was almost the same as the 2W1 #3 construct described by Wu *et al*. (16), in that residues 3-31 were replaced with KKTSSKGKL but the C-terminal histidine tag consisted of only four histidines instead of five.

Expression and purification of CYP1A1 was performed without modification as described (15). Expression of CYP2W1 was based on the method described for CYP1A1, with some modifications. Modifications included inoculation with 5 mL of starter culture per 1 L expression culture and growing in 2.8 L Fernbach flasks, a lower shaking speed of 225 rpm during cell growth and 200 rpm after induction, and addition of 5 mM imidazole to expression cultures to help stabilize CYP2W1. Purification of CYP2W1 was initially based on the CYP1A1 purification method, however substantial modifications were made, therefore for clarity a detailed protocol is provided below.

Purification of CYP2W1 began with thawing frozen expression cell pellets in a buffer consisting of 20 mM potassium phosphate, 20% (v/v) glycerol, 5 mM imidazole, 1 mM phenylmethanesulfonyl fluoride (PMSF), pH 7.4. Thawed and resuspended cells were lysed by French Press using a single pass with a pressure of 15,000 psi. The lysed cell suspension was then subjected to ultra-centrifugation for 30 minutes at 142,000 x g in order to isolate membranes. Pelleted membranes were gently washed twice with the buffer used in lysis, then resuspended by homogenization in an extraction buffer composed of 100 mM potassium phosphate, 500 mM NaCl, 20% (v/v) glycerol, 15 mM imidazole, 1% (w/v) CHAPS, and 1 mM PMSF, pH 7.4. Resuspended membranes were stirred for 1 hour to promote efficient protein extraction. The sample was then clarified by a second ultra-centrifugation using the above parameters. Clarified supernatant was loaded onto a 25 mL Ni-NTA column (Qiagen) equilibrated with the extraction buffer. To remove unbound and non-specifically bound proteins, the column was washed with four column volumes (CV) of extraction buffer, followed by 10 CV of a Ni-NTA wash buffer (100 mM potassium phosphate, 100 mM NaCl, 20% (v/v) glycerol, 15 mM imidazole, 9 mM CHAPS, pH 7.4). Elution of CYP2W1 was performed using a linear gradient from Ni-NTA wash buffer to Ni-NTA elution buffer (10 mM potassium phosphate, 100 mM NaCl, 20% (v/v) glycerol, 250 mM imidazole, 9 mM CHAPS, pH 7.4) over 6 CV, with addition of 2 CV of 100% Ni-NTA elution buffer to ensure complete elution. Ni-NTA fractions with $A_{426}/A_{280} > 0.8$ were pooled and diluted 5-fold with an ion-exchange wash buffer (10 mM potassium phosphate, 50 mM NaCl, 20% (v/v) glycerol, 1 mM EDTA, pH 7.4). Diluted sample was then applied to two 5-ml Hi-Trap carboxymethyl-Sepharose fast-flow columns (GE Healthcare) connected in series (total 10 ml column volume). This was first washed with 10 CV of ion-exchange wash buffer, then a 6 CV linear gradient was applied from ion-exchange wash buffer to an ion-exchange elution buffer (50 mM potassium phosphate,

500 mM NaCl, 20% (v/v) glycerol, 1 mM EDTA, pH 7.4) to elute the bound protein. An additional 2 CV of ion-exchange elution buffer was run through the column to ensure complete elution. Eluted fractions from the CM column with $A_{419}/A_{280} > 1.0$ were pooled together and concentrated to ~2 ml for application onto a Superdex 200 gel filtration column (GE Healthcare) that was run isocratically using the ion-exchange elution buffer. The major elution peak fractions with $A_{419}/A_{280} > 1.0$ were pooled, flash-frozen in aliquots, and stored at -80 °C.

The purified proteins were evaluated by SDS-PAGE to assess purity. The reduced carbon monoxide-difference assay served as a method to evaluate P450 stability (17). Quantification of both CYP1A1 and CYP2W1 for use in ligand binding assays and crystallography was performed by UV-vis spectroscopy, using the Soret peak extinction coefficient of 100 mM^{-1}cm^{-1}. This was accomplished in the final buffer for the respective proteins plus 250 mM imidazole.

5.2.3 Ligand Binding Assays

The affinities and binding modes of *seco*-duocarmycin compounds to CYP1A1 and CYP2W1 (1 µM) were measured in 2 cm tandem quartz cuvettes using the method previously described (15). Spectral binding data was determined in duplicate and fit to a quadratic equation used for tight binding (18).

5.2.4 Crystallization, Data Collection, and Structure Determination

CYP1A1 was co-crystallized with the *seco*-duocarmycin compounds (*S*)-ICT2700 and (*S*)-ICT2726 as described previously (15), with modifications listed below. Purified CYP1A1 was saturated with the respective *seco*-duocarmycin by three iterative dilution (in ion-exchange elution buffer with 0.4 M NH$_4$NO$_3$) and centrifugal ultrafiltration concentration steps. Ligand was added at 20 µM for (*S*)-ICT2726 or 100 µM for (*S*)-ICT2700 during each dilution. The CYP1A1/ICT samples were then concentrated to a final protein concentration of 20 mg/ml. Crystals of both

complexes were grown at 4 °C using the sitting-drop vapor diffusion method. For CYP1A1/(*S*)-ICT2700, crystals were grown in a 96-well plate mixing 0.75 μL CYP1A1 with 0.75 μL of crystallization solution (0.18 M sodium phosphate dibasic, 18% (w/v) PEG 3350, 9% (v/v) glycerol, 5 mM (S)-O-methyl-serine dodecylamide hydroxhloride) against a 50 μL reservoir of the same crystallization solution. Crystals of the CYP1A1/(*S*)-ICT2726 complex were grown in a 24-well plate by mixing 1 μL CYP1A1, 0.2 μL 18 mM n-decyl-β-D-maltoside, and 0.8 μL crystallization solution (0.2 M sodium phosphate dibasic, 20% (w/v) PEG 3350), equilibrated with a 100 μL reservoir of the same crystallization solution. Crystals were harvested by transferring into the respective crystallization solution containing 20% glycerol and flash cooled in liquid nitrogen. Diffraction data for the CYP1A1/(*S*)-ICT2700 crystal was collected on beamline 21-ID-G at the Advanced Photon Source LS-CAT, while data for CYP1A1/(*S*)-ICT2726 was collected on beamline 9-2 at the Stanford Synchrotron Radiation Lightsource.

Data processing for the CYP1A1/(*S*)-ICT2700 dataset was performed using HKL2000 (19), and a structure solution was obtained by molecular replacement via Phaser (20) with the CYP1A1/α-naphthoflavone structure as the search model (PDB 4I8V, molecule A), resulting in a log likelihood of 667 and translation function *Z* score of 27.3. For the CYP1A1/(*S*)-ICT2726 complex, data was processed in XDS (21) and scaled in AIMLESS (22). A molecular replacement solution for this structure was obtained from MolRep (23), again using chain A of the CYP1A1/α-naphthoflavone structure as the search model (contrast score of 30.59). Iterative model building and refinement of both structures were performed using COOT (24) and PHENIX (25), respectively. Ligand coordinates and restraints for the *seco*-duocarmycins were generated using PHENIX eLBOW (26) with AM1 geometry optimization. Data collection and refinement statistics are provided in Table 5.1. Crystal structure figures were prepared using PyMOL (27).

Table 5.1 Data collection and refinement statistics.

	CYP1A1/(*S*)-ICT2700 (6UDL)	CYP1A1/(*S*)-ICT2726 (6UDM)
Data Collection		
Space Group	$P2_12_12_1$	$P3_121$
Cell Dimensions (Å)	65.37, 196.15, 237.22	241.28, 241.28, 125.30
Molecules/a.u.	4	4
Resolution (Å)[a]	50.00-2.85 (2.90-2.85)	39.64-3.07 (3.14-3.07)
Total reflections[a]	510,182 (17,794)	783,762 (35,174)
Unique reflections[a]	72,081 (3,422)	77,258 (3,944)
Redundancy[a]	7.1 (5.2)	10.1 (8.9)
R_{pim}[a]	0.080 (0.942)	0.054 (0.631)
$<I/\sigma(I)>$ [a]	28.0 (2.1)	9.7 (1.6)
CC1/2[a]	0.990 (0.322)	0.997 (0.518)
Completeness (%)[a]	99.8 (97.3)	99.0 (85.6)
Refinement		
Resolution (Å)	48.80-2.85	39.64-3.10
No. reflections	71,709	76,831
R/R_{free} (%)	23.8 / 28.7	20.1 / 22.1
Ramachandran (%) Favored/Allowed/Outliers	96.19 / 3.81/ 0.00	97.15 / 2.85 / 0.00
No. non-H atoms/B factors ($Å^2$)		
Protein	15,015 / 68.60	15,026 / 80.62
Ligand	54 / 57.62	104 / 80.66
Heme	172 / 57.09	172 / 68.49
CHAPS	- / -	42 / 100.77
Water	1 / 49.31	- / -
RMSD bond (Å)	0.008	0.007
RMSD angle (°)	0.765	0.636
Coordinate error (max. likelihood based) (Å)	0.37	0.37

[a] Statistics for highest resolution shell shown in parentheses.

5.3 Results and Discussion

5.3.1   Seco-Duocarmycin Binding Modes and Affinities for Human CYP1A1 and CYP2W1

ICT2726 (Figure 5.1) was first evaluated for its ability to bind both CYP1A1 and CYP2W1. CYP2W1, but not CYP1A1, hydroxylates this compound on the chlorine atom and the resulting unique metabolite (4) can be used as a biomarker for the presence of CYP2W1 in tissues to identify those that might benefit from pro-duocarmycin activated *in situ* by CYP2W1. ICT2726 is a chiral compound and is produced as a mixture of the two stereoisomers at this position (3). While previous studies have used the racemic compound, in this study we were able to evaluate the individual stereoisomers for binding to both enzymes.

Binding of ligands in a cytochrome P450 active site can typically be monitored by observing shifts in the absorbance maximum of the heme Soret peak. Substrates typically shift the Soret peak to shorter wavelengths as they bind in the active site close enough to the heme iron that they displace water from its central iron and thereby shift the iron spin equilibrium from the six-coordinate, low-spin form toward the five-coordinate, high-spin form. This is typically observed in the form of UV-visible difference spectra, where such "Type I" binding is associated with decreases in absorbance at ~430 nm and increases at ~393 nm. These were exactly the changes observed when CYP1A1 was progressively titrated with both ICT2726 enantiomers (Figure 5.2A and 5.2B). Both (*S*)- and (*R*)-ICT2726 bound CYP1A1 with relatively high affinity, with K_d values of 0.23 ± 0.02 μM and 0.71 ± 0.05 μM (insets to Figure 5.2A and 5.2B), respectively. This suggests that both ICT2726 enantiomers bind in the active site such that they may be substrates for CYP1A1, producing other metabolites, but and not just the dechlorinated one.
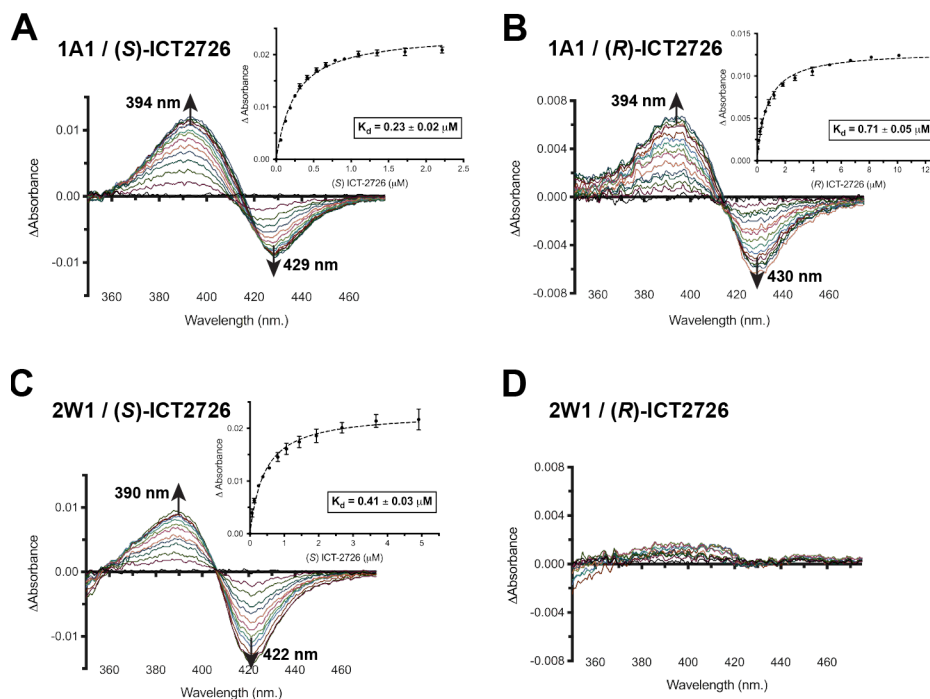
Figure 5.2 Spectral binding experiments of CYP1A1 and CYP2W1 with the *seco*-duocarmycin enantiomers of ICT2726. Representative difference binding spectra are shown of CYP1A1 (A & B) and CYP2W1 (C & D), with respective ICT2726 enantiomer. Inserts display the difference in peak-trough absorbance versus compound concentration and are fit by nonlinear regression to a tight-binding equation. The fitted compound affinities (K_d values) are reported with $\pm$ S.E. (error bars).

CYP2W1 also bound (*S*)-ICT2726 with classic Type I spectral changes (Figure 5.2C). The affinity of (*S*)-ICT2726 was also relatively high for CYP2W1, with a K_d of 0.41 ± 0.03 μM (Figure 5.2C, inset). However, (*R*)-ICT2726 addition to CYP2W1 did not result in significant spectral shifts in the difference spectra at concentrations as high as ~10 μM (Figure 5.2D). This result suggests that either the *R*-enantiomer does not bind CYP2W1 with significant affinity, or it binds but a different mode that does not perturb the water coordinated to the heme iron in the active site.

Similar titrations were used to evaluate CYP1A1 and CYP2W1 binding of the ICT2700 *seco*-duocarmycin which is bioactivated by both enzymes (Figure 5.1). ICT-2700 is also chiral at the carbon adjacent to the chloromethyl group, the region involved in formation of the cyclopropane ring essential for cytotoxic activity (Figure 5.1). ICT2700 is produced as a mixture of the two stereoisomers at this position (3,4) and previous studies have used this racemic form.

130

While the racemic form demonstrated potency in growth inhibition and cell death in CYP1A1 and CYP2W1 transfected cancer cells (3), it is unknown if differences in chirality of ICT2700 would confer bioactivation preference between the two enzymes.

Since ICT2700 is a validated substrate for both CYP1A1 and CYP2W1 enzymes, it was expected that the titrations might show similar Type I spectral shifts as observed for ICT2726 above. However, the binding modes observed with ICT2700 were markedly distinct. The dominant feature of CYP1A1 binding of both ICT2700 enantiomers were increases in absorbance eventually emerging at 412-415 nm with a smaller trough forming at 432-434 nm Figure 5.3A&B). Early in both titrations the peak is broader and for the *R*-enantiomer this is maintained through the titration yielding absorbance increases at 398 nm secondary to the primary maximum (Figure 5.3B). First, a broad peak shape is consistent with the presence of multiple binding modes for ICT2700 in the CYP1A1 active site, and there seems to be more binding heterogeneity for the *R*-enantiomer than for the *S*-enantiomer. Second, the primary maximum at ~412-415 nm suggests that ligand binding promotes oxygen interaction with the heme iron, rather than displacing the iron-coordinated water. It is possible that either ligand binding reinforces water coordination to the heme iron or that an oxygen of the ligand (e.g. the methoxy group) interacts with the heme iron. Third, the affinities for (*S*)- and (*R*)-ICT2700 for CYP1A1 were 1.9 ± 0.1 µM (Figure 5.3A, inset) and 1-2 µM (depending on the wavelength used, Figure 5.3B, inset), respectively. Thus (*S*)-ICT2726 has about an 8-fold higher affinity for CYP1A1 than (*S*)-ICT-2700, while the affinities for the *R*-enantiomers are similar.
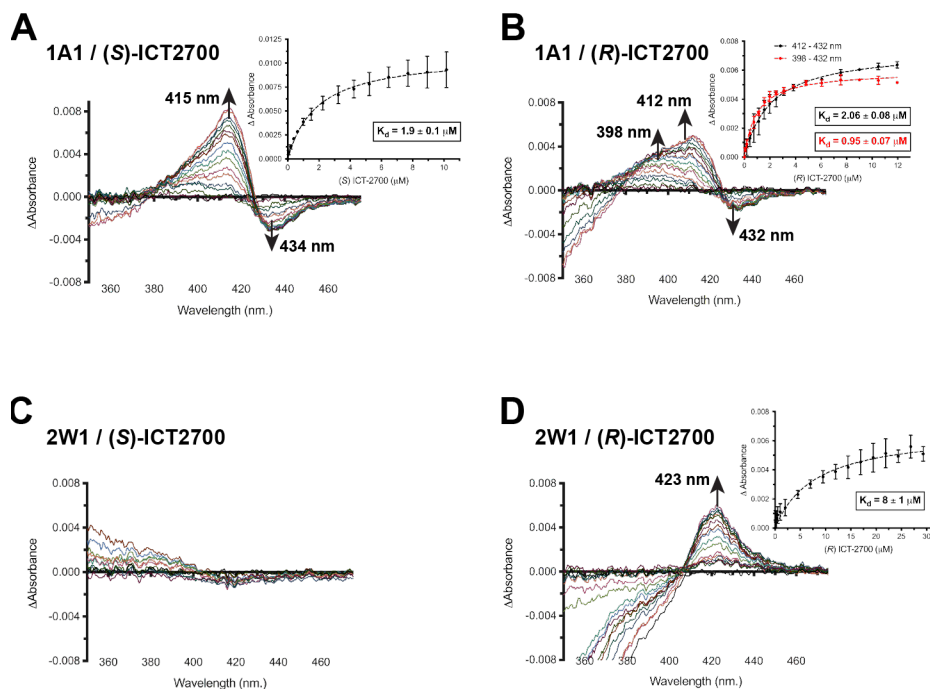
Figure 5.3 Spectral binding experiments of CYP1A1 and CYP2W1 with the *seco*-duocarmycin enantiomers of ICT2700. Difference binding spectra are shown of CYP1A1 (A & B) and CYP2W1 (C & D) binding the ICT2700 enantiomers. Inserts display the difference in peak-trough absorbance versus compound concentration, and are fit by nonlinear regression to a tight-binding equation. The fitted compound affinities (K_d values) are reported with ± S.E. (error bars).

Titrations of the ICT2700 enantiomers into CYP2W1 again revealed a distinct preference for one enantiomer. Addition of up to ~15 μM (*S*)-ICT2700 into 1 μM CYP2W1 had minimal effects on the spectra (Figure 5.3C). Again, this could indicate that either the *S*-enantiomer has weak or no affinity towards CYP2W1 or does not bind in the active site close enough to perturb the water on the heme iron. In contrast, the *R*-enantiomer produced a unique binding mode characterized primarily by a peak around 423 nm (Figure 5.3D). While there does not appear to be a clear corresponding decrease in absorbance, this could be partially obscured by changes in background absorbance caused by this compound itself in the UV range (350-380 nm). This red-shifting of the Soret peak position is consistent with spectral changes known to occur when a ligand nitrogen replaces the heme-coordinated water to coordinate itself to the heme iron. ICT2700 has two nitrogen-containing indole ring systems that are possibilities for direct iron coordination

132

(Figure 5.1), but the most likely position would be the indole on the alkylation arm as it is sterically less hindered. The affinity for this interaction is relatively weak, with a $K_d = 8 \pm 1$ μM (Figure 5.3D, inset). Since the N-Fe coordination appears to be weak, it is quite possible that this N-Fe feature helps to orient the molecule in the active site for bioactivation but also allows for the dissociation such that hydroxylation occurs at the adjacent C5 as required for bioactivation. Notably, replacement of this indole with a naphthyl moiety drastically reduced activation by CYP2W1 (and CYP1A1), which would be consistent with the nearby nitrogen directing the critical C5 towards the heme iron (3).

It is interesting that CYP2W1 appears to be distinctively affected by changes in the chirality of the chloromethyl moiety for both the ICT2700 and ICT2726 analogs. This demonstrates that distinctive structural features are present in the CYP2W1 active site that control the enantiomers in binding and/or positioning. In comparison to CYP1A1, spectral binding experiments indicate that chirality has some effects on binding affinity and possible binding modes in the CYP1A1 active site, but the effects are not as pronounced as observed with CYP2W1. Thus structures of both complexes are desirable to elucidate the key distinctive interactions.

5.3.2 Co-Crystal Structures of CYP1A1 with (*S*)-ICT2700 and (*S*)-ICT2726

Co-crystallization for both enantiomers of ICT2700 and ICT2726 were attempted for both CYP1A1 and CYP2W1 enzymes. No structures have been reported for CYP2W1 with any ligand and our efforts with ICT series compounds did not yield crystals. However, diffraction quality crystals were obtained for CYP1A1 with the (*S*)-ICT2700 and with (*S*)-ICT2726, yielding structures at 2.9 Å and 3.1 Å, respectively. The (*S*)-ICT2700 complex was solved in the orthorhombic $P2_12_12_1$ crystal form that other CYP1A1 structures have displayed, however the co-crystal structure with (*S*)-ICT2726 solved in a new crystal system, with a trigonal $P3_121$ space

133

group. Even with different symmetry, crystal contacts between molecules were shared and each structure contained four copies of the complex in the asymmetric unit. In both complexes the overall fold of CYP1A1 was as seen in previous solved structures of the enzyme (14,15). The one region of CYP1A1 that has varied conformations when different ligands are bound consists of helices F through G that form the roof of the active site (15). Both *seco*-duocarmycin complexes displayed a conformation of this region most similar to that reported when α-naphthoflavone is bound in an enclosed CYP1A1 active site (14). This includes a five-residue break in the F helix as it passes over the active site, a distinct feature which has now been observed in all CYP1A1 structures to date, as well as CYP1A2 and CYP1B1 crystal structures with α-naphthoflavone (28,29).

The (*S*)-ICT2726 ligand is present in all four CYP1A1 copies of the crystal structure and the binding mode appears to be consistent among them. The best fit to the observed electron density positions the 5-fluoroindole ring of (*S*)-ICT2726 above the heme (Figure 5.4A) with the closest carbon atoms of the six-membered ring each 4.3 Å from the iron (Figure 5.4A, red dashed lines). The fluorine projects towards a cluster of hydrophobic residues forming the bottom portion of the CYP1A1 active site. On the opposite half of the molecule the pyrrole ring pi-pi stacks with Phe224 in the F helix break. The linker between the two rings is co-planar with the two ring systems and packs against the Gly316 and Ala317 peptide bond of the I helix. These and other interactions constrain the molecule in an overall planar conformation. The only exception is the chloromethyl arm of the ligand, which is directed into the F helix break, and is in close contact (2.7 Å) to the side-chain oxygen of Asn222, which could potentially form a halogen-oxygen interaction (Figure 5.4A, yellow dashed line). Additionally, in some copies of the complex there

is evidence of placement of an active site water forming a hydrogen bond between the side chain of Ser-122 (B′/C loop) and the ligand's linker carbonyl oxygen.
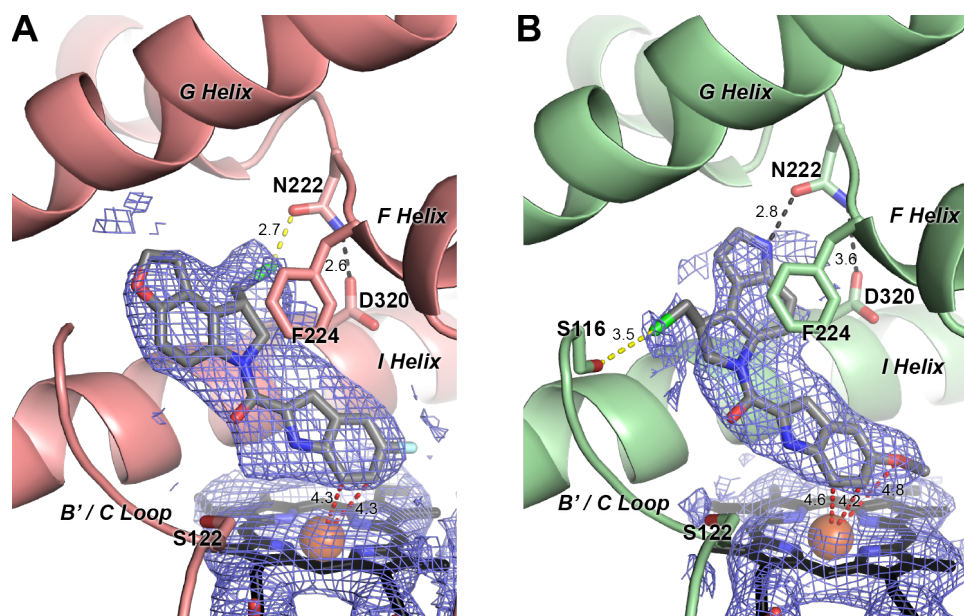
Figure 5.4 Co-crystallization structures of CYP1A1 (ribbons) bound to (A) (*S*)-ICT2726 and (B) (*S*)-ICT2700 (grey sticks). Electron density is shown as $2F_o − F_c$ composite omit map contoured at 1.0 σ (blue mesh) around the ligand and heme (black sticks with orange Fe sphere). Potential hydrogen bonds (black dashes), halogen bonds (yellow dashes), and ligand atoms in closest proximity to the heme iron (red dashes) are shown with their corresponding distances.

This binding mode is consistent with the observed binding spectra for (*S*)-ICT2726 with CYP1A1. The crystal structure reveals the fluoroindole ring in close proximity to the heme iron, which would likely displace the resting heme water, giving rise to the observed Type I shift. Although the overall binding pose might not be the same for the *R* enantiomer of ICT2726, if the primary scaffold occupies the same plane, then the approximately 3-fold lower affinity for this enantiomer and the structure suggests that the *R*-chloromethyl arm may sterically clash with Phe-224.

Overall, these interactions do not position (*S*)-ICT2726 in the CYP1A1 active site in an orientation primed for bioactivation and this is consistent with the observations that CYP1A1 does not yield the cytotoxic metabolite of the racemic version of this compound.

The second CYP1A1 structure was determined with (*S*)-ICT2700, which is bioactivated by both CYP1A1 and CYP2W1. This molecule could only be placed into the observed electron density in two of four CYP1A1 molecules in the asymmetric unit due to ligand disorder and/or low occupancy. In these two CYP1A1 molecules, the overall conformation of (*S*)-ICT2700 is planar and the orientation similar to (*S*)-ICT2726 (Figure 5.4B). The DNA recognition motif is above the heme and the DNA-alkylating motif oriented away from the heme, though its fused ring system and the chloromethyl substituent are reversed by 180° compared to (*S*)-ICT2700. This reorientation of the DNA-alkylating ring system directs the chloromethyl arm toward the B' helix and the fused pyrrole into the F helix break. This still permits stacking between Phe224 and the aromatic pyrroloindole system of ICT2700. The indole nitrogen of this portion of the ligand makes a hydrogen bond interaction with the oxygen of Asn222 (2.8 Å). As in ICT2726, the chlorine of the chloromethyl substituent also makes a potential halogen-oxygen interaction, but in this case it is a longer interaction with the oxygen of Ser116 in the B' helix (3.5 Å, Figure 5.4B, yellow dashed line). In one molecule electron density suggested water-mediated hydrogen bonding interactions between Ser122, and the ligand linker carbonyl oxygen and nitrogen of the methoxy-indole ring similar to the CYP1A1/(*S*)-ICT2726 complex.

One of the differences between ICT2700 and ICT2726 is the substitution of a methoxy group on the DNA-recognition motif of ICT2700 vs. a fluorine substituent at this position for ICT2726. The positioning of these two groups is quite similar in a hydrophobic pocket over the heme, but the oxygen in ICT2700 is only 4.8 Å from the iron and may directly interact with the iron in solution or upon a small shift of the ligand. This would be consistent with the spectral binding information, which indicates that (*S*)-ICT2700 binds in such a way as to reinforce an oxygen-Fe interaction, but (*S*)-ICT2726 does not.

Although (*S*)-ICT2700 is bioactivated by CYP1A1 into a reactive metabolite through hydroxylation on a specific aryl-carbon on the chloromethylpyrroloindoline (Figure 5.1), the orientation of this ligand in the CYP1A1 active site places the oxidized carbon >9 Å away from the heme iron. There are two possible explanations for this. First, the orientation observed in the crystal structure may be the dominant binding pose, with a minor pose being responsible for bioactivation. This would be consistent with the reported observation that the activated species undergoing spirocyclization is a minor product rather than the major product (5). The overall ICT2700 scaffold is relatively symmetrical and flipping the compound by 180° would locate the requisite carbon near the iron. A second possibility is that in CYP1A1 it is the *R*-enantiomer of ICT2700 that is bioactivated. The spectral binding studies support at least two binding modes for this enantiomer.

5.3.3 Comparisons and Applications of CYP1A1/CYP2W1 Interactions with Seco-duocarmycins

Design of *seco*-duocarmycin prodrugs for selective *in situ* bioactivation by CYP1A1 could be of potential clinical utility in tissues such as the lung and bladder where the enzyme can be expressed at higher levels, however this enzyme is also expressed at low levels in other tissues. Thus, maintaining a low level of *seco*-duocarmycin activation may be advantageous and promoting a dominant binding mode where the alkylating domain is distant from the heme may be desirable. Such an application would not be complicated by CYP2W1 activation because this P450 is not normally expressed in adult tissues. Using CYP2W1 exclusive expression in colon cancer cells to activate *seco*-duocarmycins would require more selective compounds with minimal or no activation by CYP1A1. While there are no structures of CYP2W1 with duocarmycins or any other ligands, the binding information herein suggests differences between the two active sites that could

137

potentially be exploited. First, only CYP2W1 forms the unique ICT2726 metabolite with hydroxylation of the chloromethyl substituent, suggesting that steric restraints may differ between the two active sites such that this substituent is not located near the heme for CYP1A1. Second, while the enantiomers of both ICT compounds bound to CYP1A1, CYP2W1 appeared to display a strict preference for only one stereoisomer: *S* for ICT2726 and *R* for ICT2700. This could suggest that the CYP2W1 active site might be less flexible than that of CYP1A1. This enantiomeric preference could therefore be potentially useful in the design of advanced *seco*-duocarmycin prodrugs.

Although little is known about the substrate scope of CYP2W1, there are a number of reports suggesting a partially overlapping substrate profile with CYP1A1. In addition to the engineered *seco*-duocarmycins, CYP1A1 and CYP2W1 both metabolize substrates such as the benzothiazole anticancer compounds 5F 203 and GW 610 (30), AQ4N (31,32), all-trans-retinoic acid (33,34), and the polycyclic aromatic hydrocarbon benzo[a]pyrene (16). This indicates that shared elements in active-site topology are present between the two enzymes. CYP2W1 is still classified as an orphan enzyme with no clear defined metabolic role. Based on sequence identity, CYP2W1 groups largely with the xenobiotic-metabolizing P450 enzymes, with CYP2D6 sharing the highest identity (12). Of the six substrate recognition sites (SRS), there does seem to be relatively high identity between CYP2W1 and CYP1A1 in SRS-1 (corresponding to the B' helix region). In other SRS regions the identity is not as high, which may contribute to differences observed in the binding of the *seco*-duocarmycins. Despite the unclear role of CYP2W1 in normal human physiology or predominate substrate class, its tumor localization and ability to bioactivate *seco*-duocarmycin prodrugs, makes CYP2W1 an attractive enzyme for selective cancer

therapeutics.   The apparent selectivity of CYP2W1 (*R*)-ICT2700 serves as a potentially useful

scaffold for the design of advanced compounds.

5.4 References

1.   Zhang, X., D'Agostino, J., Wu, H., Zhang, Q. Y., von Weymarn, L., Murphy, S. E., and Ding, X. (2007) CYP2A13: variable expression and role in human lung microsomal metabolic activation of the tobacco-specific carcinogen 4-(methylnitrosamino)-1-(3-pyridyl)-1-butanone. *The Journal of pharmacology and experimental therapeutics* **323**, 570-578

2.   Ortiz de Montellano, P. R. (2013) Cytochrome P450-activated prodrugs. *Future Med Chem* **5**, 213-228

3.   Sheldrake, H. M., Travica, S., Johansson, I., Loadman, P. M., Sutherland, M., Elsalem, L., Illingworth, N., Cresswell, A. J., Reuillon, T., Shnyder, S. D., Mkrtchian, S., Searcey, M., Ingelman-Sundberg, M., Patterson, L. H., and Pors, K. (2013) Re-engineering of the duocarmycin structural architecture enables bioprecursor development targeting CYP1A1 and CYP2W1 for biological activity. *Journal of medicinal chemistry* **56**, 6273-6277

4.   Travica, S., Pors, K., Loadman, P. M., Shnyder, S. D., Johansson, I., Alandas, M. N., Sheldrake, H. M., Mkrtchian, S., Patterson, L. H., and Ingelman-Sundberg, M. (2013) Colon cancer-specific cytochrome P450 2W1 converts duocarmycin analogues into potent tumor cytotoxins. *Clinical cancer research : an official journal of the American Association for Cancer Research* **19**, 2952-2961

5.   Pors, K., Loadman, P. M., Shnyder, S. D., Sutherland, M., Sheldrake, H. M., Guino, M., Kiakos, K., Hartley, J. A., Searcey, M., and Patterson, L. H. (2011) Modification of the duocarmycin pharmacophore enables CYP1A1 targeting for biological activity. *Chemical communications* **47**, 12062-12064

6.   Shimada, T., Yun, C. H., Yamazaki, H., Gautier, J. C., Beaune, P. H., and Guengerich, F. P. (1992) Characterization of human lung microsomal cytochrome P-450 1A1 and its role in the oxidation of chemical carcinogens. *Molecular pharmacology* **41**, 856-864

7.   Lang, D., Radtke, M., and Bairlein, M. (2019) Highly Variable Expression of CYP1A1 in Human Liver and Impact on Pharmacokinetics of Riociguat and Granisetron in Humans. *Chemical research in toxicology* **32**, 1115-1122

8.   Edler, D., Stenstedt, K., Ohrling, K., Hallstrom, M., Karlgren, M., Ingelman-Sundberg, M., and Ragnhammar, P. (2009) The expression of the novel CYP2W1 enzyme is an independent prognostic factor in colorectal cancer - a pilot study. *European journal of cancer* **45**, 705-712

9.   Gomez, A., Karlgren, M., Edler, D., Bernal, M. L., Mkrtchian, S., and Ingelman-Sundberg, M. (2007) Expression of CYP2W1 in colon tumors: regulation by gene methylation. *Pharmacogenomics* **8**, 1315-1325

10.   Gomez, A., Nekvindova, J., Travica, S., Lee, M. Y., Johansson, I., Edler, D., Mkrtchian, S., and Ingelman-Sundberg, M. (2010) Colorectal cancer-specific cytochrome P450 2W1: intracellular localization, glycosylation, and catalytic activity. *Molecular pharmacology* **78**, 1004-1011

11.   Karlgren, M., Gomez, A., Stark, K., Svard, J., Rodriguez-Antona, C., Oliw, E., Bernal, M. L., Ramon y Cajal, S., Johansson, I., and Ingelman-Sundberg, M. (2006) Tumor-specific expression of the novel cytochrome P450 enzyme, CYP2W1. *Biochemical and biophysical research communications* **341**, 451-458

12.   Karlgren, M., and Ingelman-Sundberg, M. (2007) Tumour-specific expression of CYP2W1: Its potential as a drug target in cancer therapy. *Expert Opin Ther Tar* **11**, 61-67

13. Stenstedt, K., Hallstrom, M., Ledel, F., Ragnhammar, P., Ingelman-Sundberg, M., Johansson, I., and Edler, D. (2014) The expression of CYP2W1 in colorectal primary tumors, corresponding lymph node metastases and liver metastases. *Acta oncologica*

14. Walsh, A. A., Szklarz, G. D., and Scott, E. E. (2013) Human cytochrome P450 1A1 structure and utility in understanding drug and xenobiotic metabolism. *The Journal of biological chemistry* **288**, 12932-12943

15. Bart, A. G., and Scott, E. E. (2018) Structures of human cytochrome P450 1A1 with bergamottin and erlotinib reveal active-site modifications for binding of diverse ligands. *The Journal of biological chemistry* **293**, 19201-19210

16. Wu, Z. L., Sohl, C. D., Shimada, T., and Guengerich, F. P. (2006) Recombinant enzymes overexpressed in bacteria show broad catalytic specificity of human cytochrome P450 2W1 and limited activity of human cytochrome P450 2S1. *Molecular pharmacology* **69**, 2007-2014

17. Omura, T., and Sato, R. (1964) The carbon monoxide-binding pigment of liver microsomes. I. Evidence for its hemoprotein nature. *The Journal of biological chemistry* **239**, 2370-2378

18. DeVore, N. M., Smith, B. D., Wang, J. L., Lushington, G. H., and Scott, E. E. (2009) Key residues controlling binding of diverse ligands to human cytochrome P450 2A enzymes. *Drug Metab Dispos* **37**, 1319-1327

19. Otwinowski, Z., and Minor, W. (1997) Processing of X-ray diffraction data collected in oscillation mode. *Methods Enzymol* **276**, 307-326

20. McCoy, A. J., Grosse-Kunstleve, R. W., Adams, P. D., Winn, M. D., Storoni, L. C., and Read, R. J. (2007) Phaser crystallographic software. *Journal of applied crystallography* **40**, 658-674

21. Kabsch, W. (2010) XDS. *Acta Crystallogr. D* **66**, 125-132

22. Evans, P. R., and Murshudov, G. N. (2013) How good are my data and what is the resolution? *Acta Crystallogr. D* **69**, 1204-1214

23. Vagin, A., and Teplyakov, A. (1997) MOLREP: an automated program for molecular replacement. *J. Appl. Cryst.* **30**, 1022-1025

24. Emsley, P., Lohkamp, B., Scott, W. G., and Cowtan, K. (2010) Features and development of Coot. *Acta Crystallogr. D* **66**, 486-501

25. Adams, P. D., Afonine, P. V., Bunkoczi, G., Chen, V. B., Davis, I. W., Echols, N., Headd, J. J., Hung, L. W., Kapral, G. J., Grosse-Kunstleve, R. W., McCoy, A. J., Moriarty, N. W., Oeffner, R., Read, R. J., Richardson, D. C., Richardson, J. S., Terwilliger, T. C., and Zwart, P. H. (2010) PHENIX: a comprehensive Python-based system for macromolecular structure solution. *Acta Crystallogr. D* **66**, 213-221

26. Moriarty, N. W., Grosse-Kunstleve, R. W., and Adams, P. D. (2009) electronic Ligand Builder and Optimization Workbench (eLBOW): a tool for ligand coordinate and restraint generation. *Acta Crystallogr. D* **65**, 1074-1080

27. Schrodinger, L. The PyMOL Molecular Graphics System, Version 1.8.6.2.

28. Sansen, S., Yano, J. K., Reynald, R. L., Schoch, G. A., Griffin, K. J., Stout, C. D., and Johnson, E. F. (2007) Adaptations for the oxidation of polycyclic aromatic hydrocarbons exhibited by the structure of human P450 1A2. *The Journal of biological chemistry* **282**, 14348-14355

29.   Wang, A., Savas, U., Stout, C. D., and Johnson, E. F. (2011) Structural characterization of the complex between alpha-naphthoflavone and human cytochrome P450 1B1. *The Journal of biological chemistry* **286**, 5736-5743

30.   Wang, K., and Guengerich, F. P. (2012) Bioactivation of Fluorinated 2-Aryl-benzothiazole Antitumor Molecules by Human Cytochrome P450s 1A1 and 2W1 and Deactivation by Cytochrome P450 2S1. *Chemical research in toxicology* **25**, 1740-1751

31.   Yakkundi, A., McErlane, V., Murray, M., McCarthy, H. O., Ward, C., Hughes, C. M., Patterson, L. H., Hirst, D. G., McKeown, S. R., and Robson, T. (2006) Tumor-selective drug activation: a GDEPT approach utilizing cytochrome P450 1A1 and AQ4N. *Cancer Gene Ther* **13**, 598-605

32.   Nishida, C. R., Lee, M., and de Montellano, P. R. O. (2010) Efficient Hypoxic Activation of the Anticancer Agent AQ4N by CYP2S1 and CYP2W1. *Molecular pharmacology* **78**, 497-502

33.   Zhao, Y., Wan, D., Yang, J., Hammock, B. D., and Ortiz De Montellano, P. R. (2016) Catalytic Activities of Tumor-Specific Human Cytochrome P450 CYP2W1 Towards Endogenous Substrates. *Drug Metab Dispos*

34.   Marill, J., Cresteil, T., Lanotte, M., and Chabot, G. G. (2000) Identification of human cytochrome P450s involved in the formation of all-trans-retinoic acid principal metabolites. *Molecular pharmacology* **58**, 1341-1348

CHAPTER 6

Structure of an Ancestral Mammalian Family 1B1 Cytochrome P450 with Increased Thermostability[*]

6.1 Summary

Mammalian cytochrome P450 enzymes often metabolize many pharmaceuticals and other xenobiotics, a feature which is valuable in a biotechnology setting, but they are typically relatively unstable with T_{50} values ~ 30 - 40 ºC. Reconstructed ancestral cytochrome P450 enzymes tend to have variable substrate selectivity compared to related extant forms but also higher thermostability and may be an excellent approach for commercial biosynthesis of important intermediates, final drug molecules, or drug metabolites. The mammalian ancestor of the cytochrome P450 1B subfamily was herein characterized structurally and functionally, revealing differences from the extant human CYP1B1 in ligand binding, metabolism, and potential contributors to its thermostability. While human CYP1B1 has one copy of α-naphthoflavone in a closed active site, subtle amino acid substitutions outside the active site yielded an open active site with four ligand copies in the ancestor CYP1B1. A structure of the ancestor with 17β-estradiol revealed only one copy in the active site, which still had the same open conformation. Detailed comparisons between the extant and ancestor forms reveal increases in electrostatic and aromatic interactions between distinct secondary structure elements that may contribute to thermostability.

---

[*] The contents of this chapter are currently in revision: Bart, A.G., Harris, K.L., Gillam, E.M.J., & Scott, E. E. Structure of an Ancestral Mammalian Family 1B1 Cytochrome P450 with Increased Thermostability. *Journal of Biological Chemistry*.

6.2 Introduction

Cytochrome P450 enzymes are a diverse superfamily of hemoproteins, which carry out a wide variety of important physiological functions in organisms ranging from bacteria to higher animals and plants. In humans, the cytochrome P450 1 (CYP1) family consists of three genes (CYP1A1, CYP1A2 and CYP1B1). The corresponding proteins each metabolize a broad but overlapping set of endogenous and environmental chemicals including steroids, pharmaceutical compounds, and dietary pro-carcinogens. CYP1 gene expression is regulated by the aryl hydrocarbon receptor, a transcriptional regulator with roles in both development and the response to exposure to environmental toxins such as dioxins and polycyclic aromatic hydrocarbons. Many CYP1 substrates are aryl hydrocarbon receptor agonists, inducing the upregulation of CYP1 gene expression and thereby their own clearance (reviewed in (1-3)).

CYP1B1, the most recently identified of the human forms, metabolizes a wide range of compounds including xenobiotics, such as 7-ethoxyresorufin, caffeine, and theophylline (4), as well as endobiotics including testosterone, estradiol, retinol, arachidonic acid, and melatonin (4-9). CYP1B1 is expressed in numerous extrahepatic tissues including eye, brain, kidney, and breast (reviewed in (10)) and is overexpressed in various cancer cell types (11,12). This distribution is of interest given the ability of CYP1B1 to bioactivate environmental carcinogens, including polycyclic aromatic hydrocarbons and estradiol, to DNA-reactive products (13-15). CYP1B1 is essential for the immune response in mice (16,17) and CYP1B1 polymorphisms have been associated with congenital glaucoma (18,19), hinting at an important but as yet unidentified physiological role.

The physiological relevance of CYP1B1 is also reflected in its relatively high degree of conservation in vertebrates, compared to the CYP1A subfamily forms. The CYP1A and CYP1B

144

lineages were created by a gene duplication event which took place in early deuterosomes, resulting in the CYP1A/CYP1D and CYP1B/CYP1C clades. The CYP1C and CYP1D subfamilies diverged from the CYP1B and CYP1A lineages respectively after a second duplication event in fish (20-22). CYP1C forms are present in amphibia, fish, reptiles, and some avian species (20) whereas CYP1D forms are present in fish, amphibia, reptiles, and some mammals but are pseudogenes in humans (23).

Little is known about the historical function of the CYP1B/CYP1C clade aside from what has been gleaned from observing the activities of modern-day forms. In an effort to explore the evolution of the CYP1 forms, we recently reconstructed a series of CYP1 ancestors from key nodes of the evolutionary tree (24). In line with studies on other ancestral P450s, many of the CYP1 ancestors showed increased thermal tolerance compared to extant CYP1 human enzymes. N98_CYP1B1_Mammal, the predicted ancestor of mammalian CYP1B1 forms, was closest to the extant human mammalian CYP1B1 forms, sharing 81.8% sequence identity to human CYP1B1, yet had a $^{60}T_{50}$ (the temperature at which 50% of the protein remains folded after heating for 60 minutes) of 43 ºC, which is six degrees higher than that of extant human CYP1B1 (24). While P450 enzymes are of interest for use in biotechnology, the extant forms are not stable enough for such applications, but engineered forms with increased thermostability are more likely candidates.

The N98_CYP1B1_Mammal ancestor also showed intriguing differences in the metabolism of representative substrates compared to the extant human CYP1B1 enzyme. For example, human CYP1B1 predominantly metabolizes estradiol to 4-hydroxyestradiol (25). However, while both N98_CYP1B1_Mammal and an older common ancestor of all CYP1B forms (N20_CYP1B) were less active than human CYP1B1, they produced both 4- and 2-hydroxyestradiol in similar amounts. However, these ancestors both showed slightly *greater*

activity than human CYP1B1 towards testosterone. Both human CYP1B1 and the two ancestors produced similar, small amounts of 6β-hydroxytestosterone and 16α-hydroxytestosterone, plus trace quantities of two unidentified metabolites (8) 24). Thus, the reconstructed ancestors vary in both thermostability and metabolic capabilities, both important characteristics to understand for biotechnology applications (24).

To initiate an analysis of how CYP1 ancestral sequences have resulted in increased thermostability and varied substrate metabolism, structures of several ancestral forms are being pursued. Crystals of the N98_CYP1B1_Mammal ancestor were successfully produced with either estradiol or the polycyclic aromatic compound α-naphthoflavone, diffracting to limiting resolutions of 3.1 and 2.95 Å, respectively (Table 6.1). The structure of this ancestral CYP1B1 with the small, planar α-naphthoflavone permits comparison with structures of all three extant human CYP1B1, CYP1A1, and CYP1A2 enzymes generated with this same ligand (PDB 3PM0 (26), 4I8V (27), and 2HI4 (28), respectively). This is particularly useful because many cytochrome P450 enzymes from families 1-3 demonstrate substantial reconfiguration of the active site dimensions with different active site ligands. To evaluate the ligand-specific effects on N98_CYP1B1_Mammal conformation, a structure with the endogenous steroid estradiol was subsequently solved. Both represent the first reported ancestral cytochrome P450 structures and suggest structural features that may modulate catalytic activity and thermostability.

6.3 Experimental Procedures

6.3.1 Materials

pCW plasmids containing CYP1B1, N98_CYP1B1_Mammal and human NADPH-cytochrome P450 reductase (hCPR) were constructed in previous studies (7,24,26). Catalytic assays with human CYP1B1 used construct #3 from (7). All binding, catalytic assays and

crystallography for the ancestral CYP1B1 were done with the N-terminally truncated, C-terminally His-tagged version of N98_CYP1B1_Mammal (24), with the sequence shown in Figure 6.1. The chaperone co-expression plasmid, pGro7, was obtained from Prof. K. Nishihara (HSP Research Institute, Kyoto, Japan) (29) and from Takara Bio Inc. DH5αF'IQ *E. coli* cells were purchased from ThermoFisher Scientific (Scoresby, Australia).

Bactotryptone, bactopeptone and yeast extract were supplied by Becton Dickinson Pty Ltd (North Ryde, Australia). 17β-Estradiol metabolites were purchased from Steraloids Inc. (Newport, MI, USA) and kindly made available for this work by Prof. F. P. Guengerich, Vanderbilt University, USA. Emulgen 913 and 911 were obtained from Kao Chemicals (Tokyo, Japan). All other materials including α-naphthoflavone and 17β-estradiol were purchased at the highest available grade from Sigma-Aldrich-Merck (Castle Hill, Australia) where possible, or from a local supplier.

6.3.2 Preparation of Bacterial Membranes for Activity Assays

P450s and hCPR were expressed in *Escherichia coli* and isolated in bacterial membranes as previously described (30,31). P450 content was quantified by Fe(II).CO *vs*. Fe(II) difference spectroscopy (32,33). CPR was quantified by the reduction of the surrogate electron acceptor, cytochrome *c*, as previously described (34).

6.3.3 Metabolic Assays

Metabolic incubations were carried out as previously described with modifications (35). Bacterial membranes containing 0.5 μM P450 were incubated for 60 minutes at 37 °C in 100 mM potassium phosphate pH 7.4 with 25 μM α-naphthoflavone in the presence and absence of an NADPH generating system (100 mM glucose-6-phosphate, 250 μM NADP+ and 0.5 U/ml

glucose-6-phosphate dehydrogenase). Progesterone (5 µM) was added as internal standard for α-naphthoflavone assays, prior to quenching and extraction with 1 ml ethyl acetate.

α-Naphthoflavone and its metabolites were identified using a Shimadzu Nexera Ultraperformance LC system coupled to an Orbitrap Elite mass spectrometer. Chromatography was performed on an Accucore™ C30 column (150 x 2.1 mm, 2.6 um) at 0.4 ml per minute at 50°C. Buffer A comprised 1% acetonitrile, 0.1% formic acid and buffer B comprised 90% acetonitrile, 0.1% formic acid. The gradient was developed as follows: 0-0.5 mins 50% B, 0.5-3 mins linear gradient to 98% B, 3-4.5 mins 98% B, 4.5-4.6 mins linear gradient to 50% B, 4.6-5 mins 50% B. The mass spectrometer was operated in positive mode. Source parameters included S lens 60; ion spray voltage 4.5 kV; capillary temperature 380° C; heater 400° C; sheath gas and auxiliary gases 50 and 16 respectively. Data dependent acquisition was performed across 50 – 1500 m/z and the top 5 precursors selected. HCD fragmentation was optimized to use a normalized collision energy (NCE) of 60. Data was processed using Xcalibur™ software. Spectra were searched against publicly available databases. α-Naphthoflavone metabolites were quantified using UPLC-APCI-MRM with the same chromatography conditions, but with a SCIEX 5500 QTRAP mass spectrometer operating in positive multiple reaction monitoring (MRM) mode. Source parameters included: a nebulizer current of 3 µA; temperature at 500 °C; nebulizing gas (GS1) at 45; declustering potential (DP) at 120; and collision cell exit potential (CXP) of 12. For each compound the collision energy (CE), entrance potential (EP) and CXP were optimized for maximum sensitivity by manual infusion. Data was processed using both Analyst™ 1.7 and Multiquant™ 3.0 (SCIEX) software. MRM transitions used for detection are listed in Table 6.4 and the recovery of α-naphthoflavone and its metabolites were estimated based on the relative intensity of MS/MS fragment 103.

6.3.4 Protein Expression and Purification for Ligand Binding Assays and Crystallization

Expression and purification of the N98_CYP1B1_Mammal for crystallization were based on methods used for expression of human CYP1A1 for crystallography (36), but modified extensively so a detailed expression protocol is described below for clarity. The expression plasmid pCW_N98_1B1_Mammal was transformed into *E. coli* DH5α chemically competent cells already containing the plasmid pGro7 for coexpression of the molecular chaperones GroEl/GroES. Transformed cells were plated on lysogeny broth (LB)-agar supplemented with 100 μg/ml carbenicillin for selection of the P450 plasmid, and 20 μg/ml chloramphenicol for selection of the pGro7 plasmid and grown for ~18 hours at 37 °C. A single colony from this plate was inoculated into a 5 ml LB starter culture, supplemented with antibiotics described above and grown for ~7 hours at 37 °C and shaking at 250 rpm. This starter culture (50 μl) was then used to inoculate a 200 ml LB culture, supplemented with the above antibiotics, grown for ~16 hours at 37 °C with shaking at 250 rpm. Finally, this overnight culture (10 ml) was used to inoculate 250 ml cultures of Terrific Broth in 1 liter Erlenmeyer flasks containing the above antibiotics. The culture volume grown for a single purification typically totaled 2 liters or 8 flasks. These expression cultures were grown at 37 °C with 250 rpm shaking until they reached an optical density at 600 nm (O.D.$_{600}$) of 0.3. At this point chaperone expression was induced by addition of 2 mg/ml arabinose and δ-aminolevulinic acid was added to 1 mM as a heme precursor. The temperature and shaking of the cultures were then reduced to 25 °C and 225 rpm respectively. At O.D.$_{600}$ of 0.6, N98_CYP1B1_Mammal expression was induced by adding 1 mM IPTG. Cultures were grown for 48 hours after induction.

Isolation of ancestral N98_CYP1B1_Mammal was performed using a purification method that was developed for human CYP1A1 engineered for crystallization as described (36) with only

slight changes. Modifications included depletion of the detergent CHAPS during ion-exchange chromatography by using a carboxymethyl (CM) Sepharose wash buffer (10 mM potassium phosphate, 100 mM NaCl, 20% (v/v) glycerol, 1 mM EDTA, pH 7.4) for the wash step and CM elution buffer (50 mM potassium phosphate, 500 mM NaCl, 20% (v/v) glycerol, 1 mM EDTA, pH 7.4) to elute the bound protein. Additionally, the final protein buffer used during gel filtration was a lower ionic size exclusion chromatography (SEC) buffer (20 mM potassium phosphate, 20% glycerol, 0.1 M NaCl, pH 7.4). Under these conditions, the main N98_CYP1B1_Mammal peak eluted from the size exclusion column as a trimer, with a shoulder corresponding to a dimeric species. The major trimeric peak was pooled and used in ligand binding and crystallization experiments. The final purity of the protein was assessed by SDS-PAGE and the ratio of the Soret peak to the 280 nm peak. The protein appeared to be a single band on the SDS-PAGE gel and typically had $A_{416\,nm}/A_{280\,nm} = 1.2$. The protein concentration was determined using the absorbance of the Soret band and an extinction coefficient of 100 mM^{-1}cm^{-1} in the SEC buffer listed above. Finally, a reduced carbon monoxide-difference spectrum (33) revealed a peak exclusively at 450 nm, consistent with active enzyme, and no peak or shoulder at 420 nm.

6.3.5   Ligand Binding Assays

α-Naphthoflavone and 17β-estradiol binding to N98_CYP1B1_Mammal were monitored spectrophotometrically. Initial titrations in the absolute spectrum mode employed 1 μM P450 in SEC buffer in 1 cm quartz cuvettes, with additions of ligand dissolved in DMSO being added to the sample cuvette and equal volumes of ligand added to the reference cuvette only containing SEC buffer. Subsequent titrations accomplished in difference mode to focus on ligand-induced changes used 1 μM protein in 2 cm tandem quartz cuvettes and were performed as described previously (36).

6.3.6 Crystallization, Data Collection, Structure Determination, and Analysis

Purified N98_CYP1B1_Mammal was first saturated with either α-naphthoflavone or 17β-estradiol by addition of 100 μM ligand during final concentration using centrifugal ultrafiltration (Amicon Ultra-15 filters with a molecular weight cut-off of 50 kDa), once for α-naphthoflavone and three times for estradiol. Crystals of the ancestral CYP1B1 protein with α-naphthoflavone were then grown at 20 °C using the sitting-drop vapor diffusion method in 96-well plates by mixing 0.5 μL N98_CYP1B1_Mammal/α-naphthoflavone (protein at 290 μM as determined by absolute spectrum) with 0.5 μL crystallization solution (900 mM sodium citrate tribasic, 90 mM Tris base/HCl pH 7.0, 180 mM NaCl, 10% glycerol) and equilibrating against a 50 μL reservoir of the same crystallization solution. Cocrystallization with estradiol was performed at 20 °C in sitting-drop 24-well plates by mixing 0.9 μL N98_CYP1B1_Mammal/estradiol (290 μM) with 1.1 μL crystallization solution (1 M sodium citrate tribasic, 0.1 M Tris/HCl pH 7.0, 0.2 M NaCl) and equilibrating against 250 μL of the same crystallization solution. Cubic crystals grew in two to three days. Harvested crystals were cryoprotected using the respective crystallization solution supplemented with either additional 20% glycerol (α-naphthoflavone) or 22% glycerol (estradiol) before being flash cooled in liquid nitrogen. The N98_CYP1B1_Mammal/α-naphthoflavone diffraction data was collected on a single crystal at the Advanced Photon Source LS-CAT beamline 21-ID-G. The N98_CYP1B1_Mammal/estradiol diffraction data was collected on a single crystal on beamline 12-2 at the Stanford Synchrotron Radiation Lightsource.

Data processing for the N98_CYP1B1_Mammal/α-naphthoflavone dataset was performed with HKL2000 (37). The N98_CYP1B1_Mammal/estradiol dataset was processed in XDS (38) with scaling in AIMLESS (39). A molecular replacement solution for N98_CYP1B1_Mammal/α-

naphthoflavone was initially obtained using MolRep (40) using the CYP1B1/α-naphthoflavone crystal structure (PDB: 3PM0) as a search model (contrast score of 9.9). Inspection of packing and electron density as well as initial statistics after one round of refinement (R=0.34 and R_{free}=0.43) indicated a correct solution with two molecules in the asymmetric unit. A molecular replacement solution for the N98_CYP1B1_Mammal/estradiol structure was obtained using Phaser (41) and the N98_CYP1B1_Mammal/α-naphthoflavone (PDB: 6OYU) structure as a search model. The molecular replacement solution was successful with a log likelihood of 3,702 and translation function Z score of 58. For both structures multiple rounds of model building and refinement were performed using COOT (42) and PHENIX (43). Torsion angle non-crystallographic symmetry (NCS) with automatic group NCS group determination was employed in Phenix for the slightly lower resolution 17β-estradiol structure. Coordinates and restraints for α-naphthoflavone and estradiol were obtained from the CCD (Chemical ID: BHF, and EST respectively) and minimzed through PHENIX eLBOW (44) using AM1 geometry optimization.

Table 6.1 Data collection and refinement statistics.

	N98_CYP1B1_Mammal/ α-naphthoflavone (6OYU)	N98_CYP1B1_Mammal/ estradiol (6OYV)
Data Collection		
Space Group	I4	I4
Cell Dimensions (Å)	164.64, 164.64, 96.30	162.36, 162.36, 95.69
Molecules/a.u.	2	2
Resolution (Å)[a]	50.00-2.95 (3.00-2.95)	38.27-3.10 (3.31-3.10)
Total reflections[a]	207,156 (27,530)	154,025 (27,165)
Unique reflections[a]	27,530 (1,364)	22,678 (4,085)
Redundancy[a]	7.5 (6.6)	6.8 (6.6)
R_{pim}[a]	0.064 (0.788)	0.047 (0.883)
$<I/\sigma(I)>$ [a]	53.0 (5.0)	10.4 (1.2)
CC1/2[a]	0.998 (0.399)	0.998 (0.688)
Completeness (%)[a]	100 (100)	99.9 (97.6)
Refinement		
Resolution (Å)	48.15-2.95	38.27-3.10
No. reflections	26,007	22,189
R/R_{free} (%)	19.9 / 25.8	24.3 / 27.7
Ramachandran (%) Favored/Allowed/Outliers	94.41 / 5.25/ 0.34	93.66 / 5.89 / 0.45
No. non-H atoms/B factors (Å^2)		
Protein	7,244 / 54.11	7,159 / 111.56
Ligand	168 / 48.84	40 / 107.37
Heme	86 / 32.45	86 / 113.04
Glycerol	36 / 54.47	- / -
Water	44 / 38.13	- / -
RMSD bond (Å)	0.006	0.003
RMSD angle (°)	0.679	0.609
Coordinate error (max. likelihood based) (Å)	0.33	0.42

[a] Statistics for highest resolution shell shown in parentheses.

Structural comparisons with extant human P450 enzymes were executed using molecule B of N98_CYP1B1_Mammal complexed with α-naphthoflavone. While the two molecules in the asymmetric unit of each structure with both ligands are all similar, the rationale was that the α-naphthoflavone structure had higher resolution than the estradiol structure, that all of the human CYP1 structures were obtained with α-naphthoflavone as the ligand, and chain B of the α-naphthoflavone structure is most complete. By comparison chain A of the α-ancestral CYP1B1 naphthoflavone structure has an additional disordered gap for amino acids 448-452 comprising the K'-K" loop. Calculation of the active site void volumes for both N98_CYP1B1_Mammal/α-naphthoflavone and human CYP1B1 (PDB 3PM0) (26) was performed using VOIDOO (45) with probe radius of 1.4 Å and grid spacing of 1.0. For the N98_CYP1B1_Mammal/α-naphthoflavone structure it was necessary to add a network of water molecules to close the large cleft on the surface of the protein for the purposes of active site volume calculation. Structural alignments were performed using the super command in PyMOL (46). Sequence alignment was performed using CLC Genomics Workbench (47). Analysis of salt-bridges was performed in COOT (42) using a definition of ≤4 Å between the oxygen of Glu or Asp side chains and the nitrogen group(s) of Arg, His, or Lys (48,49). Aromatic and pi-cation stacking interactions were defined by selection of aromatic residues with ring-to-ring or ring-to-arginine guanidinium group distances of ≤4 Å using Schrödinger Maestro (Schrödinger, LLC, New York, NY, 2017). All salt-bridge and stacking interactions were visually inspected to ensure residue positions were well defined in the electron density. Structure figures were prepared using PyMOL (50) with electrostatic potential surfaces generated using APBS (51).

6.4 Results and Discussion

6.4.1 Comparison of Overall Structures: Ancestral CYP1B1 vs. Extant Human CYP1B1

Structures of the ancestral reconstructed mammalian CYP1B1 enzyme, N98_CYP1B1_Mammal, with α-naphthoflavone as the bound ligand revealed that this enzyme maintains a canonical cytochrome P450 fold (Figure 6.1A). Structural comparison with the extant human CYP1B1 (PDB: 3PM0) reveals the mammalian ancestor has similar Cα backbone positioning. The Cα root-mean-square deviation between the two structures with α-naphthoflavone is 1.43 Å (Figure 6.1A). While most of the boundaries for helices and beta-strand regions are also conserved, significant differences are observed in the conformation of the F helix (Figure 6.1A). First, the ancestral CYP1B1 has its F helix extended by eight residues compared to the extant human CYP1B1 (Figure 6.1B). Second, while the extant human CYP1B1 and all the other human CYP1 family enzymes have an unusual break near the middle of the F helix (26-28), the ancestral CYP1B1 F helix is intact throughout these residues (Figure 6.1B). The net result is that the C-terminus of the F helix is much farther away from the heme in the ancestral CYP1B1 structure than in the extant human structure and this substantially changes the active site accessibility and ligand binding (*vide infra*).
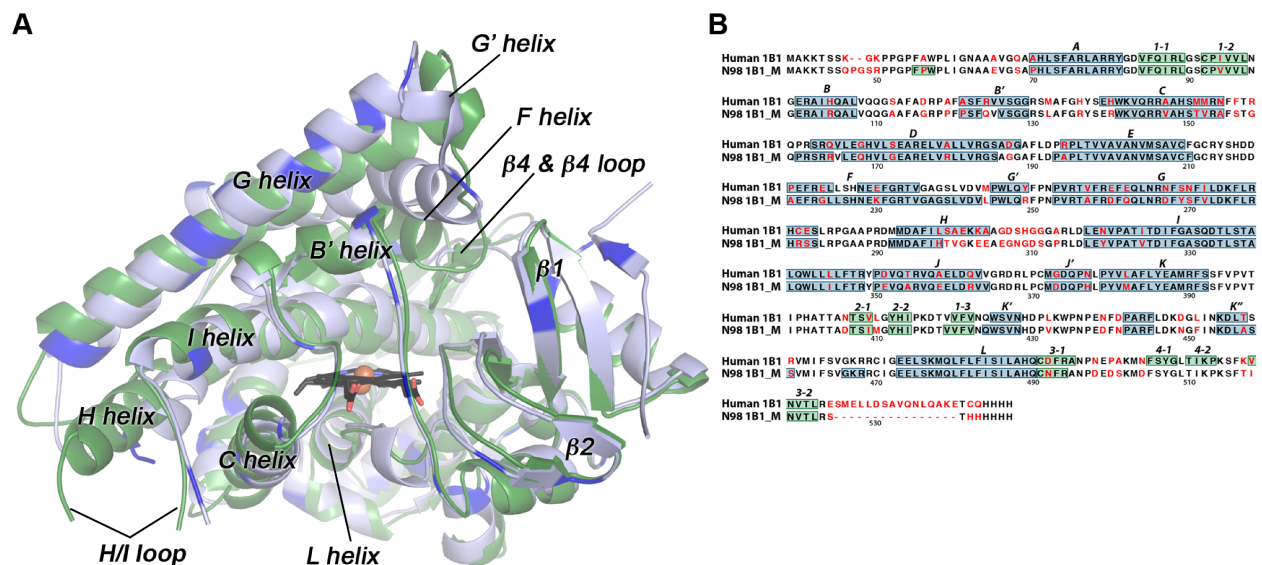
Figure 6.1 Comparisons of the mammalian ancestral and human CYP1B1 cytochrome P450 enzymes. A. The global structure of the extant human CYP1B1 (green) compared to that of the ancestral CYP1B1 (blue). Brighter blue in the ancestral CYP1B1 structure indicates the positions of differences in the amino acid sequences. Both were crystallized with α-naphthoflavone (not shown for clarity). The heme is shown as black sticks with the iron as an orange sphere. B. Aligned amino acid sequences for both enzymes are annotated with the non-conserved amino acids (in red text) and secondary structure features (helices highlighted in blue; beta strands highlighted in green; named above the sequence). Amino acid numbering corresponds to the full length human CYP1B1 sequence. N98 1B1_M is the N98_CYP1B1_Mammal sequence. Note: The extant human CYP1B1 structure (PDB 3PM0) was determined from a version of the protein that has a naturally-occurring single nucleotide polymorphism resulting in an Ala119Ser substitution.

The residues that form the immediate central active site cavity are largely conserved, as well as regions important for heme binding and proximal cysteine ligation such as the L-helix. Differences in the primary sequences of the CYP1B1 forms are distributed throughout the tertiary structure and generally occur farther from the heme and active site (Figure 6.1A, bright blue). Examination of the amino acid differences in the linear alignment (Figure 6.1B, red text) reveals some notable groupings of divergent amino acids compared to the human enzyme. Portions of the H helix and H/I loop have multiple substitutions, but there is considerable disorder in this region (Figure 6.1A) for both the human structure (amino acids 308-311 of the H/I loop disordered) and the ancestral CYP1B1 structure (amino acids 300-311 of the H/I loop disordered) which precludes structural comparisons.

6.4.2 Ancestral CYP1B1 Structure with α-Naphthoflavone

Co-crystallization of the mammalian ancestral CYP1B1 with the flavonoid α-naphthoflavone was initially pursued to facilitate comparison with the human CYP1B1 structure containing the same ligand. Surprising substantial differences were first observed in ligand binding. While the human CYP1B1 enzyme has a single copy of α-naphthoflavone (Figure **6**.**2**A) within a relatively small, planar, enclosed active site cavity, the ancestral CYP1B1 structure displays clear evidence for binding *four* copies of α-naphthoflavone within a substantially expanded active site (Figure **6**.**2**B), largely generated by reconfigurations in helix F discussed below.
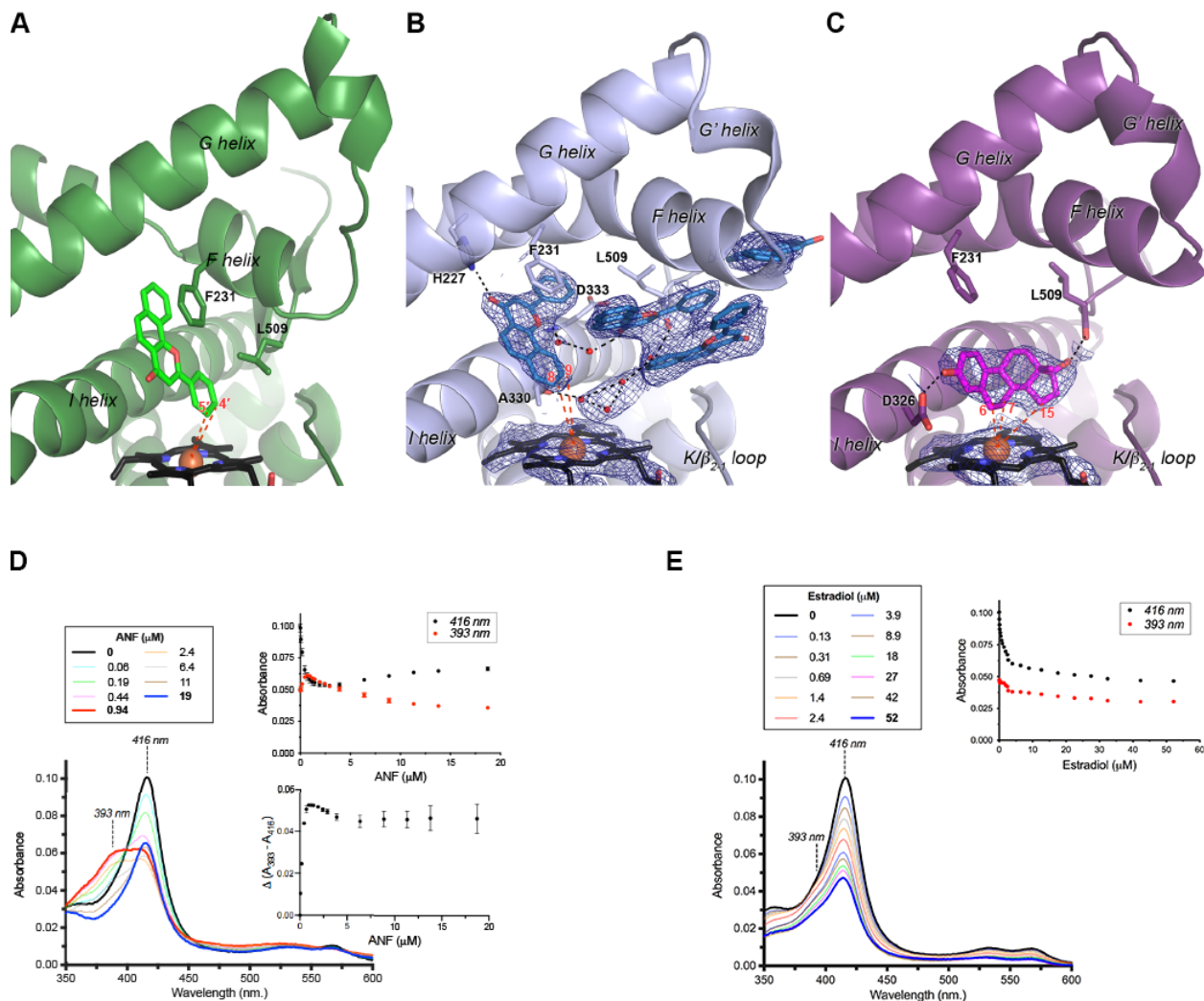
Figure 6.2 **Comparison of CYP1B1/ligand interactions.** Comparison of CYP1B1/ligand interactions. A. The extant human CYP1B1 crystal structure (PDB 3PM0, ribbons) with α-naphthoflavone (green sticks) shown from the same perspective as the ancestral CYP1B1 structures in B and C. B. The mammalian ancestral CYP1B1 structure (ribbons) with α-naphthoflavone (blue sticks) clearly indicates four copies of this ligand in the active site. All four are located higher up in the active site, while a putative water network (red spheres) is closer to the heme (black sticks). C. The mammalian ancestral CYP1B1 structure (ribbons) with estradiol (purple sticks) has the same overall structure as when α-naphthoflavone is bound, but only one copy of estradiol is present, located near the heme and oriented with C6, C7, and C15 closest to the heme (black sticks) iron (orange sphere). In both B and C, blue mesh represents electron density for the respective ligands and heme using a sigmaA-weighted composite omit map at 1 sigma. D. Titration of the mammalian ancestral CYP1B1 with α-naphthoflavone. The initial, ligand-free spectrum (main plot, black line) is consistent with water coordination of the heme iron (λmax=416 nm). As α-naphthoflavone is titrated in, the 416 nm peak decreases in intensity and a shoulder at 393 nm, consistent with water displacement by the ligand, increases to approximately equal intensity (main plot, red line=titration midpoint). However, upon further addition of α-naphthoflavone the 393 peak progressively regresses, leaving only the peak at 416 nm (main plot, blue line). The upper inset emphasizes the decrease in the 416 nm peak (black points) and the increase and subsequent decrease in the 393 nm peak (red points). Thus a simple K_d cannot be fit to these absorbance changes (lower inset). These ligand concentration-dependent spectral changes suggest that α-naphthoflavone is positioned near the heme at low ligand concentrations but relocates to allow water interaction with the heme at high ligand concentrations. The structure in B is most consistent with the high concentrations of ligand employed in crystallization. E. In contrast, titration of estradiol into the mammalian ancestral CYP1B1 reveals a progressive decrease in the 416 nm peak (main plot) associated with water coordination to the heme iron with concomitant but smaller decreases at 393 nm (upper inset).

In the ancestral CYP1B1 structure the benzochromenone core of the α-naphthoflavone closest to the heme essentially occupies the same space as it does in the human structure, tilted toward the central I helix. However the ligand is flipped by 180° such that the phenyl ring is directed toward the heme in the human structure and away from the heme in the ancestral CYP1B1 complex. As a result, in the ancestral CYP1B1 complex α-naphthoflavone atoms C8 and C9 on the fused ring are closest to the heme iron, but with distances of 7.4 and 7.2 Å respectively. This orientation is consistent with these atoms as likely sites of metabolism, as opposed to the orientation found in the human CYP1B1 structure. However, this α-naphthoflavone molecule would need to move closer to the heme (to 4-5 Å) for metabolism. In both α-naphthoflavone complexes, this ligand forms a pi-pi stacking interaction with the conserved F helix Phe-231 (Figure **6.2**A and 6.2B). This interaction was also key in α naphthoflavone binding within human CYP1A1 (27) and CYP1A2 (28). In all three human structures the positioning of this Phe helped to define the narrow and planar active site architecture. While this interaction is maintained in the ancestral enzyme, repositioning of the end of the F helix 5-8 Å toward the distal side means that Phe-231 in the F helix is located higher up in the active site, consistent with the ligand location further from the heme. An additional interaction is formed with this same copy of α-naphthoflavone in the N98_CYP1B1_Mammal structure. The F helix His-227 is a hydrogen bond donor to the α-naphthoflavone carbonyl oxygen. This interaction is not observed in the human CYP1B1 structure because the F helix break and repositioning of the C-terminal end of the F helix result in direction of this residue away from the active site cavity.

In the ancestral CYP1B1 complex the next two copies of α-naphthoflavone pack parallel with each other via pi stacking. They are mostly confined by van der Waals and/or hydrophobic interactions between the F helix and sequences immediately following the K helix. While the K

helix side is largely unperturbed compared to the human structure, the ancestral CYP1B1 F helix repositioning 5-8 Å toward the distal side opens up the active site to bulk solvent. The fourth α-naphthoflavone ligand is at the mouth of this cleft or channel. It is possible that the captured positioning of the α-naphthoflavone molecules in the ancestral structure represents a substrate entry and/or egress pathway.

The active site of the ancestral CYP1B1 enzyme also had residual electron density between the heme and one of the paired, mid-channel α-naphthoflavone molecules. This density was not consistent with α-naphthoflavone or any of the crystallization components, but rather with a water network (Figure **6.2**B). Hydrogen bonding appears to occur among these waters, as well as with atoms on the backbone of I helix residues Ala-330 and Asp-333, Leu-509 of the β4-loop, and with a carbonyl of one of the α-naphthoflavone molecules. The presence of water within the active site is not unexpected considering that the N98_CYP1B1_Mammal active site is ultimately open to bulk solvent (Figure 6.3A).

The striking differences in the conformations of the extant and ancestral CYP1B1 enzymes with α-naphthoflavone are the result of significant alterations in positioning of structural elements forming parts of the active site roof. The most significant structural change between is the conformation of the F helix (Figure 6.3A). The root-mean-square deviation for Cα in this region is 3.2 Å, compared to 1.43 Å overall. As described previously, the extant human CYP1B1 structure (and those of CYP1A1 and CYP1A2 with α-naphthoflavone) have a notable break in the F helix (Figure 6.3B, green) which is not typically observed in other family 2 P450 enzymes and which contains a conserved Phe that projects into the active site to pi stack with the planar elements of ligands (26-28). In the ancestral CYP1B1 structure this break is not observed and the F helix maintains its α-helical character as it passes above the active site (Figure 6.3B). This longer, intact

160

helix and a slight change in the tilt angle of the F helix overall mean that the C-terminal portion of the F helix is substantially farther away from the active site (Figure 6.3A). Repositioning of the F helix is accommodated by corresponding shifts in the G'- and G-helices but it is the F helix shift that is the major change opening up the channel from the active site proper to the protein surface (Figure 6.3A). In the extant human CYP1B1 structure the N-terminal half of the F helix interacts with the loop at the tip of the β4 system to close off this channel, but in the ancestral CYP1B1 structure this region is retracted in the opposite direction from the F helix shift and also contributes to the open channel, resulting in an ~16-fold increase in volume (Figure 6.3A).
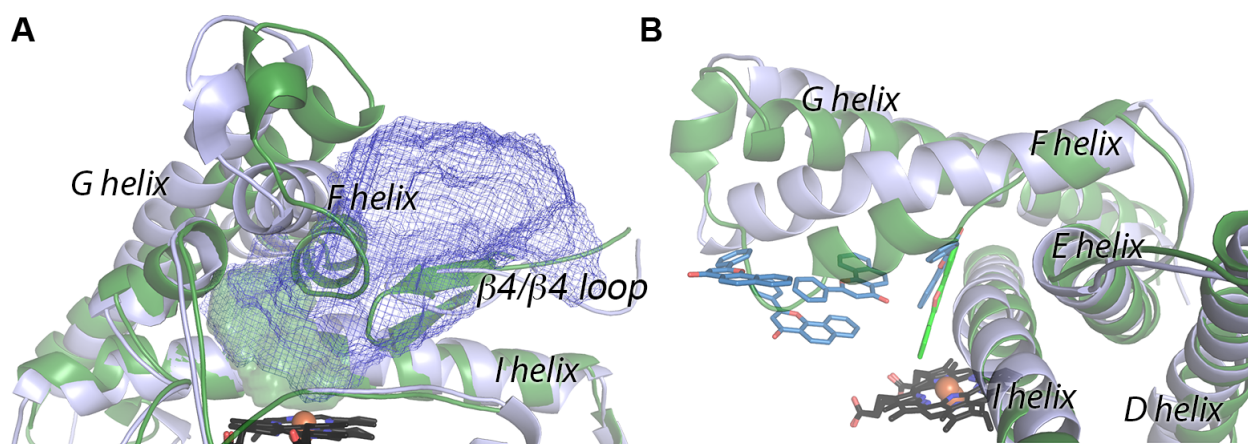
Figure 6.3 Comparison of ancestral CYP1B1 (blue) and extant human CYP1B1 (green) enzymes highlighting structural differences in helices F through G, the β4 loop, and helix I. Shown are the protein backbone (ribbons) and heme (black sticks). A) The active site for the extant human CYP1B1 (solid green) is much smaller than the active site and channel observed for the ancestral CYP1B1 (blue mesh). B) α-naphthoflavone ligands (colored sticks).

Another region of significant structural difference between the extant and ancestral enzyme structures occurs in the middle of the I helix as it crosses the heme and forms one wall of the active site. While the overall backbone and side-chain positions of the I helix are highly conserved, in the ancestral enzyme a single helical turn (residues 329-333) has a significant bulge such that Ala-330 protrudes into the lower part of the active site cavity (Figure 6.3B). This potentially restricts the ligand α-naphthoflavone from obtaining closer proximity to the heme in the ancestral structure.

6.4.3 Ancestral CYP1B1 Titrations with α-Naphthoflavone

To further probe α-naphthoflavone binding and interactions near the heme, the effects of ligand binding on the heme coordination were monitored by changes in the Soret heme absorbance. The as-isolated ancestral CYP1B1 protein has its Soret peak absorbance maximum at 416 nm (Figure **6**.2D, black spectrum), consistent with water coordination to the heme iron as is typical for isolated P450 enzymes in the oxidized state. Titration of this enzyme with α-naphthoflavone to concentrations at or below the protein concentration produced partial high-spin character with absorbance increases at 393 nm and decreases at 416 nm (Figure **6**.2D, red spectrum). This response is consistent with α-naphthoflavone binding in the active site and partially displacing coordinated water from the heme. Indeed, difference spectra showing these initial titrations are characteristic of these "type I" spectral changes (not shown). However, when adding α-naphthoflavone in excess of the ancestral N98-CYP1B1-Mammal enzyme concentration, the high-spin component at 393 nm began to decrease, eventually returning to a Soret maximum at absorbance at 416 nm indicating water binding to the heme (Figure **6**.2D, blue spectrum). This increase and subsequent decrease in the absorbance at 393 nm is more easily seen in Figure **6**.2D (upper inset, red points). With the reversal in absorbance maximum half way through the titration, the typical plot for the absorbance change vs. ligand concentration is not hyperbolic and cannot be fit to a simple two-state model for K_d determination (Figure **6**.2D, lower inset). Human CYP1B1 only shows this latter "reverse type I" spectral change upon binding α-naphthoflavone (52), which is likely the result of ligand binding in such a way as to promote water ligation. Overall, the spectral changes observed for the ancestral CYP1B1 enzyme are consistent with α-naphthoflavone binding near the heme iron at lower concentration where the ligand:P450 stoichiometry is 1:1 or

lower and reverting to water-coordinated heme when additional molecules pack into the protein, as observed in the crystal structure.

6.4.4 Ancestral CYP1B1 Metabolism of α-Naphthoflavone

Both the human CYP1B1 and N98_CYP1B1_Mammal enzymes convert α-naphthoflavone to three monooxygenated products (Figure 6.4, M1, M2, M3). M1 was the major product in both cases (12 ± 4% and 20 ± 6% relative yield for human CYP1B1 and N98_CYP1B1_Mammal respectively), followed by M2 (~1%), and M3 (<0.05%). Application of a 2-tailed, unpaired Student's *t*-test suggested there was no significant difference between the ratio of M1:M2 produced by the two P450 enzymes (however N98_CYP1B1_Mammal had a slightly higher ratio of M2:M3 compared to human CYP1B1 (15:1 vs. 13:1, p<0.01).
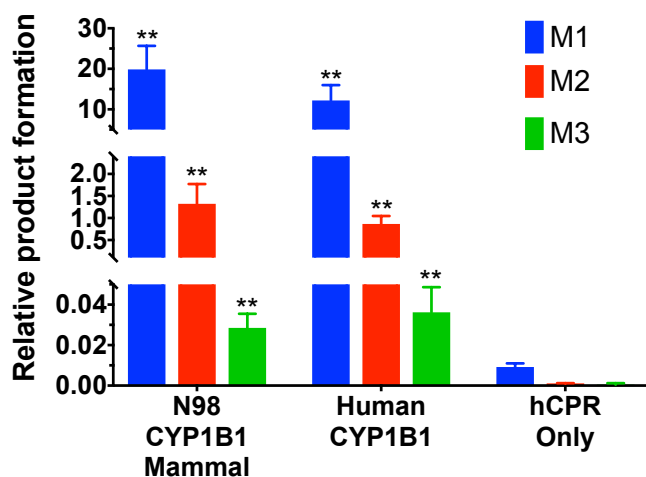
Figure 6.4 Metabolism of α-naphthoflavone by ancestral and extant CYP1B1 forms. The percentages of α-naphthoflavone converted to each of three metabolites (M1, M2 and M3) by the extant human CYP1B1 and the ancestral N98_CYP1B1_Mammal are compared to a negative control (bacterial membranes containing human NADPH-cytochrome P450 reductase but no P450). Reactions were carried out at 37 °C for 1 hour, with 0.5 μM P450 and 25 μM α-naphthoflavone. α-Naphthoflavone and its metabolites were analyzed by LC-MS/MS and quantified by the relative size of MS/MS fragment 103, which is present in the mass spectra of both. Data is the mean ± SD of n=3 reactions. Asterisks indicate statistically significant differences to the negative control (unpaired 2-tailed Student's t-test, * p<0.05, ** p<0.01, *** p<0.001).

Human CYP1B1 has previously been shown to metabolize α-naphthoflavone to more polar, unidentified metabolites (53), but α-naphthoflavone is also a potent inhibitor of human CYP1B1(4). In the current studies each of the three products produced by both ancestral and

human enzymes had a mass of 289, consistent with the addition of a single oxygen. While these metabolites could not be identified unambiguously by LC-MS alone, and the quantities produced precluded identification by NMR, the fragmentation patterns of M1 and M2 are consistent with an oxide or hydroxyl group added to one of the terminal rings, in positions 5-10 (Figure 6.7). The substrate specificity of the human CYP1 enzymes frequently overlaps so M1, the major metabolite for both human CYP1B1 and N98_CYP1B1_Mammal, may be the 5,6-oxide reported for human CYP1A1 and CYP1A2 (Figure 6.7) (54). Similar reasoning suggests that M2 may result from 7-hydroxylation and M3 from 6- or 9-hydroxylation as observed for rat CYP1A1 (Figure 6.8).

6.4.5 Ancestral CYP1B1 Structure with 17β-Estradiol

One of the key questions that arises from the ancestral CYP1B1 crystal structure with α-naphthoflavone is whether the open conformation of the protein was induced by the stacking of multiple ligand molecules within the active site channel or whether this is an intrinsic feature of the ancestral CYP1B1 protein. In order to potentially answer this question attempts were made to co-crystallize with several other ligands. 17β-Estradiol could be co-crystallized with the ancestral CYP1B1 by employing crystallization conditions similar to those yielding the α-naphthoflavone structure. The global structure of the mammalian ancestral 1B1 bound to 17β-estradiol was highly similar to the structure bound to α-naphthoflavone, with a root-mean-square deviation of 0.57 Å. Thus, the 17β-estradiol-bound structure also had a large channel from the active site proper extending between the F helix and β4-loop to the protein surface. However, only one copy of 17β-estradiol was present, located directly adjacent to the heme in the active site proper (Figure **6.2**C). Despite the open conformation, density was not observed for ordered water molecules in the 17β-estradiol structure. From this we can conclude that the overall open protein conformation observed is not dependent on the specific ligand or number of copies of the ligand. Thus it is likely that the

additional three α-naphthoflavone molecules take advantage of the open channel to bind fortuitously. As always, however, one cannot exclude the possibility that multiple protein conformations occur and that the specific conformation selected is dependent on its facility to pack into crystals for structure determination.

Within the active site, the positioning of sidechains is also largely conserved compared to the same ancestral enzyme bound to α-naphthoflavone. 17β-Estradiol extends across the heme, with its flat, unsubstituted planar α−surface approximately orthogonal to the heme plane and the steroidal A and B rings packing against the against the I-helix Gly-329-Ala-330 peptide bond (Figure **6**.2C). Because 17β-estradiol is positioned closer to the heme than α-naphthoflavone it does not interact with Phe-231 or other F helix residues, but 17β-estradiol does appear to make two hydrogen bonds with active site residues. The 17β-estradiol C3 hydroxyl is a hydrogen bond donor to the backbone carbonyl of Leu-509 in the β4 loop, while the C17 hydroxyl hydrogen bonds with the side chain of Asp-326 in the I helix. The overall result is that 17β-estradiol carbons 7 (4.2 Å), 15 (4.9 Å), and 6 (5.1 Å) are closest to the heme iron (Figure **6**.2C).

6.4.6   Ancestral CYP1B1 Titrations with 17β-Estradiol

Titration of the ancestral CYP1B1 protein with 17β-estradiol resulted in monotonic decreases in the Soret band at 416 nm, associated with Fe-water coordination, but no increases in absorbance at 393 nm corresponding to the high-spin state (Figure **6**.2E and 6.2E upper inset). Studies clearly indicate that this is a result of ligand binding and not protein instability as the reduced, carbon monoxide difference spectra of samples from the end of a titration are the same as those at the beginning of the titration (not shown). Corresponding titrations done in difference mode indicate 17β-estradiol binds with a classic type 1 binding mode, but the maximal response

is approximately four-fold weaker in comparison to α-naphthoflavone binding. Overall, however, these observations correspond to positioning of 17β-estradiol in the ancestral CYP1B1 structure.

6.4.7   Ancestral CYP1B1 Metabolism of 17β-Estradiol

It has been previously observed that the ancestral CYP1B1 enzyme is ~9-fold less active towards 17β-estradiol than human CYP1B1 (24) but also shows differences in the regioselectivity. Extant human CYP1B1 produces 4-hydroxy-17β-estradiol as the major metabolite, with smaller amounts of 2-hydroxyestradiol and trace amounts of a third hydroxy-17β-estradiol metabolite likely to be 15α-hydroxy-17β-estradiol. The ancestral CYP1B1 enzyme produces these same three metabolites but in approximately equimolar amounts (24). The orientation of 17β-estradiol observed in the crystallographic structure is consistent with the formation of 15α-hydroxy-17β-estradiol, but to form the 2- and 4-hydroxymetabolites, 17β-estradiol would need to reorient in the active site so that C2 and C4 were presented to the Fe for catalysis at these positions.

The regioselectivity of extant CYP1B1 forms for 4- or 2-hydroxylation is known to vary among species: human, dog, and monkey isoforms preferentially produce 4-hydroxy-17β-estradiol, while rodent isoforms produce more 2-hydroxy-17β-estradiol (55). This preference has been attributed to the residue at position 395 (55). Forms containing Val at this position produced more 4-hydroxy-17β-estradiol, while those containing Leu produced more 2-hydroxy-17β-estradiol, and exchanging these two residues reversed the regioselectivity. The current results suggest that additional factors influence regioselectivity because while the ancestral CYP1B1 has Val at position 395 position, it does not exhibit a strong preference for either 2- or 4-hydroxylation. In the ancestral CYP1B1 structure with 17β-estradiol, the terminal methyl of Val-395 is 3.6 Å from C16.

6.4.8   Structural Changes to the Redox Partner Binding Surface

One final notable structural difference between the extant and ancestral CYP1B1 structures occurs on the opposite side of the heme from the active site, on the proximal surface of the protein comprising part of the surface that binds the redox partner NADPH-cytochrome P450 reductase required for catalysis. In particular, the loop between the C and D helices contains three positively-charged Arg residues that have been implicated in electrostatic interactions with the negatively-charged surface of the reductase. This loop has different conformations in all three structures (Figure 6.5A). In the extant human CYP1B1 structure the C/D loop is positioned closer to the H helix (Figure 6.5A, green), while in the ancestral CYP1B1 structure with α-naphthoflavone it is displaced in the opposite direction, toward the L helix (Figure 6.5A, blue). In the ancestral CYP1B1 structure with 17β-estradiol the C/D loop adopts an intermediate conformation (Figure 6.5A, purple). In the ancestral CYP1B1 structures the C/D loop conformations are coincident with similar shifting of the H helix on one side and the loop preceding the J' helix on the opposite side. As a result, the placement of the positively charged C/D loop guanidine groups is different for all three structures. These differences are reflected in the surface shape and exposed charge for this region (Figure 6.5B, 6.5C, and 6.5D), in which the ancestral CYP1B1 structures display a less prominent concavity and positive charge. The C/D loop region in P450 enzymes is thought to be a critical binding surface for reductase, so it is possible that changes in the charged features in this region affect reductase binding for the ancestral CYP1B1 enzyme. The ancestral CYP1B1 has similar catalytic activity for α-naphthoflavone as the human CYP1B1 enzyme, suggesting that its C/D-loop conformation is compatible with reductase binding. However when the ancestral CYP1B1 enzyme is bound to 17β-estradiol, the enzyme has much lower activity towards production of all three metabolites than human CYP1B1. One possible explanation for this is that

the conformation of the CD loop observed in this structure prevents effective reductase binding and/or electron transfer.
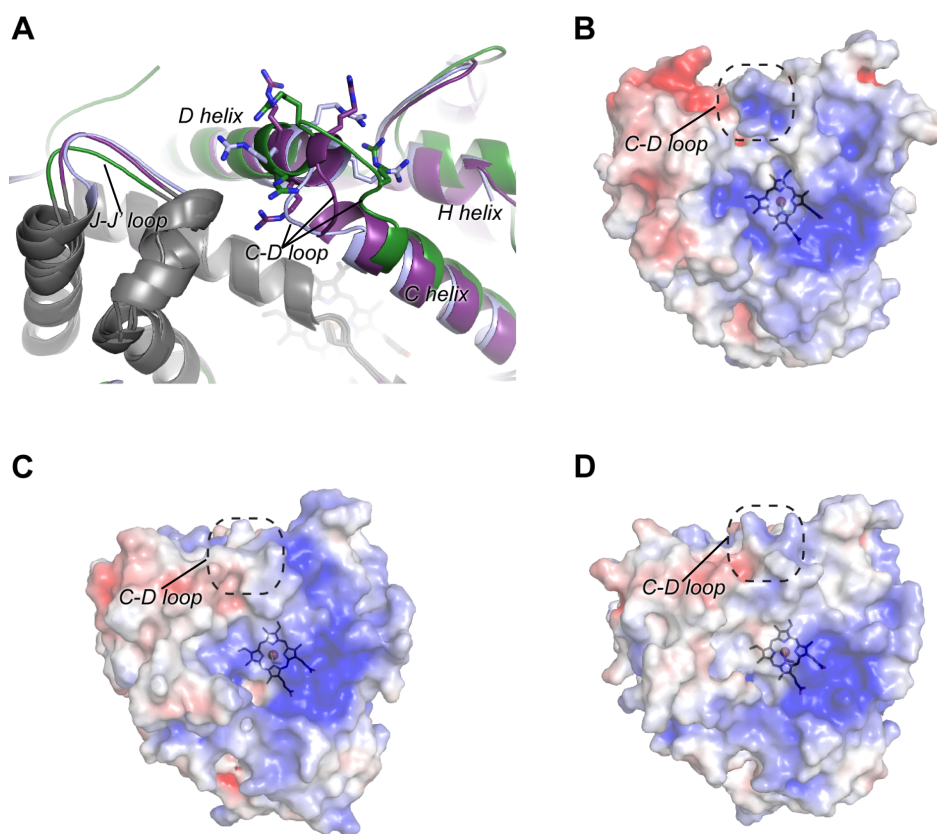
Figure 6.5   Comparison of the proximal surface of extant human CYP1B1 and ancestral CYP1B1.   A) Significant conformational differences are observed in the region of the C-D loop region of the human CYP1B1 (green) vs. the ancestral CYP1B1 crystallized with α-naphthoflavone (blue) vs. the ancestral CYP1B1 crystallized with estradiol (purple). As a result three positively-charged Arg residues (sticks) are repositioned, some of which have been implicated in binding the negatively-charged surface of its redox partner NADPH-cytochrome P450 reductase. B-D) Electrostatic surfaces (blue, positive; red, negative) for the proximal, reductase-binding surfaces of B) extant human CYP1B1 crystallized with α-naphthoflavone, C) the ancestral CYP1B1 crystallized with α-naphthoflavone, and D) the ancestral CYP1B1 crystallized with estradiol.

6.4.9   Structural Elements and Interactions Proposed to Confer Thermostability

A key consideration in engineering P450 enzymes for biocatalysis is thermostability. In the previous literature, several structural features have been proposed to contribute to thermostability, especially when comparing mesophilic and thermophilic P450s. This information is based on a limited dataset of four thermophilic P450 enzymes for which structures are available (48,56-58). A recent meta-analysis of these structures compared to their mesophilic P450 relatives (49) concluded that cytochrome P450 thermostability may correlate with: 1) smaller, more

compact enzymes, especially due to N-terminal truncation and shorter loops; 2) a preference for charged and hydrophobic residues vs. non-charged, polar and Ala residues; 3) increased salt bridges, particularly complex, extended salt-bridged networks; and perhaps 4) extended clusters of aromatic side chains. These enzymes were all soluble, microbial cytochrome P450 enzymes.

The advantages of using bacterial cytochrome P450 enzymes for biocatalysis often includes better stability, but many of them are highly specific for their substrates and the products generated. If a particular soluble P450 can be identified that performs a commercially useful transformation (59) or can be engineered to do so (60-63), then this is may be the most advantageous route. However, many of the less stable mammalian cytochrome P450 enzymes have evolved to intrinsically bind and metabolize a wide diversity of foreign compounds and may be more commercially useful if one could engineer in thermostability.

Although the difference in thermostability of the ancestral mammalian CYP1B1 enzyme compared to extant human CYP1B1 is not as dramatic as thermophilic *vs*. mesophilic bacterial P450 enzymes, it does provide one of the first real opportunities to determine if some of the same four concepts can confer increased thermostability in eukaryotic microsomal P450s.

First, the overall protein size and lengths of loops and N- and C-termini were compared. The ancestral CYP1B1 and extant human CYP1B1 structures reveal loop regions of similar length (Figure 6.1A and 6.1B). Only small differences are observed in a few of the loops and they are not always in the anticipated direction. The D/E loop is three residues *longer* in the ancestral CYP1B1 enzyme (Figure 6.1B). Likewise, the H/I loop appears to be six residues *longer* in the ancestral enzyme, a region that is disordered in both enzymes. A three-residue helical segment occurs in the ancestral CYP1B1 enzyme corresponding to the human K"/L loop, while a short, 2-strand β-sheet (the β-4 sheet) occurs in the human enzyme (Figure 6.1B). Although both enzymes

were truncated to remove the N-terminal transmembrane helix for crystallization, there are obvious differences in the remaining N-termini. In the ancestral CYP1B1 enzyme residues 48-60 could be modeled but not residues 61-67 (due to insufficient density to trace the backbone). By comparison the human CYP1B1 structure could only be modeled beginning at residue 68 where the A helix begins. Since they are present in the construct crystallized, the absence of electron density for residues 48-60 in the human 1B1 structure must be due to high flexibility. It is not obvious from the primary sequence why this part of the ancestor would be more stable, but this region forms a small beta-strand (Phe-55-Trp-57) that interacts with β-sheet 1. Additionally Trp-57 forms a potential face-to-edge aromatic interaction with Phe-74 (A-helix). At the C-terminal end of the protein, the ancestor is sixteen residues shorter, reducing the overall size by 2 kDa. In human CYP1B1 only six residues in the extended C-terminus could be modeled. However these were packing against symmetry related molecules (26) and may be more conformationally flexible in solution. This shorter C-terminus in the ancestral CYP1B1 enzyme is perhaps comparable to the shorter N-termini observed in soluble thermophilic P450 enzymes and may reduce conformational flexibility.

Second, since thermophilic bacterial P450 enzymes seemed to have more charged and hydrophobic residues and fewer non-charged, polar and Ala residues than related mesophilic P450 enzymes, the amino acid compositions of the ancestral CYP1B1 and extant human CYP1B1 were compared. The charged amino acids and non-charged but polar amino acids were very similar (≤0.5% different). The more thermostable ancestral CYP1B1 has 2% *fewer* hydrophobic amino acids, which is opposite to the trends in soluble P450 enzymes. Conversely, the ancestral enzyme also had 1% *fewer* Ala residues, which is consistent with the thermostable bacterial P450 trends. Of the twelve times that Ala in human CYP1B1 was replaced by another amino acid in the

ancestral CYP1B1, 11 of these substitutions were to non-conserved amino acids (Pro (5), Glu (3), Arg (1) or Ser (1)).

Third, salt bridge pairs and networks were compared between the two structures. In the extant human CYP1B1 structure thirteen two-residue salt bridges were found, while in the ancestor CYP1B1 structure fourteen were present. Evaluation of salt-bridge networks involving three or more residues revealed that human CYP1B1 had six and the ancestral CYP1B1 had eight (Table 6.2). It is useful to examine two-residue salt-bridges and networks that are *unique* to only one of the CYP1B1 enzymes (Figure 6.6A and 6.6B, spheres). In the extant human CYP1B1 five of the seven unique two-residue interactions and the one unique network occur within the same structural element, generally with residues found in close proximity within the primary sequence (Figure 6.6, black text; Table 6.2, red text but not bolded). Two unique two-residue salt-bridge occur between secondary structural elements (Figure 6.6A, colored text; Table 6.2, red and bolded text). In the mammalian ancestor, of the six unique two-residue salt-bridge interactions (Figure 6.6B, grey spheres), three of them occur between different secondary structure elements (Figure 6.6B, spheres with colored text; Table 6.2, red bolded text). Additionally, of the three unique networks in the ancestor (Figure 6.6B, black spheres), all three occur between secondary structure elements (Figure 6.6B, colored text; Table 6.2, red, bold text). Such interactions likely help stabilize multiple regions of the protein, and could be a contributor to the thermostability of the ancestor.
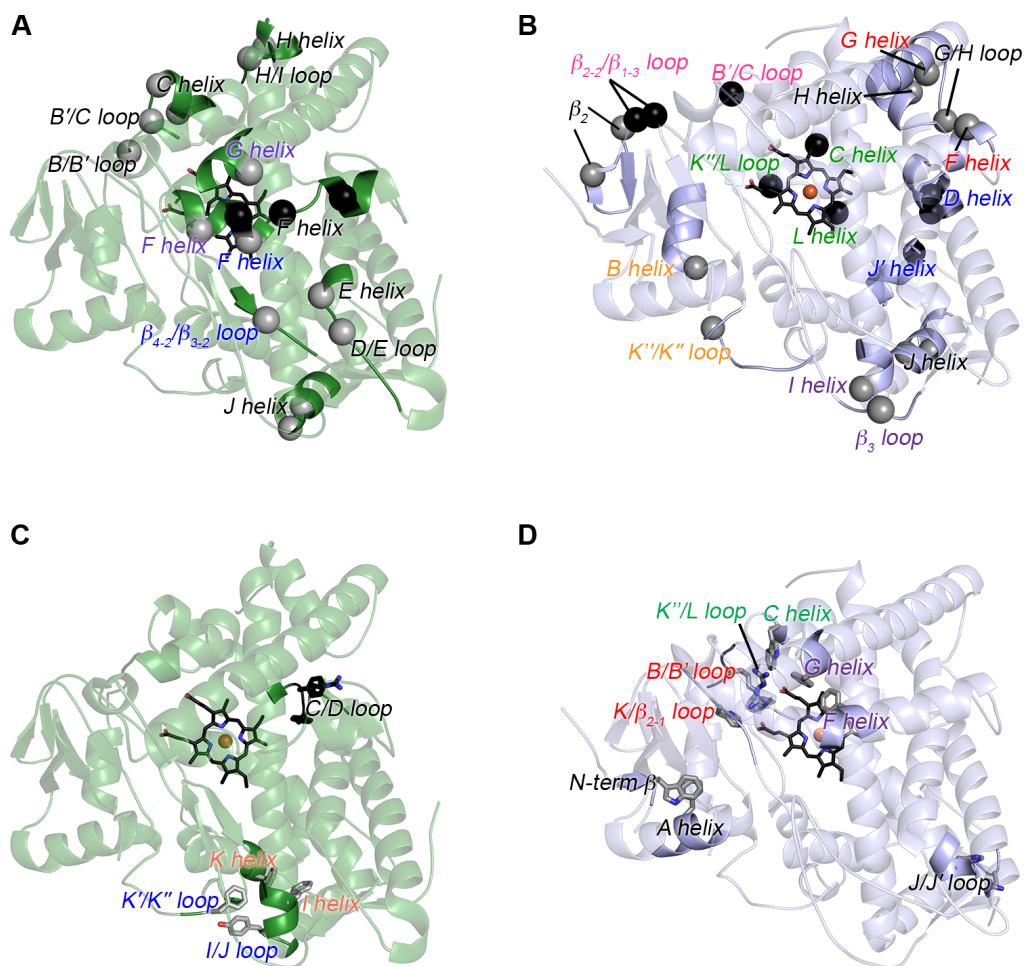
Figure 6.6 Analysis of unique salt bridges and aromatic interactions in human CYP1B1 and the ancestral CYP1B1 structures, both co-crystallized with α-naphthoflavone. A) Extant human CYP1B1 (green ribbons) and B) ancestral CYP1B1 (blue ribbons) showing unique two-residue salt bridges (grey spheres) and more extended networks (black spheres). Not shown (for clarity) are instances where a single new amino acid was added to a previously existing network, one for extant CYP1B1 and two for the ancestor (see Table 6.2) C) Extant human CYP1B1 (green ribbons) and D) ancestral CYP1B1 (blue ribbons) showing unique aromatic and pi-cation stacking interactions (grey sticks). In all four images, the text indicates the secondary structure element in which the indicated residues belong, with black text indicating that the residues are in the *same* secondary structure element and colored text indicating the pairings of residues that are in *distinct* secondary structure elements.

Finally, soluble thermophilic cytochrome P450 enzymes such as CYP119A1 (56) and CYP119A2 (57) from archaea have extended networks of aromatic residues. Analysis of aromatic and/or cation-pi stacking interactions in the human and ancestral CYP1B1 proteins indicated some differences (Table 6.3). Human CYP1B1 contained six two-residue pairs, three of which had stacking interactions with a third aromatic residue. By comparison, the ancestral CYP1B1 structure had eight two-residue aromatic or pi-cation stacking pairs, with only one stacking pair interacting with a third aromatic residue. Unique aromatic and pi-cation stacking interactions

between the two proteins are shown in Figure 6.6C and 6.6D. Human CYP1B1 contains two unique two-residue aromatic interactions (Figure 6.6C, grey sticks; Table 6.3, red) and one three-residue network (Figure 6.6C, black sticks; Table 6.3, red). Two of the aromatic/pi-cation stacking two-residue pairs are composed of residues that are more distant in the primary sequence and likely facilitate interactions between different parts of the tertiary protein structures (Figure 6.6C, colored text labels; Table 6.3, red bold). By comparison, the ancestral structure has five unique two-residue aromatic interactions (Figure 6.6D). Four of these interaction pairs occur between residues found in distinct secondary structure elements and thus are more likely to contribute to global protein structure.

6.5 Conclusions

The first structural evaluation of a reconstructed ancestral cytochrome P450 has reinforced several existing concepts about enzyme functionality and stability but also suggested some new ones. The ancestral CYP1B1 enzyme retains most of the active site residues of the extant human CYP1B1 enzyme and retains some of the metabolic capabilities and metabolite stoichiometries for some substrates (in this case α-naphthoflavone) while showing very different metabolic capacity and metabolite ratios for others (*e.g.* 17β-estradiol). Subtle amino acid substitutions outside the active site seem to control overall protein conformation, in this case restoring the helical nature of the entire F helix and opening up a broad channel from the active site to the protein surface. While ideas about shorter loops contributing to thermostability did not appear to apply here, a C-terminal truncation may be relevant. The somewhat more thermostable ancestral enzyme did show a few more electrostatic and aromatic interactions that could contribute to thermostability, but the locations of such interactions between distinct secondary structure elements, often far apart in the

173

primary sequence, may be more critical. Additional structures will be required to determine if these trends continue in even older reconstructions that have higher stability.

Table 6.2 Comparison of salt bridge interactions in extant human CYP1B1 *vs.* the ancestral CYP1B1 enzyme. Red text indicates interactions that are unique to that protein structure. These correspond to the residues show in Figures 6.6A and 6.6B, with the exception of partials, which are defined as one are two unique residues that interact with a shared network. Bold indicates that an interaction is between two distinct secondary structure elements. An asterisk indicates that the residue varies between the extant and ancestor enzymes.

Extant Human CYP1B1

2-residue salt bridges	Secondary Structure Location	Salt-bridge networks	Secondary Structure Location
D116* : H136*	B/B' loop : B'/C loop	E173 : R213: E176 : R175/ H216 : D217	D helix : E/F loop : D helix : E/F loop
E139 : K142	C helix	E223* : H227 : E230*	F helix
D192 : R194*	D/E loop : E helix	**R523 : D361 : R366**	**C-term : J helix : J/J' loop**
R233 : E260*	**F helix : G helix**	R390 : E387 : R444	K helix : K'/ K" loop
E229 : K514	**F helix : β4-2 /β3-2 loop**	R469 : E473 : K477	K"/L loop : L helix
D274 : R278	G helix	**R145 : HEM : R468/R117 : HEM : H401**	**C helix : HEM : K"/L loop : B/B' loop : K/β2-1**
D291 : H279	G/H loop : G helix	Total : 6	
D316 : K303*	H/I loop : H helix	Unique: 1 + 2 partial	
E318 : R130	**I helix : B'/C loop**		
D333 : K512	**I helix : β4-2**		
D351* : R355	J helix		
D374 : R368	J' helix : J-J' loop		
E438 : H429	K'-K" loop		
Total : 13			
Unique: 7			

Ancestral N98_CYP1B1_Mammal

2-residue salt bridges	Secondary Structure Location	Salt-bridge networks	Secondary Structure Location
R348 : E499	I helix : β3 loop	R145 : HEM : R468/R117) : HEM : H401	C helix : K"/L loop : β/β' loop : K/β2-1
R368 : D374	J/J' loop : J' helix	R444 : E387 : R390	K'/K" loop : K helix
E473 : K477	L helix	E474 : H149 : R469	L helix : C helix : K"/L loop
E220 : K275	F helix : G helix	D373* : R163 : E167	J' helix : D helix
D274 : R278	G helix	H216 : E176 : R179*	E/F loop : D helix
R290 : D294	G/H loop : H helix	R523 : D361 : R366	C-term : J helix : J/J' loop
E100 : K433	B helix : K'/K" loop	K416 : D417 : R136*	β2-2/β1-3 loop : B'/C loop
D291 : H279	G/H loop : G helix	E318 : R130 : D316	I helix : B'/C loop : H/I loop
D333 : K512	I helix : β4-2	Total : 8	
E359 : R362*	J helix	Unique: 3 + 2 partial	
D406* : H413	β2		
E438 : H429	K'-K" loop		
R213 : E173	E/F loop : D helix		
D504* : K514	β3/β4 loop region		
Total : 14			
Unique: 6 + 1 partial			

Table 6.3 Comparison of aromatic and pi-cation stacking interactions in extant human CYP1B1 *vs.* the ancestral CYP1B1 enzyme. Red text indicates interactions that are unique to that protein structure. These correspond to the residues show in Figures 6.6C and 6.6D, with the exception of partials, which are defined as one are two unique residues that interact with a shared network. Bold indicates that an interaction is between two distinct secondary structure elements. An asterisk indicates that the residue varies between the extant and ancestor enzymes.

Extant Human CYP1B1	
Aromatic or cation-pi stacking interactions	**Secondary Structure Location**
H71 : W425 : H429	A helix : K′ helix : K′-K″ loop
F120 : F123 : F134	B-B′ loop : B' helix : B'-C loop
H149 : R153	C helix
F155 : R158*/F156*	C-D loop
F346 : F384	I helix : K helix
Y349 : F440	I/J loop : K′-K″ loop
Total : 6	
Unique: 3 + 1 partial	

Ancestral N98_CYP1B1_Mammal	
Aromatic or cation-pi stacking interactions	**Secondary Structure Location**
W57 : F74	N-term-β : A helix
H71 : W425 : H429	A helix : K′ helix : K'-K″ loop
R117 : H401	B-B' loop : K-β2-1 loop
F123 : F134	B′ helix : B′-C loop
W141 : R468	C helix : K″-L loop
H149 : R153	C helix
F231 : F261	F helix : G helix
R366 : H489	J-J' loop
Total : 8	
Unique: 5	

Table 6.4 MRM transitions used for quantification of α-naphthoflavone, metabolites and internal standard.

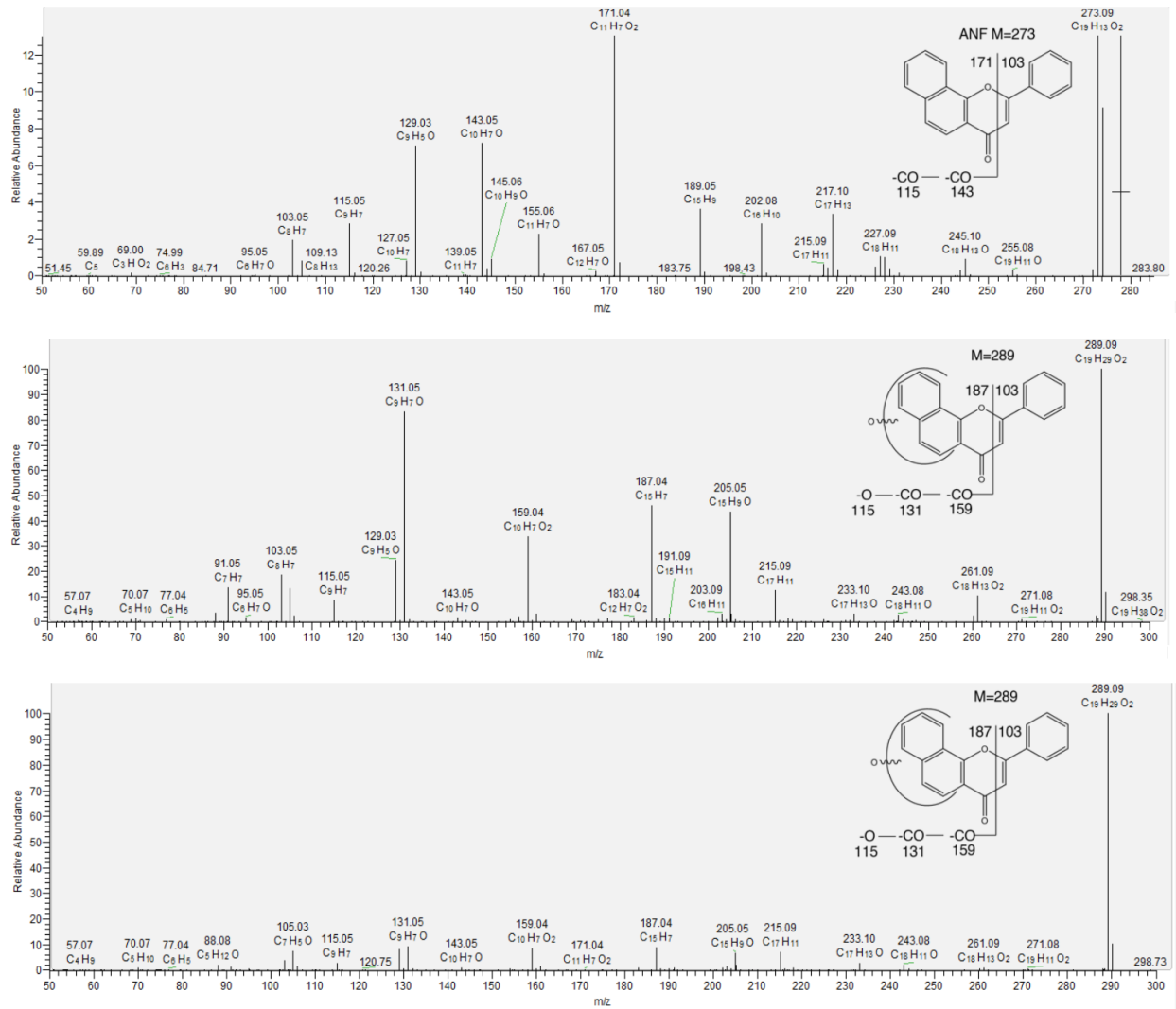| Compound	Q1	Q3	CE	EP
α-naphthoflavone	273.1	115.1	55	10
	273.1	129.1	55	10
	273.1	143.2	55	10
	273.1	171.2	55	10
	273.1	202.3	55	10
	273.1	226.2	55	10
Progesterone (IS)	315.2	97.1	28	8
	315.2	109.1	28	8
	315.2	297.2	47	8
OH-α-naphthoflavone	289.09	215.09	55	10
	289.09	131.05	55	10
	289.09	115.05	55	10
	289.09	103.05	55	10
	289.09	95.05	55	10
	289.09	77.04	55	10

Figure 6.7 Mass fragmentation of α-naphthoflavone metabolites. Tandem mass spectra and predicted fragmentation patterns of (A) α-naphthoflavone, (B) M1, and (C) M2. The fragmentation patterns of M1 and M2 are consistent with the addition of a single oxygen to the two rings indicated.
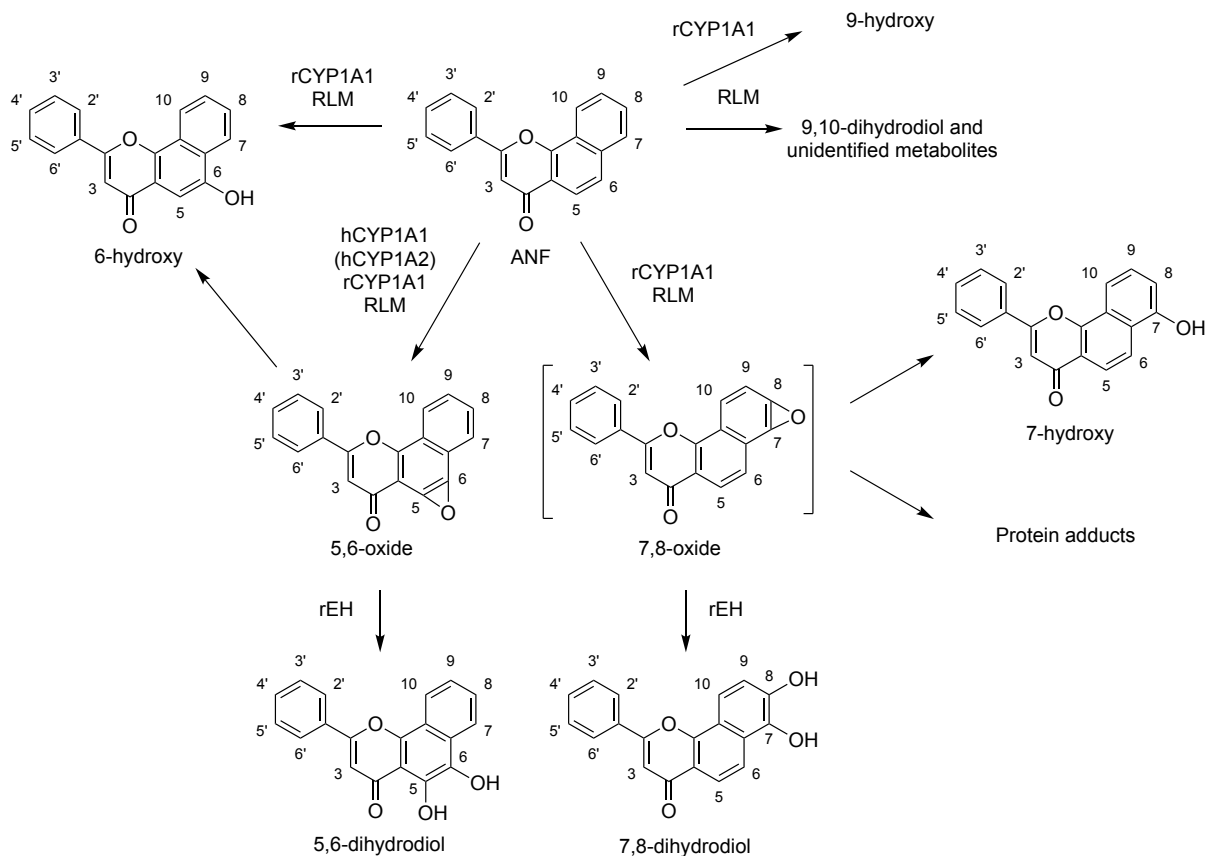
Figure 6.8 The known metabolic pathways of α-naphthoflavone (ANF) catalyzed by liver microsomes and recombinant CYP1A forms. The known α-naphthoflavone metabolic pathways catalyzed by CYP1 enzymes and rat liver microsomes (RLM) induced by either 2,3,7,8-tetrachlorodibenzodioxin *(64)*, 3-methylcholanthrene, β-naphthoflavone or phenobarbital *(65)* are summarized. The two main products of α-naphthoflavone metabolism by rat (r)CYP1A1 are the 5,6-oxide and 7,8-oxide *(64,65)*. These compounds are further metabolized by rat epoxide hydrolase (rEH) to form the respective dihydrodiols. In the absence of rEH, the 5,6-oxide is chiefly observed, as the 7,8-oxide is unstable and will interact with nucleophilic groups on proteins, or spontaneously convert to the 7-hydroxy-α-naphthoflavone product *(54,66)*. Recombinant human (h)CYP1A1, and to a lesser extent hCYP1A2, produced the 5,6-oxide as the main product, which was converted to the 5,6-dihydrodiol in the presence of rEH *(54)*. The 7,8-dihydrodiol was not observed even in the presence of rEH. Other minor metabolites produced by recombinant rCYP1A1 or induced RLM are also shown. Earlier studies *(67-69)* generally agreed with the metabolite assignments shown here, except that the 7,8-dihydrodiol was originally assigned the structure now defined as the 9,10-dihydrodiol.

REFERENCES

1. Nebert, D. W., Roe, A. L., Dieter, M. Z., Solis, W. A., Yang, Y., and Dalton, T. P. (2000) Role of the aromatic hydrocarbon receptor and [Ah] gene battery in the oxidative stress response, cell cycle control, and apoptosis. *Biochemical pharmacology* **59**, 65-85

2. Noakes, R. (2015) The aryl hydrocarbon receptor: a review of its role in the physiology and pathology of the integument and its relationship to the tryptophan metabolism. *Int J Tryptophan Res* **8**, 7-18

3. Hankinson, O. (2016) The role of AHR-inducible cytochrome P450s in metabolism of polyunsaturated fatty acids. *Drug metabolism reviews* **48**, 342-350

4. Shimada, T., Gillam, E. M. J., Sutter, T. R., Strickland, P. T., Guengerich, F. P., and Yamazaki, H. (1997) Oxidation of xenobiotics by recombinant human cytochrome P450 1B1. *Drug Metab. Dispos.* **25**, 617-622

5. Choudhary, D., Jansson, I., Stoilov, I., Sarfarazi, M., and Schenkman, J. B. (2004) Metabolism of retinoids and arachidonic acid by human and mouse cytochrome P450 1B1. *Drug Metab Dispos* **32**, 840-847

6. Hayes, C. L., Spink, D. C., Spink, B. C., Cao, J. Q., Walker, N. J., and Sutter, T. R. (1996) 17b-Estradiol hydroxylation catalysed by human cytochrome P450 1B1. *Proc. Natl. Acad. Sci. USA* **93**, 9776-9781

7. Shimada, T., Wunsch, R. M., Hanna, I. H., Sutter, T. R., Guengerich, F. P., and Gillam, E. M. J. (1998) Recombinant human cytochrome P450 1B1 expression in *Escherichia coli*. *Archives of biochemistry and biophysics* **357**, 111-120

8. Crespi, C. L., Penman, B. W., Steimel, T. D., Smith, T., Yang, C. S., and Sutter, T. R. (1997) Development of a human lymphoblastoid cell line constitutively expressing human CYP1B1 cDNA: Substrate specificity with model substrates and promutagens. *Mutagenesis* **12**, 83-89

9. Ma, X. C., Idle, J. R., Krausz, K. W., and Gonzalez, F. J. (2005) Metabolism of melatonin by human cytochromes P450. *Drug Metabolism and Disposition* **33**, 489-494

10. Murray, G. I., Melvin, W. T., Greenlee, W. F., and Burke, M. D. (2001) Regulation, function, and tissue-specific expression of cytochrome P450 CYP1B1. *Annual review of pharmacology and toxicology* **41**, 297-316

11. Murray, G. I., Taylor, M. C., McFadyen, M. C. E., McKay, J. A., Greenlee, W. F., Burke, M. D., and Melvin, W. T. (1997) Tumor-specific expression of cytochrome P450 CYP1B1. *Cancer research* **57**, 3026-3031

12. McKay, J. A., Melvin, W. T., Ah-See , A. K., Ewen, S. W., Greenlee, W. F., Marcus, C. B., Burke, M. D., and Murray, G. I. (1995) Expression of cytochrome P450 CYP1B1 in breast cancer. *FEBS Letters* **374**, 270-272

13. Shimada, T., Hayes, C. L., Yamazaki, H., Amin, S., Hecht, S. S., Guengerich, F. P., and Sutter, T. R. (1996) Activation of chemically diverse procarcinogens by human cytochrome P-450 1B1. *Cancer Res.* **56**, 2979-2784

14. Shimada, T., Gillam, E. M. J., Oda, Y., Tsumura, F., Sutter, T. R., Guengerich, F. P., and Inoue, K. (1999) Metabolism of benzo[a]pyrene to trans-7,8-dihydroxy-7,8-dihydrobenzo[a]pyrene by recombinant human cytochrome P4501B1 and purified liver epoxide hydrolase. *Chemical research in toxicology* **12**, 623-629

15. Oda, Y., Aryal, P., Terashita, T., Gillam, E. M. J., Guengerich, F. P., and Shimada, T. (2001) Metabolic activation of heterocyclic amines and other procarcinogens in *Salmonella*

typhimurium umu tester strains expressing human cytochrome P4501A1, 1A2, 1B1, 2C9, 2D6, 2E1, and 3A4 and human NADPH-P450 reductase and bacterial O-acetyltransferase. *Mutat. Res. Genet. Toxicol. Environ. Mutagen.* **492**, 81-90

16.   Dragin, N., Shi, Z., Madan, R., Karp, C. L., Sartor, M. A., Chen, C., Gonzalez, F. J., and Nebert, D. W. (2008) Phenotype of the Cyp1a1/1a2/1b1-/- triple-knockout mouse. *Molecular pharmacology* **73**, 1844-1856

17.   Ward, J. M., Nikolov, N. P., Tschetter, J. R., Kopp, J. B., Gonzalez, F. J., Kimura, S., and Siegel, R. M. (2004) Progressive glomerulonephritis and histiocytic sarcoma associated with macrophage functional defects in CYP1B1-deficient mice. *Toxicol. Pathol.* **32**, 710-718

18.   Stoilov, I., Akarsu, A. N., and Sarfarazi, M. (1997) Identification of three different truncating mutations in cytochrome P4501B1 (CYP1B1) as the principal cause of primary congenital glaucoma (Buphthalmos) in families linked to the GLC3A locus on chromosome 2p21. *Hum. Mol. Genet.* **6**, 641-647

19.   Vasiliou, V., and Gonzalez, F. J. (2008) Role of CYP1B1 in glaucoma. *Annual review of pharmacology and toxicology* **48**, 333-358

20.   Jönsson, M. E., Woodin, B. R., Stegeman, J. J., and Brunstrom, B. (2011) Cytochrome P450 1 genes in birds: evolutionary relationships and transcription profiles in chicken and Japanese quail embryos. *PLoS One* **6**, e28257

21.   Goldstone, J. V., Goldstone, H. M. H., Morrison, A. M., Tarrant, A., Kern, S. E., Woodin, B. R., and Stegeman, J. J. (2007) Cytochrome P450 1 genes in early deuterostomes (tunicates and sea urchins) and vertebrates (chicken and frog): origin and diversification of the CYP1 gene family. *Mol. Biol. Evol.* **24**, 2619-2631

22.   Goldstone, H. M. H., and Stegeman, J. J. (2006) A revised evolutionary history of the CYP1A subfamily: gene duplication, gene conversion, and positive selection. *Journal of Molecular Evolution* **62**, 708-717

23.   Kawai, Y. K., Ikenaka, Y., Fujita, S., and Ishizuka, M. (2010) The CYP1D subfamily of genes in mammals and other vertebrates. *Mamm. Genome* **21**, 320-329

24.   Harris, K. L., Gumulya, Y., Foley, G., Syed, P., Janosik, T., Sandinge, A., Andersson, S., Jurva, U., Bodén, M., and Gillam, E. M. J. (unpublished) Insights into the evolution of an enzyme involved in chemical defense: resurrection and functional characterization of ancestral cytochrome P450 family 1 (CYP1) enzymes.

25.   Hayes, C. L., Spink, D. C., Spink, B. C., Cao, J. Q., Walker, N. J., and Sutter, T. R. (1996) 17 beta-estradiol hydroxylation catalyzed by human cytochrome P450 1B1. *Proc Natl Acad Sci U S A* **93**, 9776-9781

26.   Wang, A., Savas, U., Stout, C. D., and Johnson, E. F. (2011) Structural characterization of the complex between alpha-naphthoflavone and human cytochrome P450 1B1. *The Journal of biological chemistry* **286**, 5736-5743

27.   Walsh, A. A., Szklarz, G. D., and Scott, E. E. (2013) Human cytochrome P450 1A1 structure and utility in understanding drug and xenobiotic metabolism. *The Journal of biological chemistry* **288**, 12932-12943

28.   Sansen, S., Yano, J. K., Reynald, R. L., Schoch, G. A., Griffin, K. J., Stout, C. D., and Johnson, E. F. (2007) Adaptations for the oxidation of polycyclic aromatic hydrocarbons exhibited by the structure of human P450 1A2. *The Journal of biological chemistry* **282**, 14348-14355

29. Nishihara, K., Kanemori, M., Kitagawa, M., Yanagi, H., and Yura, T. (1998) Chaperone coexpression plasmids: differential and synergistic roles of DnaK-DnaJ-GrpE and GroEL-GroES in assisting folding of an allergen of Japanese cedar pollen, Cryj2, in *Escherichia coli*. *Appl Environ Microbiol* **64**, 1694-1699

30. Notley, L. M., de Wolf, C. J. F., Wunsch, R. M., Lancaster, R. G., and Gillam, E. M. J. (2002) Bioactivation of tamoxifen by recombinant human cytochrome P450 enzymes. *Chemical research in toxicology* **15**, 614-622

31. Gillam, E. M., Baba, T., Kim, B. R., Ohmori, S., and Guengerich, F. P. (1993) Expression of modified human cytochrome P450 3A4 in *Escherichia coli* and purification and reconstitution of the enzyme. *Archives of biochemistry and biophysics* **305**, 123-131

32. Johnston, W. A., Huang, W., De Voss, J. J., Hayes, M. A., and Gillam, E. M. (2008) Quantitative whole-cell cytochrome P450 measurement suitable for high-throughput application. *J Biomol Screen* **13**, 135-141

33. Omura, T., and Sato, R. (1964) The carbon monoxide-binding pigment of liver microsomes. I. Evidence for its hemoprotein nature. *The Journal of biological chemistry* **239**, 2370-2378

34. Guengerich, F. P. (2008) Analysis and characterization of enzymes and nucleic acids. in *Principles and Methods in Toxicology* (Hayes, A. W. ed.), 5 Ed., Raven Press, New York. pp 1973-2040

35. Hunter, D. J. B., Behrendorff, J. B. Y. H., Johnston, W. A., Hayes, P. Y., Huang, W., Bonn, B., Hayes, M. A., De Voss, J. J., and Gillam, E. M. J. (2011) Facile production of minor metabolites for drug development using a CYP3A shuffled library. *Metab. Eng.* **13**, 682-693

36. Bart, A. G., and Scott, E. E. (2018) Structures of human cytochrome P450 1A1 with bergamottin and erlotinib reveal active-site modifications for binding of diverse ligands. *The Journal of biological chemistry* **293**, 19201-19210

37. Otwinowski, Z., and Minor, W. (1997) Processing of X-ray diffraction data collected in oscillation mode. *Methods Enzymol* **276**, 307-326

38. Kabsch, W. (2010) XDS. *Acta Crystallogr. D* **66**, 125-132

39. Evans, P. R., and Murshudov, G. N. (2013) How good are my data and what is the resolution? *Acta Crystallogr. D* **69**, 1204-1214

40. Vagin, A., and Teplyakov, A. (1997) MOLREP: an automated program for molecular replacement. *J. Appl. Cryst.* **30**, 1022-1025

41. McCoy, A. J., Grosse-Kunstleve, R. W., Adams, P. D., Winn, M. D., Storoni, L. C., and Read, R. J. (2007) Phaser crystallographic software. *Journal of applied crystallography* **40**, 658-674

42. Emsley, P., Lohkamp, B., Scott, W. G., and Cowtan, K. (2010) Features and development of Coot. *Acta Crystallogr. D* **66**, 486-501

43. Adams, P. D., Afonine, P. V., Bunkoczi, G., Chen, V. B., Davis, I. W., Echols, N., Headd, J. J., Hung, L. W., Kapral, G. J., Grosse-Kunstleve, R. W., McCoy, A. J., Moriarty, N. W., Oeffner, R., Read, R. J., Richardson, D. C., Richardson, J. S., Terwilliger, T. C., and Zwart, P. H. (2010) PHENIX: a comprehensive Python-based system for macromolecular structure solution. *Acta Crystallogr. D* **66**, 213-221

44. Moriarty, N. W., Grosse-Kunstleve, R. W., and Adams, P. D. (2009) electronic Ligand Builder and Optimization Workbench (eLBOW): a tool for ligand coordinate and restraint generation. *Acta Crystallogr. D* **65**, 1074-1080

45.   Kleywegt, G. J., and Jones, T. A. (1994) Detection, delineation, measurement and display of cavities in macromolecular structures. *Acta Crystallogr. D* **50**, 178-185

46.   DeLano, W. L. (2017) The PyMOL Molecular Graphics System. version 1.8.6.2 Ed., Schrodeinger, LLC, New York

47.   CLC Genomics Workbench. 11.0 Ed.

48.   Yano, J. K., Blasco, F., Li, H., Schmid, R. D., Henne, A., and Poulos, T. L. (2003) Preliminary characterization and crystal structure of a thermostable cytochrome P450 from *Thermus thermophilus*. *The Journal of biological chemistry* **278**, 608-616

49.   Harris, K. L., Thomson, R. E. S., Strohmaier, S. J., Gumulya, Y., and Gillam, E. M. J. (2018) Determinants of thermostability in the cytochrome P450 fold. *Bba-Proteins Proteom* **1866**, 97-115

50.   Schrodinger, L. The PyMOL Molecular Graphics System, Version 1.8.6.2.

51.   Baker, N. A., Sept, D., Joseph, S., Holst, M. J., and McCammon, J. A. (2001) Electrostatics of nanosystems: application to microtubules and the ribosome. *Proceedings of the National Academy of Sciences of the United States of America* **98**, 10037-10041

52.   Shimada, T., Tanaka, K., Takenaka, S., Foroozesh, M. K., Murayama, N., Yamazaki, H., Guengerich, F. P., and Komori, M. (2009) Reverse type I binding spectra of human cytochrome P450 1B1 induced by flavonoid, stilbene, pyrene, naphthalene, phenanthrene, and biphenyl derivatives that inhibit catalytic activity: a structure-function relationship study. *Chem. Res. Toxicol.* **22**, 1325-1333

53.   Shimada, T., Yamazaki, H., Foroozesh, M., Hopkins, N. E., Alworth, W. L., and Guengerich, F. P. (1998) Selectivity of polycyclic inhibitors for human cytochrome P450s 1A1, 1A2, and 1B1. *Chemical research in toxicology* **11**, 1048-1056

54.   Bauer, E., Guo, Z., Ueng, Y. F., Bell, L. C., Zeldin, D., and Guengerich, F. P. (1995) Oxidation of benzo[a]pyrene by recombinant human cytochrome P450 enzymes. *Chemical research in toxicology* **8**, 136-142

55.   Nishida, C. R., Everett, S., and Ortiz de Montellano, P. R. (2013) Specificity determinants of CYP1B1 estradiol hydroxylation. *Molecular pharmacology* **84**, 451-458

56.   Yano, J. K., Koo, L. S., Schuller, D. J., Li, H., Ortiz de Montellano, P. R., and Poulos, T. L. (2000) Crystal structure of a thermophilic cytochrome P450 from the archaeon *Sulfolobus solfataricus*. *The Journal of biological chemistry* **275**, 31086-31092

57.   Oku, Y., Ohtaki, A., Kamitori, S., Nakamura, N., Yohda, M., Ohno, H., and Kawarabayasi, Y. (2004) Structure and direct electrochemistry of cytochrome P450 from the thermoacidophilic crenarchaeon, *Sulfolobus tokodaii* strain 7. *J. Inorg. Biochem.* **98**, 1194-1199

58.   Ho, W. W., Li, H., Nishida, C. R., de Montellano, P. R., and Poulos, T. L. (2008) Crystal structure and properties of CYP231A2 from the thermoacidophilic archaeon *Picrophilus torridus*. *Biochemistry* **47**, 2071-2079

59.   Serizawa, N., and Matsuoka, T. (1991) A two component-type cytochrome P-450 monooxygenase system in a prokaryote that catalyzes hydroxylation of ML-236B to pravastatin, a tissue-selective inhibitor of 3-hydroxy-3-methylglutaryl coenzyme A reductase. *Biochimica et biophysica acta* **1084**, 35-40

60.   Fasan, R., Chen, M. M., Crook, N. C., and Arnold, F. H. (2007) Engineered alkane-hydroxylating cytochrome P450(BM3) exhibiting nativelike catalytic properties. *Angewandte Chemie* **46**, 8414-8418

61. Glieder, A., Farinas, E. T., and Arnold, F. H. (2002) Laboratory evolution of a soluble, self-sufficient, highly active alkane hydroxylase. *Nat. Biotechnol.* **20**, 1135-1139

62. Jung, S. T., Lauchli, R., and Arnold, F. H. (2011) Cytochrome P450: taming a wild type enzyme. *Curr. Opin. Biotechnol.* **22**, 809-817

63. Lewis, J. C., and Arnold, F. H. (2009) Catalysts on Demand: Selective Oxidations by Laboratory-Evolved Cytochrome P450 BM3. *Chimia* **63**, 309-312

64. Andries, M. J., Lucier, G. W., Goldstein, J., and Thompson, C. L. (1990) Involvement of cytochrome P-450c in alpha-naphthoflavone metabolism by rat liver microsomes. *Mol. Pharmacol.* **37**, 990-995

65. Vyas, K. P., Shibata, T., Highet, R. J., Yeh, H. J., Thomas, P. E., Ryan, D. E., Levin, W., and Jerina, D. M. (1983) Metabolism of alpha-naphthoflavone and beta-naphthoflavone by rat liver microsomes and highly purified reconstituted cytochrome P-450 systems. *J. Biol. Chem.* **258**, 5649-5659

66. Vyas, K. P., Shibata, T., Highet, R. J., Yeh, H. J., Thomas, P. E., Ryan, D. E., Levin, W., and Jerina, D. M. (1983) Metabolism of alpha-naphthoflavone and beta-naphthoflavone by rat liver microsomes and highly purified reconstituted cytochrome P-450 systems. *The Journal of biological chemistry* **258**, 5649-5659

67. Coombs, M. M. (1982) The influence of various enzyme inducers on the microsomal metabolism of 7,8-benzoflavone. *Carcinogenesis* **3**, 229-230

68. Coombs, M. M., Bhatt, T. S., and Vose, C. W. (1981) Microsomal metabolites of the aryl hydrocarbon hydroxylase and tumour inhibitor 7,8-benzoflavone. *Carcinogenesis* **2**, 135-140

69. Nesnow, S., and Bergman, H. (1981) Metabolism of alpha-naphthoflavone by rat liver microsomes. *Cancer Res.* **41**, 2621-2626

CHAPTER 7

Conclusions and Future Directions[*]

The work in this dissertation has been aimed towards extending our understanding of human cytochrome P450 enzyme structure and how modulations to this structure contribute to the functional capabilities of these diverse enzymes. In the course of this dissertation multiple areas have been explored to this effect. The first area addressed was to determine if differences in interaction occur between the catalytic modulator protein cytochrome b_5 and distinct drug-metabolizing P450 enzymes. Second, a P450 involved in detrimental chemical carcinogenesis and toxin formation was probed to determine its structural malleability when binding structurally diverse ligands. Lastly, research was directed toward understanding the structural basis of increased thermostability in an ancestral-reconstructed P450 enzyme.

The initial study, presented in Chapter 2, examined the structural interactions of cytochrome b_5 towards a set of human xenobiotic P450 enzymes via solution NMR. Titrations of the human P450 enzymes CYP2A6, CYP2D6, CYP2E1, and CYP3A4 into ^{15}N-labeled b_5 resulted in line-broadening, permitting the identification of individual b_5 residues involved in the different binding interfaces. Mapping those residues onto the b_5 structure revealed that the b_5 / P450 interactions were both distinct and partially conserved among the four P450 enzymes tested. The participation of individual residues was confirmed by mutagenesis. Clearly electrostatic

_____

[*] The results and discussion of the docking experiments described in this chapter have been submitted for publication in the ISSX symposium report: Bart, A.G. & Scott, E. E. Substrate Recognition by Cytochrome P450s: Applying Structure to Understand Cytochrome P450 1A1 Metabolism. *Drug Metabolism Reviews*.

interactions play a key role in b_5 binding to P450 enzymes. In addition to distinctions observed in binding surfaces, the P450 isoforms also were observed to have differing apparent affinities towards b_5. Functionally cytochrome b_5 had varied effects on product formation between the P450 enzymes in this study, where a range of b_5 modulatory behavior on P450 activity was observed. These included cytochrome b_5 enhancing, inhibiting, or having no effect on product formation. Furthermore, the research performed in this study showed that b_5 had a common propensity increase the coupling of P450 reactions, regardless of the effect on product formation.

Alterations of P450 metabolism by b_5 introduces additional complexities in the prediction of drug pharmacokinetics, and could be a significant source of interindividual variability seen in certain drugs. Comprehensive understanding of how b_5 elicit differential responses in different P450 enzymes is currently unknown, however evidence is accumulating which supports allosteric mechanisms. To fully understand the allosteric effects of b_5 on P450 enzymes will require high-resolution structural investigations of these complexes. The research in chapter 2 provides initial steps towards this, however work remains to completely define these complexes, especially the residues on the P450 side. Generation of isotopically-labeled P450 samples for probing both interaction interfaces and dynamics will involve circumventing major hurdles such as stability and aggregation of human P450 enzymes.

Research presented in Chapters 3 and 4 were broadly aimed towards understanding the extent of conformational flexibility in the human P450 CYP1A1. This work was prompted by the initial CYP1A1 structure, which demonstrates a planar enclosed active site too small to accommodate its larger and/or nonplanar substrates. In Chapter 3 CYP1A1 was successfully co-crystallized with the structurally diverse substrates bergamottin and erlotinib. The resulting structure with the furanocoumarin bergamottin showed that it was accommodated within the

CYP1A1 active site by only small perturbations of sidechains and bound in an orientation consistent with non-reactive metabolite formation observed in corresponding catalytic assays. The second new complex was with the tyrosine kinase EGFR inhibitor erlotinib, which is a lung cancer drug. Erlotinib bound to CYP1A1 in an orientation consistent with CYP1A1 oxidation of this drug to yield reactive metabolites linked to adverse pharmacological effects. In both new CYP1A1 structures, the planar portions of the substrates occupied a similar region of the active site, aromatically stacking with a key phenylalanine side chain, similar to the arrangement observed in the initial CYP1A1 crystal structure with alpha-naphthoflavone. Both new compounds perturbed residues composing the active site roof, namely F and G helical regions. While bergamottin only somewhat expanded the CYP1A1 active site volume, with erlotinib the changes were more substantial, creating a channel to the protein surface through which ligands may access the otherwise buried active site.

The new structures of CYP1A1 presented in Chapter 3 expanded the known CYP1A1 active site and conformational landscape. Ideally one would like to solve a limited number of structures to define the range of enzyme flexibility since co-crystallization of human P450 enzymes is both heavily time and resource consuming. A question remains whether a sufficient range of CYP1A1 conformation has yet been explored to serve as effective start points for computational docking. The goal for docking would be to predict orientation and thus potential site of metabolism for other CYP1A1 substrates for which experimental structures are not available. In this pursuit a series of docking runs were initiated first to validate the approach with compounds whose orientations are known from solved crystal structures, then to do so for a series of CYP1A1 substrates that are clinical tyrosine kinase inhibitors, but for which such structural information is not known. In the initial validation docking runs, the experimental CYP1A1

187

structure determined with bergamottin successfully oriented bergamottin and erlotinib a high percentage of the time, but was less successful in yielding the correct orientation of alpha-naphthoflavone (Figure 7.1B). However, the CYP1A1 structure experimentally determined with erlotinib successfully oriented all three ligands (α-naphthoflavone, bergamottin, and erlotinib) with the dominant solution being in the correct orientation. This suggests that this CYP1A1/erlotinib structure might be most useful for docking an even wider range of compounds (Figure 7.1B). Thus, subsequent tests focused on its ability to correctly predict the binding orientations of three structurally diverse tyrosine kinase inhibitors also metabolized by CYP1A1: sunitinib, gefitinib, and ponatinib (Figure 7.1C). Sunitinib is approved for renal cell carcinoma and gastrointestinal tumors (1) and is primarily N-deethylated to a nontoxic metabolite by CYP1A1 (2). Gefitinib is used in the treatment of non-small cell lung cancer and is defluorinated by CYP1A1 to an initial para-hydroxyanaline moiety that can rearrange to a reactive quinone-imine that forms glutathione (GSH) and protein adducts linked to adverse pulmonary and hepatic effects (3). Finally, ponatinib is a BCR-ABL inhibitor used in the treatment of chronic myeloid leukemia that is oxidized by CYP1A1 on the purine, ethynl linkage and methylphenyl group, proposed to generate an epoxide also leading to GSH and protein adducts (4). Only the experimental CYP1A1 structure determined with erlotinib was able to correctly dock all three new drugs in orientations consistent with the known metabolites (Figure 7.1B&C). In comparison, the CYP1A1/bergamottin structure oriented only sunitinib in an orientation consistent with its known metabolite and produced a mix of correct and incorrect orientations of gefitinib (Figure 7.1B). The original CYP1A1/alpha-naphthoflavone structure was unable to accommodate the larger compounds sunitinib and ponatinib at all and predicted orientations for gefitinib that were inconsistent with its site of metabolism.
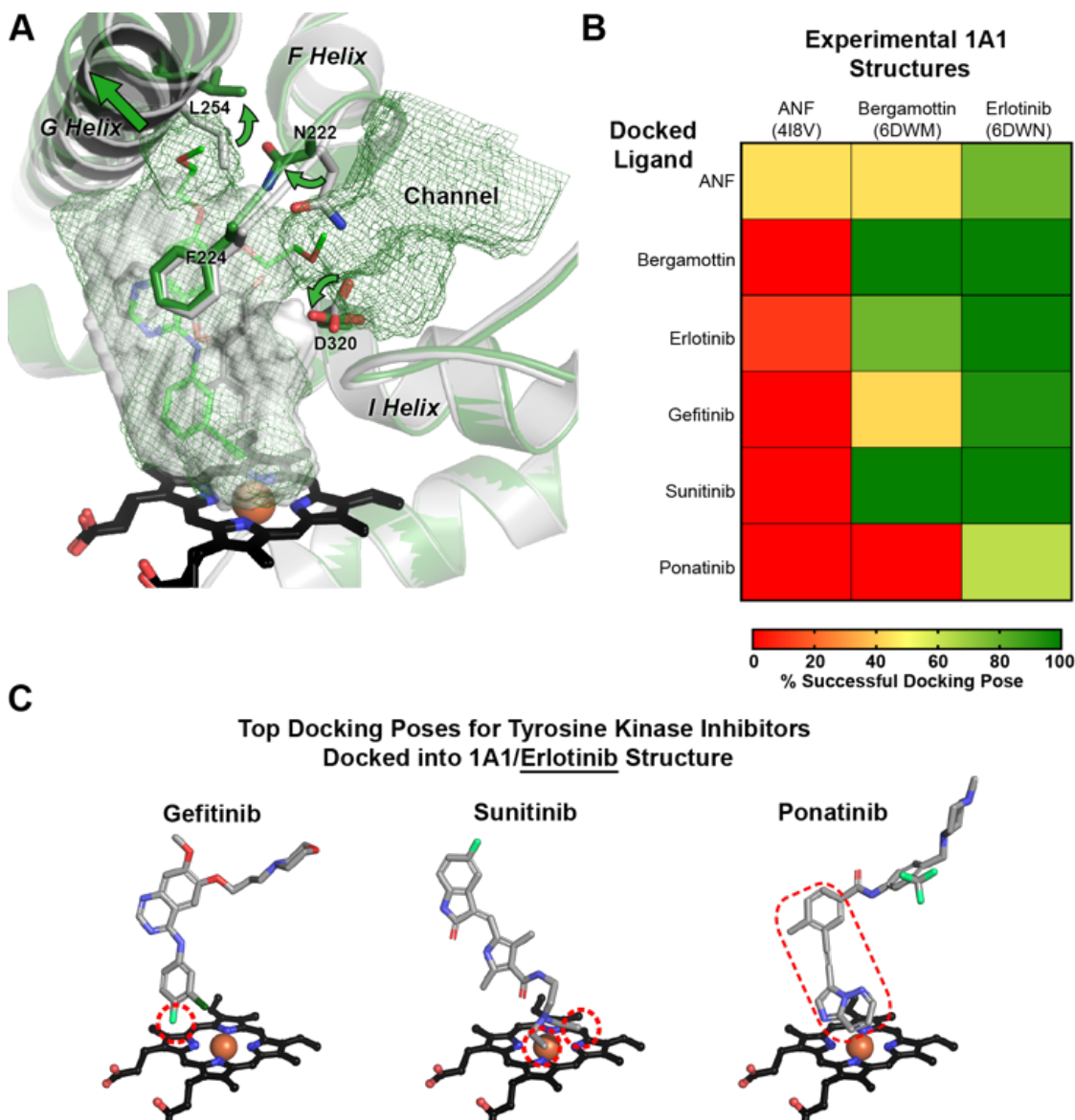
Figure 7.1 CYP1A1 experimental X-ray structures and docking results. A. Comparison of CYP1A1 active site bound to alpha-naphthoflavone (ANF) (light grey ribbons) vs. erlotinib (green ribbons), showing expansions in the active site cavity volume and shape (grey transparent surface for CYP1A1/ANF and green mesh for CYP1A1/erlotinib). Green arrows highlight differences in secondary structure elements or residues. B. Summary of docking results using the three currently available CYP1A1 crystal structures with various ligands metabolized by CYP1A1. The experimental structures and corresponding PDB codes are listed across the top and the ligand redocked or docked into each structure is listed on the left side. The percentage of docking poses that successfully recapitulated orientations consistent with the experimental structure (ANF, bergamottin, erlotinib) and/or known metabolites (gefitinib, sunitinib, ponatinib) are color coded according to the legend. C. Docking into the experimental CYP1A1/erlotinib structure was most successful in orienting known sites of metabolism (indicated red dashes) with 6 Å to the heme iron.

The CYP1A1 expanded active site cavity with a channel, identified in the

CYP1A1/erlotinib structure, performed the best in correctly orienting test compounds with a range

of sizes and structures. Other members of the P450 family 1, CYP1A2 and CYP1B1, are similarly

189

represented in the PDB by only one or two structures and may undergo similar conformational changes, but this is unknown at present. Finally, for CYP1A1 this new structural information may be useful in the redesign of clinical agents like gefitinib and ponatinib to remove metabolic liabilities related to patient toxicities and to better anticipate toxic metabolites for future pharmaceutical agents.

Even further conformational changes of CYP1A1 were observed when binding the candidate pan-Pim kinase inhibitor GDC-0339, presented in Chapter 4. In this structure CYP1A1 repositions one of the key elements in the active site, Phe224, outside the active site cavity. This side chain normally forms one side of the active site, confining it to a planar topology. Repositioning Phe224 serves to both accommodate some of the non-planar features of the ligand, as well as potentially priming the CYP1A1 active site for metabolism involving a proposed non-planar tetrahedral intermediate. These findings reinforce the concept that P450 enzymes are highly flexible and can adapt their active site for diverse substrates and reactions.

The work presented in Chapter 5 describes the binding and structural characterization of *seco*-duocarmycin prodrugs with CYP1A1 and CYP2W1. The question specifically addressed was if selectivity between the two P450 enzymes could be achieved by changes in the chirality of the analogs. Spectral binding experiments demonstrated that the *seco*-duocarmycin analogs ICT2700 (bio-activated by CYP1A1 and CYP2W1) and ICT2726 (not bioactivated by the P450 enzymes), bound CYP1A1 with relatively high affinity, but differed in spectral binding mode between ICT2700 and ICT2726. The change in chirality caused only slight alterations in binding affinity and/or mode for CYP1A1. However these same analogs displayed very distinct binding modes for CYP2W1. Additionally, CYP2W1 appeared to be very sensitive to changes in the analog chirality.

Moreover, Chapter 5 presents two co-crystal structures of specific enantiomers of ICT2700 and ICT2726 in complex with CYP1A1. The orientation of (*S*)-ICT2700 in the active site supported generation of metabolites that would not undergo bio-activation. This is contrary to results of CYP1A1 metabolism of racemic ICT2700, which showed formation of a bio-activated metabolite. This result could indicate CYP1A1 enantiomeric selectivity for bioactivation or the crystal structure only captured a predominate pose, since multiple CYP1A1-mediated metabolites of the racemic analog have been observed previously. In the other structure solved, CYP1A1 bound to (*S*)-ICT2726, orientation of this compound was not supportive for bio-activation, consistent with the absence of an activated metabolite during previous metabolism studies. Assays to test bioactivation of the *seco*-duocarmycin enantiomers are still ongoing, but the binding and structural study presented herein suggests changes in the chirality of the molecules can modulate binding and possibly orientations of these compounds. Ultimately the ongoing goal of this project is in the development of selective CYP2W1 *seco*-duocarmycin prodrugs for specific colon tumor bioactivation.

Finally, in Chapter 6 structural examination of an ancestral-resurrected P450 enzyme was reported in order to determine elements that may contribute to its increased thermostability. The structure of the mammalian ancestor CYP1B1 enzyme displayed significant expansions in active site cavity compared to human CYP1B1, which allowed the ancestral enzyme to bind multiple copies of the ligand alpha-naphthoflavone. There are multiple structural features that could contribute to the increased thermostability of the ancestral 1B1. These include greater structuring of the N-terminal region and increased salt-bridge and aromatic stacking interactions between secondary structures composed of residues distant in the primary sequence. This structure serves as a potential starting point for further enzyme engineering, with the eventual goal of producing

industrially viable P450 biocatalysts. Additionally, other ancestral reconstructed forms within Family 1, as well as other P450 families, are being pursued in order to determine whether the structural alterations we have observed in the N98-1B1-M structure hold true for other thermostable ancestors. Structural trends observed could lead to incorporating structure-based rational design to enhance P450 thermostability.

In summary, the research described herein has improved our structural understanding of human P450 enzymes in multiple aspects. The initial descriptions of the cytochrome b_5 complex with clinically relevant human P450 enzymes will aid future efforts of high-resolution structures of the complexes, with the goal of understanding how b_5 differentially effects P450 metabolism. Our improved knowledge of CYP1A1 structural flexibility makes it a source for enhancing predictions of detrimental metabolite formation and as a tool in further design of selective pro-duocarmycin cancer drugs. Lastly the structure of the first reconstructed ancestral P450 lays a groundwork in understanding the evolution of P450 structure and development of versatile P450 biocatalysts for biotechnological uses.

7.1 References

1.   Goodman, V. L., Rock, E. P., Dagher, R., Ramchandani, R. P., Abraham, S., Gobburu, J. V. S., Booth, B. P., Verbois, S. L., Morse, D. E., Liang, C. Y., Chiclambaram, N., Jiang, J. X., Tang, S., Mahjoob, K., Justice, R., and Pazdur, R. (2007) Approval summary: Sunitinib for the treatment of imatinib refractory or intolerant gastrointestinal stromal tumors and advanced renal cell carcinoma. *Clinical Cancer Research* **13**, 1367-1373

2.   Zhao, Q., Zhang, T., Xiao, X. R., Huang, J. F., Wang, Y., Gonzalez, F. J., and Li, F. (2019) Impaired clearance of sunitinib leads to metabolic disorders and hepatotoxicity. *Brit J Pharmacol* **176**, 2162-2178

3.   Li, X., Kamenecka, T. M., and Cameron, M. D. (2009) Bioactivation of the epidermal growth factor receptor inhibitor gefitinib: implications for pulmonary and hepatic toxicities. *Chemical research in toxicology* **22**, 1736-1742

4.   Lin, D., Kostov, R., Huang, J. T. J., Henderson, C. J., and Wolf, C. R. (2017) Novel Pathways of Ponatinib Disposition Catalyzed By CYP1A1 Involving Generation of Potentially Toxic Metabolites. *Journal of Pharmacology and Experimental Therapeutics* **363**, 12-19